UNIVERSITEIT VAN PRETORIA
UNIVERSITY OF PRETORIA
YUNIBESITHI YA PRETORIA

AB-stacked bilayer graphene films obtained on dilute Cu(Ni) foils using atmospheric pressure chemical vapour deposition

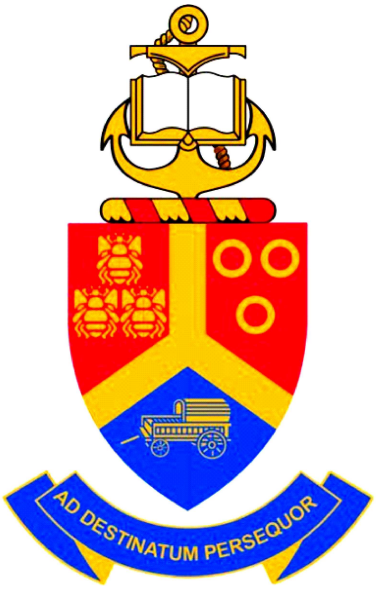

by

Moshawe Jack Madito

Submitted in partial fulfilment of the requirements for the degree

Philosophiæ Doctor (PhD)

in the Department of Physics

in the Faculty of Natural and Agricultural Sciences

University of Pretoria

Pretoria

Supervisor: Prof. N. Manyala

April 2016

University of Pretoria, Pretoria 0028, South Africa

Declaration

I hereby declare that the matter embodied in this thesis, *AB-stacked bilayer graphene films obtained on dilute Cu(Ni) foils using atmospheric pressure chemical vapour deposition*, is the result of investigations carried out by me under the supervision of Prof. N. Manyala, in the Physics department at the University of Pretoria South Africa and that it has not been submitted elsewhere for the award of any degree or diploma. In keeping with the general practice in reporting scientific observations, due acknowledgement has been made whenever the work described is based on the findings of other investigators.

SIGNATURE STUDENT:..... DATE:.....

Dedication

Hierdie tesis word gewy aan my ma, Mev M. A. Madito vir al wat sy voorsien het om my te help om hierdie mylpaal in my lewe te bereik, en ter nagedagtenis ann my oorlede suster, Kedibone Madito, mag die Here God haar siel in vrede laat rus.

This thesis is dedicated to my mother, Mrs M. A. Madito for all she has provided to help me to achieve this milestone in my life, and to the memory of my late sister, Kedibone Madito, may the Lord God rest her soul in peace.

Onse Vader wat in die hemele is, laat u Naam geheilig word... Amen.

Our Father in heaven, Hallowed be your name... Amen.

Acknowledgements

I would like to express my deep and sincere gratitude to my supervisor Prof. N. Manyala for his effort to ensure the quality of this work, which included innovative suggestions and positive criticisms. His continuous motivation, moral support and parental guidance have been of immense importance. My sincere thanks to the administrative staff Mrs E. Meyburgh and Mrs S. Seymore for all the assistance. I also thank the examiners for their valuable time, recommendation and suggestions.

Many thanks to the sponsors for financial support. This study was sponsored by the South African Research Chairs Initiative of the Department of Science and Technology, National Research Foundation (NRF) of South Africa (Grant No. 97994) and the financial support from the University of Pretoria.

My sincere thanks to Prof. Yury Gogotsi's group at Drexel University (United States) for its assistance on the XPS measurements, Dr. N. Mathe and Ms. R. Rikhotso at CSIR National Centre for Nano-structured Materials for their assistance with the TEM/SAED measurements, Dr. M. Madhuku at iThemba LABS for his assistance on the PEXI measurements, Mr S. Mpelane at the University of Johannesburg for his assistance on the HRTEM/SAED measurements, Prof. A. Hofmann at the University of Johannesburg for his assistance on the micro-Raman imaging, Mr W. A. Jordaan and Dr. C. J. Oliphant at National Metrology Institute of South Africa for their assistance on the TOF-SIMS and EBSD measurements, Dr. L. Prinsloo at the University of Pretoria for her assistance on the Raman measurements, Dr. E. Omotoso at the University of Pretoria for his assistance on the thermal evaporation and Dr. A. Bello at the University of Pretoria for proofreading manuscripts and thesis. My sincere thanks to the entire Microscopy centre at the University of Pretoria, especially Antoinette for all the assistance on the FE-SEM and AFM.

I would like to express my appreciation to Prof. N. Manyala's group members at the University of Pretoria for the assistance, support and useful discussions. I also thank my colleague postgraduate students at the University of Pretoria for the valuable and constructive interactions.

Lastly, I would like to thank my brother Modise, my sister Gadihele and my mother for their encouragements, moral support, love and prayers. I am greatly indebted to my daughter Reyaoboka Botlhale and her mother Ms. M. H. Mojaki (and her brothers and sisters) for their moral support, love and prayers. I humbly document my sincere thanks to my friend Mr. S. Mphanya (and his brothers) for his assistance and support through the difficult times.

Kind regards

Jack Madito

Abstract

Despite its favourability as a substrate in chemical vapour deposition (CVD), copper (Cu) substrate has a challenge of growing uniform large-area bilayer graphene films with continuous Bernal (AB) stacking. However, copper/nickel (Cu/Ni) thin films are known to grow uniform large-area AB-stacked bilayer graphene films. In this study, large-area or wafer-scale (on the scale of an entire foil) AB-stacked bilayer graphene films were prepared on commercial dilute Cu(0.5 at% Ni) foils (MaTeck) and Ni doped Cu foils (Alfa Aesar) using atmospheric pressure chemical vapour deposition (AP-CVD).

The Ni doped concentration and the Ni distribution in dilute Cu(Ni) foils were confirmed with inductively coupled plasma optical emission spectrometry (ICP-OES) and Proton-induced X-ray emission (PIXE). The electron backscatter diffraction (EBSD) maps showed that foils have continuous (001) surface orientation (Alfa Aesar) and diverse crystallographic surface (MaTeck). The increase in Ni surface concentration in foils was investigated with time-of-flight secondary ion mass spectrometry (TOF-SIMS) and X-ray photoelectron spectroscopy (XPS).

The quality of graphene, the number of graphene layers and the layers stacking order in synthesized bilayer graphene films were confirmed by Raman spectroscopy and electron diffraction measurements. A four point probe station was used to measure the sheet resistance of graphene films. In the Raman optical microscope images, a wafer-scale monolayer and large-area or wafer-scale bilayer graphene films were distinguished and confirmed with Raman spectra intensities ratios of 2D to G peaks. The Raman data and the electron diffraction data suggest a Bernal stacking order in the prepared bilayer graphene films. A four-point probe sheet resistance of graphene films confirmed a bilayer graphene film sheet resistance distinguished from that of monolayer graphene.

Wafer-scale AB-stacked bilayer graphene films were obtained on prepared dilute Cu(Ni) alloy foils. However, in commercial dilute Cu(0.5 at% Ni) foils, only large-area AB-stacked bilayer graphene films on monolayer graphene background could be obtained and the diverse crystallographic surface of a foil (EBSD data) could be a reason for incomplete wafer-scale bilayer graphene film. Since different Cu surfaces grow graphene films with different thicknesses. For instance, high index Cu surfaces and low index Cu(001), Cu(101) surfaces are known to grow multilayer graphene and Cu(111) surface to grow monolayer graphene.

This study clearly showed the capability of a dilute Cu(Ni) foil (Alfa Aesar) (prepared dilute Cu(Ni) alloy foil) for growing a wafer-scale AB-stacked bilayer graphene film (substrate size, $\approx$400 mm^2) compared to a commercial Cu(0.5 at% Ni) foil (MaTeck) which showed large-area bilayer graphene ($\approx$900 μm^2) and a pure Cu foil which showed discrete bilayer graphene domains (lateral size of $\approx$10 μm) on a monolayer graphene background. The capability of a dilute Cu(Ni) foil for growing a wafer-scale AB-stacked bilayer graphene film was ascribed to the (001) continuous surface orientation of a foil and the metal surface catalytic activity of Cu and Ni in a dilute Cu(Ni) foil. The results obtained in this study demonstrate the interest and potential insight of using dilute Cu(Ni) alloy foils as substrates in CVD for the synthesis of large-area (or wafer-scale) AB-stacked bilayer graphene films. This study contributes substantially to the on-going research on the growth of high-quality large-area AB-stacked bilayer graphene films on metal substrates using CVD.

Table of Contents

List of Figures

List of Figure does not include figures found in the publications (including the supporting information) presented at the end of chapter 5, 6 and 7.

List of Tables

List of Tables does not include tables found in the publications (including the supporting information) presented at the end of chapter 5, 6 and 7.

PART I

INTRODUCTION

CHAPTER 1

Introduction

1.1 Background and motivation

Graphene, a two-dimensional (2D) one-atom-thick sheet of sp^2-bonded carbon atoms in a honeycomb crystal lattice with atoms arranged in hexagonal pattern has attracted many research interest due to its remarkable unique properties (electronic, thermal and mechanical) and holds great promise for nanoscale electronics, bioelectronics and photonics [1-8]. Additionally, graphene can be used as transparent electrode materials in transparent liquid crystal displays, solar cells and micro-supercapacitors [9,10]. Among other carbon materials, graphene is the building block of the 3-dimensional (3D) graphite with Van der Waals dispersion force holding the layers together and the interlayer separation is 0.335 nm (Figure 1.1(a)) [1].

Graphene, though has remarkable unique properties has no bandgap ($E_g = 0$ as demonstrated in figure 1.1(b)) and the lack of bandgap in its electronic band structure greatly limits its applications in electronics [1,3,11-13]. For instance, in field effect transistors, this leads to low on-off ratio, typically <10 at room temperature. It is worth mentioning here that this ratio in Bernal (AB)-stacked bilayer graphene (that consists of two superimposed graphene layers shifted with respect to each other so that the A carbon atoms (from sublattice A) of one layer are situated directly above the B carbon atoms (from sublattice B) of the other layer and this produces an electronic structure that consists of two conical conduction and two conical valence bands which meet at the Dirac point) is as high as 100 at room temperature [14,15]. Therefore, for most electronic applications that rely on the presence of a bandgap, the bandgap opening is vital.

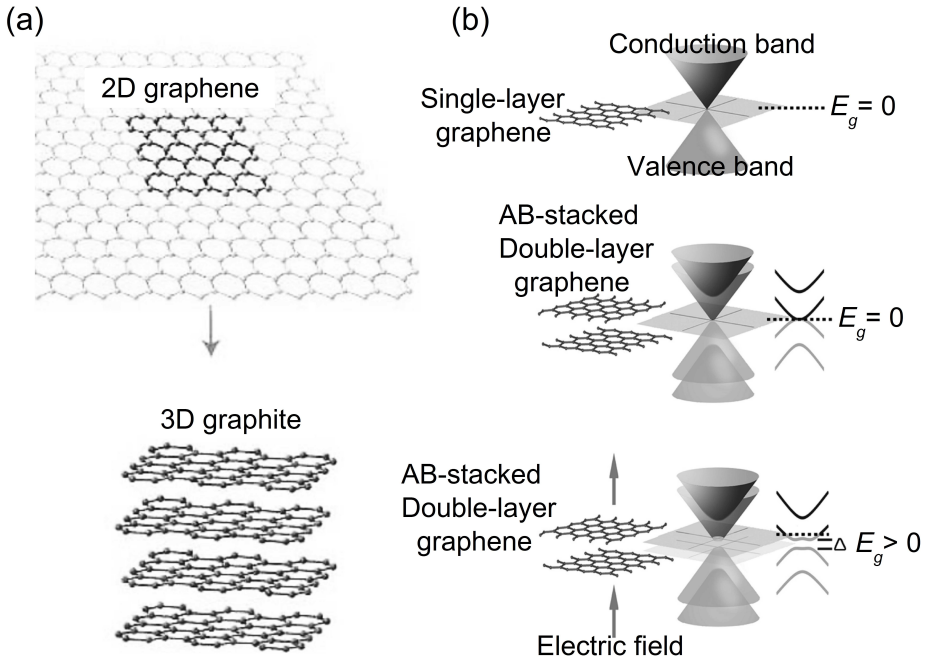

Figure 1.1: (a) Graphene, a single layer of a 2D structured carbon material is the building block of 3D graphite with Van der Waals dispersion force holding layers together and the layers have a graphitic Bernal configuration. (b) Single-layer graphene (top) with conical conduction and valence bands which meet at a point and has no bandgap. Symmetrical double-layer graphene (middle) also lacks a bandgap. Electrical fields (arrows) introduce asymmetry into the double-layer graphene structure (bottom), yielding a tunable bandgap (Δ). (Extracted from Ref. [16,23]).

Interestingly, a double (bi) layer graphene with AB stacking (mirror-like symmetry) has also zero bandgap (behaves like a metal) and if the mirror-like symmetry of the two layers is disturbed (by symmetry breaking), then it behaves like a semiconductor with a tunable bandgap that can be controlled up to 0.25 eV [1,16]. A bandgap has been observed in a one-side chemically doped bilayer graphene and also in AB-stacked bilayer graphene by applying a perpendicular electric field (breaking the mirror-like symmetry) between the two superimposed layers (Figure 1.1(b)) [1,3,4,11,13,16-18]. Therefore, AB-stacked bilayer graphene, because of its tunable bandgap (which determines transport and optical properties) it shows advantages over monolayer graphene, for instance, in applications such as field-effect transistors and light detectors [19-22]. Hence, graphene synthesis has been focused on growing high-quality and large-area AB-stacked bilayer graphene.

Chemical vapour deposition (CVD) is one of the most commonly used technique to

produce AB-stacked bilayer graphene films due to its ability to produce high-quality and large-area or wafer-scale graphene with a controllable number of layers [24-28]. In addition, atmospheric-pressure CVD (AP-CVD) is technologically more accessible for graphene growth and allows high growth temperatures (below substrates melting points) without sublimation of substrates. In CVD graphene growth, metal substrates (e.g. Cu, Ni, Fe, Pd, Pt) are used to promote graphene synthesis by a surface growth/mediated mechanism or by segregation/precipitation [13,29-33]. CVD synthesis of graphene starts with the decomposition of hydrocarbon (e.g. methane (CH_4)) into active carbon atoms that initially aggregate and assemble into graphene film on catalytic metal substrates.

Copper (Cu) is a favourable catalytic metal substrate due to its very low solubility of carbon (i.e. <0.001 at% at 1000 °C) [34], low cost, high etchability and capability of growing a homogeneous (wafer-scale) monolayer graphene film. Due to its low solubility of carbon, Cu grows graphene predominantly during hydrocarbon exposure through surface growth mechanism (surface adsorption and nucleation of active carbon species and graphene growth) as demonstrated with a schematic view in figure 1.2(a). Nonetheless, Cu substrate (typically grows monolayer graphene) has a challenge of growing uniform large-area bilayer or multilayer graphene films with continuous AB stacking [4,24,30,35]. Such challenge is typically ascribed primarily to the low decomposition rate of hydrocarbon gas on the substrate surface [24,25,36]. The lower decomposition rate of hydrocarbon gas (e.g. CH_4) by Cu is advantageous for wafer-scale monolayer graphene growth but disadvantageous for wafer-scale bilayer graphene growth as it requires more carbon atoms. It is impossible to supply sufficient carbon atoms for large-area multilayer graphene growth on pure Cu surface [34,36-45]. Generally, a bilayer graphene obtained on pure Cu foil is known to be incomplete (having smaller areas of bilayer on a monolayer graphene background) with a significant fraction of randomly rotated layers of graphene (non-AB stacked) [25,46-50].

In CVD graphene growth, nickel (Ni) is also a favourable catalytic metal substrate in multilayer graphene growth for energy storage applications [51,52]. In contrast to Cu, Ni is known to have higher decomposition rate of hydrocarbon and higher solubility of carbon (i.e. about 1.3 at% at 1000 °C [53]) and as a result, during hydrocarbon exposure more active carbon species are adsorbed onto the metal surface and thereafter (due to concentration gradient), more carbon atoms diffuse into the metal and some of the diffused carbon atoms segregate/precipitate to

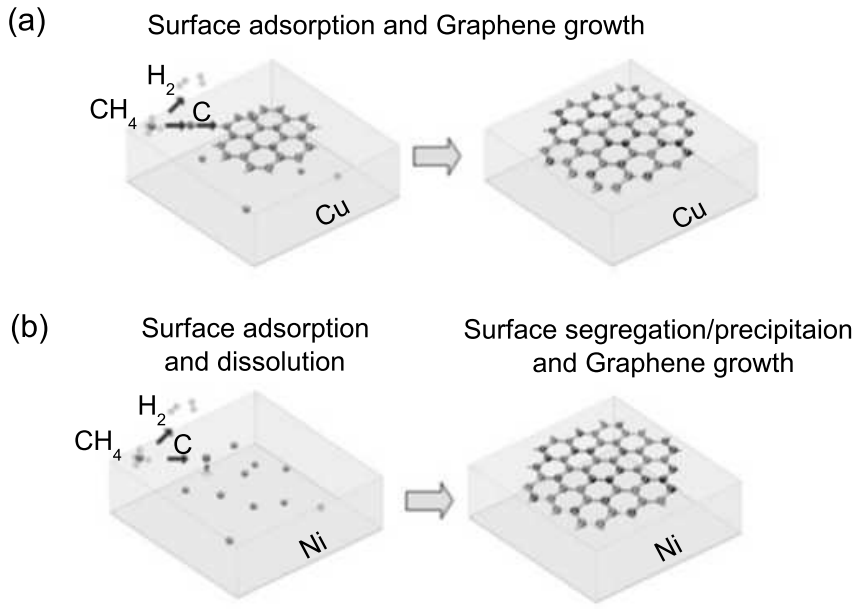

Figure 1.2: Schematic view of the possible different CVD growth mechanisms of graphene films on (a) Cu (surface growth/mediated mechanism) and (b) Ni (dissolution-precipitation growth mechanism) substrates. In both (a) and (b), firstly, the hydrocarbon molecules (CH_4) are adsorbed on the metal surfaces and decompose into active carbon species (C) and H_2 adsorbed on the catalyst surface. Secondly, on Cu surface, there is nucleation of active carbon species and graphene growth, but on Ni surface, more carbon diffuse into the metal and some of the diffused carbon segregate/precipitate to the surface upon metal cooling to grow graphene. In both substrates, the inactive species of H_2 desorb from the substrates surfaces.

the surface upon metal cooling to grow graphene film. In brief, CVD graphene growth on Ni substrate grows predominantly during cooling of a substrate after exposure to hydrocarbon for few minutes through dissolution-precipitation growth mechanism (surface adsorption and dissolution and surface segregation/precipitation of carbon atoms which grow graphene) as shown with a schematic view in figure 1.2(b). However, due to this growth mechanism, Ni typically grows multilayer graphene film which has non-uniform and randomly rotated layers of graphene due to non-uniform segregation/precipitation of carbon atoms from different grains surfaces and grain boundaries [24,31,46,47].

Interestingly, since CVD synthesis of graphene on Cu substrate (is limited to the surface of the catalyst) favours monolayer and that on Ni favours multilayer, a Cu surface engineered with Ni has a capability of growing large-area multilayers, bilayer in particular, of graphene. In previous

studies, Cu/Ni thin films and non-dilute commercial Cu-Ni foils (Table 1.1) have demonstrated such capability and including the growth of large-area AB-stacked bilayer graphene [24,25,49].

Ref.	Growth conditions	Growth substrates	Ni content (bulk and surface) in substrates during growth	Preferential surface orientation of growth substrates
[49]	1×10^{-4} Torr background pressure, 1050 °C , 10 sccm CH_4 for 10 min	Cu-Ni foil Cu(88.0 wt%) Ni(9.9 wt%) (commercial)	Bulk: 11 at% Surface:-	-
[25]	1×10^{-2} Torr background pressure, 1050 °C , under CH_4 for 3 min	Cu-Ni foil Cu(67.8 wt%) Ni(31.0 wt%) (commercial)	Bulk: 33 at% Surface:-	(111) and (100)
[24]	1.5×10^{-1} Torr background pressure, 920 °C , 3 sccm CH_4 for 2 min	Cu/Ni thin films Cu(1200 nm) Ni(400 nm)	Bulk: 33 at% Surface:≈3 at%	Bulk: (111)

Table 1.1: Summary of CVD graphene growth conditions, growth substrate, Ni content in bulk and surface of growth substrates during graphene growth and the preferential surface orientation of growth substrates found in the literature for CVD growth of a large-area (or wafer-scale) high-quality AB-stacked bilayer graphene films. Wu [49] and Chen [25] obtained large-area high-quality AB-stacked bilayer graphene films with terraces of monolayer graphene and Liu [24] obtained wafer-scale high-quality AB-stacked bilayer graphene films.

Furthermore, in CVD graphene growth, background pressure and temperature play important roles since they influence the kinetics of the CVD processes (Table 1.1). Contrary to low-pressure CVD which has a lower density of impurities and residual gas due to high vacuum, AP-CVD grows defective/low-quality graphene layers on Cu substrates at lower CVD temperatures around 900 °C[54]. However, at temperatures higher than 900 °C (i.e. ≈1000 °C), the system grows high-quality graphene layers [54].

In non-dilute commercial Cu(88.0 wt%)-Ni(9.9 wt%) [49] and Cu(67.8 wt%)-Ni (31.0 wt%) [25] foils (listed in table 1.1), Ni have bulk concentrations of 11 at% [49] and 33 at% [25] and the Cu/Ni thin films have 25 at% [24]. These Cu-Ni substrates have much higher Ni bulk concentrations compared to a dilute Cu(Ni) foil to be used in this study (see table 1.1). CVD graphene growth on

non-dilute Cu(Ni) foils is known to propagate from segregation/precipitation processes which lead to variation in the thickness uniformity and stacking order in multilayer graphene films [25,46,47].

In multilayer graphene growth, a Cu foil with a continuous (001) surface crystallography (to be used in this study) is advantageous since it typically grows multilayer graphene domains and (111) surface in other Cu-Ni substrates (Table 1.1) is disadvantageous since it favourably grows monolayer graphene.

Briefly, in table 1.1, though we aim at the same outcome of growing a large-area (or wafer-scale) high-quality AB-stacked bilayer graphene films as the work of Wu [49], Chen [25] and Liu [24], our CVD graphene growth conditions, substrate, Ni content in the bulk and surface of the substrate during graphene growth and the preferential surface orientation of the substrate are different from those of Wu [49], Chen [25] and Liu [24] and have different effects in CVD graphene growth.

Moreover, it will be interesting to study the capability of a dilute Cu(Ni) foil for growing large-area (or wafer-scale) multilayers of graphene, especially AB-stacked bilayer graphene using atmospheric pressure AP-CVD. This idea of a dilute Cu(Ni) foil is aimed at obtaining high surface concentration of Ni (≈2 at%) in dilute Cu(Ni) foil through bulk-to-surface diffusion of Ni while maintaining the bulk concentration of Ni low (<1 at%) in Cu(Ni) foil during hydrocarbon exposure for graphene growth (see schematic view in figure 1.3). During CVD graphene growth, the driving force behind bulk-to-surface diffusion of Ni in dilute Cu(Ni) foil will be the chemical potential gradient and that takes place until the total energy of the crystal is lowest (equilibrium is reached) [55].

Nevertheless, a dilute Cu(Ni) foil with a Ni surface concentration in the range of 1-3 at% is expected to grow a large-area AB-stacked bilayer graphene predominantly during the hydrocarbon exposure for several minutes in accordance with the study of Liu *et al.* [24] (listed in table 1.1) which synthesized a high-quality and large-area AB-stacked bilayer graphene film using Cu/Ni thin films which had a Ni surface concentration <3 at% during low pressure CVD growth. For a Cu foil to have a surface layer composition of about 97 at% Cu and 3 at% Ni through bulk-to-surface diffusion of Ni (Ni surface segregation) during growth in the temperature range of 900-1000 °C, it should have about 0.5 at% Ni bulk concentration and Ni segregation driving energy of about 30 kJ/mol as suggested by the following equilibrium surface segregation model

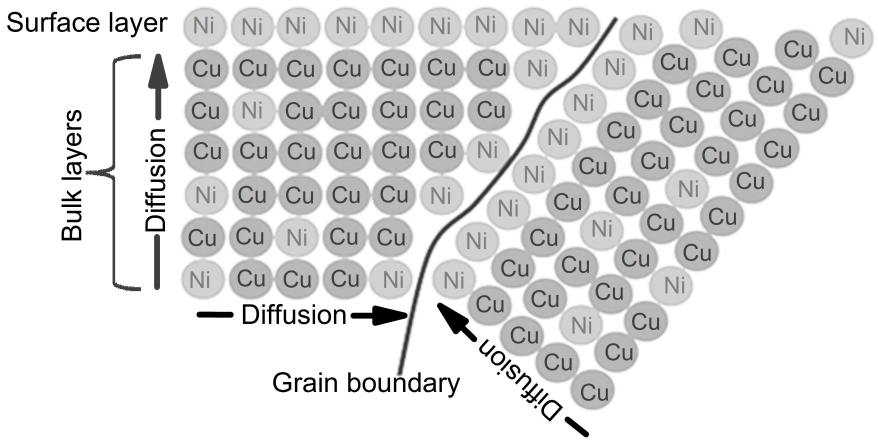

Figure 1.3: Schematic view of a dilute Cu(Ni) foil after bulk-to-surface and interface (grain boundary) diffusion of Ni in dilute Cu(Ni) foil which gives higher Ni surface concentrations compare to Ni bulk concentration. The bulk-to-surface and interfaces diffusion at high crystal temperatures takes place due to thermodynamic minimization of the total energy of the crystal.

(Langmuir- McLean equation) [55-58]):

$$\frac{X^{\phi}(T)}{1-X^{\phi}(T)} = \frac{X^{B}}{1-X^{B}}\exp(-\Delta G/RT) \tag{1.1}$$

where $X^{\phi}(T)$ is the relative surface concentration at temperature, T, X^{B} is the bulk concentration of solute atoms in the crystal, ΔG is the segregation energy and R is the gas constant.

In accordance with the results in reference [24], a CVD substrate (Cu foil) with a surface layer composition of >97 at% Cu and <3 at% Ni is expected to grow a large-area (or wafer-scale) bilayer graphene with an AB-stacked yield of >95 % which is attributed to the surface catalytic graphene growth mode. As a result, this study proposes the use of homogeneous dilute Cu(0.5 at% Ni) foil for large-area (or wafer-scale) AB-stacked bilayer graphene growth using AP-CVD in the temperature range of 900-1000 °C.

1.2 Aims and objectives

Despite the previous works on the growth of AB-stacked bilayer graphene films on Cu/Ni thin films and non-dilute commercial Cu-Ni alloys using CVD system [24-26,46,49], a controllable CVD growth of a continuous large-area high-quality AB-stacked bilayer graphene remains a challenge for different laboratories with CVD setup for graphene growth. This study is aimed at obtaining large-area or wafer-scale AB-stacked bilayer graphene films using dilute Cu(0.5 at% Ni) foils in AP-CVD. This includes preparation and analysis of dilute Cu(0.5 at% Ni) foils.

The objectives are:

(i) Electropolishing and doping of polycrystalline annealed Cu foils (Alfa Aesar 99.8 %) for graphene growth with a small concentration of Ni (i.e. 0.5 at %).

(ii) Inductively coupled plasma optical emission spectrometry (ICP-OES), Proton-induced X-ray emission (PIXE), electron backscatter diffraction (EBSD), X-ray diffraction (XRD), time-of-flight secondary ion mass spectrometry (TOF-SIMS) and X-ray photoelectron spectroscopy (XPS) characterizations of the Ni doped Cu foils and commercial dilute Cu(0.5 at% Ni) foils (MaTeck).

(iii) Synthesis of large-area (wafer-scale) and high-quality monolayer and bilayer graphene films on Cu and dilute Cu(Ni) foils using AP-CVD

(iv) Transfer of graphene films from foils onto 300 nm SiO_2/Si substrates and transmission electron microscopy (TEM) Cu grids.

(v) Raman spectroscopy, high-resolution transmission electron microscopy (HRTEM), field emission scanning electron microscope (FE-SEM) and four-point probe characterizations of prepared graphene films.

1.3 Thesis outline

This section presents an outline of the parts and chapters in the thesis along with a short description of each chapter.

PART II: LITERATURE OVERVIEW

Chapter 2: AP-CVD graphene growth on low carbon solubility catalysts

In this chapter, the solid solubility of carbon in solid Cu, Ni and dilute Cu(Ni) catalysts, the processing steps of the AP-CVD graphene growth on Cu and Cu(Ni) foils, the influence of the Cu surface orientations on the scalability of bilayer graphene, the kinetic processes of the AP-CVD graphene growth on Cu and Cu(Ni) foils and the temperature dependence of the Ni surface concentration in a dilute Cu(Ni) foil during AP-CVD growth are discussed.

Chapter 3: Graphene characterization techniques

The characterization of the graphene sheet is usually investigated by the quality of graphene film, the number of graphene layers, the layers stacking order and the electrical properties. The most commonly used techniques for the characterize/investigation of graphene include the following, Raman spectroscopy, transmission electron microscopy, atomic force microscopy, optical microscopy and scanning electron microscopy, X-ray photoelectron spectroscopy and four-point probe and these techniques are discussed in this chapter.

PART III: EXPERIMENT AND PROCEDURE

Chapter 4: Experimental details

This chapter describes the experimental procedures and equipment used for the production and characterizations of graphene films. This includes a description of the equipment used for Cu(Ni) foil (substrate) analysis. A considerable part of this chapter focuses on the doping of a 25 μm thick annealed Cu foil (Alfa Aesar) with 0.5 at% Ni.

PART IV: RESULTS, DISCUSSIONS AND CONCLUSIONS

Chapter 5: Raman analysis of bilayer graphene film

In this chapter, the results obtained from the characterization of monolayer and bilayer graphene films prepared on commercial dilute Cu(0.5 at% Ni) foils using AP-CVD are discussed. This includes the results obtained from the characterization of the commercial dilute Cu(0.5 at% Ni) foil substrate. The publication (including the supporting information) which details the experimental

procedure and results discussed in this chapter is presented at the end of the chapter.

Chapter 6: A dilute Cu(Ni) alloy for synthesis of AB-stacked bilayer graphene

This chapter discusses the doping of an annealed Cu foil from Alfa Aesar for graphene growth with a small concentration of Ni (≈0.5 at%) to obtain a dilute Cu(0.5 at% Ni) foil for synthesis of high-quality large-area or wafer-scale AB-stacked bilayer graphene films using AP-CVD. This includes the results obtained from the characterization of substrates (both un-doped and Ni doped Cu foils) and bilayer graphene films obtained from un-doped and Ni doped Cu foils. The capability of a Ni doped Cu foil for growing a large-area bilayer graphene film compared to un-doped Cu foil using AP-CVD is demonstrated in this chapter. The publication which details the experimental procedure and results discussed in this chapter is presented at the end of the chapter.

Chapter 7: A wafer-scale AB-stacked bilayer graphene film

This chapter discusses the AP-CVD synthesis and characterization of high-quality and wafer-scale ($\approx 20 \times 20$ mm^2) AB-stacked bilayer graphene film obtained on a dilute Cu(0.61 at% Ni) foil. The discussion includes the results from the characterization of graphene films obtained from pure Cu and dilute Cu(0.61 at% Ni) foils, and characterization of Cu(0.61 at% Ni) foil substrate. The publication (including the supporting information) which details the experimental procedure and results discussed in this chapter is presented at the end of the chapter.

Chapter 8: General conclusions and future work

This final chapter draws a general conclusion outlining the results obtained in this study. A summary of growth substrates and high-quality bilayer graphene coverage obtained on these substrates using CVD and CH_4 as a carbon source found in literature and this study is also presented in this chapter. This includes a brief discussion on the possible future work.

Bibliography

1. H. Aoki, M. S. Dresselhaus, eds., Physics of Graphene, Springer, New York, 2014.
2. Y. Zhang, T. Tang, C. Girit, Z. Hao, M.C. Martin, A. Zettl, et al., Direct observation of a widely tunable bandgap in bilayer graphene, Nature. 459 (2009) 820-823.
3. W.J. Yu, L. Liao, S.H. Chae, Y.H. Lee, X. Duan, Toward tunable band gap and tunable dirac point in bilayer graphene with molecular doping, Nano Letters. 11 (2011) 4759-4763.
4. W. Liu, H. Li, C. Xu, Y. Khatami, K. Banerjee, Synthesis of high-quality monolayer and bilayer graphene on copper using chemical vapor deposition, Carbon. 49 (2011) 4122-4130.
5. A.K. Geim, K.S. Novoselov, The rise of graphene, Nature Materials. 6 (2007) 183-91.
6. M. Freitag, H. Chiu, M. Steiner, V. Perebeinos, P. Avouris, Thermal infrared emission from biased graphene, Nature Nanotechnology. 5 (2010) 497-501.
7. F. Bonaccorso, Z. Sun, T. Hasan, A.C. Ferrari, Graphene Photonics and Optoelectronics, Nature Photonics. 4 (2010) 611-622.
8. UCSB College of Engineering, http://engineering.ucsb.edu/news/765 (accessed October 3, 2015).
9. K.S. Kim, Y. Zhao, H. Jang, S.Y. Lee, J.M. Kim, K.S. Kim, et al., Large-scale pattern growth of graphene films for stretchable transparent electrodes, Nature. 457 (2009) 706-10.
10. X. Wang, L. Zhi, K. Müllen, Transparent, conductive graphene electrodes for dye-sensitized solar cells, Nano Letters. 8 (2008) 323-7.

11. Y. Zhang, T. Tang, C. Girit, Z. Hao, M.C. Martin, A. Zettl, et al., Direct observation of a widely tunable bandgap in bilayer graphene, Nature. 459 (2009) 820-3.

12. F. Schwierz, Graphene transistors, Nature Nanotechnology. 5 (2010) 487-496.

13. Y. Xue, B. Wu, Y. Guo, L. Huang, L. Jiang, J. Chen, et al., Synthesis of large-area, few-layer graphene on iron foil by chemical vapor deposition, Nano Research. 4 (2011) 1208-1214.

14. A. Das, S. Pisana, B. Chakraborty, S. Piscanec, S.K. Saha, U. V Waghmare, et al., Monitoring dopants by Raman scattering in an electrochemically top-gated graphene transistor, Nature Nanotechnology. 3 (2008) 210-5.

15. B.N. Szafranek, G. Fiori, D. Schall, D. Neumaier, H. Kurz, Current saturation and voltage gain in bilayer graphene field effect transistors, Nano Letters. 12 (2012) 1324-1328.

16. Bilayer Graphene Gets a Bandgap | Berkeley Lab, http://newscenter.lbl.gov/2009/06/10/graphene-bandgap/ (accessed January 13, 2016).

17. T. Ohta, A. Bostwick, T. Seyller, K. Horn, E. Rotenberg, Controlling the electronic structure of bilayer graphene, Science (New York, N.Y.). 313 (2006) 951-4.

18. S.Y. Zhou, G.-H. Gweon, A. V Fedorov, P.N. First, W.A. de Heer, D.-H. Lee, et al., Substrate-induced bandgap opening in epitaxial graphene, Nature Materials. 6 (2007) 770-5.

19. K. Zou, J. Zhu, Transport in gapped bilayer graphene: The role of potential fluctuations, Physical Review B - Condensed Matter and Materials Physics. 82 (2010) 1-4.

20. T. Taychatanapat, P. Jarillo-Herrero, Electronic transport in dual-gated bilayer graphene at large displacement fields, Physical Review Letters. 105 (2010) 1-4.

21. J. Yan, M.S. Fuhrer, Charge transport in dual gated bilayer graphene with corbino geometry, Nano Letters. 10 (2010) 4521-4525.

22. K.F. Mak, C.H. Lui, J. Shan, T.F. Heinz, Observation of an electric-field-induced band gap in bilayer graphene by infrared spectroscopy, Physical Review Letters. 102 (2009) 100-103.

23. Width-Dependent Conductance of Graphene Nanoribbons - MSE 5320,

http://electronicstructure.wikidot.com/yasmin (accessed March 1, 2016).

24. W. Liu, S. Kraemer, D. Sarkar, H. Li, P.M. Ajayan, K. Banerjee, Controllable and rapid synthesis of high-quality and large-area bernal stacked bilayer graphene using chemical vapor deposition, Chemistry of Materials. 26 (2014) 907-915.

25. S. Chen, W. Cai, R.D. Piner, J.W. Suk, Y. Wu, Y. Ren, et al., Synthesis and characterization of large-area graphene and graphite films on commercial Cu-Ni alloy foils, Nano Letters. 11 (2011) 3519-3525.

26. H. Choi, Y. Lim, M. Park, S. Lee, Y. Kang, M.S. Kim, et al., Precise control of chemical vapor deposition graphene layer thickness using NiCu alloys, J. Mater. Chem. C. 3 (2015) 1463-1467.

27. C. Mattevi, H. Kim, M. Chhowalla, A review of chemical vapour deposition of graphene on copper, Journal of Materials Chemistry. 21 (2011) 3324.

28. L. Ma, W. Ren, Z. Dong, L. Liu, H. Cheng, Progress of graphene growth on copper by chemical vapor deposition: Growth behavior and controlled synthesis, Chinese Science Bulletin. 57 (2012) 2995-2999.

29. X. Li, W. Cai, J. An, S. Kim, J. Nah, D. Yang, et al., Large-area synthesis of high-quality and uniform graphene films on copper foils, Science. 324 (2009) 1312-1314.

30. A. Guermoune, T. Chari, F. Popescu, S.S. Sabri, J. Guillemette, H.S. Skulason, et al., Chemical vapor deposition synthesis of graphene on copper with methanol, ethanol, and propanol precursors, Carbon. 49 (2011) 4204-4210.

31. A. Reina, S. Thiele, X. Jia, S. Bhaviripudi, M.S. Dresselhaus, J.A. Schaefer, et al., Growth of large-area single- and Bi-layer graphene by controlled carbon precipitation on polycrystalline Ni surfaces, Nano Research. 2 (2009) 509-516.

32. S.Y. Kwon, C. V. Ciobanu, V. Petrova, V.B. Shenoy, J. Bareño, V. Gambin, et al., Growth of semiconducting graphene on palladium, Nano Letters. 9 (2009) 3985-3990.

33. G. Imamura, K. Saiki, Synthesis of nitrogen-doped graphene on Pt(111) by chemical vapor

deposition, Journal of Physical Chemistry C. 115 (2011) 10000-10005.

34. G.A. López, E.J. Mittemeijer, The solubility of C in solid Cu, Scripta Materialia. 51 (2004) 1-5.

35. A. Mohsin, L. Liu, P. Liu, W. Deng, I.N. Ivanov, G. Li, et al., Synthesis of millimeter-size hexagon-shaped graphene single crystals on resolidified copper, ACS Nano. 7 (2013) 8924-8931.

36. S. Bhaviripudi, X. Jia, M.S. Dresselhaus, J. Kong, Role of Kinetic Factors in Chemical Vapor Deposition Synthesis of Uniform Large Area Graphene Using Copper Catalyst, Nano Letters. 10 (2010) 4128-4133.

37. I. Vlassiouk, M. Regmi, P. Fulvio, S. Dai, P. Datskos, G. Eres, et al., Role of hydrogen in chemical vapor deposition growth of large single-crystal graphene, ACS Nano. 5 (2011) 6069-76.

38. H. Kim, E. Saiz, M. Chhowalla, C. Mattevi, Modeling of the self-limited growth in catalytic chemical vapor deposition of graphene, New Journal of Physics. 15 (2013) 053012.

39. A.W. Robertson, J.H. Warner, Hexagonal single crystal domains of few-layer graphene on copper foils, Nano Letters. 11 (2011) 1182-9.

40. L, H. Ci, Qiongyuhou, J.H. Zhong, J.Y. Liu, A. Dolocan, J. Zhang, et al., Growth of adlayer graphene on Cu studied by carbon isotope labeling, Nano Letters. 13 (2013) 486-490.

41. S. Nie, W. Wu, S. Xing, Q. Yu, J. Bao, S. Pei, et al., Growth from below: bilayer graphene on copper by chemical vapor deposition, New Journal of Physics. 14 (2012) 093028.

42. M. Fabiane, S. Khamlich, A. Bello, J. Dangbegnon, D. Momodu, A.T. Charlie Johnson, et al., Growth of graphene underlayers by chemical vapor deposition, AIP Advances. 3 (2013) 112126.

43. K. Yan, H. Peng, Y. Zhou, H. Li, Z. Liu, Formation of bilayer bernal graphene: layer-by-layer epitaxy via chemical vapor deposition, Nano Letters. 11 (2011) 1106-10.

44. B. Wu, D. Geng, Y. Guo, L. Huang, Y. Xue, J. Zheng, et al., Equiangular

Hexagon-Shape-Controlled Synthesis of Graphene on Copper Surface, Advanced Materials. 23 (2011) 3522-3525.

45. P. Wu, X. Zhai, Z. Li, J. Yang, Bilayer graphene growth via a penetration mechanism, Journal of Physical Chemistry C. 118 (2014) 6201-6206.

46. N. Liu, L. Fu, B. Dai, K. Yan, X. Liu, R. Zhao, et al., Universal Segregation Growth Approach to Wafer-Size Graphene from Non-Noble Metals, Nano Letters. 11 (2011) 297-303.

47. A. Reina, X. Jia, J. Ho, D. Nezich, H. Son, V. Bulovic, et al., Large area, few-layer graphene films on arbitrary substrates by chemical vapor deposition, Nano Letters. 9 (2009) 30-35.

48. X. Liu, L. Fu, N. Liu, T. Gao, Y. Zhang, L. Liao, et al., Segregation growth of graphene on Cu-Ni alloy for precise layer control, Journal of Physical Chemistry C. 115 (2011) 11976-11982.

49. Y. Wu, H. Chou, H. Ji, Q. Wu, S. Chen, W. Jiang, et al., Growth mechanism and controlled synthesis of AB-stacked bilayer graphene on Cu-Ni alloy foils, ACS Nano. 6 (2012) 7731-8.

50. W. Fang, A.L. Hsu, R. Caudillo, Y. Song, A.G. Birdwell, E. Zakar, et al., Rapid identification of stacking orientation in isotopically labeled chemical-vapor grown bilayer graphene by Raman spectroscopy, Nano Letters. 13 (2013) 1541-1548.

51. A. Bello, K. Makgopa, M. Fabiane, D. Dodoo-Ahrin, K.I. Ozoemena, N. Manyala, Chemical adsorption of NiO nanostructures on nickel foam-graphene for supercapacitor applications, Journal of Materials Science. 48 (2013) 6707-6712.

52. S. Khamlich, A. Bello, M. Fabiane, B.D. Ngom, N. Manyala, Hydrothermal synthesis of simonkolleite microplatelets on nickel foam-graphene for electrochemical supercapacitors, Journal of Solid State Electrochemistry. 17 (2013) 2879-2886.

53. W. Cai, R.D. Piner, Y. Zhu, X. Li, Z. Tan, H.C. Floresca, et al., Synthesis of isotopically-labeled graphite films by cold-wall chemical vapor deposition and electronic properties of graphene obtained from such films, Nano Research. 2 (2009) 851-856.

54. M. Fabiane, Chemical vapour deposition of graphene: Fundamental aspects of synthesis and characterization, PhD thesis, University of Pretoria, 2014.

55. J. du Plessis, Solid State Phenomena - Part B, Volume 11 (Diffusion and Defect Data), Sci-Tech Publications, Brookfield USA, 1990.

56. E.C. Viljoen, J. du Plessis, Surface segregation measurements via the linear programmed heating method: Part A-Theory, Surface Science. 431 (1999) 128-137.

57. D.R. Harries, A.D. Marwick, Non-Equilibrium Segregation in Metals and Alloys, Philosophical Transactions of the Royal Society A: Mathematical, Physical and Engineering Sciences. 295 (1980) 197-207.

58. E.C. Viljoen, J. du Plessis, Surface segregation measurements via the linear programmed heating method: Part B-Experimental and results, Surface Science. 468 (2000) 27-36.

PART II

LITERATURE OVERVIEW

CHAPTER 2

AP-CVD graphene growth on low carbon solubility catalysts

2.1 Introduction

The chemical vapour deposition (CVD) is an old technique developed in the 1880s. The CVD technique combines several scientific and engineering approaches which include fluid thermodynamics, kinetics and chemistry [1]. Since its development, the theory and mechanism of CVD have advanced significantly and is considered one of the best technique for the synthesis of high-quality thin films.

In literature, the capability of copper (Cu) catalyst to grow graphene in CVD system is ascribed primarily to the carbon solubility limit and the metal surface catalytic activity (hydrocarbon decomposition rate) of Cu. This study focuses the discussion on the solubility limit and hydrocarbon decomposition rate of Cu. This chapter presents an overview of the solid solubility of C in solid Cu, nickel (Ni) and dilute Cu(Ni) catalysts. A brief discussion on the AP-CVD (bilayer) graphene growth on Cu and dilute Cu(Ni) catalysts (low carbon solubility catalysts), the influence of the Cu surface orientations on the scalability of bilayer graphene, the kinetic processes of the AP-CVD graphene growth on Cu and Cu(Ni) foils and the temperature dependence of the surface concentration of Ni in dilute Cu(Ni) foil is also presented.

2.2 The solid solubility of carbon in solid Cu and Ni catalysts

Equilibrium phase diagram of a binary Cu-carbon system shows that carbon has a very low solid solubility in solid Cu which is in the order of few parts per million (ppm) [2]. The solid solubility of carbon in Cu increases with increasing temperature and no carbide phases are present. The solid solubility of carbon in Cu is about 7.4 ppm at 1020 °C and the enthalpy of dissolution of carbon in Cu is 35.1 kJ/mol [2]. In the literature, the data on the volume diffusion of carbon in Cu is not available. However, volume diffusion coefficient (D) of carbon in Cu at a temperature of 870 °C is estimated as $D = 3 \times 10^{-11}$ m^2/s [2]. According to Harpale *et al.* [3], a surface-to-bulk volume diffusion of carbon in Cu is restricted by preferential carbon-carbon bonds formation (i.e. C−C dimer pairs) over Cu-carbon bonds. Therefore, CVD growth of graphene on Cu occurs predominantly during the hydrocarbon exposure (through surface growth mechanism) for several minutes [4].

In contrast to Cu, carbon has a higher solid solubility in solid Ni (i.e. ≈1.3 at% (13000 ppm) at 1000 °C) [5]. The volume diffusion parameters, namely, the pre-exponential factor (D_0) and the activation energy (Q) for C diffusion in Ni are $D_0 = 1.2 \times 10^{-5}$ m^2/s and $Q = 137.3$ kJ/mol respectively [6]. A strong or preferential atom-atom interaction between carbon and Ni atoms (over carbon-carbon interaction) accelerates surface-to-bulk and volume (interstitial) diffusion of carbon in Ni [3]. A high solid solubility of carbon in solid Ni, low activation energy ($Q = 137.3$ kJ/mol) for carbon diffusion in Ni and a preferential Ni-carbon interaction could be a reason for more carbon dissolution in Ni during exposure to carbon source at high temperatures (≈1000 °C) which would lead to dissolution-precipitation growth mechanism in CVD graphene growth.

2.3 The solubility of carbon in dilute Cu(Ni) catalyst

Due to higher solubility of carbon in Ni, during CVD graphene growth carbon atoms on dilute Cu(Ni) surface could be expected to diffuse into Cu(Ni) bulk layers and precipitate upon cooling to grow layers of graphene, however, the solubility of carbon in Cu decreases with addition of Ni content (<1 at%) and, thus the following illustration is presented: The temperature dependence of the solubility, x, of solute atoms i ($i = 1$) in a dilute binary alloy with a solid solution α is given

by [2,7]

$$x_1^{\alpha} = \exp\left(-\Delta G_1^o / bRT\right) \tag{2.1}$$

where ΔG_1^o is the segregation energy for solute atoms 1 in the ideal solution ($\Delta G_1^o = 35.1$ kJ/mol for carbon in Cu [2]), b is the solvent subscript integer in a solvent-solute compound, R is the gas constant, T is the temperature in Kelvin.

Furthermore, in a dilute ternary alloy (solute atoms $i = 1$, 2 (carbon, Ni) and solvent atoms = 3 (Cu)) with a solid solution α, the temperature dependence of the solubility of solute atoms $i = 1$ can be described by the well-known Guttmann equation [7]:

$$x_1^{\alpha} = \frac{\exp\left(-\Delta G_1^o / bRT\right)}{\left\{1 + \left[\exp\left(-\Delta G'^o / \alpha RT\right) - 1\right] x_2^{\alpha}\right\}^{a/b}} \tag{2.2}$$

where $\exp\left(-\Delta G_1^o / bRT\right) = x_1^{\alpha}$ is the solubility of solute atoms 1 in the absence of solute atoms 2 (similar to equation 2.1), $x_2^{\alpha} = \exp\left(-\Delta G_2^o / bRT\right)$ is the solubility of solute atoms 2 in the absence of solute atoms 1, a and b are the subscripts integers in a solvent-solute compound and

$$\Delta G'^o \approx \Delta H'^o = \Delta H_{12}^o - \Delta H_{13}^o \tag{2.3}$$

where $\Delta H'^o$ is the difference in the segregation enthalpy for solute-solute atoms (ΔH_{12}^o) and solute-solvent atoms (ΔH_{13}^o) in the ideal solution.

Generally, $\Delta G = \Delta H - T\Delta S$, where ΔH is the segregation enthalpy, T is the temperature and ΔS is the segregation entropy. In dilute alloys, ΔS is negligible hence, $\Delta G \approx \Delta H$ and the segregation enthalpy can be approximated by [8,9]

$$\Delta H = \frac{\Delta Z}{Z}\left(\Delta H_B^{sub} - \Delta H_A^{sub}\right) \tag{2.4}$$

where Z is the bulk coordination number ($Z = 12$ for Cu crystal), ΔZ is the difference in coordination number between bulk and surface ($\Delta Z = 4$ for Cu(001)), ΔH^{sub} is the heat of sublimation for element A and B ($\Delta H_{Cu}^{sub} = 339.3$ kJ/mol and $\Delta H_{Ni}^{sub} = 430.1$ kJ/mol [10]).

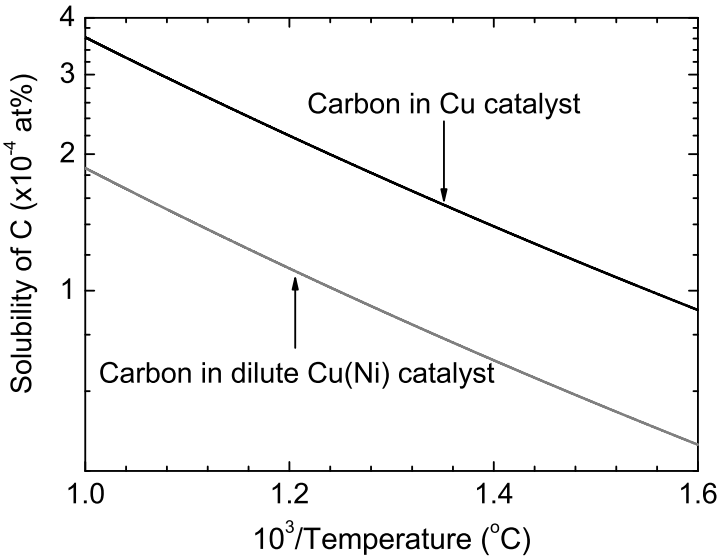

Figure 2.1: An illustration of the temperature dependence of the solubility of carbon in Cu and dilute Cu(Ni) catalysts (Calculated in this chapter using equation 2.1 and 2.2).

Following from equation 2.4, ΔH_{12}^{o} (similarly for ΔH_{13}^{o}) can be written as

$$\Delta H_{12}^{o} = \frac{\Delta Z}{Z}\left(\Delta H_{2}^{o,sub} - \Delta H_{1}^{o,sub}\right) \tag{2.5}$$

In equation 2.4, $\Delta G_{2}^{o} = 30.3$ kJ/mol for Ni in Cu(001) and from equation 2.3 and 2.5, $\Delta G^{'o} = 30.3$ kJ/mol. The temperature dependence of the solubility of carbon in Cu and in Cu(Ni) was obtained (using equation 2.1 and 2.2) as illustrated in figure 2.1. Briefly, figure 2.1 shows that the temperature dependent solubility of carbon in Cu catalyst decreases with the addition of Ni($<$1 at%) in Cu. Therefore, it can be mentioned that due to the metal-carbon interaction effects and the solubility limit, CVD graphene growth on dilute Cu(Ni) foil will occur predominantly during the hydrocarbon exposure (surface growth/mediated mechanism) rather than due to the combination of surface-to-bulk and bulk-to-surface diffusion (dissolution-precipitation growth mechanism) of carbon atoms in the foil upon cooling. It is worth mentioning that at higher Ni bulk concentrations in Cu foil (i.e. in non-dilute Cu(Ni) foil), the solubility of carbon in Cu will increase with an increase in Ni bulk content which would lead to a dissolution-precipitation growth mechanism.

2.4 Processing steps of the AP-CVD graphene growth on Cu and Cu(Ni) foils

2.4.1 Copper substrate pre-treatment

As-received Cu foil is covered by native oxide (CuO, Cu_2O), and possible contamination (due to production and handling processes) which reduces its catalytic activity. Therefore, the pre-treatment of the Cu foils has been found to be very important in removing the impurity particles on the Cu surface allowing the growth of continuous high-quality graphene and reproducibility [11,12]. The pre-treatment of the Cu foils includes electro-polishing (remove imperfection sites), aqueous acid treatment (dissolves greasy impurities) and annealing in a hydrogen reducing atmosphere at ≈1000 °C (eliminate surface structural defects and increases the Cu grains size) [12,13]. Typically the Cu foils prior to CVD graphene growth are annealed for about 30 min under a mixture of gases namely, argon (Ar) and hydrogen (H_2) [14-17].

2.4.2 Graphene growth and reaction mechanisms

In CVD, graphene grows by thermal-decomposition reactions whereby a hydrocarbon molecule splits into its elements and/or elementary molecule and the decomposition typically takes place at high temperatures (>900 °C). The thermal-decomposition reaction in CVD is governed by thermodynamics and kinetics. The kinetics defines the transport process and determines the rate-control mechanism [1,4]. In CVD growth, the background pressure or mix of gases, growth time, substrate temperature and gas flow rate can be varied. Depending on the type of catalyst (carbon solubility and hydrocarbon decomposition rate), the graphene may grow during hydrocarbon exposure through surface growth mechanism or after exposure (i.e. during substrate cooling) through dissolution-precipitation growth mechanism, as mentioned in chapter 1.

Furthermore, in AP-CVD, after annealing of a Cu foil, graphene is synthesized from a mixture of gases, Ar, H_2 and methane (CH_4) at ≈1000 °C for few minutes. Immediately after growth, the CH_4 flow is stopped and the sample is rapidly cooled down. During CVD graphene growth, Ar produces an inert atmosphere in the reaction chamber and carry away residuals out of a reaction chamber. H_2 act as a co-catalyst in formation of active surface bound carbon species required for graphene growth and etches away the weak carbon-carbon bonds (graphene edges) for the growth

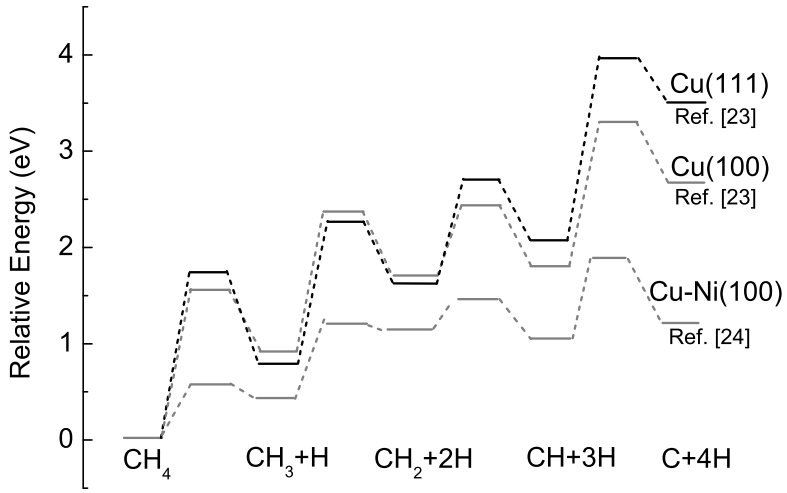

Figure 2.2: The energy profile of the dehydrogenation (decomposition) processes of CH_4 that give the final product of C atom plus four H atoms on Cu(111), Cu(100) and Cu-Ni(100) substrates surfaces (Extracted from Ref. [23] and [24]).

of bilayer or multilayer graphene [18-22]. CH_4 is commonly used as the carbon source in CVD graphene growth. In CH_4 decomposition or dehydrogenation process, the final product is carbon (C) atom plus four H atoms on the substrate surface, following the four elementary steps shown below (see figure 2.2) [23]:

$$\begin{aligned} CH_4 &\rightarrow CH_3 + H \\ CH_3 &\rightarrow CH_2 + H \\ CH_2 &\rightarrow CH + H \\ CH &\rightarrow C + H \end{aligned} \tag{2.6}$$

In figure 2.2, on a Cu surface, the final product C + 4H has higher energy than the adsorbed CH_4, suggesting that atomic C is energetically unfavourable on Cu surface [23,25]. On a Cu(100) surface, atomic C is more stable than that on a Cu(111) surface [23]. This could be one of the reasons why high index Cu planes and Cu(100) plane cause compact graphene island formation in early stages of graphene growth and Cu(111) plane preferentially grows monolayer graphene [26,27]. Interestingly, the stability of atomic C on Cu(100) surface is further improved by Ni in Cu-Ni(100) surface, as shown in figure 2.2 [24]. Briefly, following from figure 2.2, all the active

C species (CH_3, CH_2, CH and C) have much lower formation energies on the Cu-Ni surface than those on a pure Cu surface [24]. As a result, the surface concentrations of active C species on the Cu-Ni surface would be much higher than on pure Cu surface. This shows that the Cu's capability of decomposing the hydrocarbon is mainly enhanced by surface alloying of Cu with Ni [24].

Furthermore, for graphene to materialise on Cu surface, atomic C−C bonds, as suggested by equation 2.6, need to be energetically favourable on Cu surface not energetically unfavourable as suggested. Therefore, the following reaction (Equation 2.7) that shows the formation of a stable C=C bonds with sp^2 hybridization on Cu surface was considered to be important for graphene growth rather than equation 2.6 [20,28].

$$CH + CH \rightarrow C{=}C + H_2 \tag{2.7}$$

In equation 2.7, CH_4 reduces to CH plus CH reaction which leads to a formation of graphene (C=C bonds with sp^2 hybridization) and H_2 which detaches from the Cu surface and get swept away by the carrier (Ar) gas flow. Additionally, C=C bonds containing hydrogen are energetically unfavourable on Cu surface with low adsorption energies (desorb or decompose at very low temperatures) [29-32].

Cu substrate weakly interacts with graphene with a graphene-metal separation of 0.33 nm, which is close to the interlayer distance (0.335 nm) of the van der Waals gap in multilayer graphene or graphite [33]. In contrast to Cu, Ni is a strongly interacting metal and the graphene-metal separation is around 0.21 nm [33]. This suggests that Cu-Ni surface strongly interact with graphene compared to a pure Cu surface.

After the growth step, the CH_4 flow is stopped and samples are rapidly cooled down to room temperature and transferred onto different substrates. The atmosphere used during cooling process is similar to that of the annealing step (i.e. a mixture of gases, Ar and H_2) which prevents oxidation of the substrate and graphene functionalization with oxygen containing groups.

In a dilute Cu(Ni) foil, at graphene growth temperature of ≈1000 °C, more than 96 at% of the elemental composition of a foil surface is Cu and less than 4 at% is Ni. As a result, graphene growth on a dilute Cu(Ni) foil will predominantly follow similar reaction mechanisms and kinetic processes as those of a pure Cu. Because of the higher catalytic activity of Ni (higher

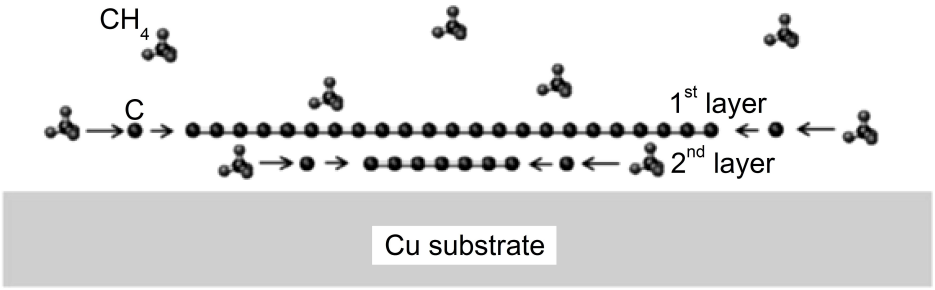

Figure 2.3: Schematic view of the underlayer growth mechanism (nucleation and growth) of bilayer graphene. Hydrocarbon (CH_4) decomposes on the Cu foil surface, generating active C species that diffuse under the graphene sheet (first layer of graphene) to grow the second layer of graphene (Extracted from Ref. [36]).

decomposition rate of hydrocarbons), a dilute Cu(Ni) foil will have more supply of active C species (due to much lower formation energies of active C species) required for a uniform multilayer graphene growth. Additionally, a dilute Cu(Ni) foil has a reduced solid solubility of C compared to Cu foil, while the temperature dependent solubility of C in Cu catalyst decreases with the addition of Ni ($<$1 at%) in Cu.

2.4.3 Bilayer (underlayer) graphene growth

Due to the low solubility of C in Cu foils, Cu substrate predominantly grows monolayer graphene (it has a challenge of growing uniform large-area bilayer graphene) during hydrocarbon exposure [17,34,35]. This monolayer graphene, in bilayer graphene growth, is viewed as the first layer of graphene and the second layer (underlayer) grows beneath the first graphene sheet since CVD graphene growth depends on the substrate surface to supply the growth species by decomposing hydrocarbon molecules (see the schematic view in figure 2.3) [36,37]. The first and second layer of graphene grows by surface growth mechanism (surface adsorption and nucleation of carbon species to grow graphene) and have the same initial nucleation centres [37].

C diffusing from outside the interfaces between the first layer and Cu surface cannot reach the second layer, because once it diffuses to the edge of the first layer graphene it gets captured by the first layer due to the strong and favourable C$-$C bond. However, due to a weak interaction

between Cu surface and graphene sheet (with a graphene-metal separation of 0.33 nm), it has been observed that many hydrocarbon gas molecules readily diffuse through open channels at the edges of the first layer into the interface between Cu surface and graphene sheet and decompose on the metal surface to supply C for the second layer graphene growth [33,38,39]. Therefore, the limited space in the interface between the substrate surface and graphene sheet has a lower partial pressure of hydrocarbon gas compared to gas outside the interface between the first layer and the Cu surface. As a result, the second layer has a decreased growth rate and improved crystal quality. Li *et al.* [36] has shown that the second layer grows at a rate about two orders of magnitude slower than the first layer.

Since hydrocarbon gas molecules readily diffuse through open channels at the edges of the first layer into the interface between Cu surface and graphene sheet, the second layer growth terminates when the first layer grains merge together (terminating the first layer growth) [36]. In summary, CVD graphene growth of the first and second layers terminates simultaneously. Thus, a large-area bilayer graphene can be obtained by using slower growth rate for monolayer graphene (first layer) during growth and that can be attained by using a relatively low methane gas flow rate (low methane concentrations), and lower temperatures in the range of 900-1000 °C, but less than 1000 °C since this temperature is commonly used to grow high-quality CVD monolayer graphene) [4,36].

2.5 Influence of the Cu surface orientations on the scalability of bilayer graphene

Figure 2.4 shows SEM images (Figure 2.4(a)) of the Cu-Ni foil (weight percent: 67.8 % Cu and 31.0 % Ni) with as-grown graphene on regions corresponding to regions identified with EBSD mapping (Figure 2.4(b)) of the same sample [26]. In the early stage of graphene growth, there are different levels of coverage of graphene on different metal grains, as shown in figure 2.4, the graphene coverage in (111) grain is much lower than that in (100) and (110) grains. This could be as a result of lower formation energies of active C species on a Cu(100) and (110) surfaces compare to Cu(111) surface (discussed in figure 2.2). Therefore, graphene film (multilayers) preferentially grows on the Cu(100) surface [23,40]. On the other hand, C species have higher diffusion rate on Cu(111) surface and preferentially grows monolayer graphene [27].

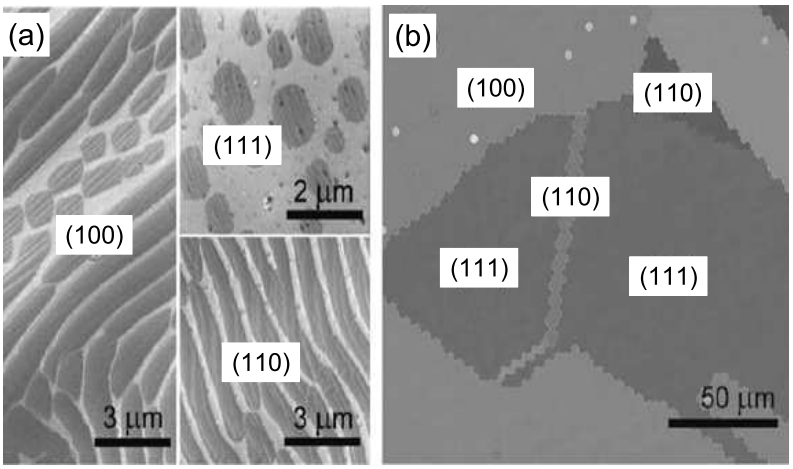

Figure 2.4: (a) SEM images of the Cu-Ni foil (weight percent: 67.8 % Cu and 31.0 % Ni) with as-grown graphene on regions corresponding to regions in (b) EBSD mapping of the same sample (Extracted from Ref. [26]).

In polycrystalline Cu foils, graphene preferentially nucleates on the grain boundaries similar to Ni foil and grow onto adjacent different grains surfaces signifying that the graphene films grow continuously across grains boundaries of Cu surface and over an entire foil [41,42]. Additionally, graphene growth on the Cu(111) surface which is preferentially monolayer is known to spill over into the adjacent grains surfaces which have slower growth rate and preferentially grow multilayers (e.g. Cu(100) and high index Cu planes) [27]. Though CVD graphene is known to grow over an entire foil, growth of a wafer-scale bilayer graphene film on a polycrystalline Cu foil consisting of Cu(111) grains is not possible since Cu(111) surface preferentially grow monolayer graphene. Therefore, in an attempt to grow a wafer-scale bilayer graphene film the idea will be to use a polycrystalline Cu foil that has a continuous Cu(100) surface and no Cu(111) surface grains.

2.6 Kinetic processes of the AP-CVD graphene growth on Cu and Cu(Ni) foils

The kinetics (cooling rate and background pressure during growth) of the CVD process has an important effect on the graphene growth rate, thickness uniformity through a substrate and the density of defects [4,17,18]. In a view of the kinetics of the AP-CVD process, a schematic view in figure 2.5 illustrates a steady-state gas flow of a mixture of Ar, H_2 and CH_4 gases on the surface

of a Cu catalyst during CVD graphene growth at ≈1000 °C. As shown in figure 2.5, it is assumed that between the steady-state bulk gas flow and the catalyst surface there exist a static boundary layer with thickness δ [4]. During isothermal CVD graphene growth, several processes take place, namely [4,17,18,21];

(1) Diffusion of hydrocarbon molecules (e.g. CH_4) from the steady-state bulk gas flow through the boundary layer onto the catalyst surface.

(2) Adsorption (and desorption) of hydrocarbon molecules on the catalyst surface.

(3) Decomposition of hydrocarbon molecules into active C species (CH_3, CH_2, CH and C) and H_2 adsorbed on the catalyst surface (see equation 2.7).

(4) Desorption of inactive species from the surface, H_2 in particular, which diffuse through the boundary layer into the bulk gas flow and get swept away by the carrier (Ar) gas flow.

(5) Aggregation of active C species and formation of nucleation sites on the catalyst surface, lateral surface diffusion and attachment of active C species to nucleation sites to materialise graphene (C=C bonds formation).

Therefore, isothermal CVD graphene growth involves predominantly two processes that coexist, one that takes place in the boundary layer and the other one on the catalyst surface. These two processes can be classified into two regions (fluxes) [4]:

(i) Mass transport region ($F_{\text{mass-transport}}$, the flux of active species through the boundary layer).

(ii) Surface reaction region ($F_{\text{surface-reaction}}$, the rate at which the active species are consumed at the surface of the catalyst to form graphene).

Assuming first-order kinetics and first-order rate kinetics, the two fluxes can be expressed as [4]

$$F_{\text{mass-transport}} = h_{\text{gass}} \left(X^{B}_{\text{gass}} - X^{S}_{\text{species}} \right) \tag{2.8}$$

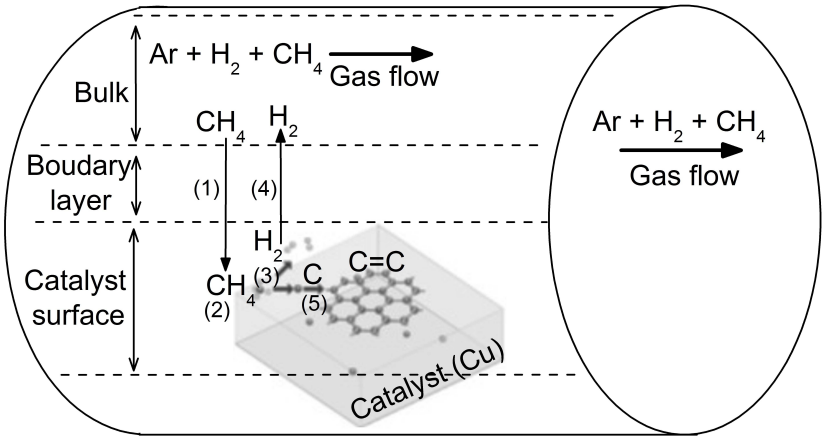

Figure 2.5: An illustration of the processes involved during isothermal CVD graphene growth using low carbon solid solubility catalyst.

and

$$F_{\text{surface-reaction}} = K_{\text{surface}} X^{S}_{\text{species}} \tag{2.9}$$

where h_{gass} is the mass-transport coefficient, K_{surface} is the surface-reaction constant, X^{B}_{gass} is the concentration of gas in the bulk and X^{S}_{species} is the concentration of the active species at the catalyst surface.

These fluxes are in series and at steady-state,

$$F_{\text{mass-transport}} = F_{\text{surface-reaction}} = F_{\text{total-flux}} \tag{2.10}$$

Therefore, total flux, $F_{\text{total-flux}}$, can be written as [4]

$$F_{\text{total-flux}} = X^{B}_{\text{gass}} \frac{K_{\text{surface}} \times h_{\text{gass}}}{(K_{\text{surface}} + h_{\text{gass}})} \tag{2.11}$$

In equation 2.11, mass-transport coefficient and the surface-reaction constant coexist and in CVD graphene growth, the slower of the two fluxes is the rate-limiting process. During isothermal

AP-CVD graphene growth at ≈1000 °C, surface reactions occur much faster due to the dependence on the Arrhenius term and the rate of mass-transport or the mass-transport coefficient is low due to the high or atmospheric background pressure [4]. As a result, $K_{surface} \gg h_{gass}$, hence mass transport through the boundary layer is a rate-limiting process. Ideally, in isothermal AP-CVD graphene growth on Cu catalyst using CH_4, to grow a monolayer graphene film a low CH_4 concentration gas composition should be used, while a multilayer graphene film with a uniform thickness across a substrate-scale requires a high CH_4 concentration gas composition. In this instance, a high CH_4 concentration gas composition would supply enough or more active C species required for a multilayer graphene growth. In the AP-CVD graphene growth setup, the thickness of the boundary layer is fixed through geometric effects of the gas flow and of the CVD chamber.

Nonetheless, Bhaviripudi *et al.* [4] using a range of CH_4 gas compositions in isothermal AP-CVD graphene growth on Cu catalyst has shown that growth varied from monolayer graphene at low CH_4 concentrations to multilayer domains on a monolayer graphene background at higher CH_4 concentrations. A challenge of Cu catalyst of growing large-area bilayer or multilayer graphene with uniform thickness suggests that surface reactions, hydrocarbon decomposition rate, in particular, do not occur much faster than mass transport through the boundary layer onto the catalyst surface as discussed above. However, that does not change mass transport rate-limiting process (AP-CVD) into surface reaction rate-limiting process (low pressure (LP-CVD)) discussed by Bhaviripudi *et al.* [4]. In literature, such challenge of Cu is ascribed primarily to the low decomposition rate of hydrocarbon (low catalytic activity) which leads to the insufficient supply of active C species for graphene multilayers to materialise [4,16,26].

Therefore, effort has been made to improve the low Cu decomposition rate of hydrocarbon by alloying Cu with Ni which has higher decomposition rate of hydrocarbon and Ni has shown a capability of improving the catalytic activity of Cu to grow large-area multilayer or bilayer graphene by lowering the formation energies of the active C species (CH_3, CH_2, CH and C) on the Cu surface which lead to much higher surface concentrations of C species required for multilayer graphene growth [15,16,24,26,43-45].

2.7 Ni surface concentration in dilute Cu(Ni) foil during AP-CVD graphene growth

Ni surface concentration in dilute Cu(Ni) foil during AP-CVD graphene growth will increase through bulk-to-surface diffusion. Bulk-to-surface diffusion is a process by which the total energy of the crystal (Gibbs free energy) consisting of two or more components is minimized by the diffusion of atoms from the bulk layers of the crystal into the surface layer [49,50]. For a crystal consisting of component *i*, the change in Gibbs free energy per total number of moles of component *i* is given by [51-53]

$$\left(\frac{\delta G}{\delta n_i}\right)_{T,P,n_{j\neq i}} = \mu_i \tag{2.12}$$

where μ_i is the chemical potential of component *i*,

In equation 2.12, μ_i may be viewed as the rate of change of the total Gibbs free energy of the system when, holding the temperature, T and the pressure, P constant while a very small amount of the component i is added to the system without changing the number of moles of the other component j. Therefore, if the chemical substance is free to move from one place to another, it moves spontaneously to the state of lower chemical potential. This change in Gibbs free energy (chemical potential) result in an enrichment of the surface layer of the crystal by element *i* in the crystal and is referred to as the segregation energy.

During CVD graphene growth, a catalyst temperature is increased at a constant heating rate from room temperature to the desired growth temperature, and immediately after growth the temperature of the graphene/catalyst is decreased rapidly to room temperature. In view of a dilute Cu(0.61 at% Ni) catalyst, a temperature increase results in bulk-to-surface diffusion of Ni (due to the dependence on the Arrhenius term) which increases the surface concentration of Ni in the catalyst foil. Such increase in the surface concentration of Ni could be well-described by a semi-infinite solution of Fick's diffusion equation [46]. In the semi-infinite solution of Fick, the surface enrichment factor (β) at temperature, T, is given by

$$\beta(T) = \frac{X^S(T) - X^B}{X^B} \tag{2.13}$$

where $X^S(T)$ is the surface concentration at temperature, T and X^B is the bulk concentration of the diffusing solute atoms (X^B = 0.61 at% in a dilute Cu(0.61 at% Ni) catalyst).

The temperature dependence of the enrichment factor in the semi-infinite solution of Fick is given by [46]

$$\frac{X^S(T)-X^B}{X^B} = \left\{ \frac{4D_0}{\pi\alpha d^2} \left[\frac{RT^2}{Q} \exp(-Q/RT) \right] \right\}^{\frac{1}{2}} \tag{2.14}$$

where D_0 is the pre-exponential factor, Q is the activation energy ($D_0 = 7.0 \times 10^{-5}$ m^2/s and $Q = 225.0$ kJ/mol for Ni diffusion in Cu [6]), α is the constant heating rate, d is interlayer distance ($d = 0.181$ nm in Cu(001)), R is the gas constant and T is the crystal temperature.

Equation 2.14 could well describe the temperature dependence of the surface concentration of Ni in dilute Cu(0.61 at% Ni) catalyst, however, cannot describe the temperature dependence of the maximum (or equilibrium) surface concentration of Ni in a catalyst. Nonetheless, the temperature dependence of the maximum surface concentration of Ni in a catalyst could be described by the well-known Langmuir-McLean equation [46,47]:

$$\frac{X^\phi(T)}{1-X^\phi(T)} = \frac{X^B}{1-X^B} \exp(-\Delta G/RT) \tag{2.15}$$

where $X^\phi(T)$ is the relative surface concentration at temperature, T, $X^\phi(T) = \frac{X^S(T)}{X^M}$, X^M is the attainable maximum surface concentration ($X^M = 25$ at% in Cu(001) [48]) of solute atoms in the crystal surface, ΔG is the segregation energy (ΔG = 30.3 kJ/mol for Ni in Cu(001)).

Now, using the semi-infinite solution of Fick (Equation 2.14) and the Langmuir- McLean equation (Equation 2.15), a view of the temperature dependence of the Ni surface concentration in a dilute Cu(0.61 at% Ni) catalyst during AP-CVD graphene growth was obtained as shown in figure 2.6. In figure 2.6, an increase in catalyst temperature increases the surface concentration of Ni (described by Fick solid-line) until it reaches a maximum (or equilibrium) surface concentration of 8.1 at% (determined by Fick and Langmuir-McLean solid-lines intersection) and a further increase in temperature result in a decrease in surface concentration of Ni due to surface-to-bulk diffusion of Ni or due to the sublimation of Ni, but at these catalyst temperatures (<1000 °C) and higher background pressure (atmospheric pressure) the sublimation of Ni (and Cu) is suppressed. At a

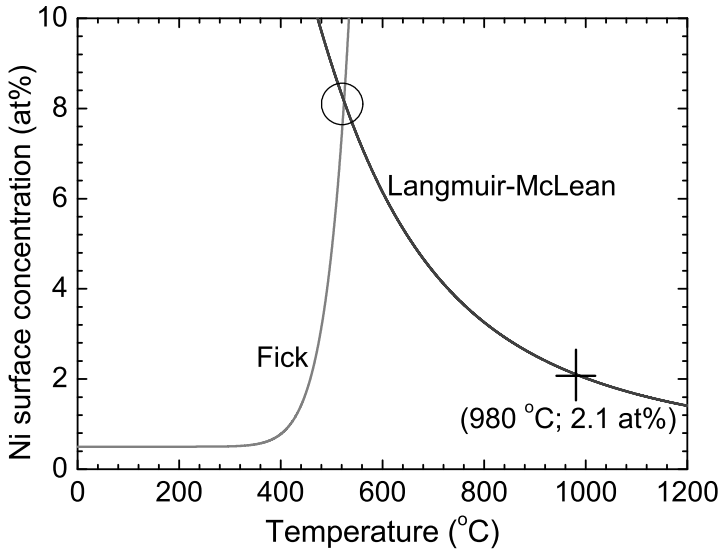

Figure 2.6: An illustration of the temperature dependence of the Ni surface concentration in a dilute Cu(0.61 at% Ni) catalyst at a constant heating rate of α = 0.5 °C/s (Calculated in this chapter using equation 2.14 and 2.14, see supporting information for the publication presented in chapter 7).

CVD growth temperature of 980 °C a surface concentration of Ni is 2.1 at% in Cu(0.61 at% Ni) catalyst (Figure 2.6).

In figure 2.6, It can be seen that Fick's equation predicts that the surface concentration increases to infinity as temperature increases to infinity and hence it cannot predict the maximum attainable (or equilibrium) surface concentration as observed experimentally in bulk-to-surface diffusion measurements [46,48,49]. The Fick equation (Equation 2.14) accurately describes the kinetics of bulk-to-surface diffusion at lower surface concentrations (lower temperatures). In bulk-to-surface diffusion, high surface concentration (equilibrium) is reached at higher temperatures after diffusion kinetics and this is well-described by Langmuir-McLean equation since it accounts for attainable maximum surface concentration (X^M) [46]. Nonetheless, without using two separate expressions (semi-infinite solution of Fick and Langmuir- McLean equation), the rate of surface concentration change of Ni in dilute Cu(Ni) foil could be calculated using modified Darken equations [46,48-50]:

$$
\begin{aligned}
\frac{\partial X_i^{\phi}}{\partial t} &= \frac{M_i^{(B_1\to\phi)} X_i^{B_1}}{d^2}\left[\Delta G + RT\ln\left(\frac{X_i^{B_1}(1-X_i^{\phi})}{X_i^{\phi}(1-X_i^{B_1})}\right)\right], \\
\frac{\partial X_i^{B_1}}{\partial t} &= \frac{M_i^{B} X_i^{B_2}}{d^2}\left[RT\ln\left(\frac{X_i^{B_2}(1-X_i^{B_1})}{X_i^{B_1}(1-X_i^{B_2})}\right) - RT\ln\left(\frac{X_i^{B_1}(1-X_i^{\phi})}{X_i^{\phi}(1-X_i^{B_1})}\right)\right], \\
&\vdots \\
\frac{\partial X_i^{j}}{\partial t} &= \frac{M_i^{B} X_i^{j+1}}{d^2}\left[RT\ln\left(\frac{X_i^{(j+1)}(1-X_i^{(j)})}{X_i^{(j)}(1-X_i^{(j+1)})}\right) - RT\ln\left(\frac{X_i^{(j)}(1-X_i^{(j-1)})}{X_i^{(j-1)}(1-X_i^{(j)})}\right)\right],
\end{aligned}
\tag{2.16}
$$

where ϕ is the surface layer, B_1 and B_2 are the first (subsurface layer) and second bulk layers respectively, X_i^{ϕ} is the relative surface concentration of the i-th atom in the j-th layer, X_i^{B} is the bulk concentration of the segregating atoms, ΔG is the segregation energy of the segregating atoms, M_i is the mobility, $M_i = D/RT$ where D is the diffusion coefficient in Arrhenius equation, d is the thickness of the segregated layer, R is the gas constant and T is the temperature.

In the Darken approach, the crystal is divided into discrete atomic layers parallel to the surface layer and the changes in concentrations in the layers are described by a set of coupled differential equations (Equation 2.16) which is solved numerically for an increasing temperature T [48]. Darken equations use (or yield) both the diffusion parameters (D_0 and Q) and the segregation energy. Therefore, substituting the values for diffusion parameters and the segregation energy (used in equation 2.14 and 2.15) into equation 2.16, the temperature dependence of Ni surface concentration in dilute Cu(Ni) foil was obtained (see figure 2.7) which shows a similar temperature dependence as discussed using equation 2.14 and 2.15.

In the Darken equations, it can be seen that the bulk concentration of the segregating atoms (or impurities) act as a surface layer supplier ($B_1 \to \phi$) to reach high impurity surface concentrations in dilute metal alloys. Therefore, since the impurities in the high purity Cu foils have much lower bulk concentrations, in a few ppm (see table 2.1) they will not reach high surface concentrations. However, those with much higher segregation energy (>100 KJ/mol) are more likely to reach high surface concentrations.

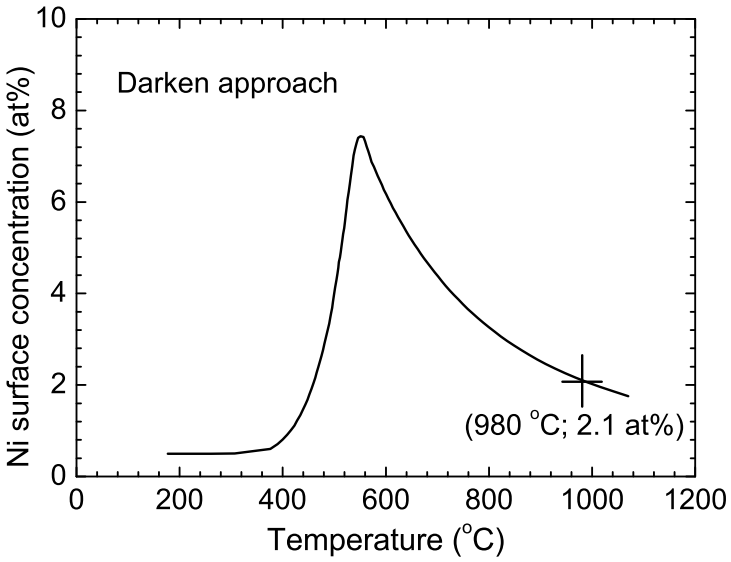

Figure 2.7: The temperature dependence of the Ni concentration in the surface layer of a dilute Cu(Ni) foil at a constant heating rate of α = 0.5 °C/s (Calculated in this chapter using equation 2.16).

Trace chemical analysis of copper (ppm weight)

H																	He
Li < 0.001	Be < 0.001										B < 0.005	C 3.5	N <1	O 30	F < 0.05	Ne
Na < 0.005	Mg < 0.005										Al 0.01	Si 0.35	P 41	S 6.3	Cl 0.12	Ar
K < 0.01	Ca < 0.01	Sc < 0.001	Ti < 0.005	V < 0.001	Cr 0.01	Mn 0.02	Fe 0.83	Co 0.007	Ni 2.2	Cu Matrix	Zn < 0.01	Ga < 0.05	Ge < 0.05	As 0.54	Se 0.61	Br < 0.005	Kr
Rb < 0.005	Sr < 0.005	Y < 0.005	Zr < 0.005	Nb < 0.005	Mo 0.05	Tc	Ru < 0.005	Rh <1	Pd 0.12	Ag 12	Cd < 0.01	In < 0.005	Sn 0.12	Sb 0.85	Te < 0.05	I < 0.05	Xe
Cs < 0.005	Ba < 0.005	La < 0.005	Hf < 0.005	Ta <1	W < 0.005	75 Re < 0.005	Os < 0.005	Ir < 0.005	Pt < 0.005	Au < 0.01	Hg < 0.01	Tl < 0.001	Pb 0.34	Bi 0.08	Po	At	Rn
Fr	Ra	Ac															

Ce < 0.005	Pr < 0.005	Nd < 0.005	Pm	Sm < 0.005	Eu < 0.005	Gd < 0.005	Tb < 0.005	Dy < 0.005	Ho < 0.005	Er < 0.005	Tm < 0.005	Yb < 0.005	Lu < 0.005
Th < 0.0001	Pa	U < 0.0001											

Table 2.1: Trace chemical analysis results for impurities in high-purity copper (Extracted from Ref. [54]).

Bibliography

1. H.O. Pierson, Handbook of chemical vapor deposition: principles, technology and applications, 2nd ed., William Andrew Publishing, LLC, New York, 1999.

2. G.A. López, E.J. Mittemeijer, The solubility of C in solid Cu, Scripta Materialia. 51 (2004) 1-5.

3. A. Harpale, M. Panesi, H.B. Chew, Communication: Surface-to-bulk diffusion of isolated versus interacting C atoms in Ni(111) and Cu(111) substrates: A first principle investigation, The Journal of Chemical Physics. 142 (2015) 061101.

4. S. Bhaviripudi, X. Jia, M.S. Dresselhaus, J. Kong, Role of Kinetic Factors in Chemical Vapor Deposition Synthesis of Uniform Large Area Graphene Using Copper Catalyst, Nano Letters. 10 (2010) 4128-4133.

5. W. Cai, R.D. Piner, Y. Zhu, X. Li, Z. Tan, H.C. Floresca, et al., Synthesis of isotopically-labeled graphite films by cold-wall chemical vapor deposition and electronic properties of graphene obtained from such films, Nano Research. 2 (2009) 851-856.

6. W.F. Gale, T.C. Totemeier, eds., Smithells Metals Reference Book, 8th ed., Butterworth-Heinemann, Oxford UK, 2004.

7. M. Guttmann, The Link Between Equilibrium Segregation and Precipitation in Ternary Solutions Exhibiting Temper Embrittlement, Metal Science. 10 (1976) 337-341.

8. K. Wandelt, C.R. Brundle, Evidence for Crystal-Face Specificity in Surface Segregation of CuNi Alloys, Physical Review Letters. 46 (1981) 1529-1532.

9. S. Hofmann, R. Frech, W. Germany, Application of Auger Electron Spectrometry to Trace Analysis: Determination of Less Than 10 ppm Sulfur in Copper, Analytical Chemistry. 57 (1985) 716-719.

10. D.R. Lide, CRC Handbook of Chemistry and Physics, 63rd ed., CRC Press, Inc., 2005.

11. S.M. Kim, A. Hsu, Y.-H. Lee, M. Dresselhaus, T. Palacios, K.K. Kim, et al., The effect of copper pre-cleaning on graphene synthesis, Nanotechnology. 24 (2013) 365602.

12. B. Zhang, W.H. Lee, R. Piner, I. Kholmanov, Y. Wu, H. Li, et al., Low-temperature chemical vapor deposition growth of graphene from toluene on electropolished copper foils., ACS Nano. 6 (2012) 2471-6.

13. Y.-P. Hsieh, Y.-W. Wang, C.-C. Ting, H.-C. Wang, K.-Y. Chen, C.-C. Yang, Effect of Catalyst Morphology on the Quality of CVD Grown Graphene, Journal of Nanomaterials. 2013 (2013) 1-6.

14. Y. Xue, B. Wu, Y. Guo, L. Huang, L. Jiang, J. Chen, et al., Synthesis of large-area, few-layer graphene on iron foil by chemical vapor deposition, Nano Research. 4 (2011) 1208-1214.

15. H. Choi, Y. Lim, M. Park, S. Lee, Y. Kang, M.S. Kim, et al., Precise control of chemical vapor deposition graphene layer thickness using Ni_xCu_{1-x} alloys, J. Mater. Chem. C. 3 (2015) 1463-1467.

16. W. Liu, S. Kraemer, D. Sarkar, H. Li, P.M. Ajayan, K. Banerjee, Controllable and rapid synthesis of high-quality and large-area bernal stacked bilayer graphene using chemical vapor deposition, Chemistry of Materials. 26 (2014) 907-915.

17. W. Liu, H. Li, C. Xu, Y. Khatami, K. Banerjee, Synthesis of high-quality monolayer and bilayer graphene on copper using chemical vapor deposition, Carbon. 49 (2011) 4122-4130.

18. P.R. Kidambi, C. Ducati, B. Dlubak, D. Gardiner, R.S. Weatherup, M.B. Martin, et al., The parameter space of graphene chemical vapor deposition on polycrystalline Cu, Journal of Physical Chemistry C. 116 (2012) 22492-22501.

19. D.H. Jung, C. Kang, M. Kim, H. Cheong, H. Lee, J.S. Lee, Effects of Hydrogen Partial

Pressure in the Annealing Process on Graphene Growth, The of Physical Chemistry C. 118 (2014) 3574-3580.

20. M. Losurdo, M.M. Giangregorio, P. Capezzuto, G. Bruno, Graphene CVD growth on copper and nickel: role of hydrogen in kinetics and structure, Physical Chemistry Chemical Physics. 13 (2011) 20836.

21. I. Vlassiouk, S. Smirnov, M. Regmi, S.P. Surwade, N. Srivastava, R. Feenstra, et al., Graphene Nucleation Density on Copper: Fundamental Role of Background Pressure, Journal Physical Chemistry C. 117 (2013) 18919-18926.

22. I. Vlassiouk, M. Regmi, P. Fulvio, S. Dai, P. Datskos, G. Eres, et al., Role of hydrogen in chemical vapor deposition growth of large single-crystal graphene, ACS Nano. 5 (2011) 6069-76.

23. W. Zhang, P. Wu, Z. Li, J. Yang, First-principles thermodynamics of graphene growth on Cu surfaces, Journal of Physical Chemistry C. 115 (2011) 17782-17787.

24. T. Wu, X. Zhang, Q. Yuan, J. Xue, G. Lu, Z. Liu, et al., Fast growth of inch-sized single-crystalline graphene from a controlled single nucleus on Cu-Ni alloys, Nature Materials. 15 (2015) 43-47.

25. Z. Sun, Z. Yan, J. Yao, E. Beitler, Y. Zhu, J.M. Tour, Growth of graphene from solid carbon sources, Nature. 468 (2010) 549-52.

26. S. Chen, W. Cai, R.D. Piner, J.W. Suk, Y. Wu, Y. Ren, et al., Synthesis and characterization of large-area graphene and graphite films on commercial Cu-Ni alloy foils, Nano Letters. 11 (2011) 3519-3525.

27. J.D. Wood, S.W. Schmucker, A.S. Lyons, E. Pop, J.W. Lyding, Effects of polycrystalline Cu substrate on graphene growth by chemical vapor deposition, Nano Letters. 11 (2011) 4547-4554.

28. H. Chen, W. Zhu, Z. Zhang, Contrasting behavior of carbon nucleation in the initial stages of graphene epitaxial growth on stepped metal surfaces, Physical Review Letters. 104 (2010) 1-4.

29. G. Jones, F. Studt, F. Abild-Pedersen, J.K. Nørskov, T. Bligaard, Scaling relationships for adsorption energies of C2 hydrocarbons on transition metal surfaces, Chemical Engineering Science. 66 (2011) 6318-6323.

30. L.-Q. Lee, D.-H. Shi, Y.-J. Zhao, P.-L. Cao, Acetylene adsorption on Cu(111) and stepped Cu(111): theoretical study, Journal of Physics: Condensed Matter. 7 (1995) 6449-6457.

31. A. V. Zeigarnik, R.E. Valdés-Pérez, O.N. Myatkovskaya, C-C Bond Scission in Ethane Hydrogenolysis, The Journal of Physical Chemistry B. 104 (2000) 10578-10587.

32. T.S. Marinova, P.K. Stefanov, Adsorption and thermal evolution of acetylene on a Cu(100) surface, Surface Science. 191 (1987) 66-74.

33. A. Dahal, M. Batzill, Graphene-nickel interfaces: a review, Nanoscale. 6 (2014) 2548.

34. A. Guermoune, T. Chari, F. Popescu, S.S. Sabri, J. Guillemette, H.S. Skulason, et al., Chemical vapor deposition synthesis of graphene on copper with methanol, ethanol, and propanol precursors, Carbon. 49 (2011) 4204-4210.

35. A. Mohsin, L. Liu, P. Liu, W. Deng, I.N. Ivanov, G. Li, et al., Synthesis of millimeter-size hexagon-shaped graphene single crystals on resolidified copper, ACS Nano. 7 (2013) 8924-8931.

36. W. Li, Q., Chou, H., Zhong, J.H., Liu, J.Y., Dolocan, A., Zhang, J., Zhou, Y., Ruoff, R.S., Chen, S. and Cai, Growth of adlayer graphene on Cu studied by carbon isotope labeling, Nano Letters. 13 (2013) 486-490.

37. S. Nie, W. Wu, S. Xing, Q. Yu, J. Bao, S. Pei, et al., Growth from below: bilayer graphene on copper by chemical vapor deposition, New Journal of Physics. 14 (2012) 093028.

38. E. Starodub, N.C. Bartelt, K.F. McCarty, Oxidation of Graphene on Metals, The Journal of Physical Chemistry C. 114 (2010) 5134-5140.

39. R. Mu, Q. Fu, L. Jin, L. Yu, G. Fang, D. Tan, et al., Visualizing chemical reactions confined under graphene, Angewandte Chemie (International Ed. in English). 51 (2012) 4856-9.

40. L. Hansen, P. Stoltze, K.W. Jacobsen, J.K. Nørskov, Self-diffusion on copper surfaces,

Physical Review B. 44 (1991) 6523-6526.

41. J. Gao, J. Yip, J. Zhao, B.I. Yakobson, F. Ding, Graphene nucleation on transition metal surface: structure transformation and role of the metal step edge, Journal of the American Chemical Society. 133 (2011) 5009-15.

42. Y. Zhang, L. Gomez, F.N. Ishikawa, A. Madaria, K. Ryu, C. Wang, et al., Comparison of Graphene Growth on Single-Crystalline and Polycrystalline Ni by Chemical Vapor Deposition, The Journal of Physical Chemistry Letters. 1 (2010) 3101-3107.

43. N. Liu, L. Fu, B. Dai, K. Yan, X. Liu, R. Zhao, et al., Universal Segregation Growth Approach to Wafer-Size Graphene from Non-Noble Metals, Nano Letters. 11 (2011) 297-303.

44. X. Liu, L. Fu, N. Liu, T. Gao, Y. Zhang, L. Liao, et al., Segregation growth of graphene on Cu-Ni alloy for precise layer control, Journal of Physical Chemistry C. 115 (2011) 11976-11982.

45. Y. Wu, H. Chou, H. Ji, Q. Wu, S. Chen, W. Jiang, et al., Growth Mechanism and Controlled Synthesis of AB-Stacked Bilayer Graphene on Cu-Ni Alloy Foils, ACS Nano. (2012) 7731-7738.

46. E.C. Viljoen, J. du Plessis, Surface segregation measurements via the linear programmed heating method: Part A-Theory, Surface Science. 431 (1999) 128-137.

47. D.R. Harries, A.D. Marwick, Non-Equilibrium Segregation in Metals and Alloys, Philosophical Transactions of the Royal Society A: Mathematical, Physical and Engineering Sciences. 295 (1980) 197-207.

48. E.C. Viljoen, J. du Plessis, Surface segregation measurements via the linear programmed heating method: Part B-Experimental and results, Surface Science. 468 (2000) 27-36.

49. J. du Plessis, G.N. van Wyk, A model for surface segregation in multicomponent alloys-part III: The kinetics of surface segregation in a binary alloy, Journal of Physics and Chemistry of Solids. 50 (1989) 237-245.

50. J. du Plessis, Solid State Phenomena - Part B, Volume 11 (Diffusion and Defect Data), Sci-Tech Publications, Brookfield USA, 1990.

51. C.H. Lupis, Chemical Thermodynamics of Materials, North-Holland, Amsterdam, 1983.

52. S. Stølen, T. Grande, Chemical Thermodynamics of Materials, John Wiley & Sons, 2004.

53. G. N. Lewis; M. Randall, Thermodynamics, 2nd ed., McGraw-Hill, New York, 1961.

54. S. Cronjé, TEM investigation of rapidly deformed Cu and Mo shaped charge liner material, MSc thesis, University of the Free State, 2007.

CHAPTER 3

Graphene characterization techniques

3.1 Introduction

In CVD graphene growth, as-grown graphene on a substrate usually is transferred onto different substrates (either by chemically etching of substrates or by bubbling graphene sheet from the substrates) for characterization of the graphene sheet for various applications. The characterization of the graphene sheet is usually investigated by the quality of graphene film, the number of graphene layers, the layers stacking order and the electrical properties. The characterization relies on the atomic/band structure of graphene which differs for mono, bi, and multilayer graphene. The most commonly used techniques for the characterization/investigation of graphene include the following, Raman spectroscopy, transmission electron microscopy, atomic force microscopy, optical microscopy and scanning electron microscopy, X-ray photoelectron spectroscopy and four-point probe resistance. In graphene characterization, these techniques have proven to be complementary to each other, not only because different information can be obtained from each technique, but also because some techniques give direct information (do not require data processing) and some give analysis over a very small area in few nanometres (i.e. information acquired from different techniques are interrelated in terms of spatial resolution).

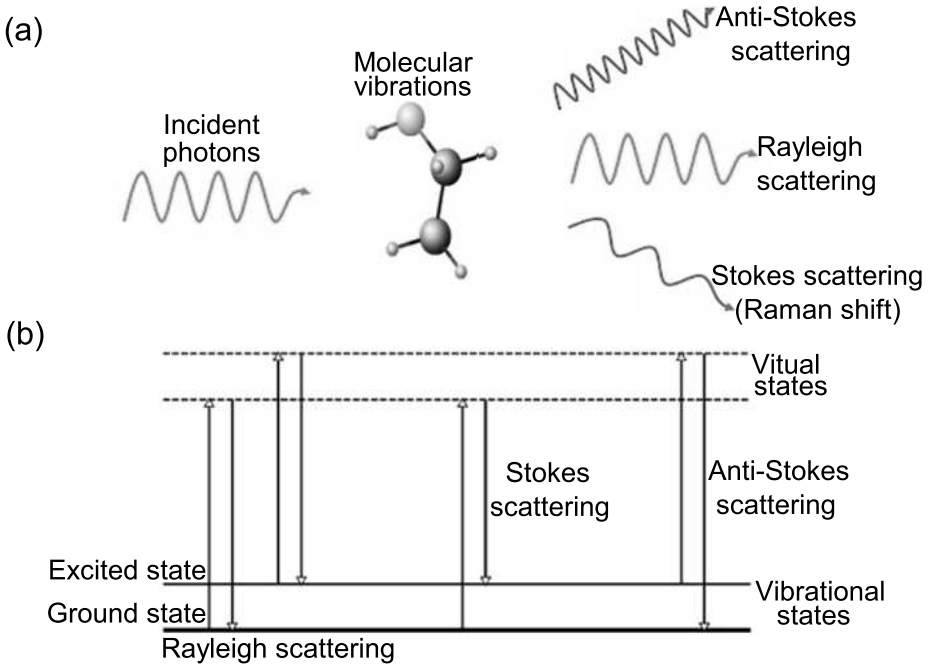

Figure 3.1: (a) Schematic diagram of light scattering by Rayleigh, Stokes and Anti-Stokes scattering processes in a vibrating molecule due to the time-dependent perturbation introduced by an incident photon of energy $\hbar\omega_L$. (b) Schematic view of energy level diagram of a perturbed system showing Rayleigh scattering (elastic scattering), Stokes and Anti-Stokes scattering processes (inelastic scattering).

3.2 Raman spectroscopy

Raman spectroscopy is a non-destructive technique which provides detailed information about chemical structure/phase, crystallinity and molecular interactions. In this spectroscopy technique, there is a scattering of photons (from a high-intensity laser light source) by phonons upon the interaction of photons with the chemical bonds within a material/sample (Figure 3.1(a)). The interaction of photons with the chemical bonds within a sample creates a time-dependent perturbation of the Hamiltonian [1].

The perturbation introduced by an incident photon of energy $\hbar\omega_L$ increases the ground state energy (E_{GS}) to a total energy of $E_{GS}+\hbar\omega_L$ which does not correspond to a stationary state hence a system is viewed to be on a virtual level (Figure 3.1(b)) [1,2]. Since the system has no stationary state (i.e. is in the unstable situation), the photon is emitted by the perturbed system and the system goes back to the stationary state (ground state). When it returns to its initial state and the frequency of the emitted photon is the same as the incident one, this is called Rayleigh scattering (elastic

scattering) (Figure 3.1(b)) [1,3].

On the other hand, as the sample returns to a stationary state (with a much lower probability) a photon can lose part of its energy in the interaction process and scattered from sample with a lower energy $\hbar\omega_{Sc} = \hbar\omega_L - \hbar\Omega$ ($\hbar\Omega$ is a phonon energy). This corresponds to the Stokes (S) process (inelastic scattering) [1,3]. Initially, if the sample is in the excited vibrational state, and after the photon interaction the system returns to its ground state, the photon leaves the sample with an increased energy $\hbar\omega_{Sc} = \hbar\omega_L + \hbar\Omega$. This corresponds to the Anti-Stokes (AS) process [1,3]. Between S and AS, S is the most probable [1], therefore, Raman spectra are S measurements plots of the intensity of the scattered photon as a function of the difference between incident and scattered photon energy (known as Raman shift). Generally, a Raman spectrum features a number of peaks and each peak corresponds to a specific molecular bond vibration, including individual bonds such as C−C, C=C.

Raman spectroscopy in graphene studies is a well-known powerful technique to determine, among others, the number of graphene layers, the stacking order and the interlayer interactions in few layers graphene sample [4-8].

The unit cell of monolayer graphene contains two carbon atoms, A and B from sublattice A and B respectively (Figure 3.2) which means two sets of 2s and 2p states corresponding to 8 electrons per unit cell which fill the 4 lower 3 σ and 1π bonding energy bands (valence bands) and the 4 higher 3 σ* and 1π* anti-bonding energy bands (conduction bands) remain unoccupied. Therefore, there are two π electrons per unit cell which occupy the lower π band. In energy dispersion curves, the upper π* and the lower π bands are degenerate at the *K* points (Figure 3.2).

Since the unit cell of monolayer graphene consists of two carbon atoms (A and B), there is six phonon dispersion bands (see calculated phonon dispersion relation of graphene in reference [10]). Three of the six phonon dispersion bands are acoustic branches (A) and the other three are optic (O) phonon branches and two of the three branches corresponds to the optical modes which are in-plane transverse optical mode (iTO) and longitudinal optical mode (LO) [1,5,11]. The directions of the vibrations are with respect to the direction of the nearest carbon-carbon atoms and, therefore, the phonon modes are classified as longitudinal (L) when the vibrations are parallel to the A-B carbon-carbon directions and as transverse (T) when the vibrations are perpendicular to the A-B carbon-carbon directions [5]. Near the zone center (Γ point), the iTO and LO modes

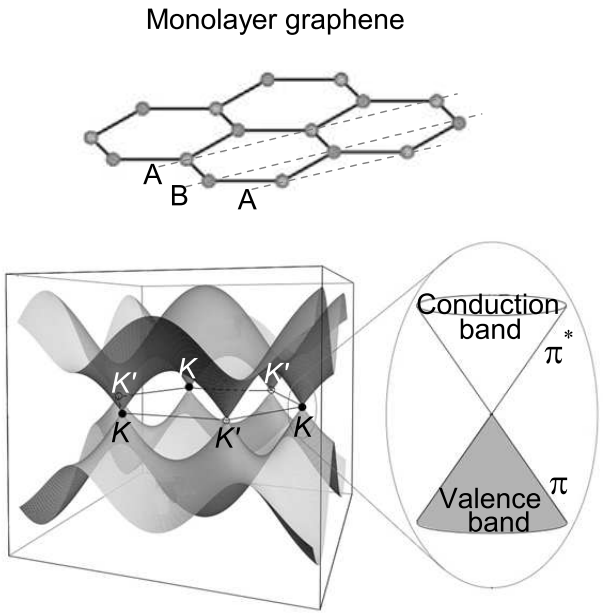

Figure 3.2: The atomic structure of monolayer graphene consists of a hexagonal lattice showing two carbon atoms A (from sublattice A) and B (from sublattice B). This produces an electronic structure of narrowed bands (conduction and valence bands) that touch at a point (Dirac point). A band structure showing hexagonal lattice points shows two in equivalent contact points K and K' in the first Brillouin zone of graphene [2,9].

correspond to the vibrations of the sublattice A against the sublattice B (i.e. between K and K' points in the first Brillouin zone of graphene as shown in figure 3.2) and they are Raman active modes responsible for the main Raman features namely G, D and 2D bands [1,2,5,10,12].

The origins of the main Raman features (G, D and 2D bands) are as follows (illustrated in figure 3.3):

(i) The G mode at about 1580 cm^{-1} involves the in-plane bond-stretching motion of pairs of carbon sp^2 atoms and it originates from a first-order Raman scattering process (only one-phonon scattering is involved).

(ii) The D mode at about 1350 cm^{-1} (also known as a disorder-induced band) involves phonons near the K zone boundary and is only active in the presence of disorder in graphene. The band originates from a second-order Raman scattering process (double-resonance), involving one iTO phonon and one defect. The absence of the D-band in Raman spectra

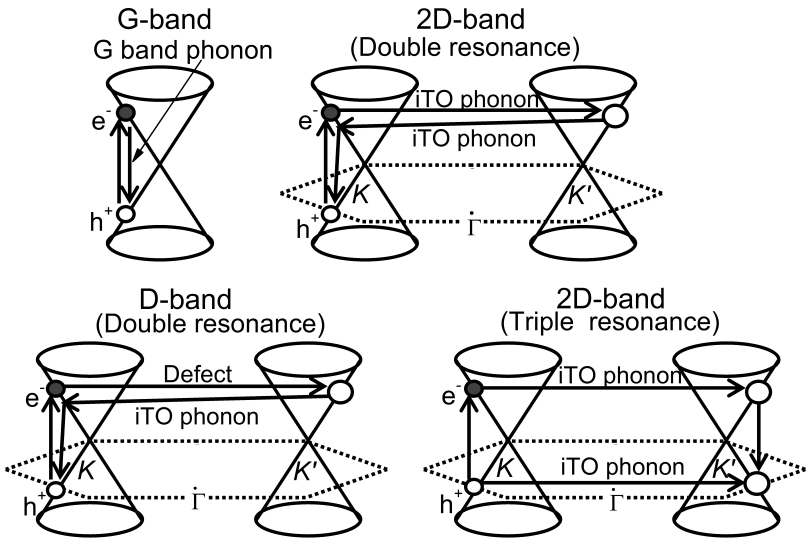

Figure 3.3: A schematic view of Raman scattering processes responsible for the Raman main features G, 2D and D bands in graphene film (Adapted from Ref. [5]).

demonstrates high-quality graphene.

(iii) The 2D mode at about 2700 cm^{-1} originate from a second-order Raman scattering process (double-resonance) and involves two iTO phonons near the *K* zone boundary. The 2D mode also originates from triple-resonance, and in contrast to double resonance process, in the triple resonance process all steps are resonant and this could lead to a more intense 2D-band (relative to the G-band) as seen in monolayer graphene. Hence, this could be one of the reasons of why the 2D-band is more intense than the G-band in monolayer graphene (see figure 3.4).

The double-resonance process starts with an electron of wave-vector **k** around *K* absorbing a photon (of energy E_{laser}), then, the electron is inelastically scattered by a phonon (of wavevector q and energy E_{phonon}) to a point (with wavevector **k** + **q**) near the K' point. Thereafter, the electron is scattered back to a **k** state by a phonon and recombines with a hole, emitting a photon. In the D band, the electron is elastically scattered by defects in the crystal and inelastically scattered by a phonon. In triple-resonance Raman scattering process, instead of the electron being scattered back by a phonon the hole will be scattered by a phonon (of wavevector **+q**) to a point near the K' point. The electron-hole recombination at a point near the K' point is resonant. Near the zone center

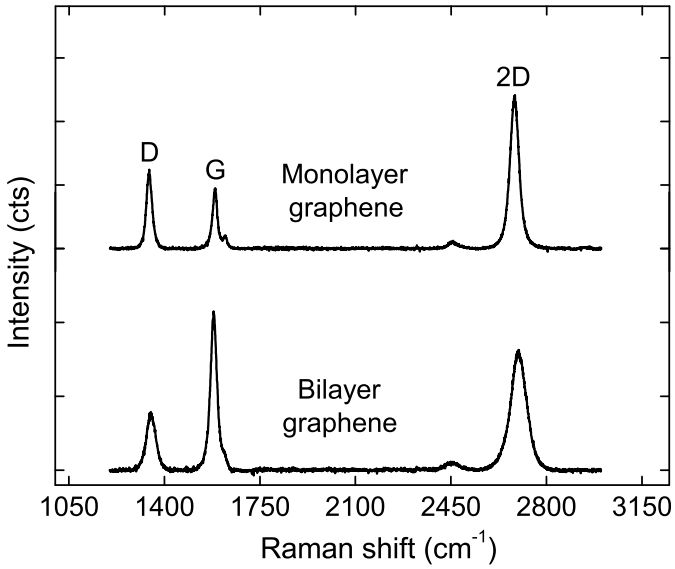

Figure 3.4: Raman spectra of low-quality (high-density of defects) monolayer and bilayer graphene films obtained on Cu foils using APCVD and transferred onto SiO_2/Si substrates for characterization. The excitation source: 532 nm laser with a laser power below 1 mW on the sample to avoid laser induced heating (Extracted from Ref. [13]).

(Γ point), the iTO modes correspond to the vibrations of the sublattice A against the sublattice B (between K and K' points in the first Brillouin zone of graphene) [5].

As discussed in the previous paragraphs, the main features that are observable in the Raman spectra of a high-quality monolayer and bilayer graphene are the G and 2D bands; however, in the case of a disordered graphene or at the edge of a graphene sheet, a disorder-induced D-band appears in the Raman spectra as shown in figure 3.4.

Furthermore, the atomic structure of a bilayer graphene consists of two layers of monolayer graphene (shown in figure 3.5(a)) which are arranged in a graphitic Bernal (AB) stacked configuration where the carbon atoms, B, (from sublattice B) of one layer are situated directly above the carbon atoms, A, (from sublattice A) of the other layer [2,14]. This produces an electronic structure that consists of hyperbolic bands (two conduction and two valence bands), two of which touch at a point (Dirac point) (Figure 3.5(a)). Clearly, a band structure of an AB-stacked bilayer graphene is different from that of a monolayer graphene (Figure 3.2 and 3.5). It is worth mentioning that a band structure of a non-AB stacked (turbostratic) bilayer graphene is similar to that of a monolayer graphene, hence stacking/configuration in multilayer (bilayer)

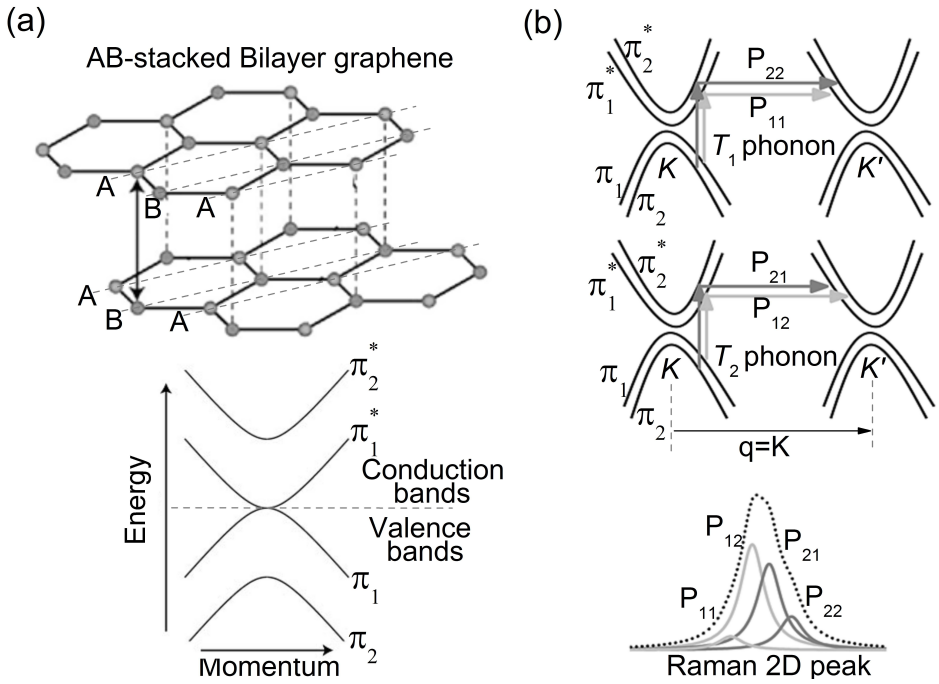

Figure 3.5: (a) Schematic view of the atomic structure of AB-stacked bilayer graphene which consists of two single graphene layers shifted with respect to each other so that the B carbon atoms (from sublattice B) of one layer are situated directly above the A carbon atoms (from sublattice A) of the other layer. This produces an electronic structure that consists of hyperbolic bands, π_1 and π_2 bands (two conduction and two valence bands), two of which touch at the Dirac point [14]. (b) The resonance Raman processes due to electronic band split are indicated as P_{11}, P_{22}, P_{12} and P_{21}, and give rise to four peaks in the Raman 2D peak [8,15].

graphene is important since it influences the optical and electronic properties of graphene.

In a band structure of AB-stacked bilayer graphene, the upper (lower) and lower (upper) branches of the valence (conduction) band are referred to as $\pi_1(\pi_1^*)$ and $\pi_2(\pi_2^*)$ respectively (Figure 3.5) [4,5,15,16]. Since 2D-band originates from second-order Raman process (double-resonance) that involves two iTO phonons, the electronic band split causes splitting of the phonon bands into two components such that the electron-phonon scattering occurs with two phonons with T_1 and T_2 symmetries [4,8]. For T_1 and T_2 phonons the scattering occurs between bands of the same symmetry (i.e. π_1 and π_1^* or π_2 and π_2^*) and bands of different symmetries (i.e. π_1 and π_1^*) respectively. T_1 and T_2 phonon processes are labelled as P_{ij} (with the relative magnitudes of the phonon wavevectors q), where $i(j)$ denote an electron scattered from (to) each conduction band $\pi_{i(j)}^*$(Figure3.5(b)). The P_{11}, P_{22}, P_{12} and P_{21} scattering processes originating from an iTO phonon giving rise to four peaks in the Raman 2D spectrum with wavenumbers at approximately 2655,

2680, 2700, and 2725 cm^{-1} respectively, and Full width at half maximum (FWHMs) equal that of monolayer graphene 2D peak [4,8]. These four peaks are normally fitted as four Lorentzian to 2D peak to demonstrate AB stacking in bilayer graphene (see figure 3.6) [4,5,8,15,16]. The amplitudes of the two Lorentzian (inner peaks in 2D peak) have almost the same intensity and are higher than the other two (outer peaks in 2D peak) similar to Lorentzian usually obtained for high-quality exfoliated AB-stacked bilayer graphene [4,5,8]. The Lorentzian amplitudes depend on the laser energy which is normally maintained constant during the experiment. In monolayer graphene, the 2D peak has a single Lorentzian feature (Figure 3.6).

In figure 3.4 and 3.6 (the distinction between Raman spectra of monolayer and bilayer graphene), the G peak intensity for bilayer graphene is twice that of monolayer graphene (Figure 3.4). The G-band position gives insight into the number of layers present in the graphene film, however, it can be affected by film conditions such as temperature, doping, and small amounts of strain present in the film. Nonetheless, the G-band intensity which is less susceptible to conditions mentioned above shows a behaviour that follows a linear trend as the number of layers increases from mono to multilayer [4,5,8,15,16]. The Raman 2D peaks FWHMs and positions for monolayer and bilayer graphene are different (Figure 3.6(a)). Figure 3.6(b) clearly shows a Raman 2D peak single Lorentzian feature of a monolayer graphene and four Lorentzian of bilayer graphene which demonstrates AB stacking order.

Generally, the 2D peaks FWHMs for monolayer graphene are in the range of 26-38 cm^{-1} and the peaks positions are at lower wavenumbers, and in contrast to monolayer graphene, the 2D peaks FWHMs for bilayer graphene are in the range of 39-65 cm^{-1} (with a cut-off FWHM of about 70 cm^{-1}) and the peaks positions are at higher wavenumbers [8,16,17]. In addition, the 2D to G peaks intensities ratio (I_{2D}/I_G), for monolayer graphene are in the range of about 2.5-4.5, while for bilayer graphene are in the range of 0.5-2.2 [8,16,18]. By observing the differences in the 2D and the G peaks intensity ratios, the 2D peak frequency (peak width and position) and line shape, the number of graphene layers contained in graphene films can be obtained and also the stacking order or interlayer interactions in few layers graphene films [8,15,16].

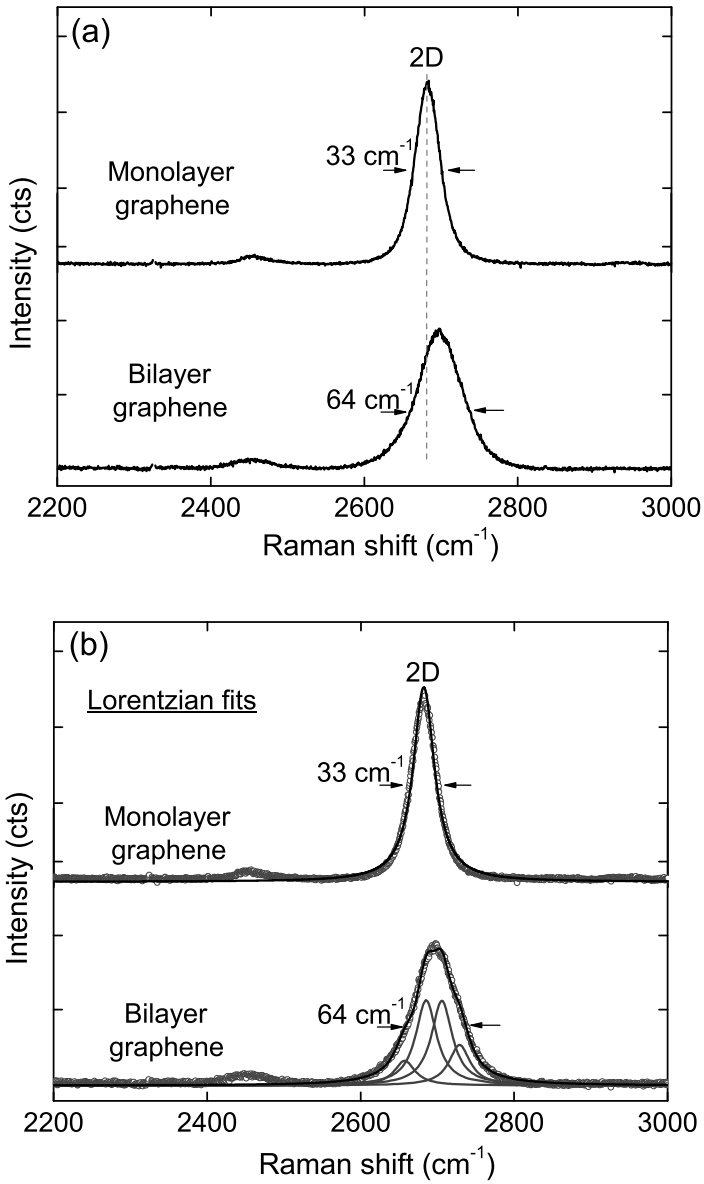

Figure 3.6: (a) The distinction between Raman 2D peaks of monolayer and bilayer graphene (from figure 3.4). (b) Raman 2D peak single Lorentzian feature of a monolayer graphene and four Lorentzian of bilayer graphene each with FWHM equal that of monolayer graphene 2D peak (33 cm^{-1} in this case) (Extracted from Ref. [13]).

3.3 Transmission electron microscopy (TEM)

Transmission electron microscopy is a technique that involves a beam of focused high-energy electrons (under ultra-high vacuum conditions) which is transmitted through a very thin sample and interacts with the sample as it passes through. The transmitted electrons are then used to

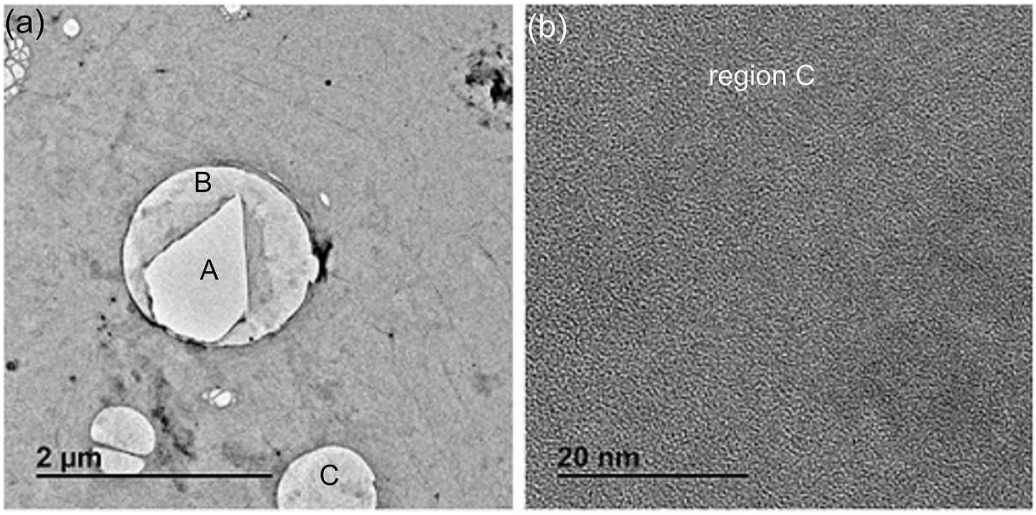

Figure 3.7: (a) Low magnification TEM image of bilayer graphene film transferred on a lacey carbon TEM grid (region A, B and C shown in holes of a lacey carbon TEM grid show an area without graphene (A) and with graphene (B and C)). (b) A high magnification TEM image of graphene in region C of figure (a) (See supporting information for the publication presented in chapter 7 Ref. [21]).

generate an image of a sample. Different types of images can be obtained in TEM from different interactions of the electron beam with a sample. For instance, an image of electron diffraction patterns is obtained from elastically scattered electrons (diffracted beam), bright field image from unscattered electrons (transmitted beam) and dark field image from elastically scattered electrons (diffracted beam) [19,20].

Figure 3.7 shows typical bright field TEM images (at low and high magnification) of bilayer graphene film transferred on a lacey carbon TEM grid. In this figure, region A, B and C show holes of a lacey carbon TEM grid with graphene sheet and these holes allow a transmission of electrons through a graphene sheet.

Figure 3.8 shows a typical electron diffraction pattern (from graphene areas shown in figure 3.7) which shows two sets of hexagonal diffraction spots (diffraction rings from crystalline graphene layers). The diffraction rings intensity profile which is indexed using the Miller-Bravais indices (*hkl*) for graphite shows peaks at $d = 0.123$ nm and peak $d = 0.213$ nm which correspond to indices (1-210) for outer ring (layer 1) and (1-110) for inner ring (layer 2) respectively [22]. In AB-stacked bilayer graphene (shown with a schematic view in the figure), the relative intensities of the spots in the outer ring are twice the intensities of the spots in the inner ring [4,16,22]. In

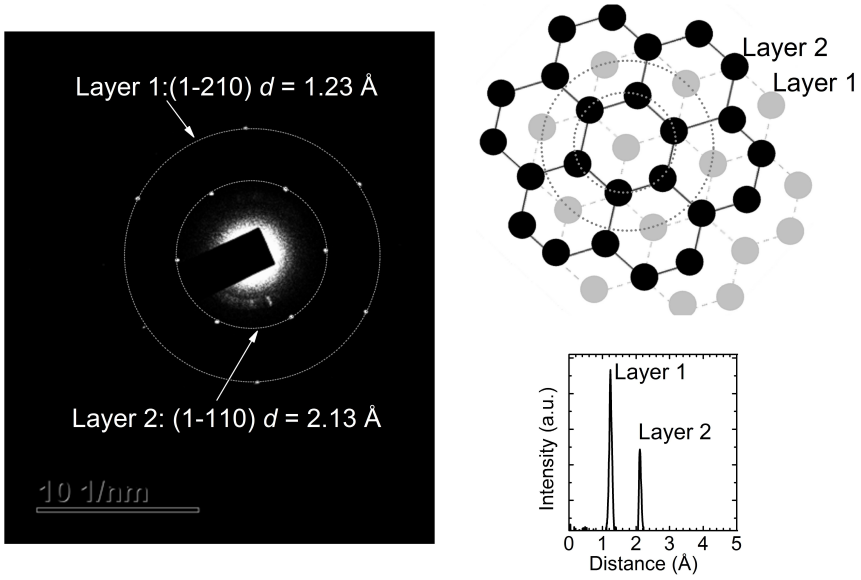

Figure 3.8: Selected area electron diffraction (SAED) pattern from an area (region C) showed in Figure 3.7(b) and shows two sets of hexagonal diffraction spots (rings). The diffraction rings intensity profile of two sets of hexagonal diffraction spots shows that the relative intensities of the spots in the outer ring (layer 1) are twice the intensities of the spots in the inner ring (layer 2) which shows a bilayer graphene with a Bernal stacking order (See publication presented in chapter 7 Ref. [21]).

monolayer graphene, the relative intensities of the spots in the outer ring are equal to the intensities of the spots in the inner ring [22]. Therefore, TEM gives direct information about the number of layers (from graphene edge image fringes (not observed in images presented in this section)) and the stacking order in multilayer graphene, particularly bilayer graphene [23,24].

3.4 Atomic force microscopy (AFM)

Atomic Force Microscopy is a high-resolution imaging technique used to study surface roughness (topography and morphology) of samples. AFM operates either on contact or non-contact (or tapping) mode by measuring the force between a cantilever tip and the sample surface. In AFM imaging (contact mode), a force between the sample surface (in contact with a tip) and the cantilever tip bends the cantilever when the tip encounters features on the sample surface. This deflection is sensed and reflected by a laser beam onto a segmented photodiode from which the AFM topographic map of the sample surface is obtained (Figure 3.9). In non-contact or tapping

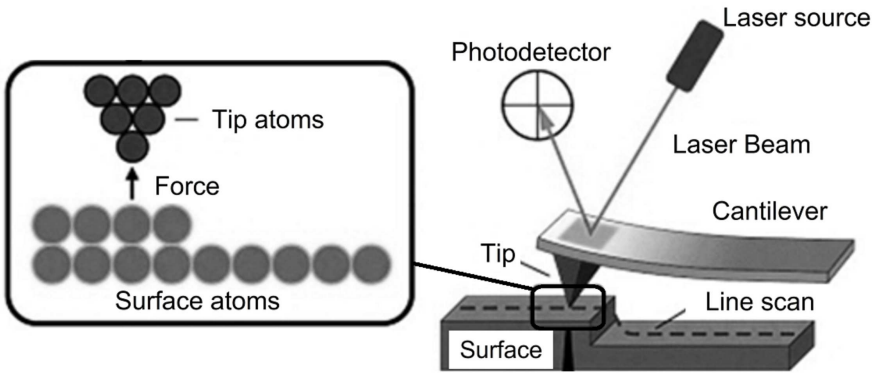

Figure 3.9: Schematic diagram of an AFM and it operates either on contact or non-contact (or tapping) mode by measuring the force between a cantilever tip and the sample surface to produce a topographic image (Extracted from Ref. [25]).

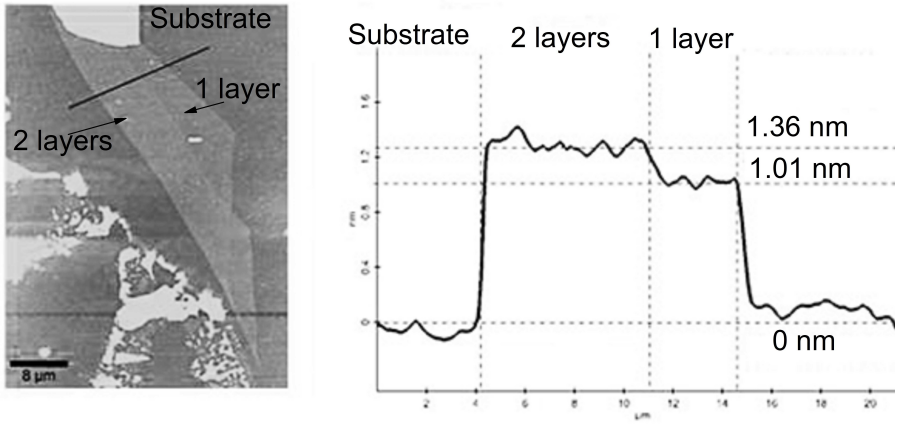

Figure 3.10: Atomic force microscope image of a graphene sheet with varying thickness (1 layer and 2 layers graphene) and the corresponding height profile of the sample obtained along a solid line in the image (Extracted from Ref. [30]).

mode, the sample surface is in intermittent contacts with the cantilever tip (the tip oscillate over the sample), however, the deflection of the cantilever is still sensed and reflected as in contact mode to produce a height image. In brief, AFM has been so far a direct method to identify/distinguish single and multilayers graphene, as shown in figure 3.10 [26-29].

3.5 Optical microscopy and scanning electron microscopy (SEM)

Optical or light microscopy involves visible light which is transmitted through or reflected from the sample to allow a clear view or image of the sample [31]. In optical microscopy, a higher contrast per graphene layer can be achieved from a reflection spectrum (by using a normal white light source) of graphene layers on oxide layer of a silicon substrate; however, oxide thickness must be optimized to reach maximum sensitivity (high contrast per graphene layer with different thicknesses) at a wavelength of interest [27,32]. The contrast C(λ) as a function of wavelength (λ), between a graphene sheet and SiO_2 substrate, is generated using the following expression [27]:

$$C(\lambda) = \frac{R_0(\lambda) - R_(\lambda)}{R_0(\lambda)} \tag{3.1}$$

where $R_0(\lambda)$ is the reflection intensity from the SiO_2/Si substrate and $R(\lambda)$ is the reflection intensity from graphene sheet.

Therefore, a clear contrast difference for graphene layers with varying thicknesses (1 to about 10 layers) can be observed on ≈300 nm SiO_2/Si substrate (see figure 3.11, graphene layers on 285 nm SiO_2/Si) [27,33]. Since the optical microscopy of graphene sheets displays the image colour contrast between monolayer and multilayer graphene films; it is used to distinguish between monolayer and multilayer graphene (over a large area of a film) indicating variation in the film thickness [13,27,33,34].

Scanning electron microscopy (SEM) is a technique which involves a beam of focused electrons under ultra-high vacuum conditions and is used to analyse materials on a micron to the nanometer scale. The analyses can yield information about topography, morphology, composition and crystallography of materials (using other analysers integrated into SEM system) [19]. When a focused beam of high-energy primary electrons impinges the surface of a sample, among others, it generates low energy secondary electrons. An image of the sample surface (about topography and morphology) is therefore constructed by measuring secondary electron intensity as a function of the position of the scanning primary electron beam [19]. Practically in the SEM at a given accelerating voltage and electron beam parameters, the desired image contrast can be achieved. Similar to the optical microscope, SEM of graphene sheets displays the image colour contrast

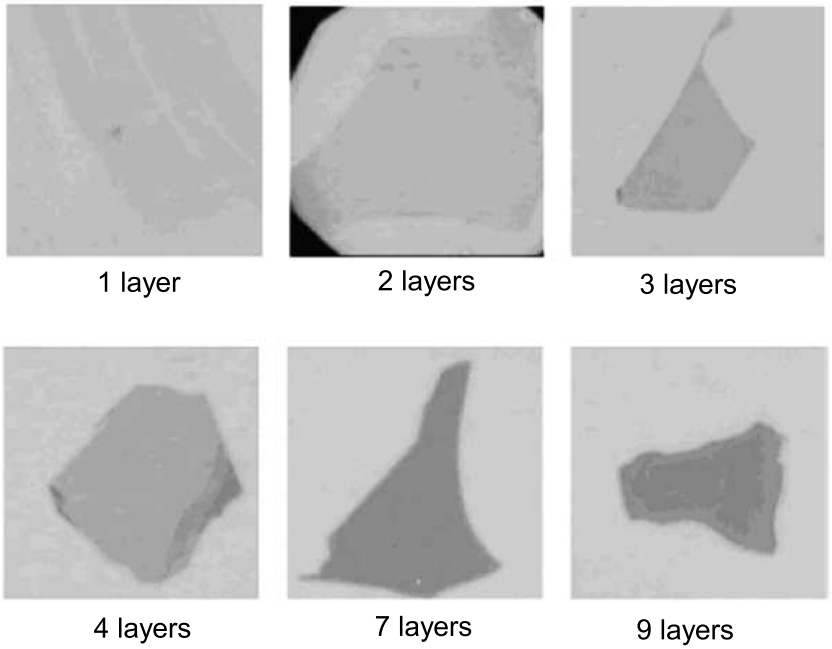

Figure 3.11: The optical images showing a clear contrast difference for graphene layers with different thicknesses on 285 nm SiO_2/Si substrates (Extracted from Ref. [27]).

between monolayer and multilayer graphene films (see figure 3.12) hence it is also used to distinguish between monolayer and multilayer graphene, however, it does not require an oxide layer with an optimized thickness as a graphene substrate as seen in optical microscopy.

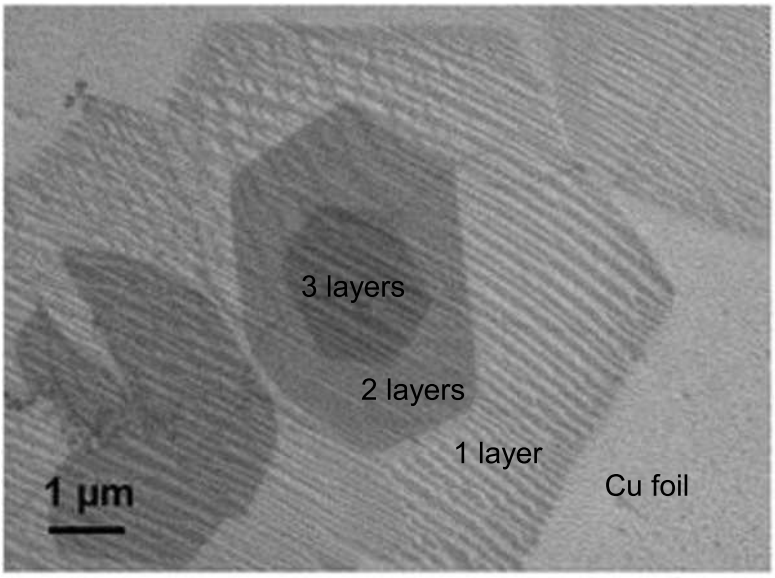

Figure 3.12: Scanning electron microscopy image showing a clear contrast difference for graphene layers with different thicknesses on a copper foil (Extracted from Ref. [35]).

3.6 X-ray photoelectron spectroscopy (XPS)

X-Ray photoelectron spectroscopy involves irradiation of the solid surface of a sample with a beam of X-rays (Al-Kα or Mg-Kα) while measuring the number and the kinetic energy of elastically scattered electrons (photoelectrons) that are emitted from the topmost surface atomic layers (1-10 nm) of the analysed sample [36]. High surface specificity of XPS is achieved by using smaller angles of incidence or exit of the electrons, however, the angle of exit of the electrons has a greater effect as the mean free path of electrons is smaller than that of the incident X-rays. In addition, In XPS analysis, the measured binding energies (from the kinetic energies) of the detected electrons usually range between 0 and 1000 eV. For this energy range, the inelastic mean free path of the electrons is in the order of a few nm which corresponds to the topmost surface atomic layers of the analysed sample [36]. The kinetic energy (KE) of the ejected electron depends upon the photon energy ($h\nu$) and the binding energy (BE) of the electron in the core-shell of an atom and is usually analysed with a hemispherical energy analyser (see figure 3.13).

In XPS spectrum, peaks appear from atoms emitting electrons of a particular characteristic energy. The energies and intensities of these electrons (photoelectron peaks) enable identification and

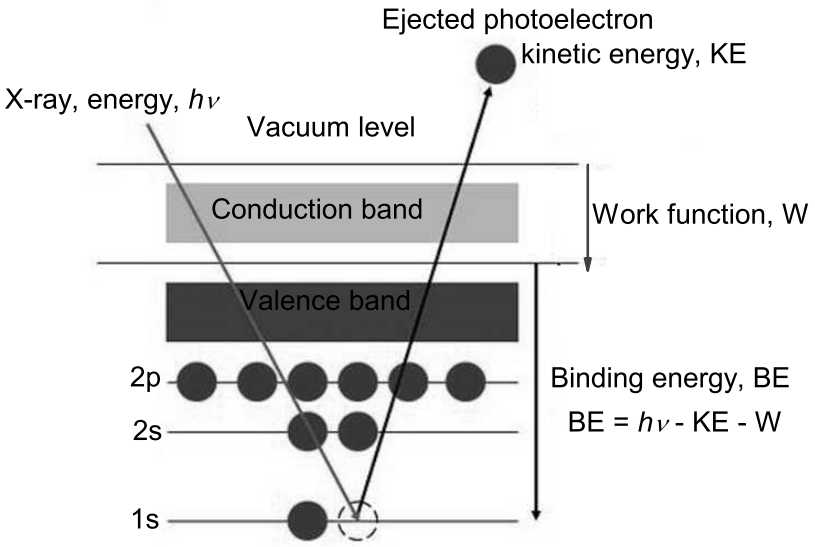

Figure 3.13: Schematic view of the photoemission process in XPS: Incident photon energy, $h\nu$ is absorbed by a core level electron, if $h\nu >$ BE then the electron is ejected from the atom with kinetic energy, KE. This is then detected by an analyser and the binding energy, BE of the ejected electron is determined by, BE = $h\nu$ − KE − W, where W is the work function of the electron analyser, not the analysed material (Extracted from Ref. [37,38]).

quantification of the surface chemistry of a material (elemental composition, chemical state and electronic state of the elements). Usually, XPS analysis is coupled with ion sputtering with noble gas ions (e.g. Ar^+) for surface cleaning and depth profiling and analysis are carried out under ultra-high vacuum conditions.

XPS analysis of the surface chemistry of carbon materials, graphene in this study, typically shows a carbon peak (C 1s) at a binding energy of about 284.5 eV (see figure 3.14). A spectral analysis/deconvolution of this peak gives information about the surface chemistry of the analysed carbon material. For instance, in figure 3.14, the C 1s core level spectra of as-grown graphene film was fitted with sp^2 C=C peak at 284.5 eV (graphene component), C−O−C peak at 286.2 eV, C=O peak at 287.4 eV, O−C=O peak at 289.4 eV (oxide components) and $\pi-\pi^*$ peak at 291.5 eV (satellite peak/electrons transition) and the position of these peaks is usually determined by reference to, XPS handbooks, Binding Energy-NIST (National Institute of Standards and Technology), XPS Database and other studies such as references [39-41] for graphene. Therefore,

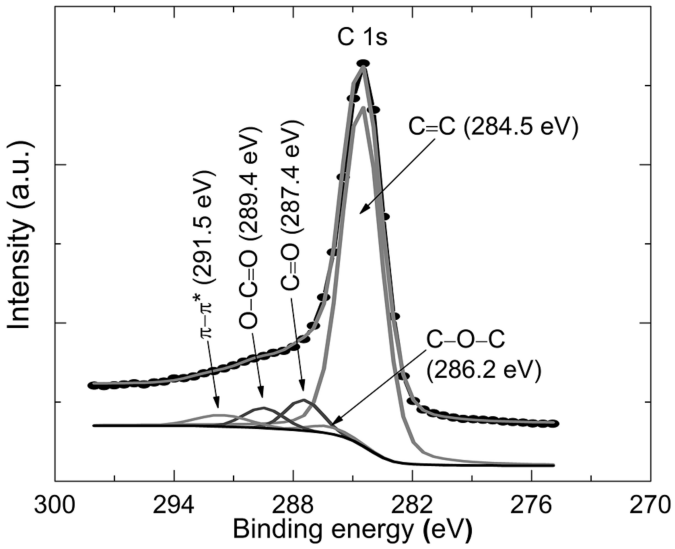

Figure 3.14: The high-resolution C 1s core level spectra of as-grown graphene film on a foil, fitted with sp^2 C=C peak at 284.5 eV (graphene component), C−O−C peak at 286.2 eV, C=O peak at 287.4 eV, O−C=O peak at 289.4 eV (oxide components) and $\pi-\pi^*$ peak at 291.5 eV (satellite peak/electrons transition) (See publication presented in chapter 7 Ref. [21]).

all fitted peaks give information about the sp^2 hybridization property of graphene, oxygen content present in graphene and the $\pi-\pi^*$ electrons transition which enhances the carbon to carbon bonds in graphene and confirms the high quality of graphene [2,40,41].

3.7 Four-point probe (graphene film sheet resistance)

The four-point probe is typically used to determine the bulk resistivity of the semiconductors. Resistivity is a very important parameter in semiconductors since it can be directly related to the impurity content of a semiconductor [42]. If the film thickness, t is known, the sheet resistance can be calculated by dividing bulk resistivity by the film thickness. As a result, a four-point probe can be used to obtain a sheet resistance of the thin film of a known thickness. In a four-point probe/sheet resistance measuring system, two electrodes are used for sourcing a DC current, *I*, (through the outer two probes) and the other two for measuring the corresponding voltage drop, *V* (see a schematic view in figure 3.15). From a measured voltage drop the sheet resistance can be

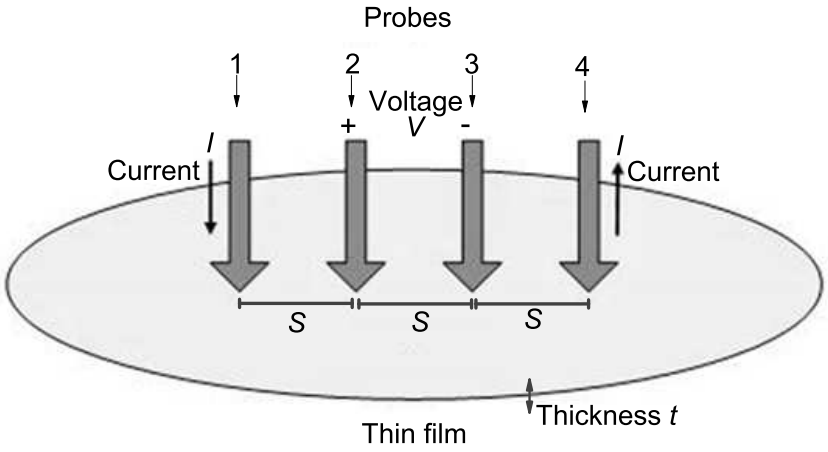

Figure 3.15: Schematic view of a four-point probe/sheet resistance measuring system, two outer probes source a DC current, I, and the other two measure the corresponding voltage drop, V. In thin films, thin film thickness, t is much smaller than an equal distance, S between probes ($t \ll S$).

calculated using an approach which relies on a geometric factor:

$$R_{sheet} = k\frac{V}{I} \tag{3.2}$$

where the factor k is a geometric factor.

Figure 3.16 shows the sheet resistance of monolayer and bilayer graphene films which was obtained using this approach.

Therefore, sheet resistance (R_{sheet}) is a measure of the electrical resistance of a sheet and is related to carrier density and mobility as follows [42,43]:

$$R_{sheet} = \frac{1}{q \times n \times \mu} \tag{3.3}$$

where q is the charge, n is the carrier density and μ is the mobility.

In equation 3.3, the carrier density (n) and the mobility (μ) are primarily ascribed to different band

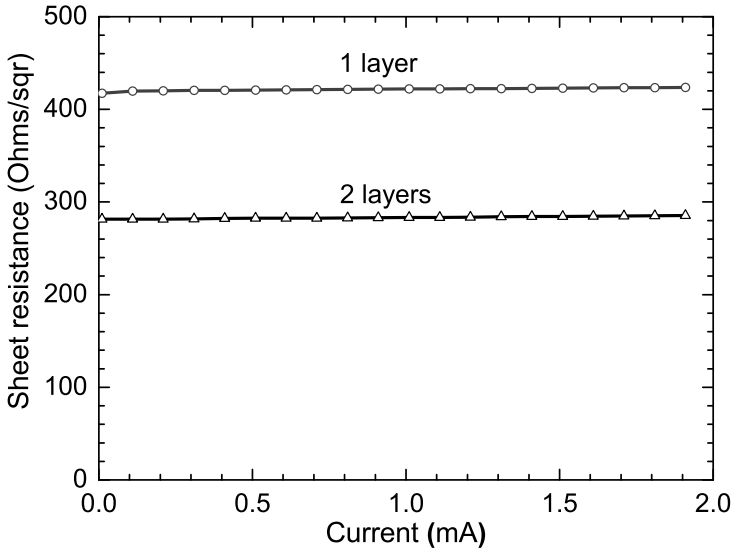

Figure 3.16: A four-point probe sheet resistance (measured at room temperature) of monolayer (1 layer) and bilayer graphene (2 layers) films transferred onto SiO_2/Si substrates (See supporting information for the publication presented in chapter 7 Ref. [21]).

structures and scattering mechanisms by impurities and defects present in thin films. In addition, the mobility of the carriers depends on temperature [2,44,45]. As a result, in monolayer and bilayer graphene films, at low temperatures (about 4 K), a monolayer graphene has high mobility, low carrier density and hence high sheet resistance, but a bilayer graphene has high mobility, high carrier density and therefore, a low sheet resistance (see figure 3.16) [44]. Therefore, the sheet resistance can be used to identify/distinguish single and multilayers graphene since sheet resistance increases with the decrease in graphene film thickness (number of layers of graphene). The sheet resistance shows a strong dependence of the electrical prosperities on graphene film thickness, primarily relate to the interlayer coupling [44,45].

Bibliography

1. A.C. Ferrari, D.M. Basko, Raman spectroscopy as a versatile tool for studying the properties of graphene, Nature Nanotechnology. 8 (2013) 235-46.

2. H. Aoki, M. S. Dresselhaus, eds., Physics of Graphene, Springer, New York, 2014.

3. C. Casiraghi, A. Hartschuh, E. Lidorikis, H. Qian, H. Harutyunyan, T. Gokus, et al., Rayleigh imaging of graphene and graphene layers, Nano Letters. 7 (2007) 2711-7.

4. A.C. Ferrari, J.C. Meyer, V. Scardaci, C. Casiraghi, M. Lazzeri, F. Mauri, et al., Raman Spectrum of Graphene and Graphene Layers, Physical Review Letters. 97 (2006) 187401.

5. L.M. Malard, M.A. Pimenta, G. Dresselhaus, M.S. Dresselhaus, Raman spectroscopy in graphene, Physics Reports. 473 (2009) 51-87.

6. J.M. Caridad, F. Rossella, V. Bellani, M.S. Grandi, E. Diez, Automated detection and characterization of graphene and few-layer graphite via Raman spectroscopy, Journal of Raman Spectroscopy. 42 (2011) 286-293.

7. J.M. Caridad, F. Rossella, V. Bellani, M. Maicas, M. Patrini, E. Diez, Effects of particle contamination and substrate interaction on the Raman response of unintentionally doped graphene, Journal of Applied Physics. 108 (2010) 084321.

8. M.J. Madito, A. Bello, J.K. Dangbegnon, C.J. Oliphant, W.A. Jordaan, T.M. Masikhwa, et al., Raman analysis of bilayer graphene film prepared on commercial Cu(0.5 at% Ni) foil, Journal of Raman Spectroscopy. (2015). doi:10.1002/jrs.4848.

9. J.-N. Fuchs, Dirac fermions in graphene and analogues: magnetic field and topological

properties, UPMC, Paris (main), 2013.

10. M. Lazzeri, C. Attaccalite, L. Wirtz, F. Mauri, Impact of the electron-electron correlation on phonon dispersion: Failure of LDA and GGA DFT functionals in graphene and graphite, Physical Review B. 78 (2008) 081406.

11. M.S. Dresselhaus, A. Jorio, R. Saito, Characterizing Graphene, Graphite, and Carbon Nanotubes by Raman Spectroscopy, Annual Review of Condensed Matter Physics. 1 (2010) 89-108.

12. A.C. Ferrari, J. Robertson, Interpretation of Raman spectra of disordered and amorphous carbon, Physical Review B. 61 (2000) 14095-14107.

13. M.J. Madito, A. Bello, J.K. Dangbegnon, C.J. Oliphant, W.A. Jordaan, D.Y. Momodu, et al., A dilute Cu(Ni) alloy for synthesis of large-area Bernal stacked bilayer graphene using atmospheric pressure chemical vapour deposition, Journal of Applied Physics. 119 (2016) 015306.

14. M. Freitag, Graphene: Trilayers unravelled, Nature Physics. 7 (2011) 596-597.

15. Y. Zhang, T. Tang, C. Girit, Z. Hao, M.C. Martin, A. Zettl, et al., Direct observation of a widely tunable bandgap in bilayer graphene, Nature. 459 (2009) 820-3.

16. W. Fang, A.L. Hsu, R. Caudillo, Y. Song, A.G. Birdwell, E. Zakar, et al., Rapid identification of stacking orientation in isotopically labeled chemical-vapor grown bilayer graphene by Raman spectroscopy, Nano Letters. 13 (2013) 1541-1548.

17. S. Chen, W. Cai, R.D. Piner, J.W. Suk, Y. Wu, Y. Ren, et al., Synthesis and characterization of large-area graphene and graphite films on commercial Cu-Ni alloy foils, Nano Letters. 11 (2011) 3519-3525.

18. W. Liu, S. Kraemer, D. Sarkar, H. Li, P.M. Ajayan, K. Banerjee, Controllable and rapid synthesis of high-quality and large-area bernal stacked bilayer graphene using chemical vapor deposition, Chemistry of Materials. 26 (2014) 907-915.

19. R.F. Egerton, Physical Principles of Electron Microscopy: An Introduction to TEM, SEM,

and AEM, Springer Science & Business Media, 2006.

20. A.W. Robertson, J.H. Warner, Atomic resolution imaging of graphene by transmission electron microscopy, Nanoscale. 5 (2013) 4079-93.

21. M.J. Madito, N. Manyala, A. Bello, J.K. Dangbegnon, T.M. Masikhwa, D.Y. Momodu, A wafer-scale Bernal-stacked bilayer graphene film obtained on a dilute Cu (0.61 at% Ni) foil using atmospheric pressure chemical vapour deposition, RSC Adv. 6 (2016) 28370-28378.

22. A. Dato, V. Radmilovic, Z. Lee, J. Phillips, M. Frenklach, Substrate-Free Gas-Phase Synthesis of Graphene Sheets, Nano Letters. 8 (2008) 2012-2016.

23. J.C. Meyer, A.K. Geim, M.I. Katsnelson, K.S. Novoselov, T.J. Booth, S. Roth, The structure of suspended graphene sheets, Nature. 446 (2007) 60-3.

24. Y. Wu, H. Chou, H. Ji, Q. Wu, S. Chen, W. Jiang, et al., Growth Mechanism and Controlled Synthesis of AB-Stacked Bilayer Graphene on Cu-Ni Alloy Foils, ACS Nano. (2012) 7731-7738.

25. Atomic Force Microscopy - What is it?, http://www.keysight.com/main/editorial.jspx?ckey=1774141&lc=eng&cc=ZA (accessed March 27, 2016).

26. A. Gupta, G. Chen, P. Joshi, S. Tadigadapa, P.C. Eklund, Raman scattering from high-frequency phonons in supported n-graphene layer films, Nano Letters. 6 (2006) 2667-73.

27. Z.H. Ni, H.M. Wang, J. Kasim, H.M. Fan, T. Yu, Y.H. Wu, et al., Graphene thickness determination using reflection and contrast spectroscopy, Nano Letters. 7 (2007) 2758-2763.

28. S. Ye, H. Huang, C. Yuan, F. Liu, M. Zhai, X. Shi, et al., Thickness-Dependent Strain Effect on the Deformation of the Graphene-Encapsulated Au Nanoparticles, Journal of Nanomaterials. 2014 (2014) 1-6.

29. P. Nemes-Incze, Z. Osvá Th, K. Kamará S, L.P. Biró, Anomalies in thickness measurements of graphene and few layer graphite crystals by tapping mode atomic force microscopy,

(2008).

30. M. Fabiane, Chemical vapour deposition of graphene: Fundamental aspects of synthesis and characterization, PhD thesis, University of Pretoria, 2014.

31. Molecular Expressions Microscopy Primer: Anatomy of the Microscope - Introduction, http://micro.magnet.fsu.edu/primer/anatomy/introduction.html (accessed March 25, 2016).

32. X. Wang, M. Zhao, D.D. Nolte, Optical contrast and clarity of graphene on an arbitrary substrate, Applied Physics Letters. 95 (2009) 2009-2011.

33. P. Blake, E.W. Hill, A.H. Castro Neto, K.S. Novoselov, D. Jiang, R. Yang, et al., Making graphene visible, Applied Physics Letters. 91 (2007) 2007-2009.

34. H. Zhou, W.J. Yu, L. Liu, R. Cheng, Y. Chen, X. Huang, et al., Chemical vapour deposition growth of large single crystals of monolayer and bilayer graphene, Nature Communications. 4 (2013) 2096.

35. X. Tang, N. Reckinger, O. Poncelet, P. Louette, F. Ureña, H. Idrissi, et al., Damage evaluation in graphene underlying atomic layer deposition dielectrics, Scientific Reports. 5 (2015) 13523.

36. M.P. Seah, Quantification of AES and XPS, in: D. Briggs, M.P. Seah (Eds.), Practical Surface Analysis by Auger and X-Ray Photo- Electron Spectroscopy, 2nd ed., John Wiley & Sons Ltd., Chichester, 1990.

37. X-Ray Photoelectron Spectroscopy (XPS), https://www.ifw-dresden.de/de/institute/institut-fuer-komplexe-materialien/abteilungen/mikro-und-nanostrukturen/available-methods/xps/ (accessed March 27, 2016).

38. A.B. Christie, X-ray photoelectron spectroscopy, in: J.M. Walls (Ed.), Methods of Surface Analysis, Cambridge University Press, Cambridge, 1989.

39. Y. V. Butenko, S. Krishnamurthy, A.K. Chakraborty, V.L. Kuznetsov, V.R. Dhanak, M.R.C. Hunt, et al., Photoemission study of onionlike carbons produced by annealing nanodiamonds, Physical Review B. 71 (2005) 075420.

40. M. Hsiao, S. Liao, M. Yen, C. Teng, S. Lee, N. Pu, et al., Preparation and properties of a graphene reinforced nanocomposite conducting plate, Journal of Materials Chemistry. 20 (2010) 8496.

41. S. Ogawa, T. Yamada, S. Ishidzuka, A. Yoshigoe, M. Hasegawa, Y. Teraoka, et al., Graphene Growth and Carbon Diffusion Process during Vacuum Heating on Cu (111)/ Al_2O_3 Substrates, Japanese Journal of Applied Physics. 52 (2013) 110122.

42. B.G. Streetman, S. Banerjee, Solid State Electronic Devices, 5th ed., Prentice Hall, New Jersey, 2000.

43. Y. Liu, W. Li, M. Qi, X. Li, Y. Zhou, Z. Ren, Study on temperature-dependent carrier transport for bilayer graphene, Physica E: Low-Dimensional Systems and Nanostructures. 69 (2015) 115-120.

44. W. Zhu, V. Perebeinos, M. Freitag, P. Avouris, Carrier scattering, mobilities, and electrostatic potential in monolayer, bilayer, and trilayer graphene, Physical Review B. 80 (2009) 235402.

45. C. Cobaleda, E. Diez, M. Amado, S. Pezzini, F. Rossella, V. Bellani, et al., Quantum Hall effect in monolayer, bilayer and trilayer graphene, Journal of Physics: Conference Series. 456 (2013) 012006.

PART III

EXPERIMENTAL DETAILS

CHAPTER 4

Experimental details

4.1 Introduction

This chapter describes the experimental procedures and equipment used for the production and characterizations of graphene films. The graphene films are prepared with the aim of obtaining a wafer-scale ($\approx 20 \times 20$ mm^2) AB-stacked bilayer graphene film using AP-CVD. The first part of this chapter focuses on growing large-area high-quality AB-stacked bilayer graphene on commercial Cu(0.5 at% Ni) foil, followed by Raman analysis of the obtained bilayer graphene film. This includes a description of the equipment used for Cu(0.5 at% Ni) foil (substrate) analysis.

A considerable part of this chapter focuses on the doping of a 25 μm thick annealed Cu foil (Alfa Aesar) with 0.5 at% Ni for the synthesis of large-area Bernal-stacked bilayer graphene using AP-CVD. A Ni doping of this particular Cu foil is motivated by a continuous single surface orientation (001) of a foil. This part of the chapter also describes equipment used for substrate analysis. The last part of this chapter describes the approach used to achieve a wafer-scale AB-stacked bilayer graphene.

Parts of this chapter are published in the following journals:

(i) Raman analysis of bilayer graphene film prepared on commercial Cu(0.5 at% Ni) foil
M.J. Madito *et al.*, Journal of Raman Spectroscopy, 47, 553-559 (2016).

(ii) A dilute Cu(Ni) alloy for synthesis of large-area Bernal stacked bilayer graphene using atmospheric pressure chemical vapour deposition
M.J. Madito *et al.*, AIP: Journal of Applied Physics, 119, 015306 (2016).

(iii) A wafer-scale Bernal-stacked bilayer graphene film obtained on a dilute Cu(0.61 at% Ni) foil using atmospheric pressure chemical vapour deposition
M.J. Madito *et al.*, RSC Advances, 6, 28370-28378 (2016).

4.2 Experimental procedure

4.2.1 Raman analysis of bilayer graphene film

Graphene growth

High purity (99.9 %) dilute Cu(0.5 at% Ni) foil samples (20×20 mm^2 and 0.5 mm thick) were ordered from MaTeck (package list No. 14040413-860).

Samples were electro-polished and cleaned for graphene growth as follows [1]:

(i) In the electrochemical cell, the Cu(0.5 at% Ni) foil sample (to be polished) was connected to the anode and a Cu plate (30 mm in diameter and 2 mm thick) to the cathode of the cell and the electro-polishing solution contained 1000 mL of water, 500 mL of ortho-phosphoric acid, 500 mL of ethanol, 100 mL of isopropyl alcohol, and 10 g of urea.

(ii) A DC power supply was used to supply constant voltage/current in the electrochemical cell and a voltage in the range of 3.0-6.0 V was applied for about 3 min.

(iii) After electropolishing, the Cu(0.5 at% Ni) foils were rinsed with deionized water and immersed in aqueous nitric acid for 30 s to dissolve off the electro-polishing solution residues on the foil surface, washed with deionized water again followed by ultra-sonic bath with acetone and isopropanol and dry-blowing with N_2 to remove water residues.

After cleaning, the Cu(0.5 at% Ni) foils were loaded into the centre of AP-CVD quartz tube setup (Figure 4.1(a)) for monolayer and bilayer graphene growth. Figure 4.1(b), shows a temperature profile of AP-CVD measured directly inside quartz tube centre (located at the furnace centre) with

an external chromel-alumel thermocouple (Type K) and the measured temperature was recorded as sample temperature for graphene growth. Samples loaded in AP-CVD were annealed under Ar (300 sccm) and H_2 (9 sccm) flow for 30 min at 1050 °C before the growth of graphene. After annealing, a monolayer graphene was synthesized from a mixture of gases, Ar (300 sccm): H_2 (9 sccm): CH_4 (15 sccm) and a bilayer graphene from a mixture of Ar (300 sccm): H_2 (9 sccm): CH_4 (10 sccm) at 980 °C for exactly 9 min. Immediately after growth, the CH_4 flow was stopped and the quartz tube was pushed to the cooler region of the furnace and samples rapidly cooled down to room temperature and offloaded from AP-CVD quartz tube.

Graphene transfer onto SiO_2 substrate

The graphene films were transferred onto 300 nm thick SiO_2/Si substrates as follows:

(i) A thin layer of polymethyl methacrylate (PMMA) (average Mw 996 000 by GPC) dissolved in chlorobenzene at a concentration of 46 mg/mL was spin-coated on the as-grown graphene films on Cu(0.5 at% Ni) foils at 3000 rpm for 30 s [2].

(ii) PMMA deposited on graphene films/Cu(0.5 at% Ni) foils was cured at 115 °C for 5 min [3].

(iii) PMMA/graphene/ Cu(0.5 at% Ni) foil samples were placed in 1 M iron nitrate ($Fe(NO_3)_3$) to etch off Cu and transferred using a polyethylene terephthalate (PET) to the 5% hydrochloride (HCl) and deionized water to dissolve the ($Fe(NO_3)_3$), and then onto SiO_2 substrates [4].

(iv) Finally, PMMA was removed from a PMMA/Graphene/SiO_2 samples using acetone [3].

Graphene characterization

Graphene/SiO_2/Si samples (graphene films) were characterized with the following techniques:

(i) Raman spectroscopy (WITec Alpha 300 micro-Raman imaging system with 532 nm excitation laser), Raman spectra were measured at room temperature with the laser power set below 2 mW in order to minimize heating effects.

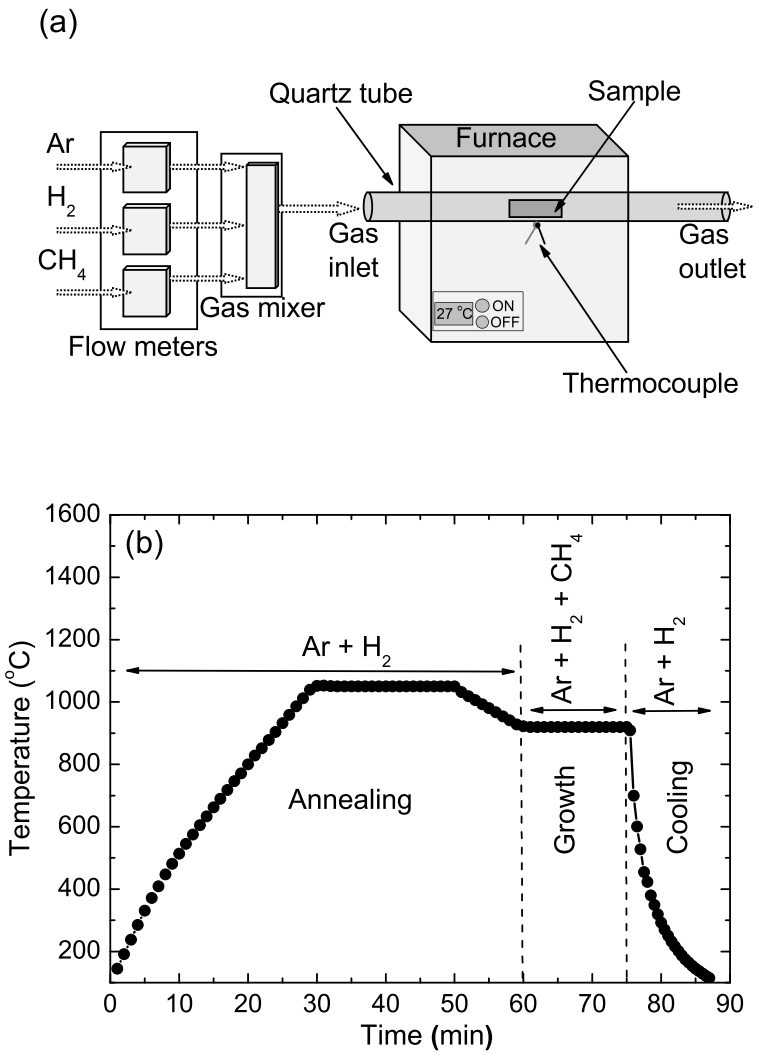

Figure 4.1: (a) A schematic view of AP-CVD setup showing a connection from Ar, H_2 and CH_4 gas cylinders through gas flow meters and gas mixer into a quartz tube. (b) A temperature profile of AP-CVD measured directly inside quartz tube centre (located at the furnace centre) with an external chromel-alumel thermocouple (Type K) and the measured temperature was recorded as sample temperature for graphene growth.

(ii) Four point probe station, the graphene films sheet resistance measurements were carried out under ambient conditions (i.e. room temperature and pressure) using a Signatone four point probe station.

Substrate characterization

A Cu(0.5 at% Ni) foil was analyzed with the following techniques:

(i) Electron backscatter diffraction (EBSD) performed in an LEO 1525 field-emission gun scanning electron microscope at an acceleration voltage of 25 kV using the Oxford INCA crystal software.

(ii) X-ray diffraction (XRD) patterns were collected using an XPERT-PRO diffractometer (PANalytical BV, Netherlands) with reflection geometry at 2θ values ranging from 30-70° with a step size of 0.01°. Co $K1\alpha$ radiation with a wavelength of 0.17890 nm was used as the X-ray source and a tube was operated at 50 kV and 30 mA.

(iii) Proton-induced X-ray emission (PIXE), a beam energy of 3.0 MeV and target current of 200 pA was used for analysis. The tandem accelerator of iThemba LABS in Gauteng was used to irradiate samples with 3.0 MeV protons.

(iv) Time-of-flight secondary ion mass spectroscopy (TOF-SIMS) performed using the TOF-SIMS5 Ion-TOF system. The mass spectra were calibrated to the following mass peaks in positive mode: Al, Na, Ni, Fe, Si, C, C_2H_5 K and Cu. The analysis was carried out over an area of 500×500 μm^2 and ion sputter gun area of 1000×1000 μm^2.

Electron backscatter diffraction is an SEM-based method (integrated into SEM system) and unlike SEM which provides information about sample surface topography and morphology, EBSD provides information about sample surface microstructural crystallography. EBSD involves interaction between an electron beam and a tilted crystalline sample surface, and the diffracted electrons create a pattern (i.e. diffraction pattern) on a detector fluorescent screen with Kikuchi bands (analyzed by the software to derive the crystal orientation) which are characteristic of the sample crystal structure and orientation [5].

X-ray powder diffraction is an analytical technique primarily used for bulk phase identification (crystal structures and atomic spacing/d-spacing) of crystalline samples. In XRD, X-rays generated by a cathode ray tube are filtered (to produce monochromatic radiation), collimated and directed towards the sample and the interaction of the incident X-rays with the sample produces diffracted ray (constructive interference) when Bragg's Law ($n\lambda = 2dsin\theta$), conditions

are satisfied, where n is a positive integer, λ is the wavelength of incident X-rays, d is the interplanar spacing and θ is the scattering angle. XRD pattern (characteristic of the crystal structure (set of d-spacings) which is unique for each material) is obtained by measuring the intensity of scattered X-rays as a function of scattering angle.

Particle induced X-ray emission is a powerful non-destructive elemental analysis technique and has high sensitivity (in the order of few ppm). In PIXE, a beam of protons(MeV) defined by a series of collimators, passes through an irradiator chamber onto the sample to be analyzed and dumped into a Faraday cup connected to a beam integrator. Irradiated sample, emit X-rays which are detected by a silicon detector and the pulses generated by the detector are analyzed in a multi-channel analyzer to generate a spectrum. A typical spectrum consists of a number of peaks corresponding to the K_α and K_β X-rays of the elements present in the sample. The number of counts in a peak is a measure of the amount of the corresponding element in the sample [6].

Time-of-Flight Secondary Ion Mass Spectrometry is a surface-sensitive analytical method that uses a pulsed finely focused ion beam which causes secondary ions and ion clusters to be emitted from the very topmost surface layer of the sample. These ions are then accelerated into a flight tube and their exact mass is determined by measuring the exact time at which they reach the detector (i.e. time-of-flight) and from the exact mass and intensity of the SIMS peak, the element or molecular fragments can be determined. Three operational modes are available using ToF-SIMS: surface spectroscopy, surface imaging and depth profiling [7]. Under typical operating conditions, ToF-SIMS analysis include: (a) a mass spectrum that surveys all atomic masses over a range of 0-10 000 amu, (b) the rastered electron beam that produces maps of any mass of interest on a sub-micron scale, and (c) depth profiles are produced by sequential sputtering of surface layers by ion beam [7].

4.2.2 A dilute Cu(Ni) alloy for synthesis of AB-stacked bilayer graphene

Thermal deposition and annealing (a dilute Cu(Ni) alloy preparation)

Few Cu foil samples (30×30 mm^2) (to be prepared the same way) were obtained from a high purity (99.8 %) 25 μm thick annealed Cu foil from Alfa Aesar (shown in figure 4.2). Samples were immersed in aqueous nitric acid for 30 s to dissolve surface impurities on foils, then in distilled water followed by a ultra-sonic bath with acetone and isopropanol and dry-blowing with

Figure 4.2: A Photograph of a high purity (99.8 %) 25 μm thick annealed Cu foil obtained from Alfa Aesar for graphene growth.

N_2 to remove water residues [8].

The cleaned Cu foils were loaded into a vacuum chamber of a thermal evaporator for Ni deposition. The thickness of the Ni layer (i.e. $d_{\mathrm{Ni}} = 116$ nm) required for doping 25 μm thick Cu foil with 0.5 at% Ni was obtained using the expressions:

$$d_{\mathrm{Ni}} = \frac{m_{\mathrm{Ni}}\rho_{\mathrm{Cu}}}{m_{\mathrm{Cu}}\rho_{\mathrm{Ni}}} d_{\mathrm{Cu}} \tag{4.1}$$

and

$$m_{\mathrm{Ni}} = \frac{M_{\mathrm{Ni}}X_{\mathrm{Ni}}}{M_{\mathrm{Cu}}(1-X_{\mathrm{Ni}})} m_{\mathrm{Ni}} \tag{4.2}$$

where d_{Cu} is the Cu foil thickness, ρ_{Cu} is the Cu density, ρ_{Ni} is the Ni density, m_{Cu} is the mass of the Cu foil, m_{Ni} is the mass of the Ni layer to be deposited, X_{Ni} is the Ni concentration (in at%) to be added into Cu foil, M_{Ni} and M_{Cu} is the molar mass of the Ni and Cu respectively.

Therefore, a thin layer of high purity (99.99 %) Ni (116 nm) was thermally evaporated onto Cu foil sample at a rate of 0.1 nm/s in a vacuum chamber with a pressure of 3×10^{-3} Pa. The deposition of a thin layer of Ni was repeated on extra three Cu foil samples. After evaporation, Cu/Ni samples were loaded in AP-CVD quartz tube (see figure 4.1(a)) under argon atmosphere. Samples were annealed at 950 °C for 8 h with argon flow rate of 500 sccm to obtain Cu(Ni) alloy foils. For the foils annealed at 950 °C and 8 h conditions, the concentration distribution (C) of Ni in Cu foil with

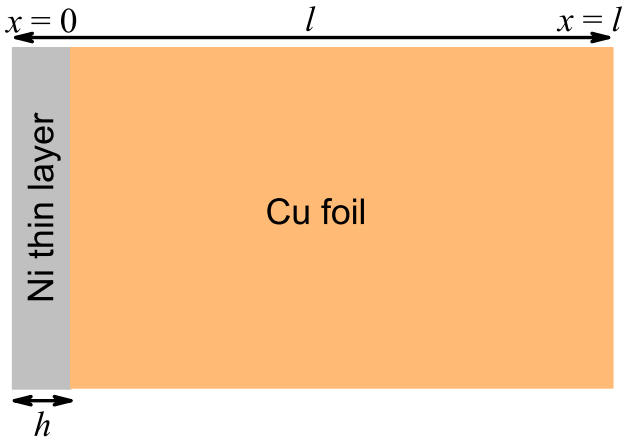

Figure 4.3: Graphical representation of the sample configuration showing the boundary conditions for equation 4.3. Mathematically: $0 \leq x \leq l$; $C(x) = 0$ for $x > h$ and $t = 0$; $C(x) = C_0$ for $0 \leq x \leq h$ and $t = 0$; $\partial C/\partial x = 0$ at $x = l$ for $t \geq 0$ [9].

a sample thickness l and the surface located at $x = 0$, where the Ni source layer with a thickness h is restricted (demonstrated with schematic diagram in figure 4.3), was calculated in terms of diffusion depth x using Fick's solution for finite systems (see figure 4.4) [9]:

$$C = \frac{1}{2} C_0 \sum_{n=-\infty}^{\infty} \left[\text{erf}\left(\frac{h + 2nl - x}{2\sqrt{Dt}} \right) + \text{erf}\left(\frac{h - 2nl + x}{2\sqrt{Dt}} \right) \right] \tag{4.3}$$

where C_0 is the initial concentration of Ni on the Cu surface, $D = D_0 \exp(-Q/RT)$ is the diffusion coefficient (D_0 is the pre-exponential factor, Q is the activation energy ($D_0 = 7.0 \times 10^{-5}$ m^2/s and $Q = 225.0$ kJ/mol for Ni diffusion in Cu [10]), R is the gas constant and T is the temperature).

Figure 4.4 (calculation for a Cu foil sample 1 in table 4.1) suggests that the annealing process yielded Ni concentration distribution in 25 μm thick Cu foil that is 99.8 % uniform. Before and after deposition of the Ni films onto the Cu foils, the masses of the samples were measured with Denver instrument balance (model SI-234) with repeatability or standard deviation of $<\pm 0.1$ mg. After annealing, the masses of the samples were measured again and found to have increased compared to the masses of the samples before Ni deposition, and from Ni masses, the concentrations were found as listed in Table 4.1. An inductively coupled plasma optical emission

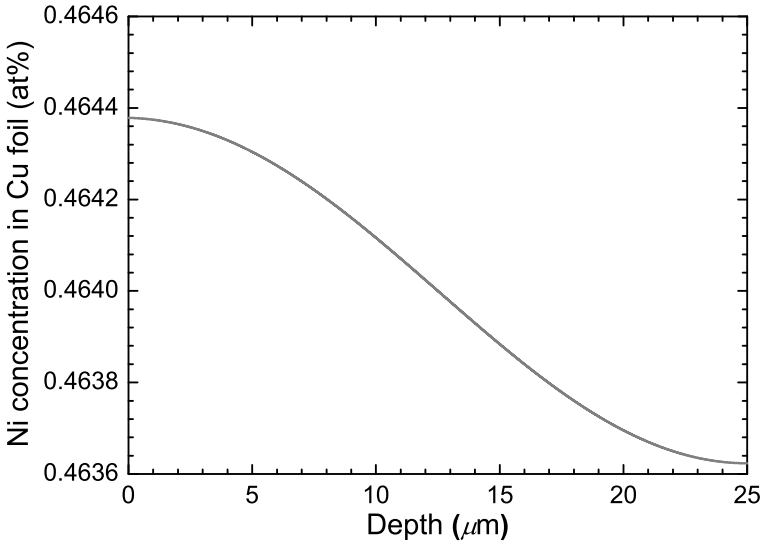

Figure 4.4: Ni concentration distribution as a function of diffusion depth in 25 μm thick Cu foil (Calculated in this chapter using equation 4.3).

spectrometry (ICP-OES) spectrometer was used to confirm the Ni concentrations listed in table 4.1. For instance, a piece of a Cu foil with a mass of 47.1 mg was cut from a Cu foil sample 1 and analysed with an ICP-OES spectrometry and was found to have a Ni amount with a mass of 0.199 mg (equivalent to 0.457 at%). Ni doped (i.e. Cu(0.46 at% Ni) foil, sample 1 in Table 4.1) and un-doped Cu foils were loaded in AP-CVD at a centre of a quartz tube for bilayer graphene growth.

Cu foils samples	Samples masses pre-deposition ($\pm$0.1 mg)	Samples masses after deposition ($\pm$0.1 mg)	Samples masses after annealing ($\pm$0.1 mg)	Ni amount in Cu foils ($\pm$0.1 mg)	Ni amount in Cu foils (at%)
1	285.4	286.9	286.6	1.2	0.455
2	268.1	269.3	269.6	1.5	0.606
3	262.0	263.3	263.4	1.4	0.579
4	251.0	252.2	252.5	1.5	0.647

Table 4.1: The masses of the samples (pre-deposition and after deposition of Ni layer and after annealing of Ni/Cu foils samples) and Ni added in Cu foils and the corresponding Ni concentrations.

Bilayer graphene growth on Cu and Cu(0.46 at% Ni) foils, graphene transfer onto SiO_2 and characterization

Bilayer graphene growth on Cu and Cu(0.46 at% Ni) (sample 1 in table 4.1) foils was prepared as discussed above, but here it was synthesised at a growth temperature of 920 °C and 1000 °C on both foils (simultaneously) for exactly 15 min. Graphene transfer onto 300 nm SiO_2/Si substrates was carried out exactly the same way as discussed above. Both foils and graphene films were characterised and the characterization techniques used are as discussed above (i.e. PIXE, EBSD, XRD, TOF-SIMS, Raman, Signatone four point probe station) and this further includes the HRTEM (Jeol JEM-2100F Field Emission Electron Microscope, with a maximum analytical resolution of 200 kV and a probe size of 0.5 nm) for obtaining the electron diffraction pattern of the prepared graphene film.

4.2.3 A wafer-scale AB-stacked bilayer graphene film

Graphene growth on Cu and Cu(0.61 at% Ni) foils, graphene transfer onto SiO_2 and characterization

Bilayer graphene growth on Cu and Cu(0.61 at% Ni) (sample 2 in table 4.1) foils was prepared as discussed above, but here it was synthesised at a growth temperature of 980 °C and for 5 min. Graphene transfer onto 300 nm SiO_2/Si substrates was carried out exactly the same way as discussed above. Figure 4.5 shows photographic images of the Cu (0.61 at% Ni) foil ($\approx 20 \times 20$ mm^2) used in AP-CVD growth of a wafer-scale bilayer graphene and transferred bilayer graphene film on 300 nm SiO_2/Si substrate with a continuous film. A monolayer graphene film on Cu foil was obtained from a mixture of Ar (300 sccm), H_2 (9 sccm) and CH_4 (15 sccm) for 2 min at a growth temperature of 1000 °C.

Samples characterization

Characterization techniques are as discussed above (i.e. TOF-SIMS, Raman, Signatone four point probe station and HRTEM). In addition, the following techniques were used.

(i) The step height analysis of graphene thickness was obtained using a Dimension Icon AFM

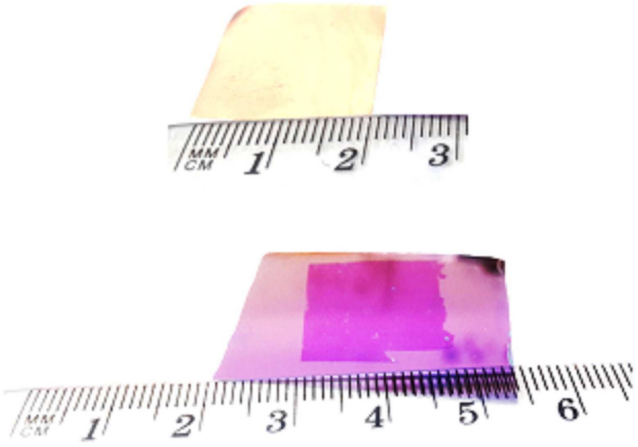

Figure 4.5: A continuous wafer-scale bilayer graphene film obtained using AP-CVD. The top-image shows a photograph of Cu(0.61 at% Ni) foil with as-grown bilayer graphene film and the bottom-image shows that of a transferred bilayer graphene film on 300 nm SiO_2/Si substrate.

(Bruker) with nanoscope analysis software in ScanAsyst contact mode.

(ii) SEM micrographs of the prepared graphene films were observed with Zeiss Ultra Plus 55 field emission scanning electron microscope (FE-SEM) operated at an accelerating voltage of 1.0 kV.

(iii) The Ni surface concentration in dilute Cu(0.61 at% Ni) foil was quantified with X-ray photoelectron spectroscopy (XPS). A Physical Electronics VersaProbe 5000 instrument was used employing a 100 μm (beam diameter) monochromatic Al-Kα to irradiate the Cu(0.61 at% Ni) foil surface. Photoelectrons were collected by 180° hemispherical electron energy analyzer. The Cu(0.61 at% Ni) foil was analyzed at a 45° angle between the foil surface and the path to the analyzer. Survey spectra were obtained at the pass energy of 117.5 eV, with a step size of 0.1 eV. The XPS spectra of elements, C 1s, Cu 2p, Ni 2p, and O 1s were measured to obtain the chemical composition of the foil surface. The spectra were obtained at the pass energy of 23.5 eV, with a step size of 0.05 eV. The spectra were obtained before and after the foil was sputtered at a rate of 0.3 nm/min with an Ar beam operating at 500 V and 150 μA for several cycles while measuring the spectra after each sputter duration. All binding energies were referenced to that of the binding energy of the Fermi level ($E_F = 0$ eV).

Bibliography

1. B. Zhang, W.H. Lee, R. Piner, I. Kholmanov, Y. Wu, H. Li, et al., Low-temperature chemical vapor deposition growth of graphene from toluene on electropolished copper foils, ACS Nano. 6 (2012) 2471-6.

2. M. Fabiane, S. Khamlich, A. Bello, J. Dangbegnon, D. Momodu, A.T. Charlie Johnson, et al., Growth of graphene underlayers by chemical vapor deposition, AIP Advances. 3 (2013) 112126.

3. M. Her, R. Beams, L. Novotny, Graphene Transfer with Reduced Residue, Physics Letters A. 377 (2013) 1-3.

4. W. Liu, S. Kraemer, D. Sarkar, H. Li, P.M. Ajayan, K. Banerjee, Controllable and rapid synthesis of high-quality and large-area bernal stacked bilayer graphene using chemical vapor deposition, Chemistry of Materials. 26 (2014) 907-915.

5. EBSD Oxford Instruments - Introduction, http://www.ebsd.com/introduction (accessed March 30, 2016).

6. S. A. E. Johansson, T.B. Johansson, Analytical application of particle induced X-ray emission, Nuclear Instruments and Methods. 137 (1976) 473-516.

7. A.M. Belu, D.J. Graham, D.G. Castner, Time-of-flight secondary ion mass spectrometry: techniques and applications for the characterization of biomaterial surfaces, Biomaterials. 24 (2003) 3635-3653.

8. S.M. Kim, A. Hsu, Y.-H. Lee, M. Dresselhaus, T. Palacios, K.K. Kim, et al., The effect of copper pre-cleaning on graphene synthesis, Nanotechnology. 24 (2013) 365602.

9. J. Crank, The Mathematics of Diffusion, 2nd ed., Clarendon Press, 1975.

10. W.F. Gale, T.C. Totemeier, eds., Smithells Metals Reference Book, 8th ed., Butterworth-Heinemann, Oxford UK, 2004.

PART IV

RESULTS, DISCUSSION AND CONCLUSION

CHAPTER 5

Raman analysis of bilayer graphene film

5.1 Introduction

In this chapter, the results obtained from the characterization of monolayer and bilayer graphene films prepared on commercial dilute Cu(0.5 at% Ni) foils using AP-CVD are discussed. This includes the results obtained from the characterization of the commercial dilute Cu(0.5 at% Ni) foil substrate. The publication (including the supporting information) which details the experimental procedure and results discussed in this chapter is presented at the end of the chapter.

It was mentioned in chapter 1 that Liu *et al*.[1] showed that Cu/Ni thin films having a surface layer composition of about 97 at% Cu and 3 at% Ni could grow a high-quality large-area AB-stacked bilayer graphene in CVD. Contrary to the study of Liu, this study, proposed a dilute Cu(0.5 at% Ni) foil which demonstrates similar surface layer composition at 980 °C (see chapter 1 and 2) [2,3].

In this chapter, high-quality large-area (or wafer-scale) monolayer and bilayer graphene films were synthesized on commercial dilute Cu(0.5 at% Ni) foils at 1000 °C and 980 °C respectively, using AP-CVD. Before graphene growth, Cu(0.5 at% Ni) foils were annealed at 1050 °C for 30 min under Ar and H_2 mixture to obtain large Cu grains. At 1050 °C, a Ni surface concentration in dilute Cu(0.5 at% Ni) foil would be 1.8 at% (see chapter 2). However, after a slow cooling to 980 °C for bilayer graphene growth, Ni surface concentration in a foil will be 2.1 at%. After growth, the graphene films were transferred onto 300 nm thick SiO_2/Si substrates using PMMA. Both prepared graphene films and commercial dilute Cu(0.5 at% Ni) foil were characterized.

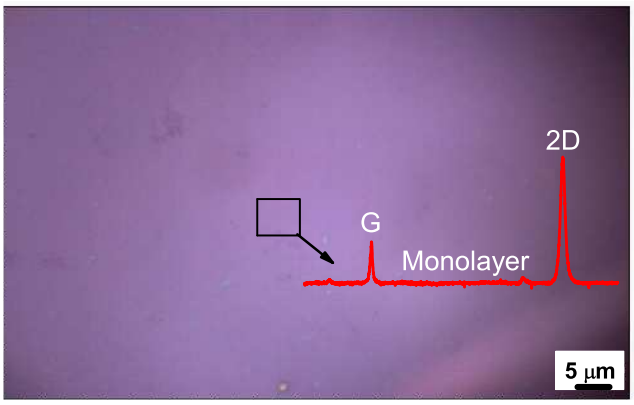

Figure 5.1: The optical microscope image obtained from monolayer graphene film transferred onto 300 nm thick SiO_2/Si substrate (The inset: Raman spectrum corresponding to area indicated as box).

5.2 Results and discussions

Figure 5.1 shows the optical microscope image obtained from a prepared monolayer graphene film which shows a wafer-scale monolayer graphene confirmed by Raman spectrum (the inset). Figure 5.2(a) and (b) show the optical microscope images obtained from different spots of the same sample of bilayer graphene film. Figure 5.2 shows large-area bilayer graphene (darker areas) with areas of monolayer graphene (lighter areas) and suggests commercial dilute Cu(0.5 at% Ni) foil surface reached ≈80 % coverage of the bilayer graphene with approximately 30×30 μm^2 areas of uniform bilayer graphene.

Figure 5.3 shows the Raman mapping (obtained from acquired 900 Raman spectra over 30×30 μm^2 area) of 2D peaks FWHMs for bilayer graphene film shown in figure 5.2. In bilayer graphene, the distribution of the FWHMs is in the range of 39-65 cm^{-1} with a cut-off FWHM of 70 cm^{-1} [4]. The 2D peaks of Raman spectra obtained from figure 5.3 were fitted with four Lorentzians each with FWHM feature of a monolayer which demonstrate the characteristics of the AB-stacked bilayer graphene (see the publication presented at the end of this chapter). Therefore, in figure 5.3, over 97 % of the 30×30 μm^2 area suggests large-area uniform AB-stacked bilayer graphene.

From the sheet resistance measurements, a monolayer graphene showed a sheet resistance of

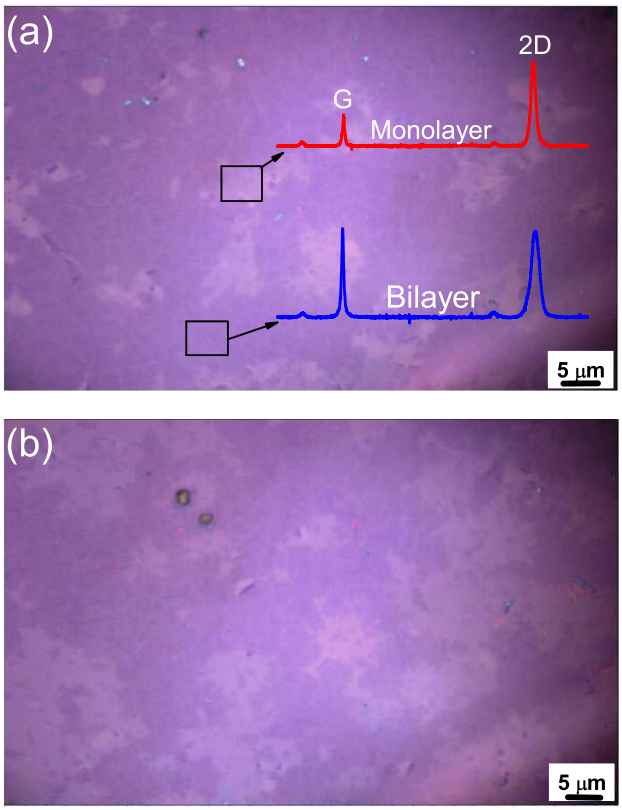

Figure 5.2: (a) and (b) The optical microscope images obtained from different spots of the same sample of bilayer graphene film transferred onto a 300 nm thick SiO_2/Si substrate.

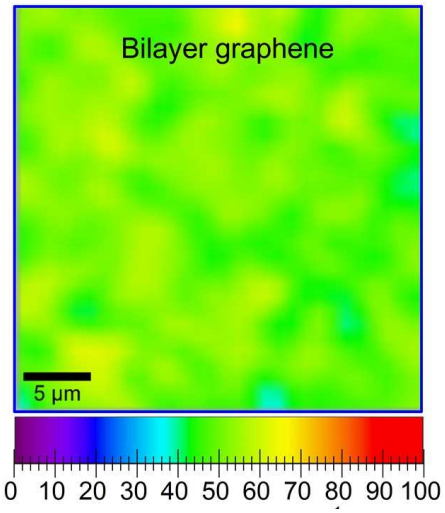

Figure 5.3: The 2D peaks FWHMs mapping (30×30 μm^2) for bilayer graphene film.

468 Ω/sqr and a bilayer graphene film of 288 Ω/sqr. These sheet resistance values compare with those measured from a monolayer (409 Ω/sqr) and bilayer graphene (287 Ω/sqr) films in reference 5.

The EBSD map for commercial Cu(0.5 at% Ni) foil showed a diverse crystallographic surface which could be a reason for incomplete wafer-scale bilayer graphene due to the influence of the Cu surface orientations in early stages of graphene growth, particularly, Cu(111) surface which typically grows monolayer graphene (discussed in chapter 2). PIXE map of Ni (Ni $K\alpha 1$) distribution in Cu(0.5 at% Ni) foil showed Ni over an analyzed area and Ni bulk concentration of 0.5 at% confirming a Ni bulk concentration in commercial dilute Cu(0.5 at% Ni) foil.

A relatively higher Ni surface concentration in Cu(0.5 at% Ni) foil was confirmed with TOF-SIMS which also showed the presence of impurities (Al, Na, Fe, Si, C_2H_5, K) in the foil surface. These impurities are expected to have much lower bulk concentrations, in a few ppm, which would result in a low surface concentration of each impurity compared to Ni. Nonetheless, the large-area part of bilayer graphene film obtained on commercial dilute Cu(0.5 at% Ni) foil was assisted by Ni surface concentration.

5.3 Publication

This section present an article published in Journal of Raman Spectroscopy, 47, 553-559 (2016). The publication (including the supporting information) details the experimental procedure and results discussed in this chapter. Although it is mentioned in this publication that the capability of a dilute Cu(0.5 at% Ni) foil to grow a large-area bilayer graphene is primarily due to the higher methane decomposition rate and carbon solubility of Ni (compare to Cu), the effect of carbon solubility of Ni in dilute Cu(0.5 at% Ni) foil would be negligible compared to the methane decomposition rate of Ni which does have a much larger effect during CVD graphene growth.

Research article

Journal of RAMAN SPECTROSCOPY

Received: 26 August 2015 Revised: 27 October 2015 Accepted: 4 November 2015 Published online in Wiley Online Library: 8 December 2015

(wileyonlinelibrary.com) DOI 10.1002/jrs.4848

Raman analysis of bilayer graphene film prepared on commercial Cu(0.5 at% Ni) foil

M. J. Madito,[a] A. Bello,[a] J. K. Dangbegnon,[a] C. J. Oliphant,[b] W. A. Jordaan,[b] T. M. Masikhwa,[a] D. Y. Momodu[a] and N. Manyala[a]*

This study reports the Raman analysis of bilayer graphene films prepared on commercial dilute Cu(0.5 at% Ni) foils using atmospheric pressure chemical vapor deposition. A bilayer graphene film obtained on Cu foil is known to have small areas of bilayer (islands) with a significant fraction of non-Bernal stacking, while that obtained on Cu/Ni is known to grow over a large area with Bernal stacking. In the Raman optical microscope images, a wafer-scale monolayer and large-area bilayer graphene films were distinguished and confirmed with Raman spectra intensities ratios of 2D to G peaks. The large-area part of bilayer graphene film obtained was assisted by Ni surface segregation because Ni has higher methane decomposition rate and carbon solubility compared with Cu. The Raman data suggest a Bernal stacking order in the prepared bilayer graphene film. A four-point probe sheet resistance of graphene films confirmed a bilayer graphene film sheet resistance distinguished from that of monolayer graphene. A relatively higher Ni surface concentration in Cu(0.5 at% Ni) foil was confirmed with time-of-flight secondary ion mass spectrometry. The inhomogeneous distribution of Ni in a foil and the diverse crystallographic surface of a foil (confirmed with proton-induced X-ray emission and electron backscatter diffraction, respectively) could be a reason for incomplete wafer-scale bilayer graphene film. The Ni surface segregation in dilute Cu(0.5 at% Ni) foil has a potential to impact on atmospheric pressure chemical vapor deposition growth of large-area bilayer graphene film. Copyright © 2015 John Wiley & Sons, Ltd.

Additional supporting information may be found in the online version of this article at publisher's web site.

Keywords: graphene Raman; Ni segregation; Cu(Ni) foil; AP-CVD graphene

Introduction

Graphene (a two-dimensional crystalline form of carbon) because of its remarkable unique properties holds great promise for nanoscale electronics and photonics. However, graphene has no bandgap, and that greatly limits its uses in electronics.[1–3] Interestingly, bilayer graphene with zero band gap behaves like a metal and, if the mirror-like symmetry of the two layers is disturbed [to give Bernal (AB) stacked bilayer graphene], then behaves like a semiconductor.[3] Studies have engineered a bandgap in graphene, bilayer graphene, in particular, that can be controlled up to 250 meV by applying a perpendicular electric field.[1–4] One of the approaches of growing an AB-stacked bilayer graphene is by chemical vapor deposition (CVD) method. The CVD approach has demonstrated an excellent capability of growing wafer-scale high-quality AB-stacked bilayer graphene.[5–8] In CVD graphene growth, copper (Cu) is the most favorable substrate because of it has lower carbon solubility (i.e. $<$0.001 at% at 1000 °C) and slow decomposition rate of methane (CH_4).[9] Graphene growth on Cu surface is catalytic processes where hydrocarbon is decomposed in the formation of carbon atoms, which initially aggregate and materialize into graphene film. The lower decomposition rate of methane by Cu is advantageous for wafer-scale monolayer graphene growth but disadvantageous for wafer-scale bilayer graphene growth as it requires more carbon atoms. In fact, it is practically impossible to supply sufficient carbon atoms for wafer-scale multilayer graphene growth on pure Cu surface.[5–15] Generally, a bilayer graphene obtained on pure Cu foil is known to be incomplete (have smaller areas of bilayer) with a significant fraction of non-AB stacking.[16–21]

Liu *et al.*[22] have shown with Cu/Ni films having a surface layer composition of about 97 at% Cu and 3 at% Ni that the lower decomposition rate of CH_4 by Cu can be enhanced by Ni [which is known to have higher carbon solubility (i.e. ~1.3 at% at 1000 °C) and decomposition rate of CH_4[23]] to grow a wafer-scale AB-stacked bilayer graphene in CVD. Preparation of such Cu/Ni films on SiO_2/Si substrates requires an extra experimental procedure (such as SiO_2/Si substrates cleaning/preparation, thickness controllable thin film deposition and annealing for thin layer interdiffusion) compare with commercially available Cu–Ni foil. However, such Cu–Ni foil at CVD graphene growth temperatures in the range of 900–1000 °C should have surface layer composition of about 97 at % Cu and 3 at% Ni to grow wafer-scale AB stack bilayer graphene in accordance with results in Reference 22.

In this study, we propose the use of homogeneous dilute Cu (0.5 at% Ni) foil, which demonstrates surface layer composition of about 97 at% Cu and 3 at% Ni in the temperature range of 920–1000 °C, calculated using surface segregation models[24,25]

* *Correspondence to: N. Manyala, Department of Physics, Institute of Applied Materials, SARCHI Chair in Carbon Technology and Materials, University of Pretoria, Pretoria, 0028, South Africa.*
E-mail: ncholu.manyala@up.ac.za

a *Department of Physics, Institute of Applied Materials, SARCHI Chair in Carbon Technology and Materials, University of Pretoria, Pretoria 0028, South Africa*

b *National Metrology Institute of South Africa, Private Bag X34, Lynwood Ridge, Pretoria 0040, South Africa*

Journal of RAMAN SPECTROSCOPY

described in the Supporting Information. The use of homogeneous dilute Cu(Ni) foil has rarely been studied for the CVD bilayer graphene growth. The objective of this study is to grow a large-area or wafer/scale high-quality bilayer graphene films on dilute Cu (0.5 at% Ni) foil using atmospheric pressure chemical vapor deposition (AP-CVD). The Raman data showed the capability of a dilute Cu (0.5 at% Ni) foil for growing a large-area bilayer graphene film. This capability of a dilute Cu(0.5 at% Ni) foil was ascribed primarily to the surface segregation of Ni in dilute Cu(0.5 at% Ni) foil (confirmed with time-of-flight secondary ion mass spectrometry) because Ni has higher methane decomposition rate and carbon solubility compare with Cu. The Raman data suggest an AB stacking order in the prepared bilayer graphene film. A prepared bilayer graphene film has a sheet resistance of 288 $\Omega\,sq^{-1}$.

Experimental

High-purity (99.9%) dilute Cu(0.5 at% Ni) foil samples ($20 \times 20\,mm^2$ and 0.5 mm thick) were ordered from MaTeck (package list no. 14040413-860). Samples were electro-polished and cleaned for graphene growth as follows: In the electrochemistry cell, the Cu (0.5 at% Ni) foil sample (to be polished) was connected to the anode and a Cu plate (30 mm in diameter and 2 mm thick) to the cathode of the cell, and the electro-polishing solution was 1000 ml of water, 500 ml of ortho-phosphoric acid, 500 ml of ethanol, 100 ml of isopropyl alcohol and 10 g of urea. A direct current power supply was used to supply constant voltage/current in the electrochemistry cell, and a voltage in the range of 3.0–6.0 V was applied for about 3 min. After electropolishing, the Cu(0.5 at% Ni) foils were rinsed with deionized water and immersed in aqueous nitric acid for 30 s to dissolve off the electro-polishing solution residues on the foil surface, then again in deionized water followed by ultrasonic bath with acetone and isopropanol and dryblowing with N_2 to remove water residues. After cleaning, Cu(0.5 at% Ni) foils were loaded in AP-CVD quartz tube setup for monolayer graphene and bilayer graphene growth successively. Samples were annealed under Ar (300 sccm) and H_2 (9 sccm) flow for 30 min at 1050 °C before the growth of graphene. After annealing, a monolayer graphene was synthesized from a mixture of gases, Ar (300 sccm), H_2 (9 sccm) and CH_4 (15 sccm), and a bilayer graphene from a mixture of Ar (300 sccm), H_2 (9 sccm) and CH_4 (10 sccm) at 980 °C for exactly 9 min. Immediately after growth, the CH_4 flow was stopped, and the quartz tube was pushed to the cooler region of the furnace and samples were rapidly cooled down to room temperature and offloaded from AP-CVD quartz tube.

The graphene films were transferred onto 300-nm-thick SiO_2/Si substrates. In the transfer, a thin layer of polymethyl methacrylate (PMMA) (average Mw ~996 000 by gel permeation chromatography) dissolved in chlorobenzene with a concentration of 46 mg ml was spin-coated on the as-grown graphene films on Cu(0.5 at% Ni) foils at 3000 rpm for 30 s. PMMA deposited on graphene films/Cu(0.5 at% Ni) foils was cured at 115 °C for 5 min. PMMA/graphene/Cu(0.5 at% Ni) foil samples were placed in 1-M iron nitrate to etch off Cu and transferred using a polyethylene terephthalate to the 5% hydrochloride (HCl) and deionized water to dissolve the iron nitrate, and then onto SiO_2 substrates. Finally, PMMA was removed using acetone.

Graphene/SiO_2/Si samples (graphene films) were characterized with Raman spectroscopy (WITec Alpha 300 micro-Raman imaging system with 532-nm excitation laser). Raman spectra were measured at room temperature with the laser power set below 2 mW in order to minimize heating effects. The graphene film sheet resistance measurements were carried out in ambient conditions (i.e. in air at room temperature and pressure) using a Signatone four-point probe station. A Cu(0.5 at% Ni) foil was analyzed with electron backscatter diffraction (EBSD) performed in a LEO 1525 field emission gun scanning electron microscope at an acceleration voltage of 25 kV using the Oxford INCA crystal software. Proton-induced X-ray emission (PIXE) was used to map Ni distribution in Cu(0.5 at% Ni) foils. Time-of-flight secondary ion mass spectroscopy (TOF-SIMS) surface imaging (elemental map) of Cu(0.5 at% Ni) foils was performed using the TOF-SIMS5 Ion-TOF system. The mass spectra were calibrated to the following mass peaks in positive mode: Al, Na, Ni, Fe, Si, C, C_2H_5, K and Cu. The analysis was carried out over an area of $500 \times 500\,\mu m^2$ and ion sputter gun area of $1000 \times 1000\,\mu m^2$.

Results and discussions

In the Raman spectrum of graphene, the main features that are observable are the G-band mode (~1590 cm^{-1}), the 2D-band mode (~2690 cm^{-1}) and the D-band mode or the disorder-induced band (1350 cm^{-1}).[1,21] The G-band originates from a normal first-order Raman scattering process in graphene and involves the sp^2-hybridized carbon atoms of the graphene layer, the 2D-band from a second-order process that involves two in-plane transverse optical mode (iTO) phonons near the *K* point and the D-band from a second-order process that involves one iTO phonon and one defect.[1,21] The Raman process can also give rise to the triple-resonance Raman process, which might explain a more intense 2D-band relative to the G-band in monolayer graphene.[1] By observing the differences in the 2D-band and the G-band intensity ratios, the 2D-band wavenumber (peak width) and line shape, the number of graphene layers contained in graphene films can be obtained and also the stacking order or interlayer interactions in few-layer graphene films.[1,21] Figure 1(a) and (b) shows the Raman optical microscope images (obtained using 100×/0.90 objective lens) of monolayer and bilayer graphene films transferred onto 300-nm-thick SiO_2/Si substrates. Importantly, the optical microscope of graphene films displays the image color contrast between monolayer and multilayer graphene films; hence, it is used to distinguish between the two. The optical microscope image for monolayer graphene [Fig. 1(a)] shows a wafer-scale graphene film and for bilayer graphene film [Fig. 1(b)] shows large-area bilayer graphene (darker areas) with smaller areas of monolayer graphene (lighter areas). Figure 1(c) shows the average Raman spectra obtained from 30-μm^2 areas of monolayer and bilayer graphene films shown in Fig. 1(a) and (b) with square boxes. The mapping of G peak intensities of the obtained Raman spectra over 30-μm^2 areas of monolayer and bilayer graphene films is shown in Fig. S2 (Supporting Information) and shows relative uniform intensity over an analyzed area. It can be seen in Fig. 1(c) that the G peak intensity scale range for bilayer graphene is twice that for monolayer graphene [also see the G peak intensity mapping in Fig. S2 (Supporting Information)] and shows a distinction between monolayer and bilayer graphene films. The G-band position can give insight into the number of layers present in the graphene film; however, it can be affected by film conditions such as temperature, doping and small amounts of strain present in the film. Nonetheless, the G-band intensity, which is less susceptible to such film conditions, shows a behavior that follows a linear trend as the number of layers increases from monolayer to multilayer graphene.[1,21,26,27]

Journal of RAMAN SPECTROSCOPY

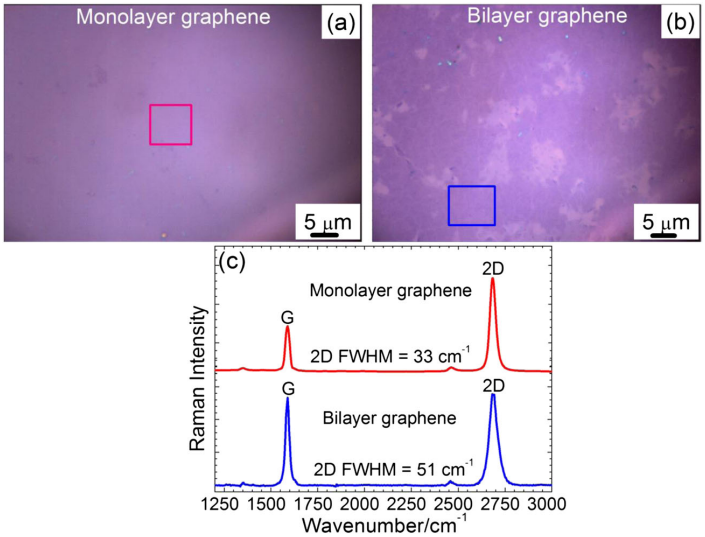

Figure 1. The Raman optical microscope images (obtained using 100×/0.90 objective lens) of (a) monolayer and (b) bilayer graphene films transferred onto 300-nm-thick SiO_2/Si substrates. (c) The average Raman spectra obtained from 30-μm^2 areas of monolayer and bilayer graphene films shown in (a) and (b) with square boxes.

In Fig. 1(c), the absence of the D-band (at ~1360 cm^{-1}) in Raman spectra demonstrates high-quality graphene because D-band appears because of the presence of impurities or defects in the translational symmetry of the carbon material's lattice.[1,21,26,27] A wafer-scale monolayer graphene obtained demonstrates a known capability of graphene of growing over grain boundaries and grains on polycrystalline Cu surface.[26] The smaller-areas of monolayer graphene present in prepared bilayer graphene demonstrate the physical challenge of supplying sufficient carbon atoms for wafer-scale multilayer graphene growth on Cu foil.[4,28] The challenge could be as a result of lower decomposition rate of methane by Cu (especially in Cu surface areas or grains where there is almost 0 at% Ni concentrations) and the diverse surface orientations present in Cu surface.[29] In addition, a similar bilayer graphene film was obtained [see the optical microscope image in Fig. S3 (Supporting Information)] through the same experimental procedure on additional dilute Cu(0.5 at% Ni) foil sample, which confirms the observed challenge of obtaining a wafer-scale bilayer graphene film on Cu.

Figure 2(a) and (b) shows the mapping of 2D peak full width at half maximum (FWHM) and the corresponding 2D to G peak intensity ratio (I_{2D}/I_G) mapping, respectively, for monolayer and bilayer graphene films. For monolayer graphene, the 2D peak FWHMs are in the range of 26–38 cm^{-1} and I_{2D}/I_G in the range of ~2.5–4.5, while for bilayer graphene, the distribution of the FWHMs is in the range of 39–65 cm^{-1} (with a cut-off FWHM of about 70 cm^{-1}) and I_{2D}/I_G in the range of 0.5–2.2. Figure 2 clearly demonstrates and distinguishes characteristic features of monolayer and bilayer graphene as expected.

In monolayer graphene, the 2D-band mode has a single Lorentzian feature.[3] In AB-stacked bilayer graphene, the electronic band splits into two conduction and two valence bands. The upper (lower) and lower (upper) branches of the valence (conduction) band are referred to as $\pi_1(\pi_1^*)$ and $\pi_2(\pi_2^*)$, respectively, as illustrated with a schematic view in Fig. 3(a).[1,21,26,27] Because 2D-band originates from second-order Raman process that involves two iTO phonons, the electronic band split causes splitting of the phonon bands into two components such that the electron–phonon scattering occurs with two phonons with symmetries T_1 and T_2.[26] For a T_1 phonon, the scattering occurs between bands of the same symmetry (i.e. π_1 and π_1^* or π_2 and π_2^*), and for a T_2 phonon, the scattering occurs between bands of different symmetries (i.e. π_1 and π_2^*). T_1 and T_2 phonon processes are labeled as P_{ij} (with the relative magnitudes of the four phonon wavevectors q), where i (j) denotes an electron

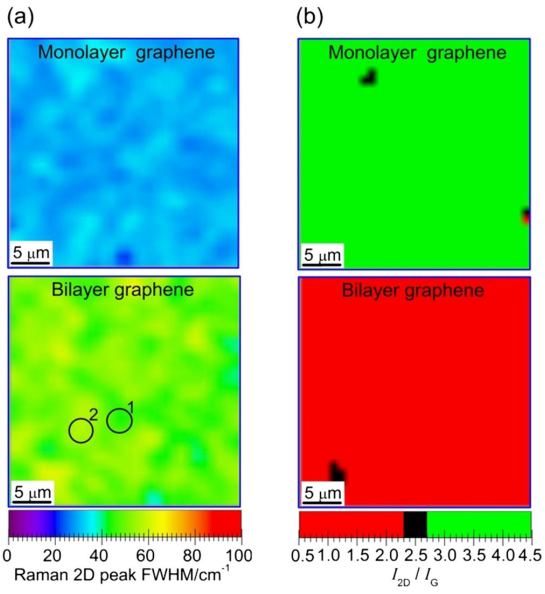

Figure 2. (a) The 2D peak full width at half maximum (FWHM) mapping and (b) the corresponding 2D to G peak intensities ratio (I_{2D}/I_G) mapping for monolayer and bilayer graphene films, respectively, transferred onto SiO_2/Si substrate (the data are the same, acquired from the 30-μm^2 area in Fig. 1).

Journal of RAMAN SPECTROSCOPY

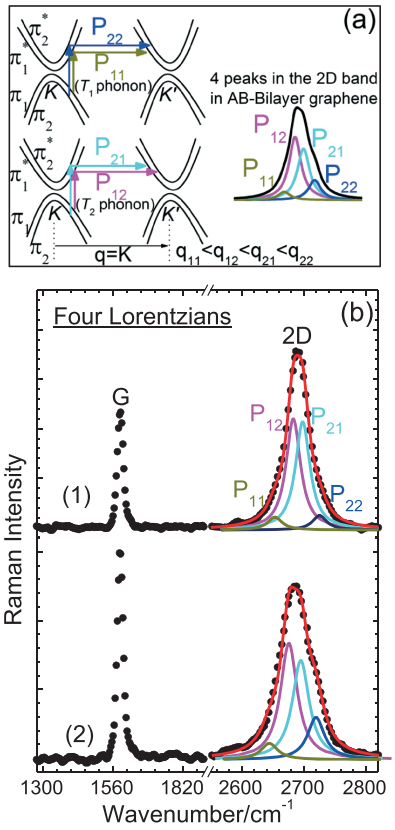

Figure 3. (a) Schematic view of the electron dispersion of bilayer graphene near the *K* and *K′* points showing both π_1 and π_2 bands. The resonance Raman processes due to electronic band split are indicated as P_{11}, P_{22}, P_{12} and P_{21} with the relative magnitudes of the four phonon wavevectors *q*.[1] (b) The Raman spectra from two different spots of bilayer graphene film [spectra 1 and 2 are from circles 1 and 2 in Fig. 2(a)] transferred onto SiO_2/Si substrate. The solid lines are Lorentzian fits of 2D peaks. AB, Bernal.

scattered from (to) each conduction band $\pi^*_{i(j)}$ (see Fig. 3(a) schematic view). The P_{11}, P_{22}, P_{12} and P_{21} scattering processes originating from an iTO phonon give rise to four peaks in the Raman 2D peak with peak wavenumbers at approximately 2655, 2680, 2700 and 2725 cm^{-1}, respectively, and FWHMs equal that of monolayer graphene 2D peak.[26] These four peaks are fitted as four Lorentzians to 2D peak.[1,21,26,27] The amplitudes of the two Lorentzians at ~2680 and ~2700 cm^{-1} (inner peaks in 2D peak) have almost the same intensity and are higher than the other two at ~2655 and ~2725 cm^{-1} (outer peaks in 2D peak) as shown with a schematic view of these peaks in Fig. 3(a) (similar to Lorentzians usually obtained for exfoliated AB-stacked bilayer graphene).[26,27] The amplitudes of the four Lorentzians depend on the laser energy, which was maintained constant in this work. Figure 3(b) shows spectra 1 and 2 from circles 1 and 2 in Fig. 2(a), and the 2D peaks are fitted with four Lorentzians each with FWHM feature of a monolayer graphene. The four Lorentzians in Fig. 3(b) demonstrate the characteristics of the AB-stacked bilayer graphene. To further investigate the possibility of large-area trilayer graphene, six Lorentzian fits were performed [Fig. S4 (Supporting Information)] and only four of six Lorentzians fitted inside 2D peak, which further confirmed bilayer graphene in the sample. In brief, the Raman spectroscopy/imaging confirms a large-area bilayer in prepared graphene film distinguished from monolayer graphene and suggests an AB stacking order in prepared bilayer graphene film. Of course, Raman spectroscopy/imaging is a well-known powerful and noninvasive technique to determine, among others, the number of graphene layers, the stacking order and the interlayer interactions in few layer graphene sample.[26,27,30,31]

Figure 4(a) shows the measured voltage drop for monolayer and bilayer graphene films, which was used to calculate the sheet resistance of graphene films [Fig. 4(b)] using an approach that relies on a geometric factor. A monolayer graphene film has a high sheet resistance (468 Ω sqr^{-1}) compare with bilayer graphene film (288 Ω sq^{-1}) because sheet resistance decreases with the increase in graphene film thickness (number of layers). The sheet resistance measured compares with those measured from a monolayer (409 Ω sq^{-1}) and bilayer graphene (287 Ω sq^{-1}) films in Reference 18. The sheet resistance is determined by the carrier density and mobility.[32] For instance, at low temperatures (~4 K), a monolayer graphene with high sheet resistance has a high Hall mobility with low carrier density.[33] In contrary, a bilayer graphene with low sheet resistance has a high Hall mobility and high carrier density.[33] These properties are used to distinguish monolayer and bilayer graphene and are ascribed to different band structures and scattering mechanisms in these layers of graphene.[3,33,34] Therefore, the sheet resistance shows a strong dependence of the electrical prosperities on graphene film thickness, primarily relating to the interlayer coupling.[33,34] These measurements of the carrier transport properties of graphene were not performed in this work.

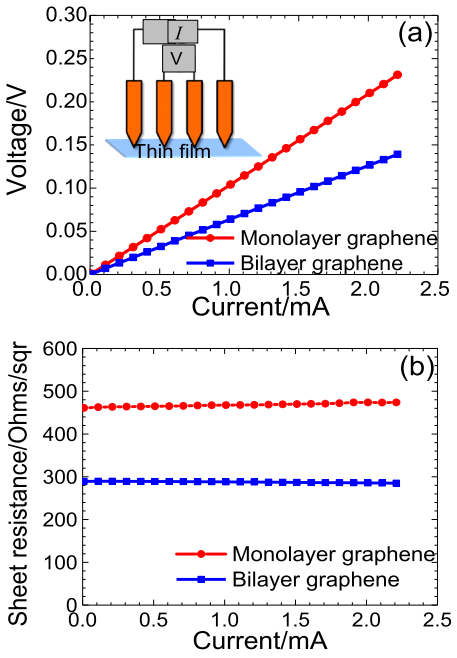

Figure 4. (a) A four-point probe-measured voltage drop for monolayer and bilayer graphene films transferred onto SiO_2/Si substrates (insert to figure shows a schematic that shows that in a four-point probe, two electrodes are used for sourcing a direct current, *I*, and the other two for measuring the corresponding voltage drop, *V*) and (b) the calculated sheet resistance of the corresponding graphene films.

Journal of RAMAN SPECTROSCOPY

Figure 5(a) and (b) shows EBSD and PIXE mapping of the grain surface orientations of the annealed Cu(0.5 at% Ni) foil surface (with an average grain size of 116 μm) and Ni concentration distribution in the annealed Cu(0.5 at% Ni) foil, respectively. An EBSD map shows a crystallographic diverse surface of Cu(0.5 at% Ni) foil, composed of terraces of low-index Cu planes (111), (101) and (001) and larger intermediate planes in accordance with the inverse pole figure orientation component coloring scheme (inset to figure). In CVD graphene growth on Cu foil, only the surface of a foil is important because the growth is limited to surface reaction. It is known that the surface crystallography of the Cu foil influences the CVD graphene growth rate. High-index Cu planes cause compact graphene island formation with growth rates faster than those on Cu(100).[18,33] A Cu(111) plane also has fast growth rate but grows monolayer graphene and influences nearby growth dynamics.[33] Meaning, graphene growth on the Cu(111) surface grows over grain boundaries into the adjacent high-index Cu surfaces. Therefore, traces of Cu(111) surface in Cu(0.5 at% Ni) foil led to smaller areas of monolayer graphene present in prepared bilayer graphene. A PIXE map for Cu(0.5 at% Ni) foil shows inhomogeneous distribution and high Ni concentration of 0.5 at%, as expected. Inhomogeneous distribution of Ni could be due to grain boundaries, different grains (orientations) and the presence of other impurities in the foil, which most likely compete with Ni for lattice sites. An observed inhomogeneous distribution of Ni in foil bulk will also be observed in the surface because of grain boundaries and different grain surface orientations. For instance, low-energy electron diffraction over-structures have shown that the maximum surface concentration of a substitutional segregating element for Cu(001), Cu(101) and Cu(111) is 25, 50 and 33 at%, respectively.[25,35,36] High Ni surface concentrations will cause faster methane decomposition and graphene growth rate as compared with surfaces with low Ni concentrations. Therefore, inhomogeneous distribution of Ni in Cu foil surface will contribute differently to graphene growth rates on different grains surfaces.

Figure 6 shows the map images of TOF-SIMS secondary ion intensities measured from a dilute Cu(0.5 at% Ni) surface (i.e. after annealing under graphene growth conditions without methane source) before surface cleaning [and after surface cleaning for 180 s with ion sputtering; Fig. S5 (Supporting Information)]. Figure 6 shows high surface concentrations (or relative intensities) of Al, Na, Ni, Fe, Si, C_2H_5 and K in Cu(0.5 at% Ni) foil, which result from impurities segregation. Impurities of Cu surface play a critical role in determining the number of graphene layers during CVD graphene growth, but the effect of each impurity is determined by a metal–carbon atomic interaction energy, metal–methane decomposition rate and metal–carbon solubility. Although Na and K alkali metals (and C_2H_5) show high relative intensities at room temperature, they will not dominate the surface during CVD growth at high temperature of 980 °C because of their very low melting points (<100 °C). Compare with other elements, high relative intensities of Na and K in foil do not necessarily show high surface concentrations of these elements because they have strong signals in TOF-SIMS. Al, Si and Fe impurities have bulk concentrations in the order of few parts per million (ppm) compare with Ni, which has 5000 ppm (0.5 at%), and hence, Ni has higher surface concentration (Fig. 6). Compare with these impurities, after surface cleaning with ion sputtering [Fig. S5 (Supporting Information)], Ni has higher bulk concentration as expected. Among impurities detected in the foil surface, Ni has strong carbon–metal atomic interaction, high

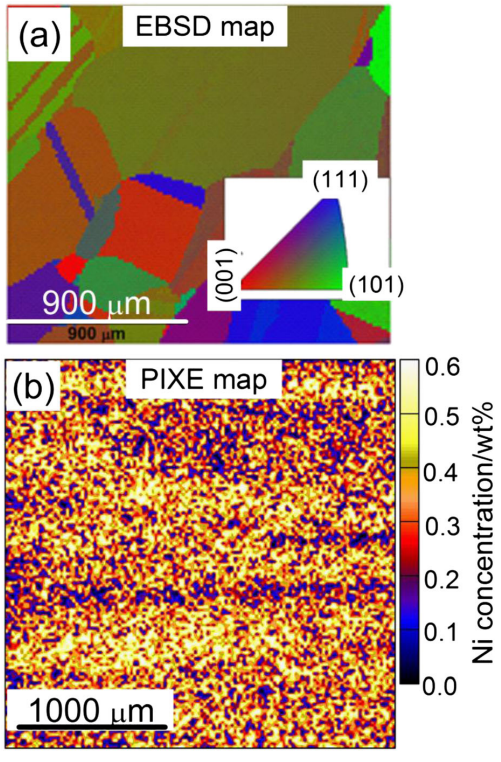

Figure 5. (a) Electron backscatter diffraction (EBSD) map of the annealed Cu(0.5 at% Ni) foil surface, and the inset to the figure is the corresponding inverse pole figure orientation component coloring scheme. (b) Proton-induced X-ray emission (PIXE) map of Ni distribution in the annealed Cu (0.5 at% Ni) foil.

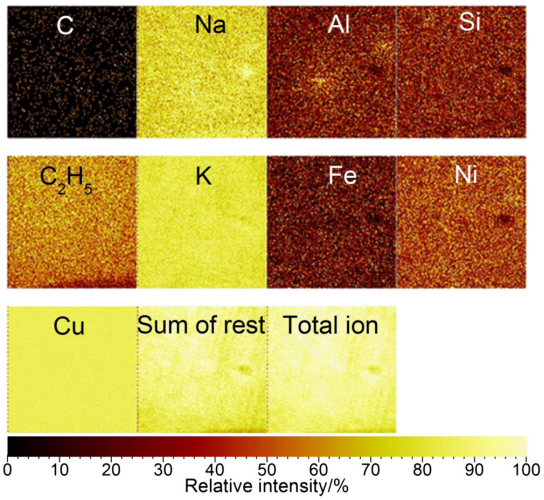

Figure 6. The map images of time-of-flight secondary ion mass spectroscopy secondary ion intensities measured from a dilute Cu(0.5 at% Ni) surface before surface cleaning with ion sputtering.

methane decomposition rate, high carbon solubility and high bulk concentration (which act as Ni supplier to reach high Ni surface concentrations).[1,21,26,37] As a result, surface Ni will contribute significantly during CVD graphene growth on Cu(0.5 at% Ni) foil.

Furthermore, the thermodynamically driven segregation of Ni in dilute Cu(0.5 at% Ni) foil can be described according to Darken description (surface segregation model), which states that segregation of impurities in dilute alloy is driven by a change in chemical potential energy, which results in the minimization of the total energy of the crystal.[25] Using surface segregation models, it can be shown that at a growth temperature of 980 °C, the Ni surface concentration is $X_{Ni}^{S} = 2.1$, 1.4 and 1.1 at% for Cu(001), Cu(111) and Cu (101) surfaces, respectively [see the calculation of Fig. S1 (Supporting Information)]. Therefore, at 980 °C, a surface layer of a dilute Cu(0.5 at% Ni) foil will have about 1.5 at% Ni on average, and the impurities with bulk concentrations in the order of few parts per million will have <0.01 at% surface concentrations. Once more, Liu *et al.*,[22] using Cu/Ni thin films with a surface layer consisting of >97 at% Cu and <3 at% Ni, have produced a large-area AB-stacked bilayer graphene film. Similarly, a dilute Cu(0.5 at % Ni) foil has produced a large-area bilayer graphene film that is suggested to be AB stacked according to Raman data. The processes such as segregation from grains and grain boundaries and the segregation dependence of different grains surfaces play a role in surface concentration build-up of segregating impurity. Therefore, in a polycrystalline foil that has crystallographic diverse surface, it is difficult to control or separate these contributions from each other (even in the calculation using surface segregation models). Therefore, the Ni surface concentration calculated using surface segregation models approximates to an actual average Ni surface concentration expected in dilute Cu(0.5 at% Ni) foil at a growth temperature of 980 °C.

Conclusions

In this study, the Raman analysis of graphene films prepared on commercial dilute Cu(0.5 at% Ni) foils using AP-CVD is reported. The AP-CVD growth of graphene films focused on growing a large-area AB-stacked bilayer graphene film. In the Raman optical microscope images, a wafer-scale monolayer and large-area bilayer graphene films were distinguished and confirmed with Raman spectra data. The Raman data suggest an AB stacking order in prepared bilayer graphene film. A four-point probe sheet resistance of graphene films confirmed a bilayer graphene film sheet resistance distinguished from that of monolayer graphene. The large-area part of bilayer graphene film obtained on dilute Cu(0.5 at% Ni) foil was assisted by Ni surface concentration because Ni has higher methane decomposition rate and carbon solubility as compared with Cu. A higher Ni surface concentration in Cu(0.5 at% Ni) foil was confirmed with time-of-flight secondary ion mass spectrometry. The inhomogeneous distribution of Ni in a foil and the diverse crystallographic surface of a foil (confirmed with proton-induced X-ray emission and EBSD respectively) could be a reason for incomplete wafer-scale bilayer graphene film. Because high-index Cu planes and low-index Cu(001) and Cu(101) planes are known to grow compact graphene and Cu(111) plane to grow monolayer graphene, which grows over grain boundaries into the adjacent grains. Although we propose a homogeneous dilute Cu(0.5 at% Ni) foil, we also suggest that a foil should consist of low-index Cu (001) or Cu(101) surfaces to archive a wafer-scale AB-stacked bilayer graphene film in AP-CVD.

Acknowledgements

This work is based on the research supported by the South African Research Chairs Initiative of the Department of Science and Technology and National Research Foundation (NRF) of South Africa (grant no. 97994). Any opinion, finding and conclusion or recommendation expressed in this material is that of the author(s), and the NRF does not accept any liability in this regard. M. J. Madito acknowledges the financial support from University of Pretoria and NRF for his PhD studies. Dr M. Madhuku is acknowledged for his assistance on the PEXI measurements from iThemba LABS.

References

[1] Y. Zhang, T.-T. Tang, C. Girit, Z. Hao, M. C. Martin, A. Zettl, M. F. Crommie, Y. R. Shen, F. Wang, *Nature* **2009**, *459*, 820.
[2] W. J. Yu, L. Liao, S. H. Chae, Y. H. Lee, X. Duan, *Nano Lett.* **2011**, *11*, 4759.
[3] H. Aoki, S. Mildred, M. S. Dresselhaus (Eds), *Physics of Graphene*, Springer, New York, **2014**.
[4] W. Liu, H. Li, C. Xu, Y. Khatami, K. Banerjee, *Carbon* **2011**, *49*, 4122.
[5] S. Bhaviripudi, X. Jia, M. S. Dresselhaus, J. Kong, *Nano Lett.* **2010**, *10*, 4128.
[6] I. Vlassiouk, M. Regmi, P. Fulvio, S. Dai, P. Datskos, G. Eres, S. Smirnov, *ACS Nano* **2011**, *5*, 6069.
[7] H. Kim, E. Saiz, M. Chhowalla, C. Mattevi, *New J. Phys.* **2013**, *15*, 053012.
[8] A. W. Robertson, J. H. Warner, *Nano Lett.* **2011**, *11*, 1182.
[9] G. A. López, E. J. Mittemeijer, *Scr. Mater.* **2004**, *51*, 1.
[10] Q. Li, H. Chou, J. H. Zhong, J. Y. Liu, A. Dolocan, J. Zhang, Y. Zhou, R. S. Ruoff, S. Chen, W. Cai, *Nano Lett.* **2013**, *13*, 486.
[11] S. Nie, W. Wu, S. Xing, Q. Yu, J. Bao, S. Pei, K. F. McCarty, *New J. Phys.* **2012**, *14*, 093028.
[12] M. Fabiane, S. Khamlich, A. Bello, J. Dangbegnon, D. Momodu, A. T. Charlie Johnson, N. Manyala, *AIP Adv.* **2013**, *3*, 112126.
[13] K. Yan, H. Peng, Y. Zhou, H. Li, Z. Liu, *Nano Lett.* **2011**, *11*, 1106.
[14] B. Wu, D. Geng, Y. Guo, L. Huang, Y. Xue, J. Zheng, J. Chen, G. Yu, Y. Liu, L. Jiang, W. Hu, *Adv. Mater.* **2011**, *23*, 3522.
[15] P. Wu, X. Zhai, Z. Li, J. Yang, *J. Phys. Chem. C* **2014**, *118*, 6201.
[16] N. Liu, L. Fu, B. Dai, K. Yan, X. Liu, R. Zhao, Y. Zhang, Z. Liu, *Nano Lett.* **2011**, *11*, 297.
[17] A. Reina, X. Jia, J. Ho, D. Nezich, H. Son, V. Bulovic, M. S. Dresselhaus, J. Kong, *Nano Lett.* **2009**, *9*, 30.
[18] S. Chen, W. Cai, R. D. Piner, J. W. Suk, Y. Wu, Y. Ren, J. Kang, R. S. Ruoff, *Nano Lett.* **2011**, *11*, 3519.
[19] X. Liu, L. Fu, N. Liu, T. Gao, Y. Zhang, L. Liao, Z. Liu, *J. Phys. Chem. C* **2011**, *115*, 11976.
[20] Y. Wu, H. Chou, H. Ji, Q. Wu, S. Chen, W. Jiang, Y. Hao, J. Kang, Y. Ren, R. D. Piner, R. S. Ruoff, *ACS Nano* **2012**, *6*, 7731.
[21] W. Fang, A. L. Hsu, R. Caudillo, Y. Song, a. G. Birdwell, E. Zakar, M. Kalbac, M. Dubey, T. Palacios, M. S. Dresselhaus, P. T. Araujo, J. Kong, *Nano Lett.* **2013**, *13*, 1541.
[22] W. Liu, S. Kraemer, D. Sarkar, H. Li, P. M. Ajayan, K. Banerjee, *Chem. Mater.* **2014**, *26*, 907.
[23] W. Cai, R. D. Piner, Y. Zhu, X. Li, Z. Tan, H. C. Floresca, C. Yang, L. Lu, M. J. Kim, R. S. Ruoff, *Nano Res.* **2009**, *2*, 851.
[24] E. C. Viljoen, J. du Plessis, *Surf. Sci.* **1999**, *431*, 128.
[25] J. du Plessis, *Solid State Phenomena - Part B, Volume 11 (Diffusion and Defect Data)*, Sci-Tech Publications, Brookfield USA, **1990**.
[26] A. C. Ferrari, J. C. Meyer, V. Scardaci, C. Casiraghi, M. Lazzeri, F. Mauri, S. Piscanec, D. Jiang, K. S. Novoselov, S. Roth, A. K. Geim, *Phys. Rev. Lett.* **2006**, *97*, 187401.
[27] L. M. Malard, M. a. Pimenta, G. Dresselhaus, M. S. Dresselhaus, *Phys. Rep.* **2009**, *473*, 51.
[28] A. Guermoune, T. Chari, F. Popescu, S. S. Sabri, J. Guillemette, H. S. Skulason, T. Szkopek, M. Siaj, *Carbon N. Y.* **2011**, *49*, 4204.
[29] J. D. Wood, S. W. Schmucker, A. S. Lyons, E. Pop, J. W. Lyding, *Nano Lett.* **2011**, *11*, 4547.
[30] J. M. Caridad, F. Rossella, V. Bellani, M. S. Grandi, E. Diez, *J. Raman Spectrosc.* **2011**, *42*, 286.
[31] J. M. Caridad, F. Rossella, V. Bellani, M. Maicas, M. Patrini, E. Díez, *J. Appl. Phys.* **2010**, *108*, 084321.
[32] Y. Liu, W. Li, M. Qi, X. Li, Y. Zhou, Z. Ren, *Phys. E Low-dimensional Syst. Nanostructures* **2015**, *69*, 115.

Journal of RAMAN SPECTROSCOPY

[33] W. Zhu, V. Perebeinos, M. Freitag, P. Avouris, *Phys. Rev. B* **2009**, *80*, 235402.
[34] C. Cobaleda, E. Diez, M. Amado, S. Pezzini, F. Rossella, V. Bellani, D. López-Romero, D. K. Maude, *J. Phys. Conf. Ser.* **2013**, *456*, 012006.
[35] E. C. Viljoen, J. du Plessis, *Surf. Sci.* **1999**, *431*, 128.
[36] E. C. Viljoen, J. du Plessis, *Surf. Sci.* **2000**, *468*, 27.
[37] A. Dahal, M. Batzill, *Nanoscale* **2014**, *6*, 2548.

Supporting information

Additional supporting information may be found in the online version of this article at publisher's web site.

5.4 Supporting information

This section present a supporting information referred to in the publication above (Chapter 5).

Raman analysis of bilayer graphene film prepared on commercial Cu(0.5 at% Ni) foil

M.J. Madito[a], A. Bello[a], J.K. Dangbegnon[a], C.J. Oliphant[b], W.A. Jordaan[b], T.M. Masikhwa[a], D.Y. Momodu[a] and N. Manyala[a*]

[a]Department of Physics, Institute of Applied Materials, SARCHI Chair in Carbon Technology and Materials, University of Pretoria, Pretoria 0028, South Africa.

[b]National Metrology Institute of South Africa, Private Bag X34, Lynwood Ridge, Pretoria 0040, South Africa

[*] Corresponding Author: Tel: +27 (0)12 420 3549 and E-mail address: ncholu.manyala@up.ac.za (N. Manyala)

Ni surface concentration calculation using surface segregation models

Part of the modified Darken equations, which defines the rate of surface concentration build-up of dope element 1 (e.g. Ni in dilute Cu(Ni) foil), is[1,2]

$$\frac{\partial X_1^S}{\partial t} = \frac{M_1 X_1^{B_1}}{d^2}\left[\Delta G + RT \ln \frac{X_1^{B_1}\left(1-\frac{X_1^S}{X^M}\right)}{\frac{X_1^S}{X^M}(1-X_1^{B_1})}\right] \quad (1)$$

where X_1^S is the surface concentration of the segregating dope element 1, X_1^B is the bulk concentration, X^M is the maximum surface concentration < 100 at%, M_1 is the mobility, $M = D/RT$ where D is the diffusion coefficient in Arrhenius equation, d is the thickness of the segregated layer, R is the gas constant and T is the temperature.

In dilute system the segregation energy (ΔG) can be approximated to segregation enthalpy (ΔH) by [3,4]

$$\Delta G \approx \Delta H = \left(\frac{\Delta Z}{Z}\right)\left(\Delta H_B^{sub} - \Delta H_A^{sub}\right) \quad (2)$$

where Z is bulk coordination number (Z = 12 for Cu crystal), ΔZ is a difference in coordination number between bulk and surface (ΔZ = 4, 3 and 2 for Cu(001), Cu(111) and Cu(101) respectively), ΔH^{sub} is heat of sublimation for element A and B ($\Delta H_{Cu}^{sub} = 339.3$ kJ/mol and $\Delta H_{Ni}^{sub} = 430.1$ kJ/mol)[5].

In Eq. S1, the rate of surface concentration build-up of dope element 1, at equilibrium, $\partial X_1^S / \partial t = 0$, and Eq. S1 reduces to the Langmuir–McLean equation[1,6]:

$$\frac{X_1^S / X^M}{1 - X_1^S / X^M} = \frac{X_1^B}{1 - X_1^B} \exp\left(\frac{-\Delta G}{RT}\right) \quad (3)$$

In Eq. S3, substituting parameters:

i. ΔG (obtained from Eq. S2 for Cu(001), Cu(111) and Cu(101)),
ii. $X_1^{B_1} = 0.5$ at % and
iii. X^M = 0.25, 0.33 and 0.50 for Cu(001), Cu(111) and Cu(101) respectively[1,6],

the temperature dependence of the Ni surface fractional concentration in dilute Cu(0.5 at% Ni) foil was obtained as shown in Fig. S1.

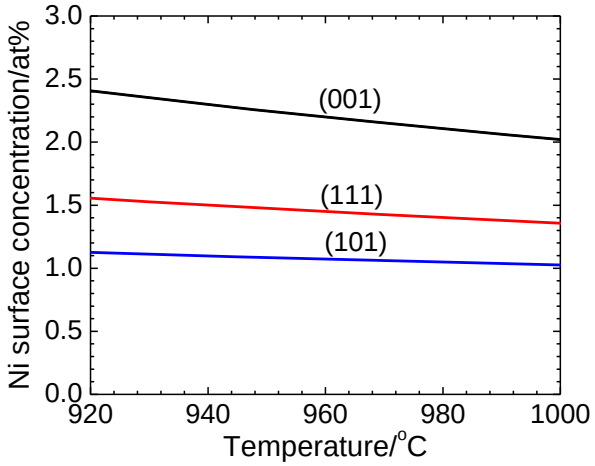

Figure. S1. The temperature dependence of the Ni surface concentration in dilute Cu(Ni) alloy obtained with Langmuir–McLean equation.

In brief, at isothermal CVD growth temperature of 980 °C the Ni surface concentration in dilute Cu(0.5 at% Ni) foil is X_{Ni}^{S} = 2.1, 1.4 and 1.1 at% for Cu(001), Cu(111) and Cu(101) surfaces respectively. Therefore, at 980 °C, a surface layer of a dilute Cu(0.5 at% Ni) foil will have about 98.5 at% Cu and 1.5 at% Ni.

Raman data

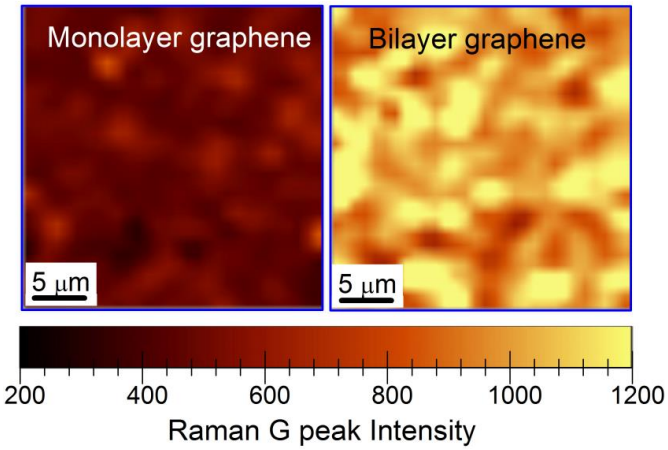

Figure. S2. The G peaks intensities mapping over 30 μm^2 area for monolayer and bilayer graphene films transferred on SiO_2/Si substrate.

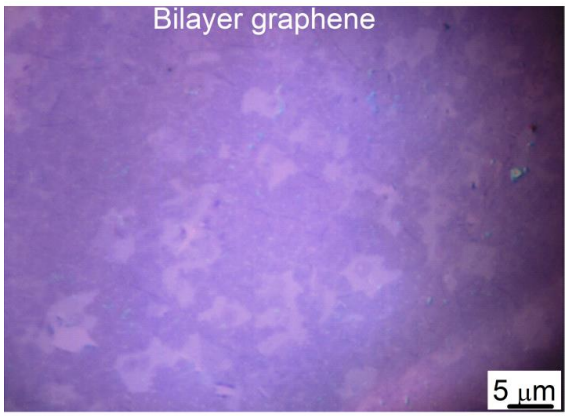

Figure. S3. The Raman optical microscope image of bilayer graphene film transferred onto 300 nm thick SiO_2/Si substrate.

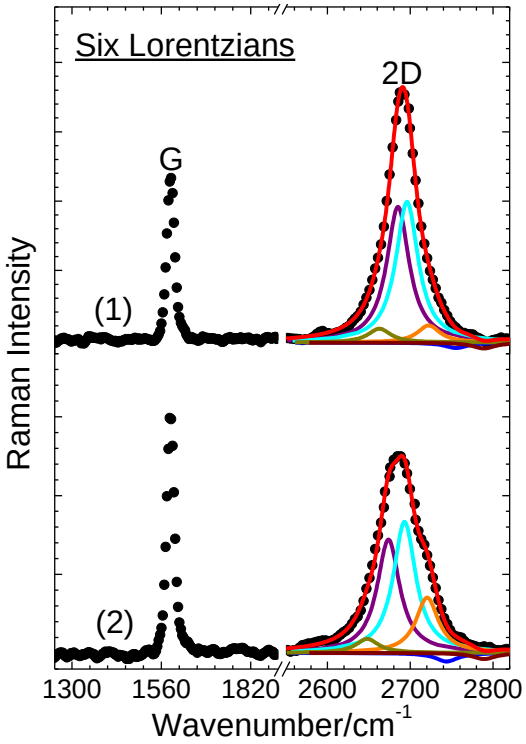

Figure. S4. The Raman spectra from two different spots of bilayer graphene film transferred onto SiO_2/Si substrate. The solid lines are Lorentzian fits of 2D peaks.

TOF-SIMS data

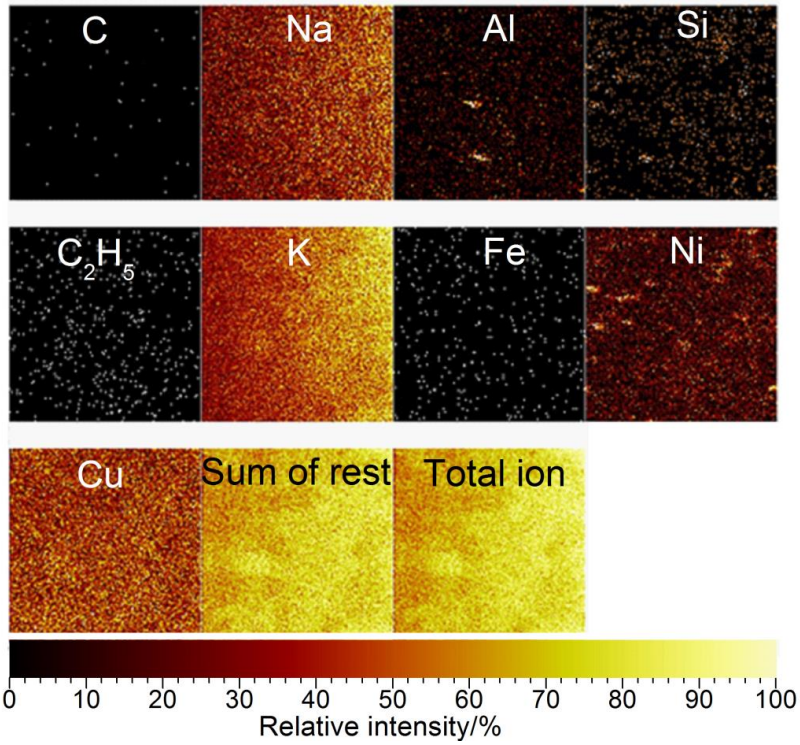

Figure. S5. The map images of TOF-SIMS secondary ion intensities measured from a dilute Cu(0.5 at% Ni) surface after surface cleaning for 180 s with ion sputtering.

S1. References

[1] J. du Plessis, *Solid State Phenomena - Part B, Volume 11 (Diffusion and Defect Data)*, Sci-Tech Publications, Brookfield USA, **1990**.

[2] E. C. Viljoen, J. du Plessis, *Surf. Sci.* **2000**, *468*, 27.

[3] S. Hofmann, R. Frech, W. Germany, **1985**, 716.

[4] K. Wandelt, C. R. Brundle, *Phys. Rev. Lett.* **1981**, *46*, 1529.

[5] R. C. Weast, M. J. Astle, Eds. , in *CRC Handb. Chem. Phys.*, CRC Press, Inc., **1982**.

[6] E. C. Viljoen, J. du Plessis, *Surf. Sci.* **1999**, *431*, 128.

5.5 Concluding remarks

This part of the study aimed at growing a high-quality large-area AB-stacked bilayer graphene film using commercial dilute Cu(0.5 at% Ni) foil as a substrate in AP-CVD. A high-quality large-area AB-stacked bilayer graphene film was successfully obtained, however, it had small areas of monolayer graphene which were attributed to the influence of the Cu surface orientations ("surface effects") in early stages of graphene growth since the presence of Cu(111) surface typically grows monolayer graphene. The large-area part of bilayer graphene film could be as a result of a high Ni surface concentration since Ni has higher methane decomposition rate compared to Cu. This chapter showed the capability of a commercial dilute Cu(0.5 at% Ni) foil for growing a large-area bilayer graphene film and suggests a possibility of growing a wafer-scale bilayer graphene film if a dilute Cu(0.5 at% Ni) foil has no Cu(111) surface.

Bibliography

1. W. Liu, S. Kraemer, D. Sarkar, H. Li, P.M. Ajayan, K. Banerjee, Controllable and rapid synthesis of high-quality and large-area bernal stacked bilayer graphene using chemical vapor deposition, Chemistry of Materials. 26 (2014) 907-915.

2. E.C. Viljoen, J. du Plessis, Surface segregation measurements via the linear programmed heating method: Part B-Experimental and results, Surface Science. 468 (2000) 27-36.

3. J. du Plessis, Solid State Phenomena - Part B, Volume 11 (Diffusion and Defect Data), Sci-Tech Publications, Brookfield USA, 1990.

4. W. Fang, A.L. Hsu, R. Caudillo, Y. Song, A.G. Birdwell, E. Zakar, et al., Rapid identification of stacking orientation in isotopically labeled chemical-vapor grown bilayer graphene by Raman spectroscopy, Nano Letters. 13 (2013) 1541-1548.

5. S. Chen, W. Cai, R.D. Piner, J.W. Suk, Y. Wu, Y. Ren, et al., Synthesis and characterization of large-area graphene and graphite films on commercial Cu-Ni alloy foils, Nano Letters. 11 (2011) 3519-3525.

CHAPTER 6

A dilute Cu(Ni) alloy for synthesis of AB-stacked bilayer graphene

6.1 Introduction

This chapter discusses the doping of an annealed Cu foil from Alfa Aesar for graphene growth with a small concentration of Ni (≈0.5 at%) to obtain a dilute Cu(0.5 at% Ni) foil for synthesis of high-quality large-area or wafer-scale AB-stacked bilayer graphene films using AP-CVD. This includes the results obtained from the characterization of substrates (both un-doped and Ni doped Cu foils) and bilayer graphene films obtained from un-doped and Ni doped Cu foils. The capability of a Ni doped Cu foil for growing a large-area bilayer graphene film compared to un-doped Cu foil using AP-CVD is demonstrated in this chapter. The publication which details the experimental procedure and results discussed in this chapter is presented at the end of the chapter.

In Cu(Ni) foil, the maximum surface concentration of Ni that would be segregated during CVD graphene growth at a growth temperature of interest is determined by Ni bulk concentration and the segregation energy, as discussed using Langmuir-McLean equation in chapter 1. For Ni bulk concentration in the range of 0.1 to 0.9 at% (in the dilute concentration range), the maximum surface concentration of Ni in dilute Cu(Ni) foil is in the range of 1 to <5 at% in the temperature range of 900-1000 °C. In this surface concentration and temperature range, the Ni bulk concentration (0.5 at%) and the CVD growth temperature (≈1000 °C) are such that the maximum surface concentration of Ni would be ≈3 at% during CVD graphene growth.

In this chapter, an annealed Cu foil from Alfa Aesar for graphene growth was doped with a small concentration of Ni (≈0.5 at%) to obtain a dilute Cu(Ni) foil. The doping of this foil was motivated by its continuous crystallographic surface composed of a single (001) orientation which is known to grow multilayer graphene domains [1-4]. In addition, since this foil is manufactured for graphene growth it was found to be of interest in this study. After Ni doping, bilayer graphene films were synthesized simultaneously on both un-doped and Ni doped Cu foils at 920 °C using AP-CVD and for a high-quality graphene, the films were synthesized at 1000 °C. After growth, the graphene films were transferred onto 300 nm thick SiO_2/Si substrates and TEM Cu grids by spin-coating a thin layer of PMMA on the as-grown graphene films. The substrates (both un-doped and Ni doped Cu foils) and bilayer graphene films transferred onto SiO_2 were characterized.

6.2 Results and discussions

PIXE maps of Ni (Ni $K\alpha 1$) distribution in foils suggest that Ni is uniform throughout foils. EBSD map of Cu foil showed a continuous crystallographic surface composed of a single (001) orientation. TOF-SIMS depth profiles obtained from both un-doped and Ni doped Cu foils showed the presence of impurities in the foils. Ni showed higher intensity ratio in the surface of a Ni doped Cu foil compared to the bulk suggesting precipitation/segregation capability of Ni.

Figure 6.1(a) and (b) show the Raman optical microscope images of graphene films obtained at a growth temperature of 920 °C on Cu and Ni doped Cu(0.46 at% Ni) foils respectively, and figure 6.1(c) and (d) show the images of graphene films obtained at growth temperature of 1000 °C on Cu and Cu(0.46 at% Ni) foils respectively. At a growth temperature of 920 °C, a bilayer graphene obtained on Cu foil shows larger areas of monolayer graphene compared to bilayer graphene obtained on Cu(0.46 at% Ni) foil suggesting higher bilayer coverage rate for Cu(Ni) foil surface. In addition, the films show low-quality graphene (high D peak intensity). However, at a growth temperature of 1000 °C the films show high-quality graphene. At 1000 °C, a bilayer graphene obtained on Cu foil show discrete bilayer graphene domains with an average lateral size of ≈10 μm and >90 % coverage. In contrast to Cu foil, a bilayer graphene obtained on Cu(0.46 at% Ni) foil shows a large-area (or wafer-scale) bilayer graphene and suggests dilute Cu(0.46 at% Ni) foil surface reached ≈98 % coverage with approximately 30×30 mm^2 area (substrate size) of uniform bilayer graphene.

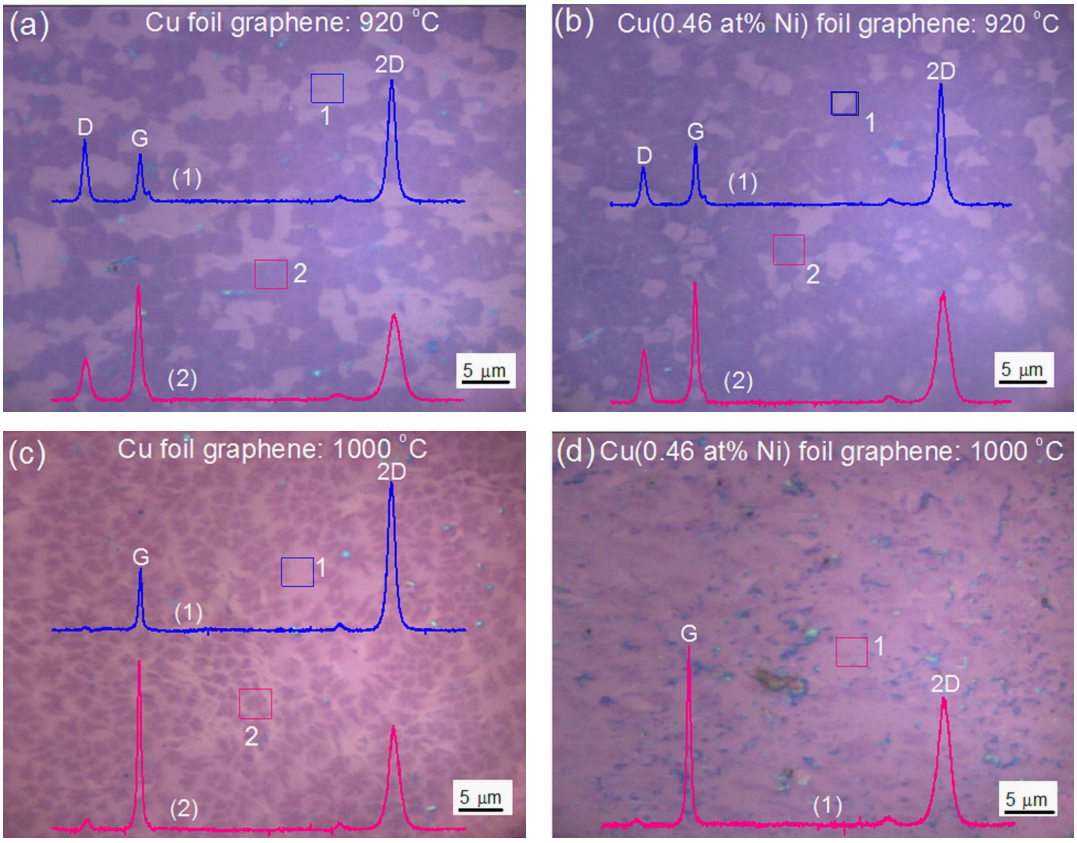

Figure 6.1: The Raman optical microscope images of graphene films obtained on (a) Cu and (b) Cu(0.46 at% Ni) foils at 920 °C and on (c) Cu and (d) Cu(0.46 at% Ni) foils at 1000 °C. The inset: Raman spectra corresponding to areas indicated as box 1 and 2.

At a growth temperature of 920 °C, a bilayer graphene film obtained on a Cu foil showed a high sheet resistance (380 Ω/sqr) compared to that obtained on Cu(Ni) foil (315 Ω/sqr) suggesting a difference in bilayer coverage. For graphene obtained on Cu(Ni) foil, the selected area electron diffraction suggested bilayer graphene with AB stacking.

6.3 Publication

This section present an article published in AIP: Journal of Applied Physics, 119, 015306 (2016). The publication details the experimental procedure and results discussed in this chapter. In the publication, figure 3, PIXE mapping of Ni $K\alpha 1$ shows Ni distribution in Cu and Cu(0.46 at% Ni) foils and PIXE mapping of Cu $K\alpha 1$ shows Cu in Cu grid. TOF-SIMS depth profiles, figure 5, are presented in sputter times since an actual sputter rate is not known.

JOURNAL OF APPLIED PHYSICS **119**, 015306 (2016)

A dilute Cu(Ni) alloy for synthesis of large-area Bernal stacked bilayer graphene using atmospheric pressure chemical vapour deposition

M. J. Madito,[1] A. Bello,[1] J. K. Dangbegnon,[1] C. J. Oliphant,[2] W. A. Jordaan,[2]
D. Y. Momodu,[1] T. M. Masikhwa,[1] F. Barzegar,[1] M. Fabiane,[1,3] and N. Manyala[1,a)]
[1]*Department of Physics, Institute of Applied Materials, SARCHI Chair in Carbon Technology and Materials, University of Pretoria, Pretoria 0028, South Africa*
[2]*National Metrology Institute of South Africa, Private Bag X34, Lynwood Ridge, Pretoria 0040, South Africa*
[3]*Department of Physics, National University of Lesotho, P.O. Roma 180, Lesotho*

(Received 13 August 2015; accepted 26 December 2015; published online 7 January 2016)

A bilayer graphene film obtained on copper (Cu) foil is known to have a significant fraction of non-Bernal (AB) stacking and on copper/nickel (Cu/Ni) thin films is known to grow over a large-area with AB stacking. In this study, annealed Cu foils for graphene growth were doped with small concentrations of Ni to obtain dilute Cu(Ni) alloys in which the hydrocarbon decomposition rate of Cu will be enhanced by Ni during synthesis of large-area AB-stacked bilayer graphene using atmospheric pressure chemical vapour deposition. The Ni doped concentration and the Ni homogeneous distribution in Cu foil were confirmed with inductively coupled plasma optical emission spectrometry and proton-induced X-ray emission. An electron backscatter diffraction map showed that Cu foils have a single (001) surface orientation which leads to a uniform growth rate on Cu surface in early stages of graphene growth and also leads to a uniform Ni surface concentration distribution through segregation kinetics. The increase in Ni surface concentration in foils was investigated with time-of-flight secondary ion mass spectrometry. The quality of graphene, the number of graphene layers, and the layers stacking order in synthesized bilayer graphene films were confirmed by Raman and electron diffraction measurements. A four point probe station was used to measure the sheet resistance of graphene films. As compared to Cu foil, the prepared dilute Cu(Ni) alloy demonstrated the good capability of growing large-area AB-stacked bilayer graphene film by increasing Ni content in Cu surface layer. © *2016 AIP Publishing LLC*.
[http://dx.doi.org/10.1063/1.4939648]

I. INTRODUCTION

Graphene as a two-dimensional structured carbon material has attracted many researchers due to its fascinating properties and potential applications.[1–4] However, its zero band gap restricts some of its applications.[1] One of the approaches of opening the band gap in graphene is synthesizing a Bernal (AB) stacked bilayer graphene that is known to exhibit a tunable band gap of up to 0.25 eV.[2–4] Amongst the common approaches used to produce AB-stacked bilayer graphene films are the chemical vapour deposition (CVD) which has attracted tremendous research activities due to its ability to produce wafer-scale high-quality graphene films with a controllable number of layers.[5–7] In CVD graphene growth, metal substrates are used to promote graphene synthesis by a surface growth mechanism or by segregation (precipitation).[8,9] Metal substrates commonly used for CVD graphene growth include nickel (Ni) and copper (Cu).[8,9]

Nevertheless, for a CVD bilayer graphene, these metal substrates have limitations or challenges. For instance, a bilayer graphene film obtained on Ni has large traces of multi-layers, and on Cu only fraction of the bilayer graphene film has AB stacking order.[4,9,10] Interestingly, a binary Cu-Ni metal alloy has shown a capacity of growing a large-area AB-stacked bilayer graphene film in comparison to pure Cu.[5,6] This was demonstrated by Chen *et al.*,[6] using commercial Cu-Ni alloy foils with 31.0 wt. % Ni, 67.8 wt. % Cu composition, and Liu *et al.*,[5] using Cu(1200 nm)/Ni(400 nm) thin films deposited onto SiO_2 substrate. The good capability of Cu-Ni alloy of growing a large-area AB-stacked bilayer graphene film as compared to Cu demonstrated a lower hydrocarbon decomposition rate (i.e., weak supply of active carbon species which materialise into graphene) of Cu surface at an optimized hydrocarbon pressure in CVD graphene growth process.[5] It is believed that active impurity atoms in Cu segregate to the Cu surface during annealing and enhance the hydrocarbon decomposition rate of Cu,[4] but the level of enhancement is related to the surface concentration of the segregated impurity atoms and the atom-atom interaction energy. In addition, as compared to Cu, Ni has higher carbon solubility and decomposition rate of methane (i.e., strong supply of active carbon species which materialise into graphene), hence it enhances the hydrocarbon (methane) decomposition rate in Cu-Ni alloy during CVD graphene growth.[5] To tune the hydrocarbon decomposition rate of Cu by doping Cu with Ni, the maximum surface concentration of Ni that will be segregated during CVD graphene growth is important and is determined by the concentration of Ni in Cu (i.e., Ni bulk concentration) and the segregation driving energy (segregation energy).[11] Liu *et al.*[5] have shown that

a)Author to whom correspondence should be addressed. Electronic mail: ncholu.manyala@up.ac.za

Cu(1200 nm)/Ni(400 nm) films having a surface layer composition of >97 at. % Cu and <3 at. % Ni grow a wafer-scale AB-stacked bilayer graphene in CVD. Now, for a Cu foil to have a surface layer composition of about 97 at. % Cu and 3 at. % Ni through Ni segregation during graphene growth in the temperature range of 900–1000 °C, it should have about 0.5 at. % Ni bulk concentration and Ni segregation driving energy of about 30 kJ/mol. Consequently, we propose the use of homogeneous dilute Cu(0.5 at. % Ni) foil for large-area AB-stacked bilayer graphene growth in CVD. Dilute Cu(Ni) foils for CVD multilayer graphene growth have not received much attention. Nonetheless, studies have used pure Cu foils,[8] Cu/Ni thin films,[5,9,13] and non-dilute commercial Cu-Ni foils (i.e., Cu(88.0 wt. %)-Ni(9.9 wt. %)[14] and Cu(67.8 wt. %)-Ni(31.0 wt. %)[6]) in CVD for graphene growth. A bilayer graphene film obtained on pure Cu foil is known to have islands of bilayer with monolayer background and significant fraction of non-AB stacking,[10] on Cu(1200 nm)/Ni(400 nm) thin films is known to grow over a large-area with AB stacking, and for non-dilute Cu-Ni foils a CVD graphene growth is known to dominate from segregation/precipitation process, which could lead to a variation in the uniformity of the bilayer graphene over large areas and a significant fraction of non-AB stacking in bilayer graphene.[14]

Despite the previous works on growth of AB-stacked bilayer graphene films using CVD system,[6,9–15] a controllable CVD growth of a continuous large-area high-quality AB-stacked bilayer graphene remains a challenge for different laboratories with CVD set-up for graphene growth. This work is aimed at preparation and analysis of dilute Cu(Ni) foils for growth of large-area AB-stacked bilayer graphene using atmospheric pressure chemical vapour deposition (AP-CVD).

II. EXPERIMENTAL

A. Thermal deposition and annealing

Few Cu foil samples (~30 × 30 mm^2) (to be prepaid the same way) were obtained from a high purity (99.8%) 25 μm thick annealed Cu foil from Alfa Aesar. Samples were immersed in aqueous nitric acid for 30 s to dissolve surface impurities on foils, then in distilled water followed by an ultra-sonic bath with acetone and isopropanol and dry-blowing with N_2 to remove water residues.[16] The cleaned Cu foils were loaded in a vacuum chamber of a thermal evaporator for Ni deposition. A thin layer of high purity (99.99%) Ni (116 nm) was thermally evaporated onto Cu foil sample at a rate of 1 Å/s in a vacuum chamber with a pressure of 3×10^{-3} Pa. The deposition of a thin layer of Ni was repeated on extra three Cu foil samples. After evaporation, Cu/Ni samples were loaded in AP-CVD quartz tube under argon atmosphere. Samples were annealed at 950 °C for 8 h with argon flow rate of 500 sccm to obtain a homogeneous distribution of Ni concentration in Cu foils. For the 950 °C and 8 h annealing conditions, the concentration distribution (C) of Ni in Cu foil with a thickness l and the surface located at $x = 0$, where the Ni source layer with a thickness h is restricted, was calculated in terms of diffusion depth x using Fick's solution for finite systems (see Fig. 1(a))[17]

$$C = \frac{1}{2} C_0 \sum_{n=-\infty}^{\infty} \operatorname{erf}\left(\frac{h + 2nl - x}{2\sqrt{Dt}}\right) + \operatorname{erf}\left(\frac{h - 2nl + x}{2\sqrt{Dt}}\right), \quad (1)$$

where C_0 is the initial concentration of Ni on the Cu surface, $D = D_0 \exp(-Q/RT)$ is the diffusion coefficient (D_0 is the pre-exponential factor, Q is the activation energy ($D_0 = 7.0 \times 10^{-5}$ m^2/s and $Q = 225.0$ kJ/mol for Ni diffusion in Cu[18]), R is the gas constant, and T is the temperature).

The annealing process yielded Ni concentration distribution in 25 μm thick Cu foil that is 99.8% uniform (see Fig. 1(a) calculation for a Cu foil sample 1 in Table I). After annealing at 950 °C, a 10.0 kV primary electron beam in scanning electron microscopy (SEM) was scanned across the Cu foil surface to obtain its micro-structural image as shown in Fig. 1(b) and shows the average grain size of 35.7 μm. Before and after deposition of the Ni films onto the Cu foils, the masses of the samples were measured with Denver instrument balance (model SI-234) with repeatability or standard deviation of $< \pm 0.1$ mg. After annealing, the masses of the samples were measured again and found to have increased, and from Ni masses the concentrations were found as listed in Table I. An ICP-OES (inductively coupled plasma optical emission spectrometry) spectrometer was used to confirm the Ni concentrations listed in Table I. For

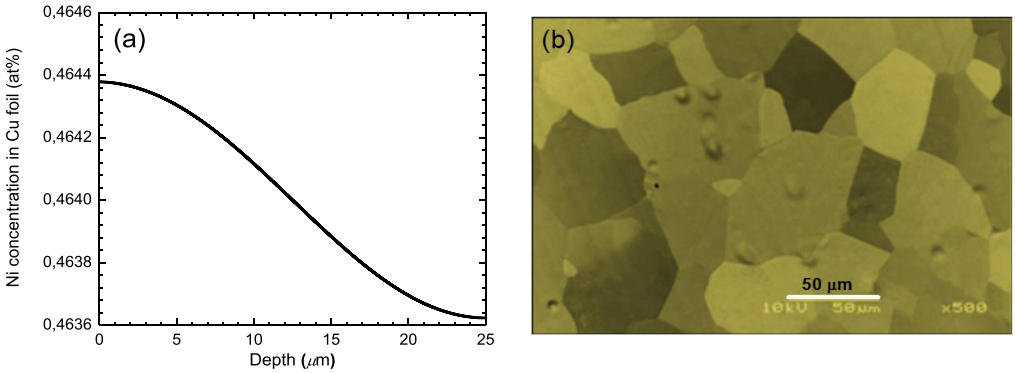

FIG. 1. (a) Ni concentration distribution as a function of diffusion depth in 25 μm thick Cu foil. (b) The micro-structure image of annealed Cu foil surface.

TABLE I. The masses of the samples and Ni added in Cu foils and the corresponding Ni concentrations.

Cu foils samples	Cu foils masses pre-deposition (±0.1 mg)	Cu foils masses after deposition (±0.1 mg)	Cu foils masses after annealing (±0.1 mg)	Ni masses in Cu foils after annealing (±0.1 mg)	Ni doped concentration (at. %)
1	285.4	286.9	286.6	1.2	0.455
2	268.1	269.3	269.6	1.5	0.606
3	262.0	263.3	263.4	1.4	0.579
4	251.0	252.2	252.5	1.5	0.647

instance, a piece of a Cu foil with a mass of 47.1 mg was cut from a Cu foil sample 1 and analysed with an ICP-OES spectrometry and was found to have a Ni amount with a mass of 0.199 mg (equivalent to 0.457 at. %).

Ni doped (i.e., Cu(0.46 at. % Ni, sample 1 in Table I)) and un-doped Cu foils were loaded in AP-CVD at a centre of a quartz tube for bilayer graphene growth (see a schematic view of AP-CVD setup in Fig. 2(a)). Figure 2(b) shows a temperature profile of AP-CVD measured directly inside quartz tube centre located at the furnace centre with external chromel–alumel thermocouple (type K), and the measured temperature was calibrated in terms of true sample temperature for graphene growth.

B. Bilayer graphene synthesis and transfer onto SiO_2

Pre-growth of graphene, Cu and Cu(0.46 at. % Ni) foils were annealed under Ar (300 sccm) and H_2 (100 sccm) flow for 60 min (see Fig. 2(b)) to obtain a clean and uniform surface. After annealing, the graphene was synthesised at 920 °C from a mixture of gases, Ar (300sccm): H_2 (9 sccm): CH_4 (10 sccm)[19] for exactly 15 min. Immediately after growth, the CH_4 flow was stopped and samples were rapidly cooled down by pushing the quartz tube to the cooler region of the furnace. At less than 80 °C, samples were off loaded from AP-CVD quartz tube and transferred onto 300 nm thick SiO_2/Si substrates.

In the transfer, a thin layer of poly methyl methacrylate (PMMA) (average Mw ~996 000 by gel permeation chromatography (GPC)) dissolved in chlorobenzene with a concentration of 46 mg/ml was spin-coated on the as-grown graphene on both Cu and Cu(Ni) foils at 3000 rpm for 30 s. PMMA/graphene/(Cu and Cu(Ni)) foil samples were placed in 1 M iron nitrate to etch off Cu and Cu(Ni).[5,6] PMMA/graphene films floated in the etchant after the foils were etched. These films were then transferred using a polyethylene terephthalate (PET) to the 5% hydrochloride (HCl), then, deionized (DI) water to dissolve the iron nitrate,[5] and subsequently the PMMA/graphene films were transferred onto SiO_2 substrates. Finally, PMMA was removed by placing samples in an acetone bath for 6 h.[20]

C. Characterizations

Proton-induced X-ray emission (PIXE) was used to map Ni distribution in Cu and Cu-Ni foils. An additional high purity (99.999%) Cu grid was used for mapping Cu signal. A beam energy of 3.0 MeV and target current of 200 pA were used for analysis. Electron backscatter diffraction (EBSD) analysis of a Cu foil was performed in a LEO 1525 field-emission gun scanning electron microscope at an acceleration voltage of 25 kV using the Oxford INCA crystal software. The X-ray diffraction (XRD) pattern of Cu foil was collected using an XPERT-PRO diffractometer (PANalytical BV, Netherlands) with reflection geometry at 2θ values ranging from 30° to 70° with a step size of 0.01°. Co $K1\alpha$ radiation with a wavelength of 1.7890 Å was used as the X-ray source, and a tube was operated at 50 kV and 30 mA. Time-of-flight secondary ion mass spectroscopy (TOF-SIMS) depth profiling was performed on Cu and Cu-Ni foils using the TOF-SIMS5 Ion-TOF system. The mass spectra were calibrated to the following mass peaks in positive mode: Al, Na, Ni, Fe, Si, C, C_2H_5, K, and Cu. For analysis, a Ga^+ primary ion beam was used, and for sputtering a Cs^+ ion beam was used. The analyses were carried out over an area of $500 \times 500\ \mu m^2$ and sputter gun area of $1000 \times 1000\ \mu m^2$ and time interval of 6 s. The graphene

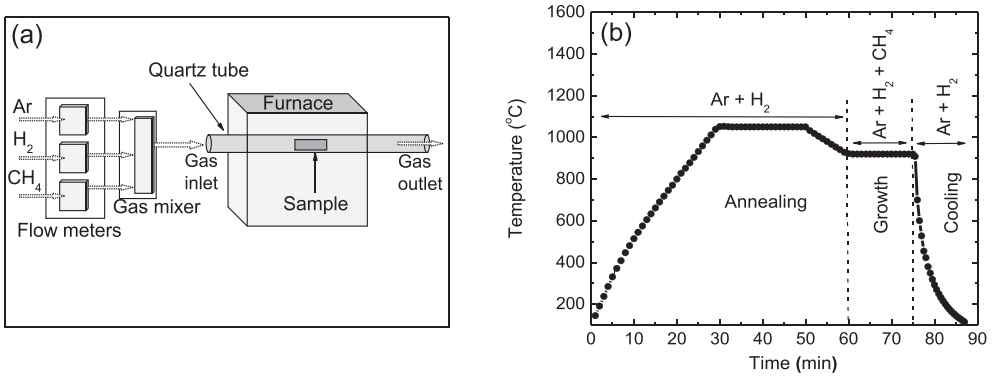

FIG. 2. (a) A schematic view of AP-CVD setup. (b) A temperature profile of AP-CVD measured directly inside quartz tube centre.

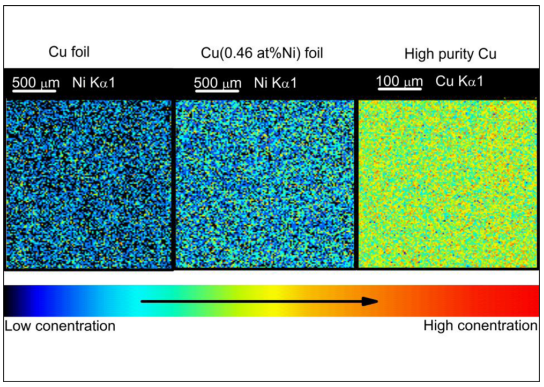

FIG. 3. PIXE maps of Ni distribution in Cu, Cu(0.46 at. % Ni) foil and high purity Cu grid.

films transferred onto SiO_2 substrates were characterized with WITec Alpha 300 micro-Raman imaging system with 532 nm excitation laser. Raman spectra were measured at room temperature with the laser power set below 2 mW in order to minimize heating effects. The graphene film sheet resistance measurements were carried out in ambient conditions (i.e., in air at room temperature and pressure) using a Signatone four point probe station. A DC current in the range of 0–1.7 mA was used. The electron diffraction pattern of prepared graphene film was obtained with high-resolution transmission electron microscopy (HRTEM) (Jeol JEM-2100F Field Emission Electron Microscope, with a maximum analytical resolution of 200 kV and a probe size under 0.5 nm).

III. RESULTS

A. PIXE, EBSD, and XRD analysis of Cu and Cu(Ni) foils

Figure 3 shows PIXE maps for Ni distribution in Cu, Cu(0.46 at. % Ni) foil and high purity Cu grid. A PIXE map for Cu(0.46 at. % Ni) foil shows high Ni concentration as compared to that of Cu foil, as expected. PIXE maps suggest that Ni distribution is uniform through foils. Figure 4(a) shows an EBSD map of Cu foil which shows a continuous crystallographic surface composed of (001) orientation in accordance with the inverse pole figure orientation component colouring scheme (the bottom inset to Fig. 4(a)), and the top inset to Fig. 4(a) shows the SEM image of a Cu foil surface that is mapped out with an EBSD. In Fig. 4(a), the scale bar is 30 μm which is about the same order of magnitude as the average grains size of the foil (i.e., 35.7 μm); hence, few grains of a Cu foil are expected to be captured within the EBSD image. Therefore, an EBSD map shows that annealed Alfa Aesar Cu foil used for graphene growth has a preferential (001) surface orientation. The EBSD data are supported by XRD data (Fig. 4(b)) showing a single diffraction intensity peak of Cu(002) orientation which is parallel to Cu(001) orientation. Nonetheless, an XRD data are not restricted to surface information, but rather bulk information hence the data are not used to obtain surface grains crystallographic information.

B. TOF-SIMS analysis of Cu and Cu(Ni) foils

Figure 5 shows depth profiles of Cu and Cu(0.46 at. % Ni) foils after annealing under conditions similar to that of graphene growth, where some of the impurities (Al, Na, Ni, Fe, Si, C_2H_5, and K) in Cu can be seen in surface and bulk regions of the samples. *In Cu foil*: Fig. 5(a) depth profile shows the presence of impurities in the bulk, and some of these impurities have higher intensities in the surface region of a foil. Though the impurities show high intensities in TOF-SIMS, they do not necessarily show high surface concentrations, since they have strong signals in TOF-SIMS. Interestingly, Ni impurity with almost zero intensity ratios in the bulk shows higher intensity ratio in the surface region and that demonstrates Ni surface precipitation/segregation capability. Similarly, *in Cu(0.46 at. % Ni) foil*: Fig. 5(b) depth profile shows the presence of impurities in both bulk and surface regions of a foil. In contrast to Cu foil, Ni has higher intensity ratio in the bulk and surface region of a foil and that demonstrates an increase in Ni bulk concentration

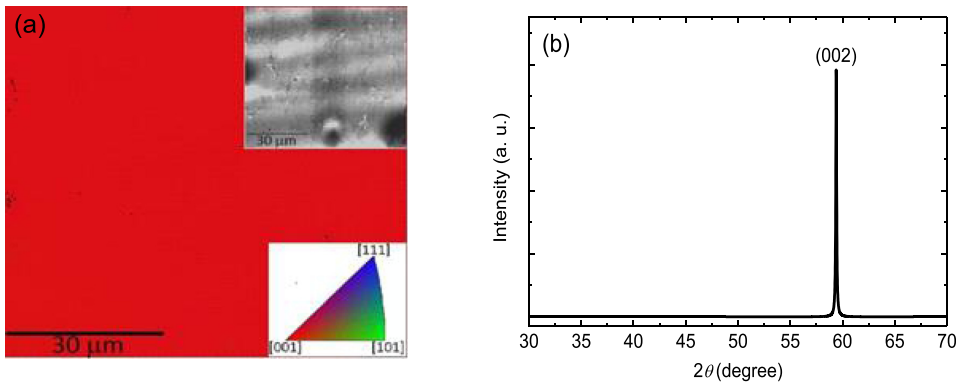

FIG. 4. (a) An EBSD map of high temperature annealed Alfa Aesar Cu foils for graphene growth (the top-right inset is SEM image of an area mapped out with EBSD, and the bottom-right inset is the EBSD map corresponding inverse pole figure orientation component colouring scheme). (b) XRD data of the annealed Cu foil.

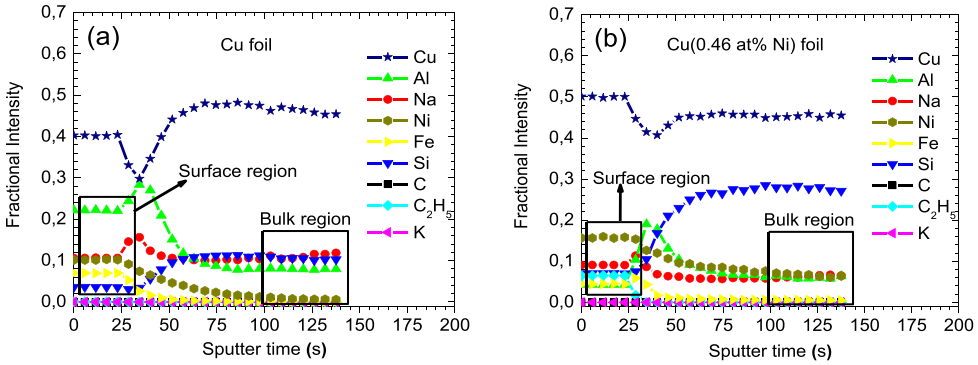

FIG. 5. TOF-SIMS depth profiles of annealed (a) Cu and (b) Cu(0.46 at. % Ni) foils.

due to Ni doped concentration. Also, Si has higher intensity ratio in the bulk of a Cu(0.46 at. % Ni) foil, which does not necessarily mean that Si has higher bulk concentration than Ni, but rather that Si has strong signals in TOF-SIMS. Nevertheless, compared to Cu foil, a higher Si intensity ratio could suggest that during Ni doping process of a Cu an extremely small amount of Si probably from the instrument was introduced as an impurity into the foil, or a measured Si signal was enhanced by ion sputtering during analysis. In both foils, all impurities are expected to have bulk concentrations in the order of few parts per million ($\leq$10 ppm) and in Ni doped foil, Ni has ~5000 ppm (~0.5 at. %). Nevertheless, the TOF-SIMS secondary-ion yield depends strongly on the matrix effects (target chemical and electronic character).

C. Raman characterization of graphene films

Figure 6(a) shows the average spectra of Raman spectra acquired from a 30 μm^2 area of graphene films obtained on Cu and Cu(0.46 at. % Ni) foils and transferred onto 300 nm thick SiO_2/Si substrates. The similarity in these average Raman spectra suggests that graphene films obtained on Cu and Cu(0.46 at. % Ni) foils are similar particularly in the number of graphene layers present in the sample. The main features that are observable are labelled, namely, the G-band mode at ~1590 cm^{-1}, the 2D-band mode at ~2690 cm^{-1}, and the D-band mode at ~1350 cm^{-1} (also known as a disorder-induced band).[1,21] A schematic view in Fig. 6(b) shows that the G-band originates from a normal first-order Raman scattering process in graphene, the 2D-band from a second-order process (double resonance Raman process) that involves two in-plane transverse optical mode (iTO) phonons near the *K* point, and the D-band from a second-order process that involves one iTO phonon and one defect.[1,21] The Raman process can also give rise to the triple-resonance Raman process, which might explain a more intense 2D-band (relative to the G-band) in monolayer graphene films.[1] By observing the differences in the 2D-band frequency and line shape, the number of graphene layers contained in graphene samples can be obtained and also the stacking order or interlayer interactions in few layers graphene sample.[21,22]

Figures 7(a) and 7(b) Raman data show the 2D peaks Full width at half maximum (FWHM) mapping and the 2D to G peaks intensity ratio (I_{2D}/I_G) mapping, respectively, for graphene films obtained on Cu and Cu(0.46 at. % Ni) foils. *Cu foil graphene*: Fig. 7(a) shows 2D peaks FWHM map with the distribution of the FWHMs in the range of 34–70 cm^{-1}, and in Fig. 7(b) the I_{2D}/I_G peaks intensities ratio is in the range of 0.9–3.0, though Fig. 7(b) shows a range of 0.8–4.4. The symmetric 2D peaks with FWHM in the range

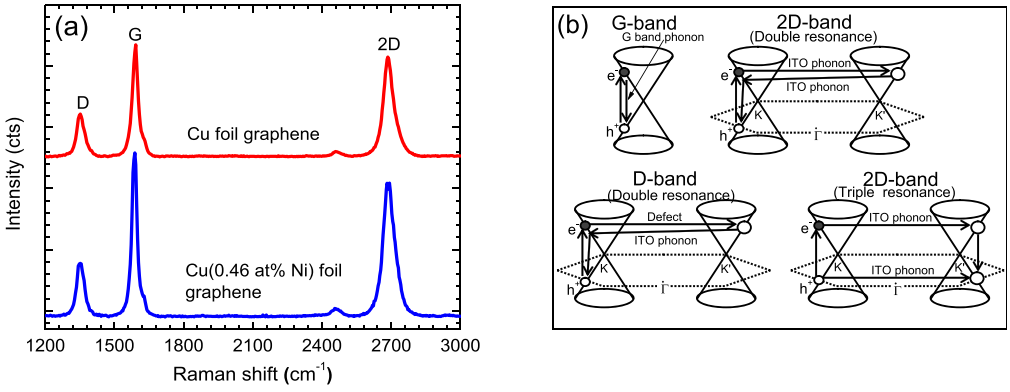

FIG. 6. (a) The average Raman spectra of spectra acquired from a 30 μm^2 area of graphene films obtained on Cu and Cu(0.46 at. % Ni) foils and transferred onto SiO_2/Si substrates. (b) A schematic view of Raman scattering processes in graphene film.[1]

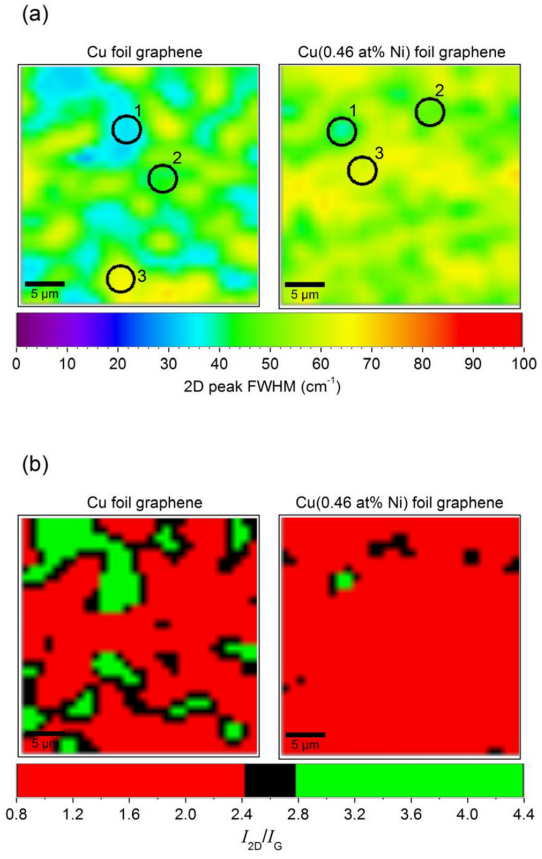

FIG. 7. Raman data: (a) The 2D peaks FWHM maps and (b) the 2D to G peaks intensity ratio (I_{2D}/I_G) for graphene films obtained on Cu and Cu(0.46 at. % Ni) foils.

of 28–37 cm^{-1} and the I_{2D}/I_G ratio $>$ 2.5 features demonstrate characteristics of monolayer graphene, and the 2D peaks with FWHM in the range of 38–70 cm^{-1} and the I_{2D}/I_G ratio in the range of 0.5 to $<$2.5 features demonstrate characteristics of bilayer graphene.[5] Therefore, the bilayer graphene film obtained on Cu foil consists of significant areas of mono and bilayer graphene. *Cu(0.46 at. % Ni) foil graphene*: Fig. 7(a) shows 2D peaks FWHM map with the distribution of the FWHMs is in the range of 37–65 cm^{-1} and the I_{2D}/I_G ratio (Fig. 7(b)) in the range of 0.9–2.8. These features demonstrate characteristics of bilayer graphene, and the 2D peaks with FWHM of 37 cm^{-1} and the I_{2D}/I_G ratio of 2.8 features demonstrate traces of monolayer graphene present in the sample.

As observed in this study, the 2D peaks with the distribution of the FWHMs in the range of approximately 25–70 cm^{-1} and the I_{2D}/I_G peaks intensities ratio in the range of approximately 0.8–4.4 correspond to monolayer and bilayer graphene features. In accordance, a tri or multilayer graphene has 2D peaks with higher FWHMs ($>$70 cm^{-1}) and lesser I_{2D}/I_G peaks intensities ratio ($<$0.8).[1,5]

Figure 8 Raman data show the D to G peaks intensity ratio (I_D/I_G) for graphene films obtained on Cu and Cu(0.46 at. % Ni) foils. The graphene films show an I_D/I_G ratio of about 0.5 and suggest that the prepared graphene films are partially defective (have higher D peak intensity relative to the G peak). High D peak intensity shows the presence of impurities or defects in the translational symmetry of the carbon material's lattice, which could be observed under electron diffraction measurements.

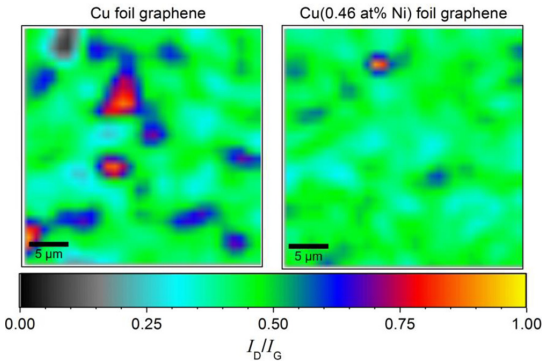

FIG. 8. Raman data: The D to G peaks intensity ratio (I_D/I_G) for graphene films obtained on Cu and Cu(0.46 at. % Ni) foils.

Furthermore, the 2D-band mode for monolayer graphene is known to show a single Lorentzian feature.[1] In AB-stacked bilayer graphene, the electronic band is known to split into two components, namely, two conduction and two valence bands where the upper (lower) and lower (upper) branches of the valence (conduction) band are labelled as $\pi_1(\pi_1^*)$ and $\pi_2(\pi_2^*)$, respectively (see a schematic view in Fig. 9(a)).[1,22] The electronic band split results into the splitting of the phonon bands into two components.[22] However, there is only one main double resonance Raman process contributing to the 2D-band. In this double resonance process with respect to the bands split, the electron–phonon scattering occurs with two phonons with symmetries T_1 and T_2. For a T_1 phonon, the scattering can occur between the π_1 and π_1^* or π_2 and π_2^* bands of the same symmetry.[1] For a T_2 phonon, the scattering occurs between bands of different symmetries (i.e., π_1 and π_2^*). T_1 and T_2 phonon processes are labelled as P_{ij}, where i (j) denote an electron scattered from (to) each conduction band $\pi_{i(j)}^*$ (demonstrated in Fig. 9(a)). The P_{11}, P_{22}, P_{12}, and P_{21} scattering processes come from an iTO phonon and give rise to four peaks in the Raman 2D peak spectrum with peak frequencies at approximately 2655, 2680, 2700, and 2725 cm^{-1}, respectively, and FWHMs equal that of monolayer graphene 2D peak.[1] These four peaks are normally fitted as four Lorentzians to 2D peak to demonstrate AB-stacked bilayer graphene.[5,10,22]

The Raman spectra from three spots marked with circles 1, 2, and 3 in Fig. 7(a) are shown in Figs. 9(b) and 9(c). *Cu foil graphene*: In Fig. 9(b), spectrum 1 (from circle 1) has a 2D peak that is single Lorentzian and that shows monolayer graphene. Spectrum 2 (from circle 2) has a 2D peak with larger FWHM of 43 cm^{-1} and is fitted with four Lorentzians each with FWHM of 31 cm^{-1} corresponding to that of a monolayer graphene.[5] The fits demonstrate characteristics of

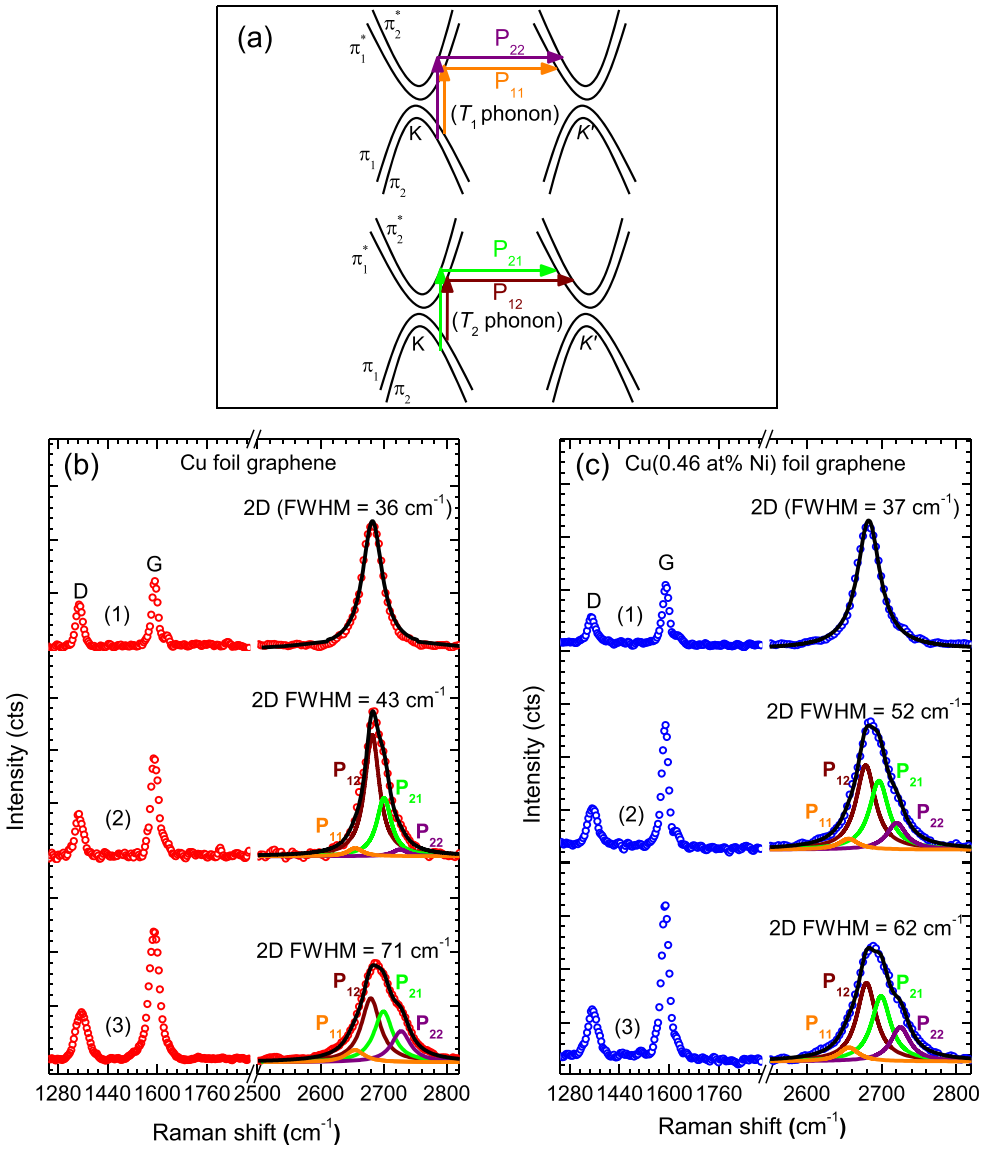

FIG. 9. (a) Schematic view of the electron dispersion of bilayer graphene near the K and K' points showing both π_1 and π_2 bands. The resonance Raman processes are indicated as P_{11}, P_{22}, P_{12}, and P_{21}.[1] (b) and (c) The Raman spectra from three different spots of graphene films obtained on Cu and Cu(0.46 at. % Ni) foils as indicated in Fig. 7(a), respectively.

bilayer graphene that is possibly non-AB stacked due to large differences in relative amplitudes of the Lorentzians. In exfoliated AB-stacked bilayer graphene, the amplitudes of the four Lorentzians are relative, two of which have higher relative intensities (almost the same intensity) than the other two.[22] Nevertheless, the relative amplitudes of the Lorentzians are known to depend on the laser energy,[1] which was maintained constant in this work. Similarly, in spectrum 3 (from circle 3), the 2D peak has larger FWHM of 71 cm^{-1} and is fitted with four Lorentzians each with FWHM of 31 cm^{-1}. The fits demonstrate characteristics of AB-stacked bilayer graphene, since the amplitudes of the four Lorentzians are relative, two of which have higher relative intensities (almost the same intensity) than the other two.[1,10,22] *Cu(0.46 at. % Ni) foil graphene*: In Fig. 9(c), spectrum 1 (from circle 1) shows single Lorentzian and that shows monolayer graphene. In Spectrum 2 (from circle 2) and 3 (from circle 3), 2D peaks show four Lorentzians each with FWHM of 31 cm^{-1}. The fits demonstrate characteristics of AB-stacked bilayer graphene. Similar to exfoliated AB-stacked bilayer graphene, the amplitudes of the four Lorentzians are relative.[22] Therefore, a graphene film obtained on Cu(0.46 at. % Ni) foil demonstrates features of a large-area AB-stacked bilayer graphene as compared to graphene film obtained on Cu foil.

Figures 10(a) and 10(b) show the Raman optical microscope images of graphene films obtained at a growth temperature of 920 °C on Cu and Cu(0.46 at. % Ni) foils, respectively, and Figs. 10(c) and 10(d) show the images of graphene films obtained at growth temperature of 1000 °C on Cu and Cu(0.46 at. % Ni) foils, respectively (the Raman spectra 1 and 2 (inset to the figures) correspond to areas 1 and 2 (boxes) in images). In Figs. 10(a)–10(c), the Raman spectra from lighter areas (box 1) correspond to that of a monolayer graphene and from darker areas (box 2) to that of bilayer graphene, and also the Raman spectrum in Fig. 10(d) corresponds to that of a bilayer graphene.[22] At a growth temperature of 920 °C, a bilayer graphene obtained on Cu foil shows larger-areas of incomplete bilayer graphene (i.e., monolayer graphene) as compared to bilayer graphene obtained on Cu(0.46 at. % Ni) foil. At a growth temperature of 1000 °C, a bilayer graphene obtained on Cu foil is also incomplete (has small-areas of bilayer on a monolayer graphene background), and bilayer graphene obtained on Cu(0.46 at. % Ni) foil shows a large-area (or wafer-scale) bilayer graphene with a much better or high-quality graphene. Clearly, the optical microscope images suggest that the bilayer graphene growth rate on Cu(0.46 at. % Ni) foil is higher as compared to Cu foil.

D. Four point probe graphene film sheet resistance

In a four-point probe/sheet resistance measuring system for thin films, two electrodes are used for sourcing a DC current, I (through the outer two probes) and the other two for measuring the corresponding voltage drop, V (see a schematic view, i.e., inset to Fig. 11(a)). Figure 11(a) shows the measured voltage drop for bilayer graphene films obtained on Cu and Cu(0.46 at. % Ni) foils and that was used to calculate the sheet resistance of graphene films (Fig. 11(b)) using an approach which relies on a geometric factor. A bilayer graphene film obtained on a Cu foil shows a high sheet resistance (380 Ω/sq) as compared to that obtained on Cu(0.46 at. % Ni) foil (315 Ω/sq) and that could be as a result of larger areas of incomplete bilayer graphene (i.e., monolayer graphene areas) present in a film obtained on Cu foil as compared to that obtained on Cu(0.46 at. % Ni) foil, since sheet resistance decreases with the increase in graphene film thickness or number of graphene layers.

E. Electron diffraction of graphene film obtained on Cu(Ni) foil

Figure 12(a) shows the TEM image of the graphene film obtained on Cu(0.46 at. % Ni) foil and transferred onto the

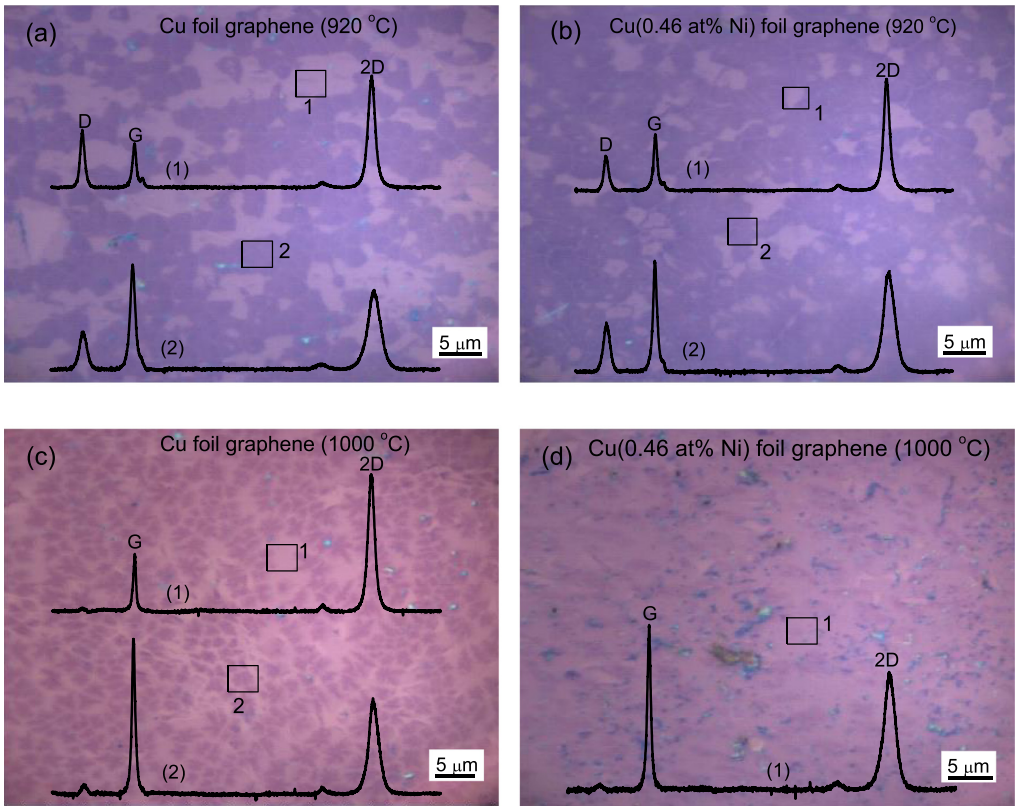

FIG. 10. The Raman optical microscope images (100×/0.90 objective) of graphene films obtained on (a) Cu and (b) Cu(0.46 at. % Ni) foils at 920 °C and on (c) Cu and (d) Cu(0.46 at. % Ni) foils at 1000 °C (transferred onto 300 nm thick SiO_2/Si substrate. The inset: Raman spectra corresponding to areas indicated as boxes 1 and 2.

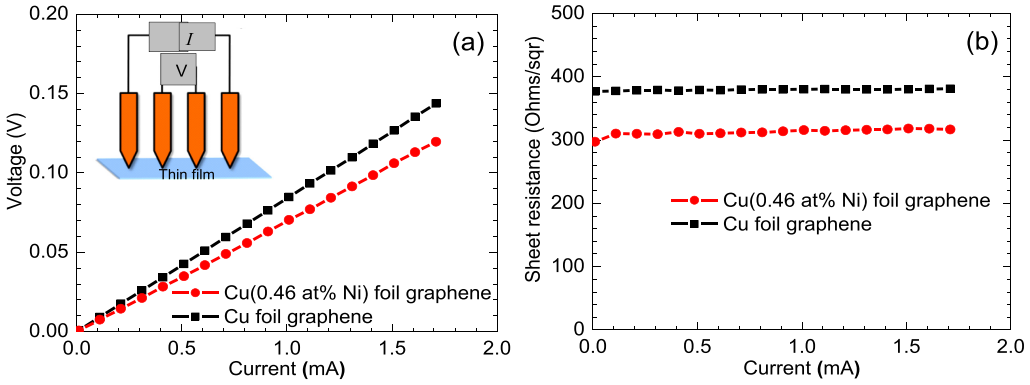

FIG. 11. (a) A four point probe measured voltage drop for bilayer graphene films obtained on Cu and Cu(0.46 at. % Ni) foils and (b) the calculated sheet resistance of the corresponding graphene films.

TEM Cu grid. Figure 12(b) inset shows the electron diffraction pattern that shows two sets of diffraction rings. The diffraction patterns were analysed with diffraction ring profiler (which was developed for phase identification in complex microstructures[23] to obtain the diffraction intensity profile (Fig. 12(b)) which shows two peaks at an inter-planar spacing of $d = 1.23$ Å (outer ring) and $d = 2.13$ Å (inner ring) corresponding to indices (1–210) and (1–110), respectively.[24] The relative intensity of the spots in the outer ring is twice that of the spots in the inner ring and that demonstrates AB stacking order.[10,22,24] The selected area electron diffraction method confirms the bilayer graphene with AB stacking and that corresponds to the bilayer graphene features observed from Raman data (i.e., 2D peaks FWHMs and peaks intensities ratio).

IV. DISCUSSION

In prepared dilute Cu(Ni) foils, Ni is uniformly distributed and the Ni content present in Cu foil (un-doped) is due to Cu foil impurities, since Alfa Aesar Cu foil for graphene growth with purity of 99.8% has about 0.2% unknown-impurities. Interestingly, Ni in Cu foils showed surface precipitation/segregation capability which is expected to enhance bilayer graphene coverage rate by enhancing the methane decomposition rate of Cu in CVD graphene growth. In CVD graphene growth on Cu foil, only the surface of a foil is important, since a growth is limited to surface reaction.[4] Meaning, in the early stage of graphene growth, the interaction between the hydrocarbon and the Cu substrate is important. Despite that the Cu-graphene interaction is relatively weak after growth, hence graphene is easily transferable from Cu substrate.[4,6] It is known that the surface orientation of the Cu foil influences the graphene growth rate and the number of layers in graphene film.[6] Studies have shown that the Cu(100) surface causes multilayer graphene growth, and high index Cu surface orientations cause compact graphene island formation with growth rates higher than those on Cu(100).[6,25] In this work, an Alfa Aesar Cu foil for graphene growth with (001) surface orientation/lattice plane which is equivalent to Cu(100) plane will have a preferential growth of multilayer graphene.[6,25] On ideal flat Cu surface, a single (001) surface orientation of a Cu foil will lead to a uniform growth rate in early stages of graphene growth. However, a high degree of uniform distribution of islands (uniform growth rate) on Cu surface is affected by an amount

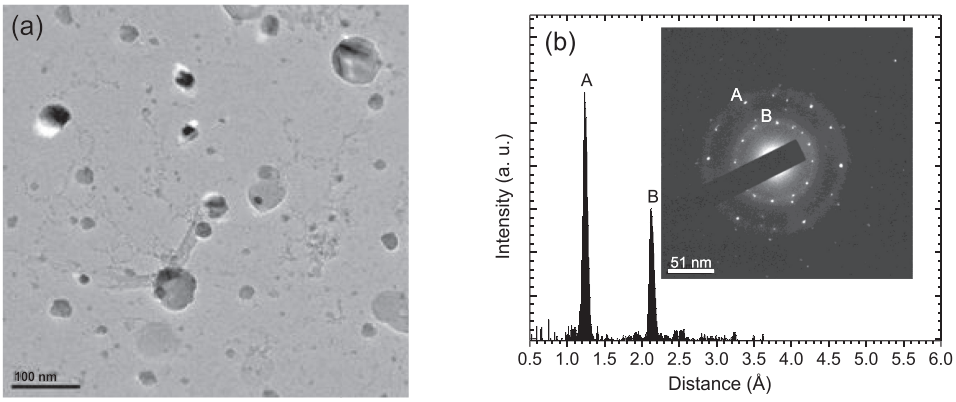

FIG. 12. (a) TEM image of the graphene film obtained on Cu(0.46 at. % Ni) foil at growth temperature of 920 °C and transferred onto TEM Cu grid. (b) The electron diffraction intensity profile of the diffraction pattern (inset to the figure) of the graphene film obtained on Cu(0.46 at. % Ni) foil.

of imperfection sites (the sharp structures) on Cu surface that are not completely removed during high-temperature annealing under hydrogen and argon gas flow. In addition, a single Cu surface orientation also leads to a uniform Ni surface concentration distribution through segregation kinetics.[26] In prepared dilute Cu(Ni) foil, the maximum surface concentration of Ni that segregated during CVD graphene growth is determined by Ni concentration in Cu (i.e., Ni bulk concentration) and Ni segregation driving energy (segregation energy). More precisely, the surface enrichment of Ni in dilute Cu(Ni) foil is driven by a change in chemical potential energy (writeable in terms of the segregation energy, ΔG), which results in the minimization of the total energy of the crystal.[26] Part of the modified Darken equations, which defines the rate of surface concentration build-up of dope element 1 (e.g., Ni in dilute Cu(Ni) foil), is[26]

$$\frac{\partial X_1^{\phi}}{\partial t} = \frac{M_1 X_1^{B_1}}{d^2}\left[\Delta G + RT \ln \frac{X_1^{B_1}\left(1 - \frac{X_1^{\phi}}{X^M}\right)}{\frac{X_1^{\phi}}{X^M}\left(1 - X_1^{B_1}\right)}\right], \quad (2)$$

where X_1^{ϕ} is the surface concentration of the segregating dope element 1, X_1^B is the bulk concentration, X^M is the maximum surface concentration <100 at. %, M_1 is the mobility, d is the thickness of the segregated layer, R is the gas constant, and T is the temperature.

In Eq. (2), as the crystal temperature increases, surface concentration build-up of dope element 1 increases until it reaches a maximum surface concentration (i.e., segregation equilibrium), then, a further increase in temperature results in desegregation. At equilibrium, $\partial X_1^{\phi}/\partial t = 0$ and Eq. (1) reduces to the Langmuir–McLean equation[26]

$$\frac{X_1^{\phi}/X^M}{1 - X_1^{\phi}/X^M} = \frac{X_1^B}{1 - X_1^B}\exp\left(\frac{-\Delta G}{RT}\right). \quad (3)$$

From a well-known thermodynamic expression, $\Delta G = \Delta H - T\Delta S$, where ΔH is segregation enthalpy, T is temperature, and ΔS is segregation entropy.[27] In a dilute system, the segregation entropy (ΔS) is negligible (generally $\Delta S/R < 1$) and $\Delta G \approx \Delta H$.[28] The segregation enthalpy can be approximated by[26,27]

$$\Delta H = \left(\frac{\Delta Z}{Z}\right)\left(\Delta H_B^{sub} - \Delta H_A^{sub}\right), \quad (4)$$

where Z is bulk coordination number ($Z = 12$ for Cu crystal), ΔZ is a difference in coordination number between bulk and surface ($\Delta Z = 4$ for Cu(001)), ΔH^{sub} is the heat of sublimation for element A and B ($\Delta H_{\text{Cu}}^{sub} = 339.3\,\text{kJ/mol}$ and $\Delta H_{\text{Ni}}^{sub} = 430.1\,\text{kJ/mol}$ (Refs. 29 and 30)).

For a dilute Cu(001)(Ni) alloy, $\Delta H = 30.3\,\text{kJ/mol}$ (from Eq. (4)), and therefore, $\Delta G = 30.3\,\text{kJ/mol}$. Now, substituting $\Delta G = 30.3\,\text{kJ/mol}$ in Eq. (3), the temperature dependence of the Ni surface concentration in dilute Cu(Ni) alloy was obtained (Fig. 13) for $X_1^B = 0.3$, 0.5, 0.7, and 0.9 at. % Ni and $X^M = 25$ at. %. (Low energy electron diffraction over-structures have shown that the maximum surface concentration of a substitutional segregating dope element for a Cu(001) is 25 at. % (Ref. 31).) The CVD graphene growths on Cu are carried-out in the temperature range of 900–1000 °C, and in this temperature range (see the inset to Fig. 13), the maximum surface concentration of Ni in dilute Cu(Ni) alloy is in the range of 1 to <5 at. %. At a growth temperature of 920 °C, a surface layer of a dilute Cu(0.46 at. % Ni) foil is expected to have a composition of about 2 at. % Ni and 98 at. % Cu. In the study of Liu *et al.*,[5] a Cu(1200 nm)/Ni(400 nm) thin film with a surface layer composition of about more than 97 at. % Cu and lesser than 3 at. % Ni at a CVD growth temperature of 920 °C demonstrated a capability of producing large-area AB-stacked bilayer graphene film. Accordingly, a dilute Cu(0.46 at. % Ni) foil has demonstrated a capability of producing large-area AB-stacked bilayer graphene film as compared to Cu foil (see the above discussion on Raman data).

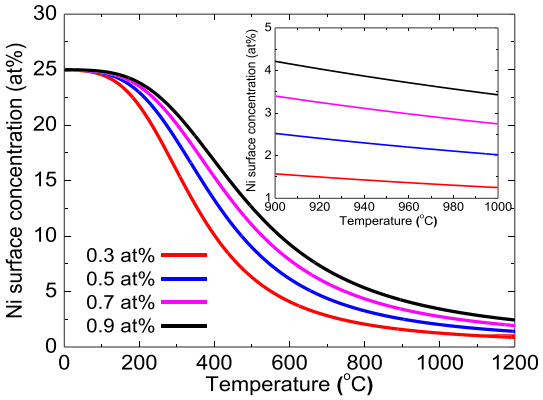

FIG. 13. The temperature dependence of the Ni surface concentration in dilute Cu(Ni) alloy obtained with Langmuir–McLean equation, the inset shows the same plot in temperature range of 900–1000 °C.

It could be expected that a proposed surface layer composition of a dilute Cu(0.46 at. % Ni) foil will be altered by Cu sublimation during CVD graphene growth. For instance, in low-pressure CVD, annealing at high temperatures ≥1000 °C leads to a significant increase in the rate of Cu sublimation.[32] However, in atmospheric pressure CVD at the same annealing temperatures (i.e., ≥1000 °C), the rate of Cu sublimation is expected to decrease significantly. In fact, at higher pressures, the sublimation of Cu is suppressed.[33]

Furthermore, under optimised AP-CVD graphene growth conditions, a bilayer graphene obtained on Cu foil showed larger-areas of incomplete bilayer graphene (i.e., small-areas of bilayer on a monolayer graphene background) as compared to large-area (or wafer-scale) bilayer graphene obtained on Cu(0.46 at. % Ni) foil and that could be due to graphene growth rate which is expected to be higher on Cu(0.46 at. % Ni) foil as compared to Cu foil, following from the enhancement of methane decomposition rate of Cu by Ni. Generally, a slower crystal growth rate yields few crystalline dislocations, and the non-AB stacking in bilayer graphene is due to the undesired dislocations between two graphene layers.[34] Therefore, a slower graphene growth rate

observable on Cu as compared to Cu(Ni) could contribute significantly to crystalline dislocations (non-AB stacking) in bilayer graphene. Nonetheless, a bilayer graphene film obtained on Cu compared to Cu-Ni alloy is known to have a significant fraction of non-AB stacking.[4,5,10] The incomplete bilayer graphene coverage though could also be viewed as an effect of H_2 etching during annealing;[32] in this study, an attempt to suppress or minimise the annealing effects of H_2 on as-grown graphene includes a rapid cooling of as-grown graphene/Cu samples. Nonetheless, H_2 effects in CVD graphene growth have positive effects. For instance, the effect of H_2 in CVD graphene growth was viewed as a co-catalyst in the formation of active surface bound carbon species required for graphene growth[32,35,36] and etches away the weak carbon-carbon bonds (graphene edges) for the growth of bilayer or multilayer graphene.[33,37] The effects of H_2 are expected to be the same for graphene films obtained on both Cu and Cu(0.46 at. % Ni) foils, since the two are synthesized simultaneously. Though CVD graphene growth on Cu surface is a catalytic process which has simplicity view, the CVD growth mechanism is complicated and depends on growth background pressure. Generally, on the Cu surface where the decomposition of hydrocarbons and the surface diffusion induced graphene growth materialise, several processes are involved which includes:[4,33,38,39]

(i) Absorption and desorption of hydrocarbon molecules on Cu.
(ii) Decomposition of hydrocarbon to form active carbon species.
(iii) Aggregation of carbon species on Cu surface (i.e., formation of nucleation sites).
(iv) Surface diffusion and attachment of carbon species to nucleation sites to materialise graphene.
(v) Etching of the as-grown graphene, etc.

Due to simultaneous CVD growth of graphene on both Cu and Cu(0.46 at. % Ni) foils, all the above-mentioned processes are expected to be the same for both Cu and Cu(0.46 at. % Ni) foils, but except for the second process (i.e., decomposition of hydrocarbon to form active carbon species). A process of the decomposition of hydrocarbon to form active carbon species could be viewed as a supply of active carbon species for graphene to materialise. Once more, as compared to Cu, Ni has higher methane decomposition rate (i.e., supply of active carbon species) and higher carbon solubility.[5,40,41] Hence, contrary to Cu, Cu(0.46 at. % Ni) foil can be expected to easily decompose hydrocarbons and provide sufficient carbon species for bilayer or multilayer graphene growth. In this instance, the assumption is that graphene growth on both Cu and dilute Cu(0.46 at. % Ni) foils occurs mostly during the hydrocarbon exposure at a constant temperature, rather than due to carbon precipitation/segregation during cooling.[5,42] Despite the assumption, carbon has very low solubility in Cu (<0.001 at. % at 1000 °C),[43] and for carbon to precipitate during cooling an equilibrium saturation of carbon atoms in Cu substrate is required,[26] which may not be possible since the CVD growth of graphene (i.e., Cu substrate exposure to carbon source) occurs over few minutes.[44,45] In addition, Harpale *et al.*[45] has demonstrated that carbon diffusion into Cu is restricted by preferential carbon-carbon bonds formation (carbon-carbon dimer pairs) over Cu-carbon bonds. Hence, graphene growth on Cu can be regarded to occur mostly during the hydrocarbon exposure at a constant temperature. At graphene growth temperatures (~1000 °C), a surface layer of a dilute Cu(0.46 at. % Ni) foil is expected to have a higher relative surface concentration of Ni due to Ni segregation.[26] In contrary to a surface layer of a dilute Cu(0.46 at. % Ni) foil, a subsurface layer is expected to have ~0 at. % Ni, since Ni enrichment of a surface layer of a dilute Cu(0.46 at. % Ni) foil will deplete the subsurface layer(s).[26] As a result, during exposure to carbon source, a surface layer of a dilute Cu(0.46 at. % Ni) foil will have both Cu-carbon and Ni-carbon bonds/interaction effects, and a subsurface layer which is mostly Cu will have preferential carbon-carbon bonds (which restrict carbon diffusion into Cu)[45] and very low carbon solubility similar to Cu. Similarly, graphene growth on dilute Cu(0.46 at. % Ni) foil can be regarded to occur mostly during the hydrocarbon exposure at a constant temperature. During CVD graphene growth, unlike Cu surface, the metal-carbon interaction effects of a dilute Cu(0.46 at. % Ni) foil surface will have both Cu-carbon and Ni-carbon interactions effects, hence a dilute Cu(0.46 at. % Ni) foil is expected to easily decompose hydrocarbons and supply sufficient active carbon species for bilayer or multi-layer graphene growth.

In previous studies, it is mentioned that a CVD substrate with a surface layer elemental composition of about 97 at. % Cu and 3 at. % Ni grows bilayer graphene with an AB-stacked yield in the range of 95%–100%, which is attributed to the surface catalytic graphene growth mode with a certain methane decomposition rate[5] and AP-CVD graphene growth on Cu substrate grow small-areas of multilayer graphene on a monolayer graphene background at higher methane concentrations (low methane concentrations grow wafer-scale monolayer graphene).[41] The capability of Cu-Ni alloy to grow large-area AB-stacked bilayer graphene as compared to Cu which is known to grow islands of bilayer graphene with a significant fraction of non-AB stacking is discussed on the basis of metal-carbon solubility and hydrocarbon decomposition rate.[4–6]

In addition, a discussion on the driving energy or mechanism behind a favorable growth of AB-stacked graphene layers on Cu-Ni alloy as compared to Cu is lacking in literature, and also this study does not have supported results to give such detailed discussion. Nonetheless, if a thermodynamic process driving a Bernal stacking of two superimposed graphene layers is viewed as a minimization of the total energy of a metal-carbon (graphene) system. Therefore, as compared to preferential carbon-carbon interactions over Cu-carbon interactions in Cu, preferential Ni-carbon interactions over Cu-carbon and carbon-carbon interactions in Cu-Ni alloy[45] suggest that a Cu-Ni-carbon system has lowest crystal energy over a Cu-carbon system, which makes it a favourable system for thermodynamic process driving a Bernal stacking of two superimposed graphene layers.

The sheet resistance obtained for bilayer graphene film obtained on a Cu(0.46 at. % Ni) foil (315 Ω/sq) compares

well with that of a large area bilayer graphene (287 Ω/sq) obtained by Chen *et al.*[6] using non-dilute commercial Cu-Ni alloy foils. The Raman and electron diffraction data showed that the graphene film obtained on Cu(0.46 at. % Ni) foil is mainly AB-stacked bilayer graphene.

Once more, Alfa Aesar Cu foils for graphene growth with purity of 99.8% have about 0.2% unknown-impurities, and Liu *et al.*[4] have demonstrated that the purity of Cu surface plays a critical role in determining the number of graphene layers. In this study, un-doped and Ni doped Cu foils are obtained from the same Alfa Aesar Cu foil, hence they have the same amount and type of unknown-impurities. So, the effect of these unknown-impurities in graphene growth is the same for both foils under the same growth conditions; hence, the effect can be ruled-out in comparison of graphene films obtained from both un-doped and Ni doped Cu foils. Though this study focuses on CVD bilayer graphene growth, the advantage of CVD technique for controlling graphene layer thickness can further be expanded to uniform multi-layer graphene growth in comparison to multi-layer graphene synthesized using chemical methods for anode material in Li-ion batteries.[46,47]

V. CONCLUSIONS

This study demonstrated the solid state diffusion doping of annealed Cu foils for graphene growth with small concentrations of Ni to obtain a dilute Cu(Ni) alloy in which the hydrocarbon decomposition rate of Cu will be enhanced by Ni during synthesis of large-area AB-stacked bilayer graphene using AP-CVD setup. As compared to Cu foil, the prepared dilute Cu(Ni) alloy demonstrated the good capability of growing large-area AB-stacked bilayer graphene by increasing Ni content in Cu surface layer thus altering a composition of a Cu surface where the decomposition of hydrocarbons and the surface diffusion induced graphene growth materialise. The methane decomposition rate of Cu surface for large-area CVD bilayer graphene growth was engineered with Ni through a well-known segregation phenomenon. The number of graphene layers contained in films and the AB stacking order of synthesized graphene films were confirmed by Raman and electron diffraction pattern measurements. The results obtained in this work demonstrated the interest and potential insight of using dilute Cu(Ni) alloy as a substrate in AP-CVD for synthesis of a large-area AB-stacked bilayer graphene film.

ACKNOWLEDGMENTS

This work is based on the research supported by the South African Research Chairs Initiative of the Department of Science and Technology and National Research Foundation of South Africa (Grant No. 97994). Any opinion, finding, and conclusion or recommendation expressed in this material are that of the author(s), and the NRF does not accept any liability in this regard. M. J. Madito acknowledges the financial support from university of Pretoria and NRF for his Ph.D. studies. Dr. M. Madhuku is acknowledged for his assistance on the PEXI measurements from iThemba LABS.

[1]*Physics of Graphene*, edited by H. Aoki and M. S. Dresselhaus (Springer, New York, 2014).
[2]Y. Zhang, T. Tang, C. Girit, Z. Hao, M. C. Martin, A. Zettl, M. F. Crommie, Y. R. Shen, and F. Wang, Nature **459**, 820 (2009).
[3]W. J. Yu, L. Liao, S. H. Chae, Y. H. Lee, and X. Duan, Nano Lett. **11**, 4759 (2011).
[4]W. Liu, H. Li, C. Xu, Y. Khatami, and K. Banerjee, Carbon **49**, 4122 (2011).
[5]W. Liu, S. Kraemer, D. Sarkar, H. Li, P. M. Ajayan, and K. Banerjee, Chem. Mater. **26**, 907 (2014).
[6]S. Chen, W. Cai, R. D. Piner, J. W. Suk, Y. Wu, Y. Ren, J. Kang, and R. S. Ruoff, Nano Lett. **11**, 3519 (2011).
[7]H. Choi, Y. Lim, M. Park, S. Lee, Y. Kang, M. S. Kim, J. Kim, and M. Jeon, J. Mater. Chem. C **3**, 1463 (2015).
[8]C. Mattevi, H. Kim, and M. Chhowalla, J. Mater. Chem. **21**, 3324 (2011).
[9]N. Liu, L. Fu, B. Dai, K. Yan, X. Liu, R. Zhao, Y. Zhang, and Z. Liu, Nano Lett. **11**, 297 (2011).
[10]W. Fang, A. L. Hsu, R. Caudillo, Y. Song, A. G. Birdwell, E. Zakar, M. Kalbac, M. Dubey, T. Palacios, M. S. Dresselhaus, P. T. Araujo, and J. Kong, Nano Lett. **13**, 1541 (2013).
[11]U. Vahalia, P. A. Dowben, and A. Miller, J. Vac. Sci. Technol., A **4**(3), 1675 (1986).
[12]A. Reina, X. Jia, J. Ho, D. Nezich, H. Son, V. Bulovic, M. S. Dresselhaus, and J. Kong, Nano Lett. **9**(1), 30 (2009).
[13]X. Liu, L. Fu, N. Liu, T. Gao, Y. Zhang, L. Liao, and Z. Liu, J. Phys. Chem. C **115**, 11976 (2011).
[14]Y. Wu, H. Chou, H. Ji, Q. Wu, S. Chen, W. Jiang, Y. Hao, J. Kang, Y. Ren, R. D. Piner, and R. S. Ruoff, ACS Nano **6**(9), 7731 (2012).
[15]S. Lee, K. Lee, and Z. Zhong, Nano Lett. **10**, 4702 (2010).
[16]S. M. Kim, A. Hsu, Y. H. Lee, M. Dresselhaus, T. Palacios, K. K. Kim, and J. Kong, Nanotechnology **24**, 365602 (2013).
[17]J. Crank, *The Mathematics of Diffusion*, 2nd ed. (Clarendon Press, Oxford, 1975).
[18]W. Gale and T. Totemeier, *Smithells Metals Reference Book*, 8th ed. (Elsevier Butterworth-Heinemann, Ltd., Oxford, UK, 2004).
[19]M. Fabiane, "Chemical vapour deposition of graphene: Fundamental aspects of synthesis and characterization," Ph.D. thesis (University of Pretoria, South Africa, 2014).
[20]M. Her, R. Beamsa, and L. Novotnya, Phys. Lett. A **377**, 1455 (2013).
[21]L. M. Malard, M. A. Pimenta, G. Dresselhaus, and M. S. Dresselhaus, Phys. Rep. **473**, 51 (2009).
[22]A. C. Ferrari, J. C. Meyer, V. Scardaci, C. Casiraghi, M. Lazzeri, F. Mauri, S. Piscanec, D. Jiang, K. S. Novoselov, S. Roth, and A. K. Geim, Phys. Rev. Lett. **97**, 187401 (2006).
[23]L. Zhang, C. M. B. Holt, E. J. Luber, B. C. Olsen, H. Wang, M. Danaie, X. Cui, X. Tan, V. Lui, W. P. Kalisvaart, and D. Mitlin, J. Phys. Chem. C **115**, 24381 (2011).
[24]A. Dato, V. Radmilovic, Z. Lee, J. Phillips, and M. Frenklach, Nano Lett. **8**(7), 2012 (2008).
[25]J. D. Wood, S. W. Schmucker, A. S. Lyons, E. Pop, and J. W. Lyding, Nano Lett. **11**, 4547 (2011).
[26]J. Du Plessis, *Solid State Phenomena—Part B*, Diffusion and Defect Data Vol. 11 (Sci-Tech Publications, Brookfield, USA, 1990).
[27]S. Stølen and T. Grande, *Chemical Thermodynamics of Materials* (John Wiley & Sons, Ltd., 2004).
[28]S. Hofmann and R. Frech, Anal. Chem. **57**, 716 (1985).
[29]*CRC Handbook of Chemistry and Physics*, 63rd ed., edited by R. C. Weast and M. J. Astle (CRC Press, Inc., 1982).
[30]K. Wandelt and C. R. Brundle, Phys. Rev. Lett. **46**, 1529 (1982).
[31]S. Higashi, H. Tochihara, V. L. Shneerson, and D. K. Saldin, Surf. Sci. **602**, 2473 (2008).
[32]P. R. Kidambi, C. Ducati, B. Dlubak, D. Gardiner, R. S. Weatherup, M. Martin, P. Seneor, H. Coles, and S. Hofmann, J. Phys. Chem. C **116**, 22492 (2012).
[33]I. Vlassiouk, S. Smirnov, M. Regmi, S. P. Surwade, N. Srivastava, R. Feenstra, G. Eres, C. Parish, N. Lavrik, P. Datskos, S. Dai, and P. Fulvio, J. Phys. Chem. C **117**, 18919 (2013).
[34]A. W. Robertson, A. Bachmatiuk, Y. A. Wu, F. Schäffel, B. Rellinghaus, B. Büchner, M. H. Rümmeli, and J. H. Warner, ACS Nano **5**(8), 6610 (2011).
[35]D. H. Jung, C. Kang, M. Kim, H. Cheong, H. Lee, and J. S. Lee, J. Phys. Chem. C **118**, 3574 (2014).
[36]M. Losurdo, M. M. Giangregorio, P. Capezzuto, and G. Bruno, Phys. Chem. Chem. Phys. **13**, 20836 (2011).
[37]X. Zhang, L. Wang, J. Xin, B. I. Yakobson, and F. Ding, J. Am. Chem. Soc. **136**, 3040 (2014).

[38]P. Lenzsolomun, M. C. Wu, and W. Goodman, Catal. Lett. **25**, 75 (1994).
[39]J. A. Venables, G. D. T. Spiller, and M. Hanbucken, Rep. Prog. Phys. **47**, 399 (1984).
[40]W. Cai, R. D. Piner, Y. Zhu, X. Li, Z. Tan, H. C. Floresca, C. Yang, L. Lu, M. J. Kim, and R. S. Ruoff, Nano Res. **2**, 851 (2009).
[41]S. Bhaviripudi, X. Jia, M. S. Dresselhaus, and J. Kong, Nano Lett. **10**, 4128 (2010).
[42]R. Muñoz and C. Gómez-Aleixandre, Chem. Vap. Deposition **19**, 297 (2013).
[43]G. A. López and E. J. Mittemeijer, Scr. Mater. **51**, 1 (2004).
[44]J. J. Lander, H. E. Kern, and A. L. Beach, J. Appl. Phys. **23**, 1305 (1952).
[45]A. Harpale, M. Panesi, and H. B. Chew, J. Chem. Phys. **142**, 061101 (2015).
[46]S. Petnikota, N. K. Rotte, M. V. Reddy, V. V. S. S. Srikanth, and B. V. R. Chowdari, ACS Appl. Mater. Interfaces **7**, 2301 (2015).
[47]S. Petnikota, N. K. Rotte, V. V. S. S. Srikanth, B. S. R. Kota, M. V. Reddy, K. P. Loh, and B. V. R. Chowdari, J. Solid State Electrochem. **18**, 941 (2014).

6.4 Concluding remarks

Alfa Aesar Cu foils for graphene growth with purity of 99.8 % have about 0.2 % unknown-impurities (the concentration of each impurity is not known). In this study, un-doped and Ni doped Cu foils are obtained from the same Alfa Aesar Cu foil, hence they have the same amount and type of unknown-impurities. So, the effect of these unknown-impurities in graphene growth is the same for both foils under the same growth conditions; hence the effect is not considered in the comparison of graphene films obtained from both un-doped and Ni doped Cu foils. Compared to Cu foil, the prepared dilute Cu(Ni) foil demonstrated the good capability of growing large-area AB-stacked bilayer graphene by increasing Ni content in Cu surface layer thus altering a composition of a Cu surface to enhance the hydrocarbon decomposition rate. The obtained results demonstrated the interest and potential insight of using dilute Ni doped Cu foil (from Alfa Aesar which is manufactured for graphene growth) as a substrate in CVD.

In the next chapter, a Ni doped Cu foil prepared in this chapter will be used to further demonstrate its capability for growing a wafer-scale AB-stacked bilayer graphene film.

Bibliography

1. S. Chen, W. Cai, R.D. Piner, J.W. Suk, Y. Wu, Y. Ren, et al., Synthesis and characterization of large-area graphene and graphite films on commercial Cu-Ni alloy foils, Nano Letters. 11 (2011) 3519-3525.

2. W. Zhang, P. Wu, Z. Li, J. Yang, First-principles thermodynamics of graphene growth on Cu surfaces, Journal of Physical Chemistry C. 115 (2011) 17782-17787.

3. L. Hansen, P. Stoltze, K.W. Jacobsen, J.K. Nørskov, Self-diffusion on copper surfaces, Physical Review B. 44 (1991) 6523-6526.

4. J.D. Wood, S.W. Schmucker, A.S. Lyons, E. Pop, J.W. Lyding, Effects of polycrystalline Cu substrate on graphene growth by chemical vapor deposition, Nano Letters. 11 (2011) 4547-4554.

CHAPTER 7

A wafer-scale AB-stacked bilayer graphene film

7.1 Introduction

This chapter discusses the AP-CVD synthesis and characterization of high-quality and wafer-scale ($\approx 20 \times 20$ mm^2) AB-stacked bilayer graphene film obtained on a dilute Cu(0.61 at% Ni) foil. The discussion includes the results from the characterization of graphene films obtained from pure Cu and dilute Cu(0.61 at% Ni) foils, and characterization of Cu(0.61 at% Ni) foil substrate. The publication (including the supporting information) which details the experimental procedure and results discussed in this chapter is presented at the end of the chapter.

In this chapter, a Ni doped Cu foil prepared as discussed in the previous chapter was used for bilayer graphene growth. It is worth mentioning that in the previous chapter, a Cu(Ni) foil used had a Ni bulk concentration of 0.46 at% and in this chapter has a Ni bulk concentration of 0.61 at%. At a growth temperature of 980 °C, both foils will have approximately the same Ni surface concentrations and hence similar hydrocarbon decomposition rates.

Bilayer graphene films were synthesized simultaneously on both Cu and Cu(0.61 at% Ni) foils at 980 °C using AP-CVD. The graphene films obtained on foils were transferred by spin coating a thin layer of PMMA on the as-grown graphene on foils. The graphene films transferred onto SiO_2 were characterized. In addition, the surface elemental composition of a dilute Cu(0.61 at% Ni) foil substrate was analyzed.

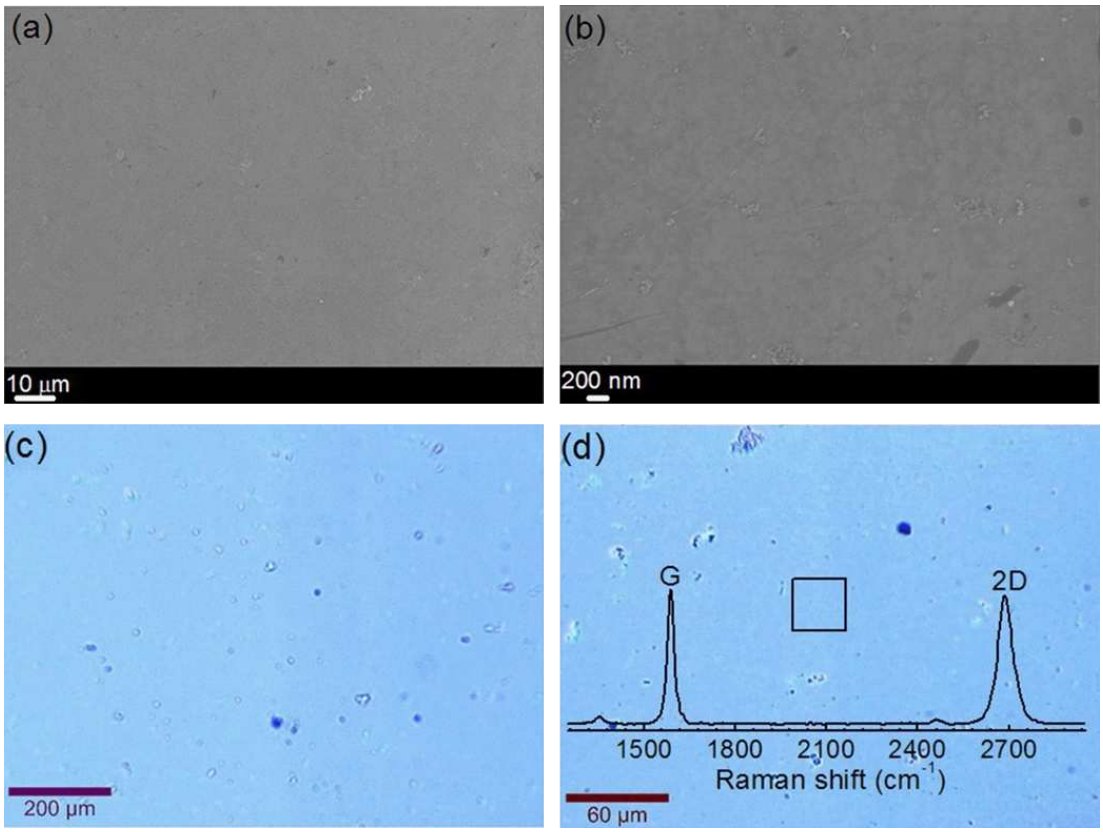

Figure 7.1: (a-b) SEM micrographs of a bilayer graphene film (at low and high magnifications respectively) obtained on a dilute Cu(Ni) foil and transferred onto 300 nm SiO_2/Si substrate. (c-d) Raman optical microscope images of a bilayer graphene film (at low and higher magnifications respectively) on 300 nm SiO_2/Si substrate. The inset: Raman spectrum corresponding to the area indicated as a box.

7.2 Results and discussions

Figure 7.1(a)-(b) (at low and high magnifications) show SEM micrographs of a bilayer graphene film obtained on a dilute Cu(0.61 at% Ni) foil, which suggests uniform and continuous graphene layers. These SEM micrographs are the same as those of other parts of the same film (see figure S5 in the supporting information for publication presented at the end of this chapter), hence figure 7.1(a)-(b) suggest a uniform and continuous graphene over entire graphene film.

Figure 7.1(c)-(d) show Raman optical microscopy images and bilayer graphene Raman spectrum (the inset) of a bilayer graphene film obtained on a dilute Cu(0.61 at% Ni) foil, which also suggest uniform and continuous graphene layers over entire graphene film. Therefore, SEM micrographs

and optical microscopy images (Figure 7.1) suggests dilute Cu(0.61 at% Ni) foil surface reached ≈98 % coverage with $\approx 20 \times 20$ mm^2 area (substrate size) of uniform bilayer graphene.

A wafer-scale bilayer graphene film obtained on a dilute Cu(0.61 at% Ni) foil has a sheet resistance of 284 Ω/sqr which compares well with a sheet resistance of large-area bilayer graphene(288 Ω/sqr) discussed in chapter 5.

After growth, a high surface concentration of Ni compared to Ni bulk concentration in dilute Cu(0.61 at% Ni) foil was confirmed and quantified (as 1.2 ± 0.2 at%) with TOF-SIMS and XPS respectively. However, a Ni surface fractional concentration of 1.2 at% could be larger since 1.2 at% is the fractional/average value of Ni concentration measured in the presence of other species rather than Cu alone by XPS.

7.3 Publication

This section present an article published in RSC Advances, 6, 28370-28378 (2016). The publication (including the supporting information) details the experimental procedure and results from the characterization of graphene films obtained from pure Cu and dilute Cu(0.61 at% Ni) foils, and characterization of Cu(0.61 at% Ni) foil substrate.

RSC Advances

PAPER

View Article Online
View Journal | View Issue

CrossMark click for updates

Cite this: *RSC Adv.*, 2016, **6**, 28370

A wafer-scale Bernal-stacked bilayer graphene film obtained on a dilute Cu (0.61 at% Ni) foil using atmospheric pressure chemical vapour deposition†

M. J. Madito, N. Manyala,* A. Bello, J. K. Dangbegnon, T. M. Masikhwa and D. Y. Momodu

Received 18th December 2015
Accepted 5th March 2016

DOI: 10.1039/c5ra27159b

www.rsc.org/advances

A bilayer graphene film was synthesized on a dilute Cu (0.61 at% Ni) foil using atmospheric pressure chemical vapour deposition (AP-CVD). Atomic force microscopy average step height analysis, scanning electron microscopy micrographs and the Raman optical microscopy images and spectroscopy data supported by selected area electron diffraction data showed that the bilayer graphene film obtained on a dilute Cu (0.61 at% Ni) foil is of high-quality, continuous over a wafer-scale (scale of an entire foil) and mainly Bernal stacked. These data clearly showed the capability of a dilute Cu (0.61 at% Ni) foil for growing a wafer-scale bilayer graphene film. This capability of a dilute Cu (0.61 at% Ni) foil was ascribed primarily to the metal surface catalytic activity of Cu and Ni catalyst. A wafer-scale bilayer graphene film obtained on a dilute Cu (0.61 at% Ni) foil has a sheet resistance of 284 Ω sq^{-1} (measured using a four-point probe station). Time-of-flight secondary ion mass spectrometry and X-ray photoelectron spectroscopy showed a high surface concentration of Ni in the dilute Cu (0.61 at% Ni) foil which altered the surface catalytic activity of the Cu to grow a wafer-scale bilayer graphene film.

Introduction

Graphene has attracted wide interest due to its promising potential applications in electronics and photonics.[1–3] However, many of these applications are restricted by the zero band gap of graphene.[4,5] Nonetheless, a considerable band gap of up to ~250 meV can be opened up in Bernal (AB) stacked bilayer graphene by applying a perpendicular electric field between the two superimposed layers.[5–7] Hence, graphene synthesis has been focused on growing high-quality and large-area AB-stacked bilayer graphene. Chemical vapour deposition (CVD) is a favourable synthesis technique for graphene since it can grow high-quality and large-area or wafer-scale graphene, which is important for electronic devices.[8,9] In addition, atmospheric-pressure CVD is technologically more accessible for graphene growth.

Generally, CVD synthesis of graphene starts with the decomposition of hydrocarbon into active carbon atoms on catalytic metal substrates (*e.g.* Cu, Ni, Fe, Pd, Pt).[5,10–14] In CVD graphene growth, Cu is a favourable catalytic metal substrate due to its very low solubility of carbon (*i.e.* <0.001 at% at 1000 °C),[15] low cost, high etchability and capability of growing a homogeneous monolayer graphene film. Despite its favourability, it is a challenge to grow uniform large-area bilayer or multilayer graphene films with continuous AB stacking on a Cu substrate.[11,16–18] Such a challenge for Cu is typically ascribed primarily to the low decomposition rate of hydrocarbon gas on the substrate surface.[17,19,20] CVD synthesis of graphene on a Cu substrate typically favours monolayer graphene growth due to the very low solubility of carbon in Cu.[19] According to Harpale *et al.*,[21] a surface-to-bulk diffusion of carbon atoms in Cu is restricted by preferential carbon–carbon bonds formation (*i.e.* carbon–carbon dimer pairs) over Cu–carbon bonds. Therefore, isothermal CVD synthesis of graphene on Cu occurs predominantly during the hydrocarbon exposure for several minutes.[19] In contrast to Cu, Ni is known to have higher decomposition rate of hydrocarbon and higher solubility of carbon (*i.e.* ~1.3 at% at 1000 °C (ref. 22)) which leads to a sufficient supply of active carbon atoms for CVD synthesis of graphene multilayers.[17,20] However, a CVD multilayer graphene film on Ni typically has non-uniform and randomly rotated layers of graphene due to non-uniform precipitation or segregation of carbon atoms from different grains surfaces and grain boundaries.[12,23]

Interestingly, since CVD synthesis of graphene on Cu substrates is limited to the surface of the catalyst (favours monolayer graphene growth), a Cu surface engineered with Ni has a capability of growing large-area multilayers of graphene due to Ni since it has higher decomposition rate of hydrocarbon

Department of Physics, Institute of Applied Materials, SARCHI Chair in Carbon Technology and Materials, University of Pretoria, Pretoria 0028, South Africa. E-mail: ncholu.manyala@up.ac.za; Fax: +27 12 420 2516; Tel: +27 12 420 3549

† Electronic supplementary information (ESI) available: Characterisation or results of monolayer and bilayer graphene films obtained on pure Cu foils. See DOI: 10.1039/c5ra27159b

compared to Cu. In previous studies, Cu/Ni thin films and commercial Cu–Ni alloys have demonstrated such capability, including the growth of large-area AB-stacked bilayer graphene.[20,24,25] In these studies, the Cu/Ni thin films have Ni concentrations >5 at% (ref. 17, 24 and 26) and commercial Cu (88.0 wt%)–Ni (9.9 wt%)[27] and Cu (67.8 wt%)–Ni (31.0 wt%)[20] foils have Ni bulk concentrations of ~11 at% (ref. 27) and ~33 at% (ref. 20) respectively, which are much higher than the Ni bulk concentration of 0.61 at% in the dilute Cu (0.61 at% Ni) foil used in this study. In non-dilute Cu–Ni foils (*i.e.* Cu foils with high Ni bulk concentrations), CVD graphene growth is known to dominate from segregation or precipitation processes which leads to variation in the thickness uniformity and stacking order in multilayer graphene films.[20,23,25,26] Therefore, the idea of a dilute Cu (0.61 at% Ni) foil is aimed at obtaining high surface concentration of Ni (1 to 3 at%) in Cu (0.61 at% Ni) foil through bulk-to-surface diffusion of Ni while maintaining a low bulk concentration of Ni (<1 at%) in Cu(Ni) foil during hydrocarbon exposure for graphene growth. Mainly, the aim of using a dilute Cu (0.61 at% Ni) foil is to obtain a large-area AB-stacked bilayer graphene predominantly during the hydrocarbon exposure for several minutes. Liu *et al.*[17] synthesized a high-quality and large-area AB-stacked bilayer graphene film using Cu (1200 nm)/Ni (400 nm) thin films which had a Ni surface concentration of about 3 at% during low pressure CVD graphene growth. Though their study shows a Ni surface concentration of about 3 at% in Cu (1200 nm)/Ni (400 nm) thin films, these films have a Ni bulk concentration of about 25 at% which could lead to CVD graphene growth by precipitation processes and that would lead to variation in the thickness uniformity and stacking order in multilayer graphene films. In addition, annealed Cu–Ni thin films have a preferential (111) surface which favourably grows monolayer graphene, in contrast, annealed Alfa Aesar Cu foil for graphene growth has a preferential (001) surface which causes compact graphene island formation. It is worth noting that the study of Liu *et al.*[17] prepared graphene films at a temperature of 920 °C and background pressure of 0.2 mbar using CVD, but we are aiming at using atmospheric background pressure (AP-CVD) and temperatures higher than 920 °C (*i.e.* 970 °C). In a simplified view of the kinetics of the CVD process which are different for both low pressure and atmospheric pressure CVD,[19] to get high quality/purity graphene layers in CVD the background pressure of the CVD substrate should be minimized to the high vacuum limit, particularly, at CVD temperatures around 900 °C (especially in the case when methane is a source of active carbon species). Therefore, the lower the background pressure of the CVD substrate (Low Pressure (LP-CVD)), the lower the density of impurities and residual gas in the system the higher the quality of graphene layers.[19] In contrast to LP-CVD, AP-CVD grows defective/low-quality graphene layers at CVD temperatures around 900 °C. However, at temperatures higher than 900 °C (*i.e.* ~1000 °C), AP-CVD grows high-quality (acceptable quality) graphene layers.

This study focused on the AP-CVD synthesis and characterization of a high-quality and wafer-scale (scale of an entire foil) AB-stacked bilayer graphene film obtained on a dilute Cu (0.61 at% Ni) foil and compared the growth to the results of AP-CVD growth under identical conditions on pure Cu foil (for monolayer and bilayer graphene films obtained on pure Cu foils see Fig. S1–S4 in the ESI†). Atomic force microscopy (AFM) average step height analysis showed the thickness of bilayer graphene, scanning electron microscopy (SEM) micrographs showed uniform and continuous graphene layers and the Raman optical microscopy images and spectroscopy data supported by selected area electron diffraction (SAED) data showed high-quality and continuous (wafer-scale) AB-stacked bilayer graphene for the graphene film obtained on the dilute Cu (0.61 at% Ni) foil, while bilayer graphene growth on the Cu foil showed bilayer domains on a monolayer graphene background (Fig. S3 and S4 in the ESI†). The wafer-scale bilayer graphene film obtained on a dilute Cu (0.61 at% Ni) foil has a sheet resistance of 284 Ω sq^{-1}. After growth, a high surface concentration of Ni compared to the Ni bulk concentration in dilute Cu (0.61 at% Ni) foil was confirmed and quantified with time-of-flight secondary ion mass spectrometry (TOF-SIMS) and X-ray photoelectron spectroscopy (XPS) respectively.

Experimental

Graphene synthesis and transfer onto 300 nm SiO_2/Si substrates

Cu foil samples (~20 × 20 mm^2) were obtained from a high purity (99.8%) 25 μm thick annealed Cu foil for graphene growth ordered from Alfa Aesar. The surface of obtained Cu foil samples was cleaned by immersing samples in aqueous nitric acid for 15 s to dissolve impurities, then in distilled water followed by a ultra-sonic bath with acetone and isopropanol and dry-blowing with N_2 to remove water residues.[28] A dilute Cu (0.61 at% Ni) foil was obtained by doping a Cu foil (mass = 268 mg) with Ni (mass = 1.5 mg). A 116 nm thin layer of high purity (99.99%) Ni was thermally evaporated onto a Cu foil in a vacuum chamber with a pressure of 3 × 10^{-3} Pa. After evaporation of Ni onto Cu, the Cu/Ni sample was annealed at 950 °C for 8 h under an argon atmosphere to obtain a homogeneous distribution of Ni concentration (0.61 at%) in Cu foil. Inductively coupled plasma optical emission spectrometry confirmed 0.61 at% Ni concentration in dilute Cu (0.61 at% Ni) foil. Pure Cu and Cu (0.61 at% Ni) foils were simultaneously loaded in AP-CVD at a centre of a quartz tube for bilayer graphene growth.

Cu and Cu (0.61 at% Ni) foils were kept under Ar (300 sccm) and H_2 (100 sccm) while the temperature was ramped from room temperature to 1050 °C at a heating rate of 0.5 °C s^{-1} and was maintained at this temperature for 20 min to obtain large Cu grains. After 20 min, the temperature was cooled at a cooling rate of −0.2 °C s^{-1} to 980 °C. At 980 °C, the bilayer graphene films on Cu and Cu (0.61 at% Ni) foils were obtained from a mixture of Ar (300 sccm), H_2 (9 sccm) and CH_4 (10 sccm) for 5 min. Immediately after growth, the CH_4 flow was closed and the quartz tube was pushed to the cooler region of the furnace where samples rapidly cooled down to 600 °C within 90 s and then to a temperature of less than 80 °C before the samples were taken out.

The graphene thin films obtained on foils were transferred onto 300 nm SiO_2/Si substrates and TEM grids for TEM/SAED measurements by spin coating (at 3000 rpm for 30 s) a thin layer of polymethyl methacrylate (PMMA) (average $M_w \sim$ 996 000 by GPC dissolved in chlorobenzene with a concentration of 46 mg mL^{-1}) on the as-grown graphene on foils. The PMMA/graphene/foils were placed in 1 M iron nitrate to etch off Cu and Cu(Ni). PMMA/graphene films floated in the etchant after the foils were etched. These films were then transferred using a polyethylene terephthalate (PET) to the 5% hydrochloride (HCl), then, to deionized (DI) water to dissolve the iron nitrate. Subsequently, the PMMA/graphene films were transferred onto 300 nm thick SiO_2/Si substrates. Finally, PMMA was removed by placing samples in the acetone bath for 6 h.[29]

Samples characterization

The step height analysis of graphene thickness was obtained using a Dimension Icon AFM (Bruker) with nanoscope analysis software in ScanAsyst contact mode. SEM micrographs of the prepared graphene films were observed with a Zeiss Ultra Plus 55 field emission scanning electron microscope (FE-SEM) operated at an accelerating voltage of 1.0 kV. Prepared graphene films were characterized with a WITec Alpha 300 micro-Raman imaging system with 532 nm excitation laser. Raman spectra were measured at room temperature with the laser power set below 2 mW in order to minimize heating effects. Electron diffraction patterns of graphene samples were obtained with high-resolution transmission electron microscopy (HRTEM) (Jeol JEM-2100F Field Emission Electron Microscope, with a maximum analytical resolution of 200 kV and a probe size under 0.5 nm). The graphene film sheet resistance measurements were carried out at room temperature using a Signatone four-point probe station, and a DC current in the range of 0–2.0 mA was used. The surface elemental map images of Cu and dilute Cu (0.61 at% Ni) foils were obtained with time-of-flight secondary ion mass spectrometry (TOF-SIMS) using a Ga^+ primary ion beam and the analyses were carried out over an area of 500 × 500 μm^2 and ion sputter gun area of 1000 × 1000 μm^2. The mass spectra were calibrated to the following mass peaks in positive mode: Al, Na, Ni, Fe, Si, C, C_2H_5, K and Cu. The Ni surface concentration in dilute Cu (0.61 at% Ni) foil was quantified with X-ray photoelectron spectroscopy (XPS). A Physical Electronics VersaProbe 5000 instrument was used employing a 100 μm monochromatic Al-Kα to irradiate the Cu (0.61 at% Ni) foil surface. Photoelectrons were collected using a 180° hemispherical electron energy analyzer. The Cu (0.61 at% Ni) foil was analyzed at a 45° angle between the foil surface and the path to the analyzer. Survey spectra were obtained at the pass energy of 117.5 eV, with a step size of 0.1 eV. The high-resolution spectra of elements, C 1s, Cu 2p, Ni 2p, and O 1s were measured to obtain the chemical composition of the foil surface. High-resolution spectra were obtained at the pass energy of 23.5 eV, with a step size of 0.05 eV. The spectra were obtained before and after the foil were sputtered at a rate of 0.3 nm min^{-1} with an Ar beam operating at 500 V and 150 μA for several cycles while measuring the spectra after each sputter duration. All binding energies were referenced to that of the binding energy of the Fermi level ($E_f = 0$ eV).

Results and discussion

Fig. 1(a) shows photographic images of the Cu (0.61 at% Ni) foil (~20 × 20 mm^2) used in AP-CVD growth of a wafer-scale (on the scale of an entire foil) bilayer graphene and transferred bilayer graphene film on 300 nm SiO_2/Si substrate with a continuous film. In Fig. 1(b), an AFM average step height profile across the graphene edge shown in the AFM micrograph shows that the thickness of the graphene film obtained on a dilute Cu (0.61 at% Ni) foil is about 1.4 nm, suggesting bilayer graphene.

The SEM micrographs in Fig. 2(a) and (b) show uniform and continuous bilayer graphene film (at low and high magnifications respectively) obtained on a dilute Cu (0.61 at% Ni) foil and transferred onto a 300 nm SiO_2/Si substrate. The area of the graphene film shown in the SEM micrographs in Fig. 2 is the same as those of other parts of the film (see Fig. S5 in the ESI†), suggesting a uniform and continuous graphene film over entire graphene film. In contrast, SEM micrographs of the bilayer graphene film obtained on pure Cu foil (Fig. S3 in the ESI†) shows non-uniform layers of graphene (lighter areas corresponding to monolayer and darker areas to multilayer (bilayer) graphene). Nonetheless, CVD synthesis of graphene on Cu favours monolayer graphene, hence its bilayer graphene shows bilayer domains on a monolayer graphene background.[19] In the high magnification image (Fig. 2(b)), it can be seen that wrinkles due to graphene transfer are fewer in the bilayer graphene compared to monolayer graphene film transferred under

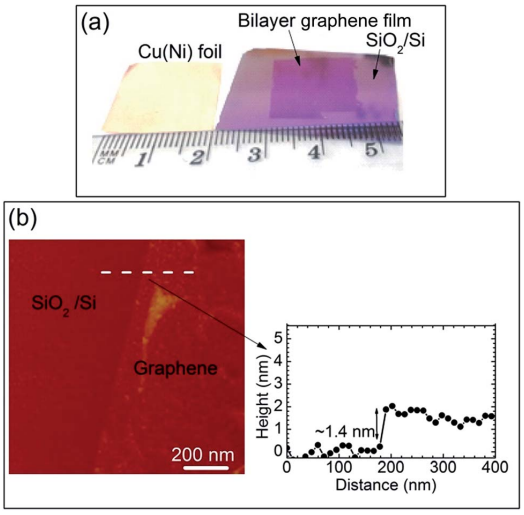

Fig. 1 A continuous wafer-scale bilayer graphene film obtained using AP-CVD. (a) Photographs of the Cu (0.61 at% Ni) foil (~20 × 20 mm^2) with an as-grown bilayer graphene film and transferred bilayer graphene film on a 300 nm SiO_2/Si substrate. (b) AFM image (showing the edge) of bilayer graphene transferred onto a SiO_2/Si substrate and height profile measured along the dotted line.

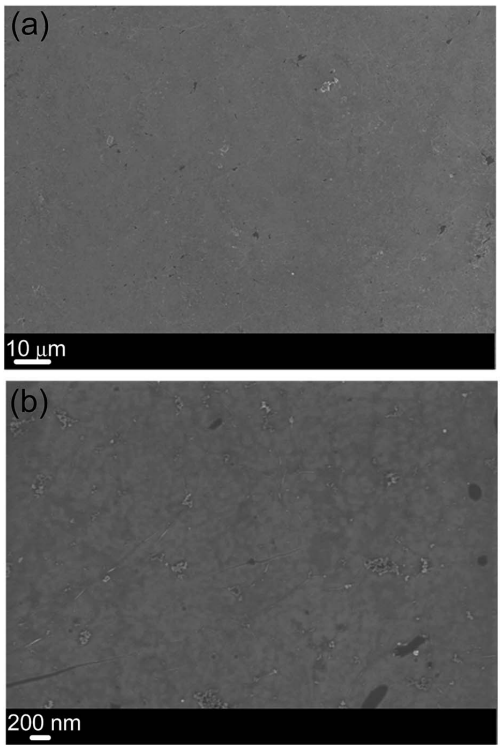

Fig. 2 (a and b) SEM micrographs of a bilayer graphene film (at low and high magnifications respectively) obtained on a dilute Cu (0.61 at% Ni) foil and transferred onto a 300 nm SiO_2/Si substrate.

identical conditions onto a 300 nm SiO_2/Si substrate (see Fig. S1(a) in the ESI†).

In the Raman spectrum of high-quality graphene, the main features that are observable are the G-band mode (~1590 cm^{-1}) and the 2D-band mode (~2690 cm^{-1}). The low intensity disorder-induced D-band (~1350 cm^{-1}) confirms the high-quality of graphene films.[30–32] Fig. 3 shows the Raman data of a bilayer graphene film obtained on a dilute Cu (0.61 at% Ni) foil and transferred onto a 300 nm SiO_2/Si substrate. In Fig. 3(a) and (b), the Raman optical microscope images (at low and higher magnifications respectively) also show a uniform and continuous graphene film over a large-area (analysed area) of graphene film obtained on a dilute Cu (0.61 at% Ni) foil in agreement with the photographic image (Fig. 1(a) for the sample transferred onto SiO_2) and SEM images (Fig. 2). Fig. 3(b) shows a slightly higher contrast than that of a monolayer graphene (Fig. S1(b) in the ESI†) since the optical microscope images of graphene films display a colour contrast between monolayer and bi or multilayer graphene films. Fig. 3(c) shows the average Raman spectrum of spectra acquired from a 30 μm^2 area (indicated with a square box in Fig. 3(b)) of a bilayer graphene film. In Fig. 3(c), the 2D peak full width at half maximum (FWHM) of 55.5 cm^{-1} compares well with the average values (53

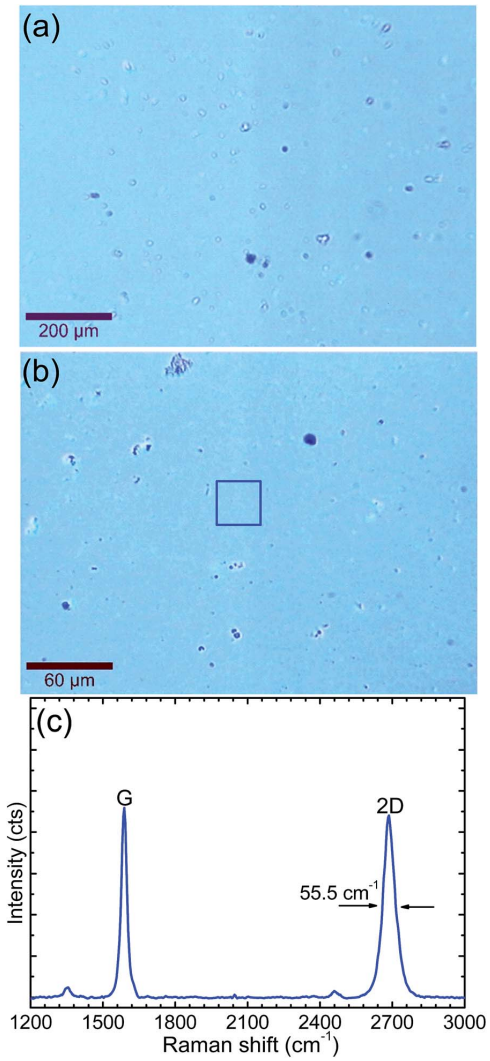

Fig. 3 (a and b) Raman optical microscope images of a bilayer graphene film (at low and higher magnifications respectively) obtained on a dilute Cu (0.61 at% Ni) foil and transferred onto a 300 nm SiO_2/Si substrate. (c) Average Raman spectrum of spectra acquired from a 30 μm^2 area (indicated with a square box in (b)) of a bilayer graphene film.

cm^{-1},[20] 60.1 cm^{-1} (ref. 33) and 51 cm^{-1} (ref. 34)) obtained by others for AB-stacked bilayer graphene films.

In the Raman spectrum of graphene, the 2D-band mode is adopted to distinguish between the numbers of layers contained in graphene sample and is also sensitive to the stacking order in few layers graphene samples.[31–33] Fig. 4(a) and (b) show the mapping of the 2D peaks FWHMs and of the corresponding 2D to G peaks intensities ratio (I_{2D}/I_G) respectively of Raman spectra acquired from 30 μm^2 areas of a bilayer graphene film obtained on a dilute Cu (0.61 at% Ni) foil. The 2D peaks FWHMs

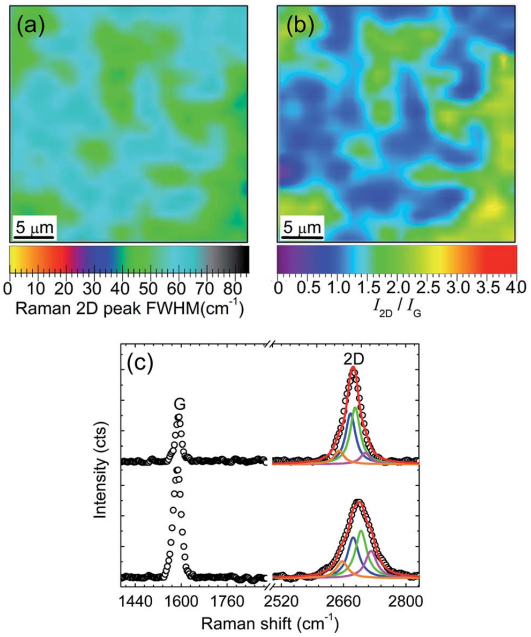

Fig. 4 (a) The mapping of 2D peaks FWHMs and (b) of the corresponding 2D to G peaks intensities ratio (I_{2D}/I_G) for bilayer graphene film obtained on a dilute Cu (0.61 at% Ni) foil and transferred onto 300 nm SiO_2/Si substrate. (c) Raman spectra from data mapped in (a) and the 2D peaks solid-lines are Lorentzians fits.

are in the range of 38–70 cm^{-1} (Fig. 4(a)), I_{2D}/I_G in the range of 0.8–2.5 (Fig. 4(b)) and the 2D peaks positions are in the range of 2685–2703 cm^{-1} (Fig. S6(c)†). Distinct from monolayer graphene features (Fig. S2 and Table S1 in the ESI†), these features demonstrate the characteristics of bilayer graphene. Similar results are obtained from other parts of the graphene film which suggest a continuous bilayer graphene film (Fig. S6 in the ESI†). Fang *et al.*[33] have identified the AB-stacked bilayer graphene with 2D peaks FWHMs in the range of ~40–70 cm^{-1} (with a cut-off FWHM of 70 cm^{-1}) using a CVD graphene prepared on Cu foil.

The 2D peak in the Raman spectrum of graphene is a double-phonon resonant Raman process involving two in-plane transverse optical (iTO) mode phonons around the *K*-point.[30–32] In monolayer graphene, the 2D peak has a single Lorentzian feature.[30] In AB-stacked bilayer graphene the electronic band splits into two conduction and two valence bands and the split causes splitting of the phonon bands into two components which give rise to four peaks in the Raman 2D peak with peak frequencies at approximately 2655, 2680, 2700, and 2725 cm^{-1} and FWHMs equal to that of monolayer graphene.[30] In AB-stacked bilayer graphene, these four peaks are fitted as four Lorentzians to the 2D peak in the Raman spectrum.[30–32] The amplitudes of these four Lorentzians are relative, meaning, two Lorentzians at ~2680 and ~2700 cm^{-1} (inner peaks in 2D peak) have almost the same intensity and are higher than the other two at ~2655 and ~2725 cm^{-1} (outer peaks in 2D peak).[32] For non-AB stacked bilayer graphene, the 2D peak is a single Lorentzian as in monolayer graphene, but with a larger FWHM and upshifted frequency from that of monolayer graphene.[31] Fig. 4(c) shows the Raman spectra from data mapped in Fig. 4(a) and the 2D peaks were fitted with four Lorentzians which demonstrate features of AB-stacked bilayer graphene.

Table 1 shows a summary of the analysis results of the Raman spectra of monolayer and bilayer graphene films obtained on Cu (shown in the ESI†) and dilute Cu (0.61 at% Ni) foils. In this table, it can be seen that graphene features of bilayer graphene obtained on Cu foil overlap with those of monolayer graphene, suggesting the presence of a significant fraction of monolayer graphene in the prepared bilayer graphene film. In contrast to the bilayer graphene film obtained on Cu foil, the bilayer graphene film obtained on Cu (0.61 at% Ni) foil shows different features compared to monolayer graphene features as would be expected in Raman analysis of monolayer and multilayer (bilayer) graphene. The Raman spectral analysis showed that the bilayer graphene film obtained on the dilute Cu (0.61 at% Ni) foil is predominantly AB-stacked bilayer graphene and that was further supported by electron diffraction analysis.

Fig. 5(a) shows a typical TEM image of the bilayer graphene film obtained on Cu (0.61 at% Ni) foil and transferred on a lacey carbon TEM grid (see Fig. S7(a) in the ESI† for the low magnification TEM image). In Fig. 5(a), regions A and B shown in a hole of a lacey carbon TEM grid show an area without graphene and with graphene respectively. Fig. 5(b) shows a typical high magnification TEM image of graphene in region B of Fig. 5(a), and (c) shows a SAED pattern from the corresponding area which shows two sets of hexagonal diffraction spots. TEM diffraction patterns were analysed using a diffraction ring profiler, which was developed for phase identification in complex microstructures.[35] Fig. 5(d) shows the diffraction rings intensity profile which was indexed using the Miller–Bravais indices (*hkil*) for graphite where peaks at $d = 1.23$ Å and peak $d = 2.13$ Å in Fig. 5(d) correspond to indices (1−210) for outer

Table 1 Summary of the analysis results of the Raman spectra of monolayer and bilayer graphene films obtained on Cu (shown in the ESI) and dilute Cu (0.61 at% Ni) foils and transferred onto 300 nm SiO_2/Si substrates for characterization

Graphene layers	CVD substrate	2D peaks positions (cm^{-1})	2D peaks FWHMs (cm^{-1})	2D/G peaks
Monolayer	Cu foil	2670–2682	28–36	2.5–4
Bilayer	Cu foil	2675–2703	28–53	0.8–4
Bilayer	Cu (0.61 at% Ni) foil	2685–2703	38–70	0.8–2.5

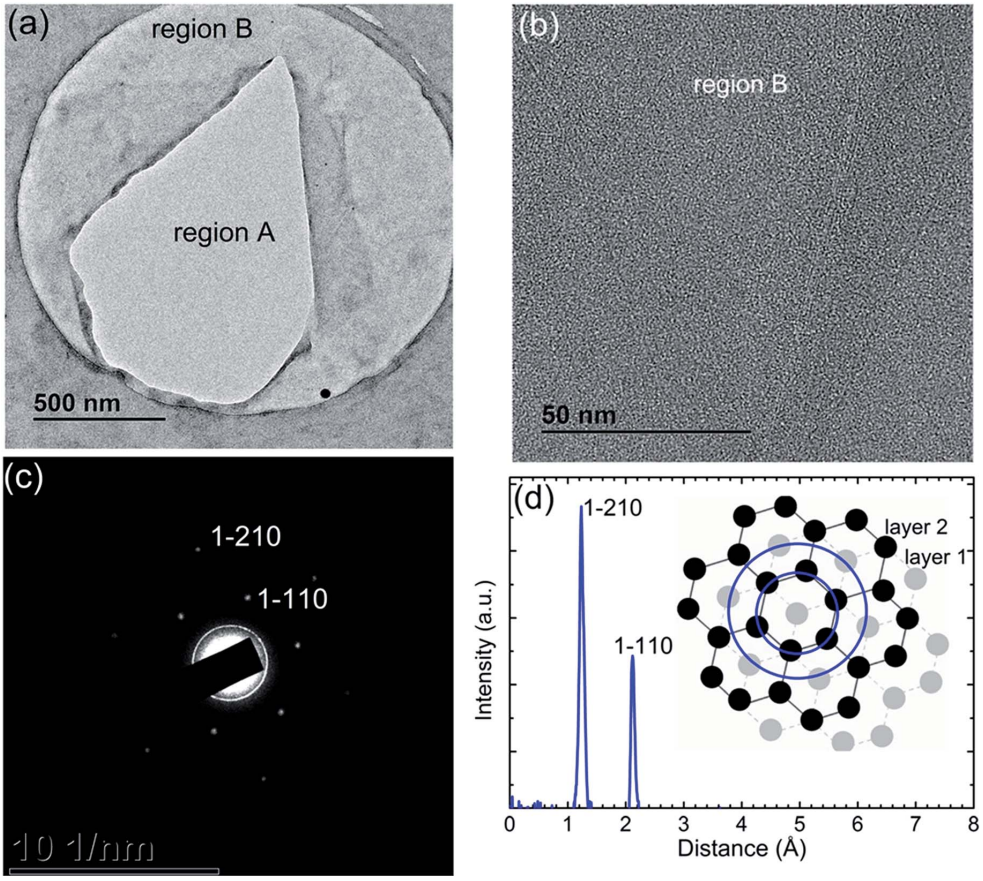

Fig. 5 (a) TEM image of bilayer graphene film obtained on Cu (0.61 at% Ni) foil and transferred onto a lacey carbon TEM grid (regions A and B shown in a hole of a lacey carbon TEM grid show an area without graphene and with graphene respectively). (b) A high magnification TEM image of graphene in region B of (a). (c) A selected area electron diffraction (SAED) pattern from an area shown in (b) and showing two sets of hexagonal diffraction spots. (d) The diffraction rings intensity profile of two sets of hexagonal diffraction spots in (c) and the inset to the figure shows a schematic view of the AB-stacked bilayer graphene and diffraction rings.

hexagon and (1−110) for inner hexagon respectively.[36] The electron diffraction patterns obtained at different positions of the graphene film show similar results (see Fig. S7 in the ESI†). It is known that the relative intensities of the spots in the outer hexagon are twice the intensities of the spots in the inner hexagon for AB-stacked bilayer graphene (shown with a schematic view in the figure inset).[32,33,36] Therefore, the diffraction data (similar to that obtained from other spots of the same film) show that the graphene film obtained on dilute Cu (0.61 at% Ni) foil is predominantly AB-stacked bilayer graphene as evidenced by relative intensities shown in Fig. 5(d) in agreement with the Raman data above.

A four-point probe/sheet resistance measuring system for thin films was used to measure the sheet resistance of the bilayer graphene film transferred onto the 300 nm SiO_2/Si substrate and was obtained as 284 Ω sq^{-1} (see Fig. S8 in the ESI†). A sheet resistance of 284 Ω sq^{-1} measured for the bilayer graphene obtained on Cu (0.61 at% Ni) foil in this study is in the same order of magnitude with that measured from AB-stacked bilayer (287 Ω sq^{-1}) graphene film in ref. 20.

Fig. 6(a) and (b) show the map images of TOF-SIMS secondary ion intensities measured from a dilute Cu (0.61 at% Ni) foil surface of the as-received sample (*i.e.* without surface sputtering with an ion gun) and after surface cleaning for 3 min with ion sputtering respectively. The foil was annealed under graphene growth conditions without methane source. Alfa Aesar Cu foil doped with Ni to obtain a dilute Cu (0.61 at% Ni) foil for graphene growth has a purity of 99.8% and about 0.2% unknown-impurities. The TOF-SIMS data (Fig. 6) shows the presence of Na, Al, Si, C_2H_5, K, Fe and Ni impurities in the Cu (0.61 at% Ni) surface and subsurface layers (bulk layers). These impurities have a potential to influence the CVD graphene growth and the effect of each impurity will be determined by its metal–carbon interaction energy, metal–methane

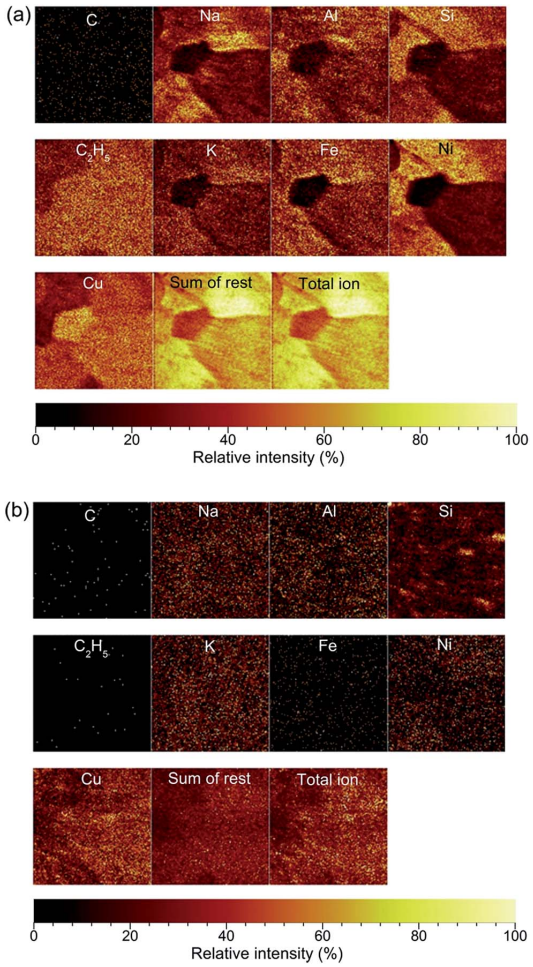

Fig. 6 (a) The map images of TOF-SIMS secondary ion intensities measured from a dilute Cu (0.61 at% Ni) foil surface of the as-received sample (*i.e.* without surface sputtering with ion gun) and (b) after surface cleaning for 3 min with ion sputtering. The foil was annealed under graphene growth conditions without methane source.

decomposition rate and metal–carbon solubility. During CVD graphene growth at high temperatures (~1000 °C), Na and K alkali-metals (and C_2H_5) will not dominate the surface due to their very low melting points (<100 °C). On the other hand, Al, Si and Fe impurities have bulk concentrations on the order of a few parts per million (<10 ppm) and Ni has 6100 ppm (0.61 at%) and hence Ni has a higher surface concentration than all other impurities detected with TOF-SIMS. In addition, Ni has strong metal–carbon atomic interaction, high metal–methane decomposition rate, high carbon solubility and as a result, Ni in the surface of a dilute Cu (0.61 at% Ni) foil will contribute significantly during the CVD graphene growth on Cu (0.61 at% Ni) foil. In brief, except for Ni which has very high bulk concentration of 6100 ppm, high relative intensities of Na, Al, Si, C_2H_5, K and Fe in Fig. 6 do not necessarily show high surface concentrations of these elements in Cu (0.61 at% Ni) foil since they have strong signals in TOF-SIMS.

It is desirable to quantify the TOF-SIMS secondary-ion intensities measured; however, the quantification in TOF-SIMS is complicated because of the strong dependence of the secondary-ion yield on the matrix effects (target chemical and electronic character).[37,38]

Furthermore, the surface fractional concentration of Ni in the dilute Cu (0.61 at% Ni) foil with an as-grown bilayer graphene film was quantified with X-ray photoelectron spectroscopy. In the analysis, a resolved angle between the foil surface and the path to the analyzer focuses analysis within the topmost (~5) atomic layers. In this instance, the topmost (~5) atomic layers consist of two atomic layers of bilayer graphene and 2 atomic layers of Cu foil. The foil surface was sputter cleaned with ions for several cycles while measuring the spectra of elements, C 1s, Cu 2p, Ni 2p (shown in Fig. 7(a)–(c)) and O 1s after each sputter cycle, to obtain the chemical composition of the foil surface (Table 2). In Fig. 7 and Table 2, it can be seen that before surface sputter cleaning, C 1s have high concentrations compared to Cu 2p substrate, O 1s (adsorbed from air) and Ni 2p and that confirms a film of graphene on the foil surface. After a 2 min sputter cycle, Ni 2p shows a surface fractional concentration of 1.2 at% and the presence of C 1s and O 1s (restricted to the surface) suggest that the analysis is within the first atomic layer of a Cu foil (see Fig. 7 and Table 2).

Interestingly, after a 5 min sputter cycle, Ni 2p, C 1s and O 1s are not detected and Cu shows a fractional concentration of 99.9 at% which correspond to a relatively pure Cu. In this instance, a 5 min sputter cleaning at a rate of 0.3 nm min^{-1} is equivalent to a removal of 1.5 nm thick material which in this instance consist of a bilayer graphene (~1 nm thick including surface adsorbed carbon and oxygen from air) and approximately the first two atomic layers of Cu (~0.5 nm). Accordingly, the analysis shown here after 5 min sputter cleaning are from the topmost subsurface atomic layers of Cu as confirmed by the absence (zero concentrations) of C 1s and O 1s which are restricted to the surface of Cu. In brief, this analysis confirms a surface alloying of Cu with Ni (similar to the TOF-SIMS data above) while maintaining relatively pure Cu in the topmost subsurface atomic layers of the Cu. However, a Ni surface fractional concentration of 1.2 at% should be larger than 1.2 at%, at least 2.1 at% as calculated in Fig. S9 in the ESI,† because 1.2 at% is the fractional/average value of Ni concentration measured in the presence of other species rather than Cu alone by XPS.

Fig. 8 shows the C 1s core level spectra of the as-grown bilayer graphene film on dilute Cu (0.61 at% Ni) foil. The fitted peaks, namely, sp^2 C=C peak at 284.5 eV (graphene component), C–O–C peak at 286.2 eV, C=O peak at 287.4 eV, O–C=O peak at 289.4 eV (oxide components) and π–π^* peak at 291.5 eV (satellite peak/electrons transition) were determined by reference to other studies.[39–41] The fitted sp^2 C=C peak has a dominating intensity which confirms the sp^2 hybridization property of graphene in the as-grown bilayer graphene film,[30,41]

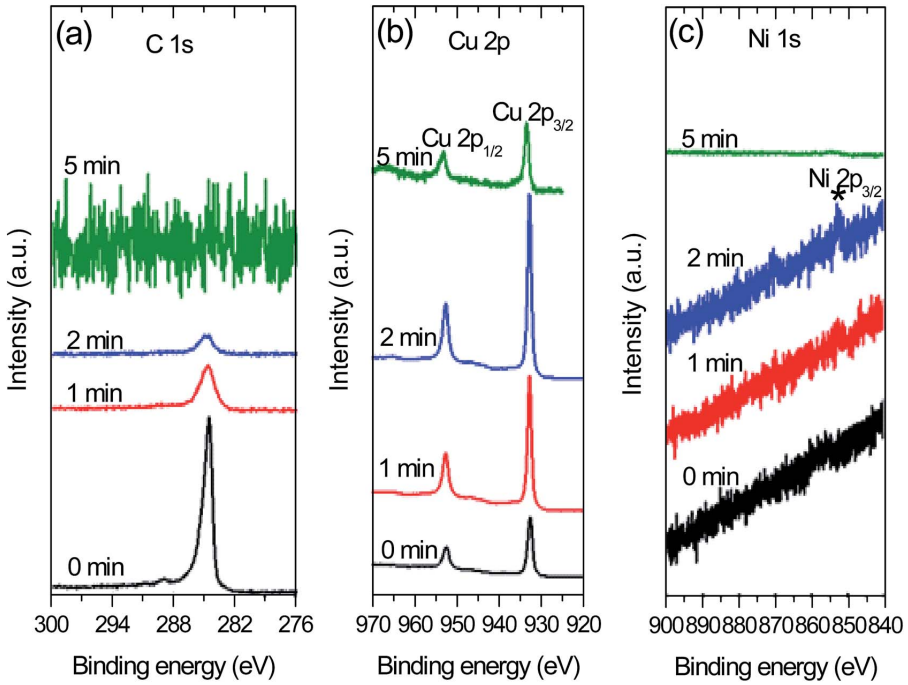

Fig. 7 The XPS spectra of (a) C 1s, (b) Cu 2p and (c) Ni 2p after different sputter cycles of a dilute Cu (0.61 at% Ni) foil with as-grown bilayer graphene film.

Table 2 XPS relative fractional concentrations of C 1s, Cu 2p, O 1s and Ni 2p after different sputter cycles of a dilute Cu (0.61 at% Ni) foil with as-grown bilayer graphene film

Sputter cycles	C 1s (at%)	Cu 2p (at%)	O 1s (at%)	Ni 2p (at%)
0 min	54.9	28.0	17.1	—
1 min	14.1	72.7	13.2	—
2 min	6.5	83.0	9.3	1.2
5 min	—	99.9	—	—

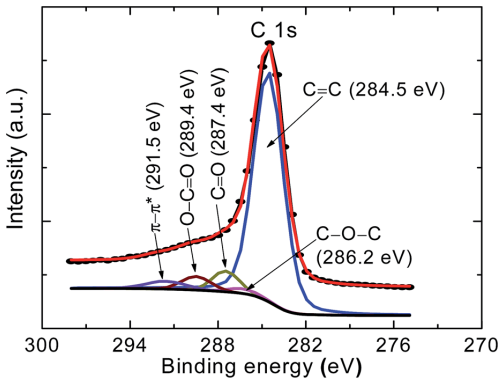

Fig. 8 The high-resolution C 1s core level XPS spectra of as-grown bilayer graphene film on dilute Cu (0.61 at% Ni) foil.

the low-intensity oxide peaks could be due to adsorbed oxygen or carbon bonded oxygen during synthesis of the graphene film. The π–π* electrons transition enhances the carbon to carbon bonds in graphene and confirms the high quality of the graphene (suggested by the Raman data) since the π–π* bonds determine the fundamental electronic properties of graphene.[30,40]

Conclusions

This study demonstrated the synthesis of a wafer-scale (on the scale of an entire foil) and high-quality AB-stacked bilayer graphene film on a dilute Cu (0.61 at% Ni) foil using AP-CVD. AFM, SEM, Raman, TEM/SAED and four-point probe/sheet resistance analysis showed that a bilayer graphene film obtained on a dilute Cu (0.61 at% Ni) foil is of high-quality, continuous (wafer-scale) and mainly Bernal stacked. This study clearly showed the capability of a dilute Cu (0.61 at% Ni) foil for growing a wafer-scale bilayer graphene film compared to a pure Cu foil which is known to grow bilayer domains on a monolayer graphene background in AP-CVD (see Fig. S3 and S4 in the ESI†). The capability of a dilute Cu (0.61 at% Ni) foil for growing a wafer-scale bilayer graphene film was ascribed to the carbon solubility and the metal surface catalytic activity of Cu and Ni in

a dilute Cu (0.61 at% Ni) foil. In a dilute Cu (0.61 at% Ni) foil, a high surface concentration of Ni compared to a low bulk concentration of Ni was confirmed with TOF-SIMS and XPS.

Acknowledgements

This work is based on research supported by the South African Research Chairs Initiative of the Department of Science and Technology and National Research Foundation (NRF) of South Africa (Grant No. 97994). M. J. Madito acknowledges the financial support from the university of Pretoria and NRF for his PhD studies. Mr W. A. Jordaan at NMISA is acknowledged for his assistance on the TOF-SIMS measurements. Dr N. Mathe and Ms R. Rikhotso at CSIR national centre for nano-structured materials are acknowledged for their assistance with the TEM/SAED measurements. Prof. Yury Gogotsi's group at Drexel University is acknowledged for its assistance on the XPS measurements.

References

1 A. K. Geim and K. S. Novoselov, *Nat. Mater.*, 2007, **6**, 183–191.
2 M. Freitag, H. Chiu, M. Steiner, V. Perebeinos and P. Avouris, *Nat. Nanotechnol.*, 2010, **5**, 497–501.
3 F. Bonaccorso, Z. Sun, T. Hasan and A. C. Ferrari, *Nat. Photonics*, 2010, **4**, 611–622.
4 F. Schwierz, *Nat. Nanotechnol.*, 2010, **5**, 487–496.
5 Y. Xue, B. Wu, Y. Guo, L. Huang, L. Jiang, J. Chen, D. Geng, Y. Liu, W. Hu and G. Yu, *Nano Res.*, 2011, **4**, 1208–1214.
6 W. J. Yu, L. Liao, S. H. Chae, Y. H. Lee and X. Duan, *Nano Lett.*, 2011, **11**, 4759–4763.
7 Y. Zhang, T. Tang, C. Girit, Z. Hao, M. C. Martin, A. Zettl, M. F. Crommie, Y. R. Shen and F. Wang, *Nature*, 2009, **459**, 820–823.
8 C. Mattevi, H. Kim and M. Chhowalla, *J. Mater. Chem.*, 2011, **21**, 3324.
9 L. Ma, W. Ren, Z. Dong, L. Liu and H. Cheng, *Chin. Sci. Bull.*, 2012, **57**, 2995–2999.
10 X. Li, W. Cai, J. An, S. Kim, J. Nah, D. Yang, R. Piner, A. Velamakanni, I. Jung, E. Tutuc, S. K. Banerjee, L. Colombo and R. S. Ruoff, *Science*, 2009, **324**, 1312–1314.
11 A. Guermoune, T. Chari, F. Popescu, S. S. Sabri, J. Guillemette, H. S. Skulason, T. Szkopek and M. Siaj, *Carbon*, 2011, **49**, 4204–4210.
12 A. Reina, S. Thiele, X. Jia, S. Bhaviripudi, M. S. Dresselhaus, J. A. Schaefer and J. Kong, *Nano Res.*, 2009, **2**, 509–516.
13 S. Y. Kwon, C. V. Ciobanu, V. Petrova, V. B. Shenoy, J. Bareño, V. Gambin, I. Petrov and S. Kodambaka, *Nano Lett.*, 2009, **9**, 3985–3990.
14 G. Imamura and K. Saiki, *J. Phys. Chem. C*, 2011, **115**, 10000–10005.
15 G. A. López and E. J. Mittemeijer, *Scr. Mater.*, 2004, **51**, 1–5.
16 W. Liu, H. Li, C. Xu, Y. Khatami and K. Banerjee, *Carbon*, 2011, **49**, 4122–4130.
17 W. Liu, S. Kraemer, D. Sarkar, H. Li, P. M. Ajayan and K. Banerjee, *Chem. Mater.*, 2014, **26**, 907–915.
18 A. Mohsin, L. Liu, P. Liu, W. Deng, I. N. Ivanov, G. Li, O. E. Dyck, G. Duscher, J. R. Dunlap, K. Xiao and G. Gu, *ACS Nano*, 2013, **7**, 8924–8931.
19 S. Bhaviripudi, X. Jia, M. S. Dresselhaus and J. Kong, *Nano Lett.*, 2010, **10**, 4128–4133.
20 S. Chen, W. Cai, R. D. Piner, J. W. Suk, Y. Wu, Y. Ren, J. Kang and R. S. Ruoff, *Nano Lett.*, 2011, **11**, 3519–3525.
21 A. Harpale, M. Panesi and H. B. Chew, *J. Chem. Phys.*, 2015, **142**, 061101.
22 W. Cai, R. D. Piner, Y. Zhu, X. Li, Z. Tan, H. C. Floresca, C. Yang, L. Lu, M. J. Kim and R. S. Ruoff, *Nano Res.*, 2009, **2**, 851–856.
23 A. Reina, X. Jia, J. Ho, D. Nezich, H. Son, V. Bulovic, M. S. Dresselhaus and J. Kong, *Nano Lett.*, 2009, **9**, 30–35.
24 H. Choi, Y. Lim, M. Park, S. Lee, Y. Kang, M. S. Kim, J. Kim and M. Jeon, *J. Mater. Chem. C*, 2015, **3**, 1463–1467.
25 Y. Wu, H. Chou, H. Ji, Q. Wu, S. Chen, W. Jiang and Y. Hao, *ACS Nano*, 2012, 7731–7738.
26 N. Liu, L. Fu, B. Dai, K. Yan, X. Liu, R. Zhao, Y. Zhang and Z. Liu, *Nano Lett.*, 2011, **11**, 297–303.
27 Y. Wu, H. Chou, H. Ji, Q. Wu, S. Chen, W. Jiang, Y. Hao, J. Kang, Y. Ren, R. D. Piner and R. S. Ruoff, *ACS Nano*, 2012, **6**, 7731–7738.
28 S. M. Kim, A. Hsu, Y.-H. Lee, M. Dresselhaus, T. Palacios, K. K. Kim and J. Kong, *Nanotechnology*, 2013, **24**, 365602.
29 M. Her, R. Beams and L. Novotny, *Phys. Lett. A*, 2013, **377**, 1–3.
30 *Physics of Graphene*, ed. H. Aoki and M. S. Dresselhaus, Springer, New York, 2014.
31 L. M. Malard, M. A. Pimenta, G. Dresselhaus and M. S. Dresselhaus, *Phys. Rep.*, 2009, **473**, 51–87.
32 A. C. Ferrari, J. C. Meyer, V. Scardaci, C. Casiraghi, M. Lazzeri, F. Mauri, S. Piscanec, D. Jiang, K. S. Novoselov, S. Roth and A. K. Geim, *Phys. Rev. Lett.*, 2006, **97**, 187401.
33 W. Fang, A. L. Hsu, R. Caudillo, Y. Song, A. G. Birdwell, E. Zakar, M. Kalbac, M. Dubey, T. Palacios, M. S. Dresselhaus, P. T. Araujo and J. Kong, *Nano Lett.*, 2013, **13**, 1541–1548.
34 S. Lee, K. Lee and Z. Zhong, *Nano Lett.*, 2010, **10**, 4702–4707.
35 L. Zhang, C. M. B. Holt, E. J. Luber, B. C. Olsen, H. Wang, M. Danaie, X. Cui, X. Tan, V. W. Lui, W. P. Kalisvaart and D. Mitlin, *J. Phys. Chem. C*, 2011, **115**, 24381–24393.
36 A. Dato, V. Radmilovic, Z. Lee, J. Phillips and M. Frenklach, *Nano Lett.*, 2008, **8**, 2012–2016.
37 A. M. Belu, D. J. Graham and D. G. Castner, *Biomaterials*, 2003, **24**, 3635–3653.
38 R. G. Wilson, *J. Appl. Phys.*, 1988, **63**, 5121.
39 Y. V. Butenko, S. Krishnamurthy, A. K. Chakraborty, V. L. Kuznetsov, V. R. Dhanak, M. R. C. Hunt and L. Šiller, *Phys. Rev. B: Condens. Matter Mater. Phys.*, 2005, **71**, 075420.
40 M. Hsiao, S. Liao, M. Yen, C. Teng, S. Lee, N. Pu, C. Wang, Y. Sung, M. Ger, C. Ma and M. Hsiao, *J. Mater. Chem.*, 2010, **20**, 8496.
41 S. Ogawa, T. Yamada, S. Ishidzuka, A. Yoshigoe, M. Hasegawa, Y. Teraoka and Y. Takakuwa, *Jpn. J. Appl. Phys.*, 2013, **52**, 110122.

7.4 Supporting information

This section present a supporting information referred to as ESI† in the publication above (Chapter 7).

A wafer-scale Bernal-stacked bilayer graphene film obtained on a dilute Cu(0.61 at% Ni) foil using atmospheric pressure chemical vapour deposition

M. J. Madito, N. Manyala*, A. Bello, J. K. Dangbegnon, T. M. Masikhwa and D. Y. Momodu

Department of Physics, Institute of Applied Materials, SARCHI Chair in Carbon Technology and Materials, University of Pretoria, Pretoria 0028, South Africa

* Corresponding Author: Tel: +27 (0)12 420 3549 and E-mail address: ncholu.manyala@up.ac.za (N. Manyala)

SEM and Raman data of monolayer graphene obtained on a pure Cu foil

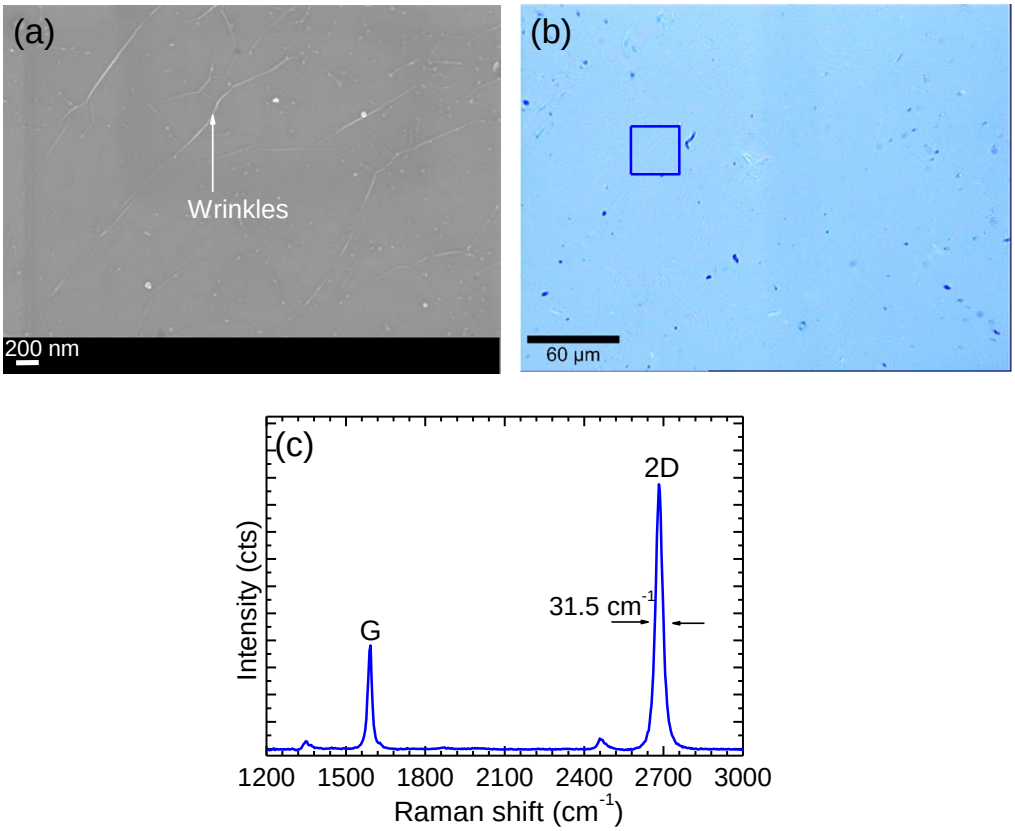

Figure S1. (a) SEM micrograph of a monolayer graphene film transferred onto 300 nm SiO_2/Si substrate. (b) Raman optical microscope image of monolayer graphene film on 300 nm SiO_2/Si substrate and the corresponding (c) average Raman spectra of spectra acquired from 30 μm^2 area (indicated with a square box in figure S1(b)) of a monolayer graphene film.

A monolayer graphene film on Cu foil was obtained from a mixture of Ar (300sccm), H_2 (9 sccm) and CH_4 (15 sccm) for 2 min at a growth temperature of 1000 °C.

.

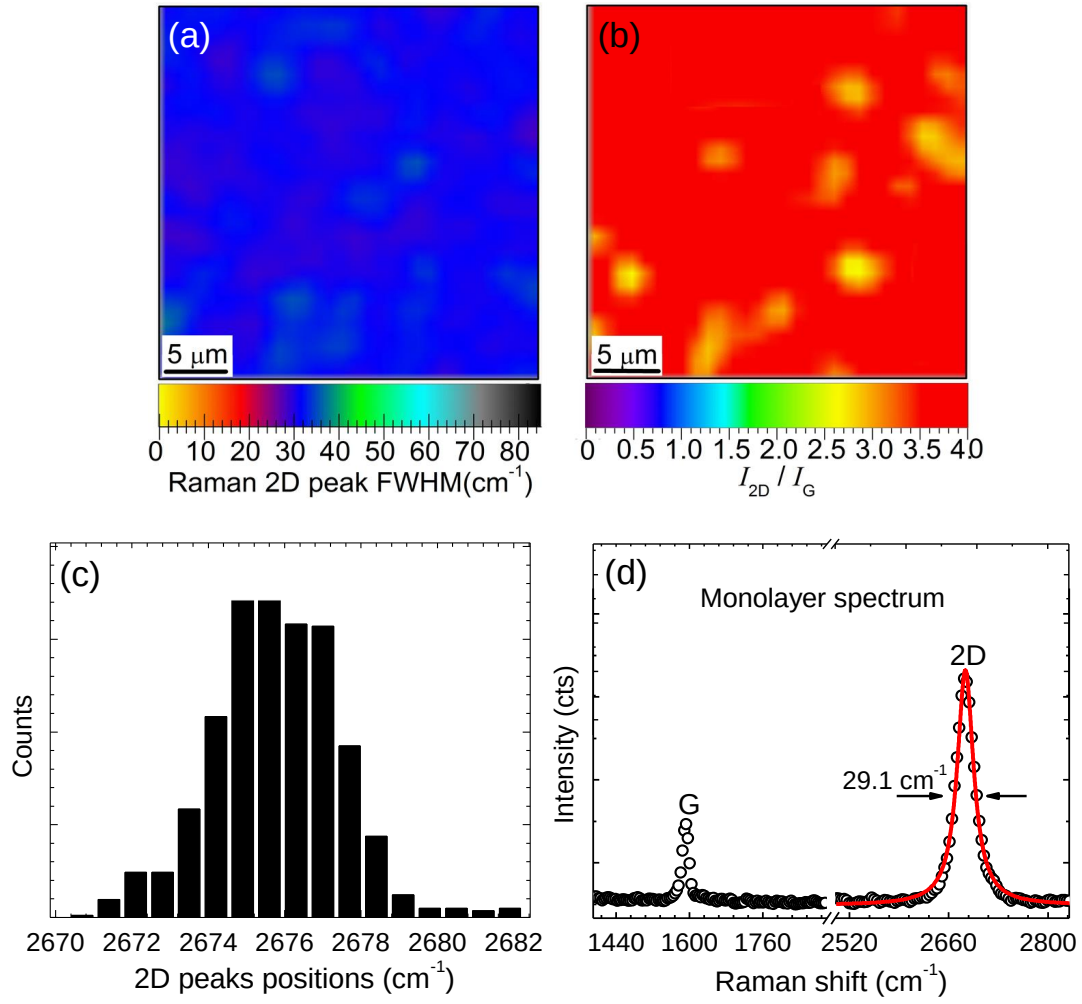

Figure S2. (a) The mapping of 2D peaks FWHMs and of the corresponding (b) 2D to G peaks intensities ratio (I_{2D}/I_G) for monolayer graphene film transferred onto 300 nm SiO_2/Si substrate. (c) The distribution of the 2D peak positions. (d) Raman spectrum from data mapped in figure S2(a) and the 2D peak solid-line is Lorentzian fit.

Table S1. Analysis results of Raman spectra of monolayer graphene film obtained on Cu foil substrate and transferred onto 300 nm SiO_2/Si for characterization.

Graphene	**CVD substrate**	**2D peaks**		**2D/G peaks**
		Position (cm^{-1})	**FWHM (cm^{-1})**	
Monolayer	Cu	2670−2682	28−36	2.5−4

SEM and Raman data of bilayer graphene obtained on a pure Cu foil

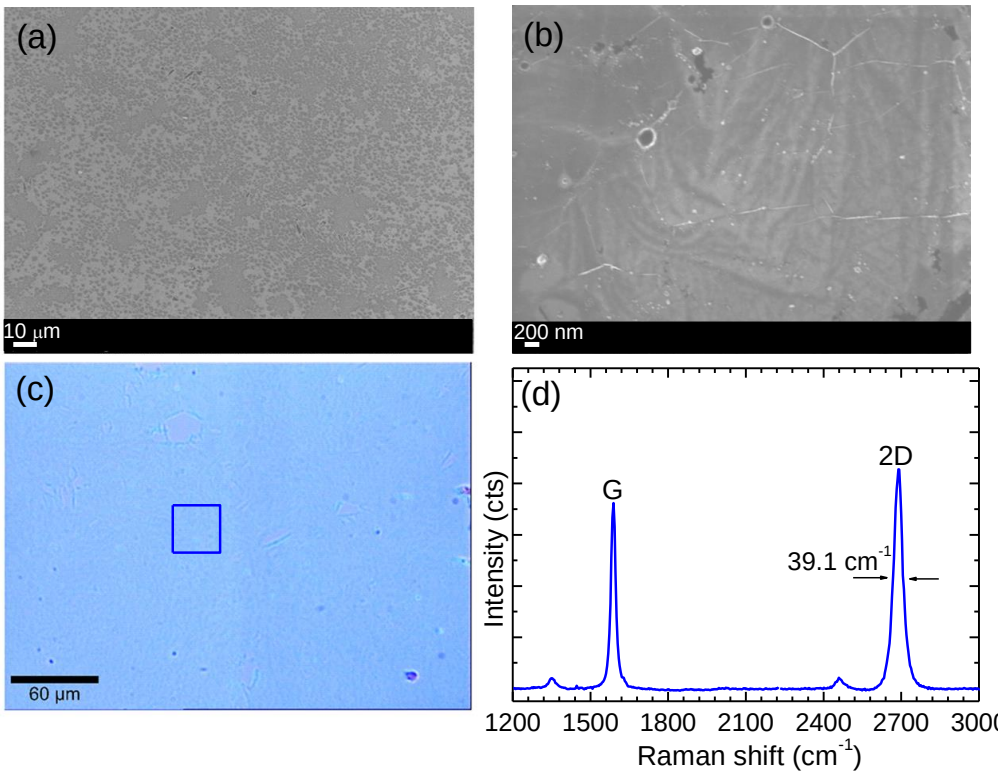

Figure S3. (a-b) SEM micrographs of a bilayer graphene film (at low and high magnifications respectively) transferred onto 300 nm SiO_2/Si substrate. (c) Raman optical microscope image of bilayer graphene film on 300 nm SiO_2/Si substrate and the corresponding (d) average Raman spectra of spectra acquired from 30 μm^2 area (indicated with a square box in figure S3(c)) of a bilayer graphene film.

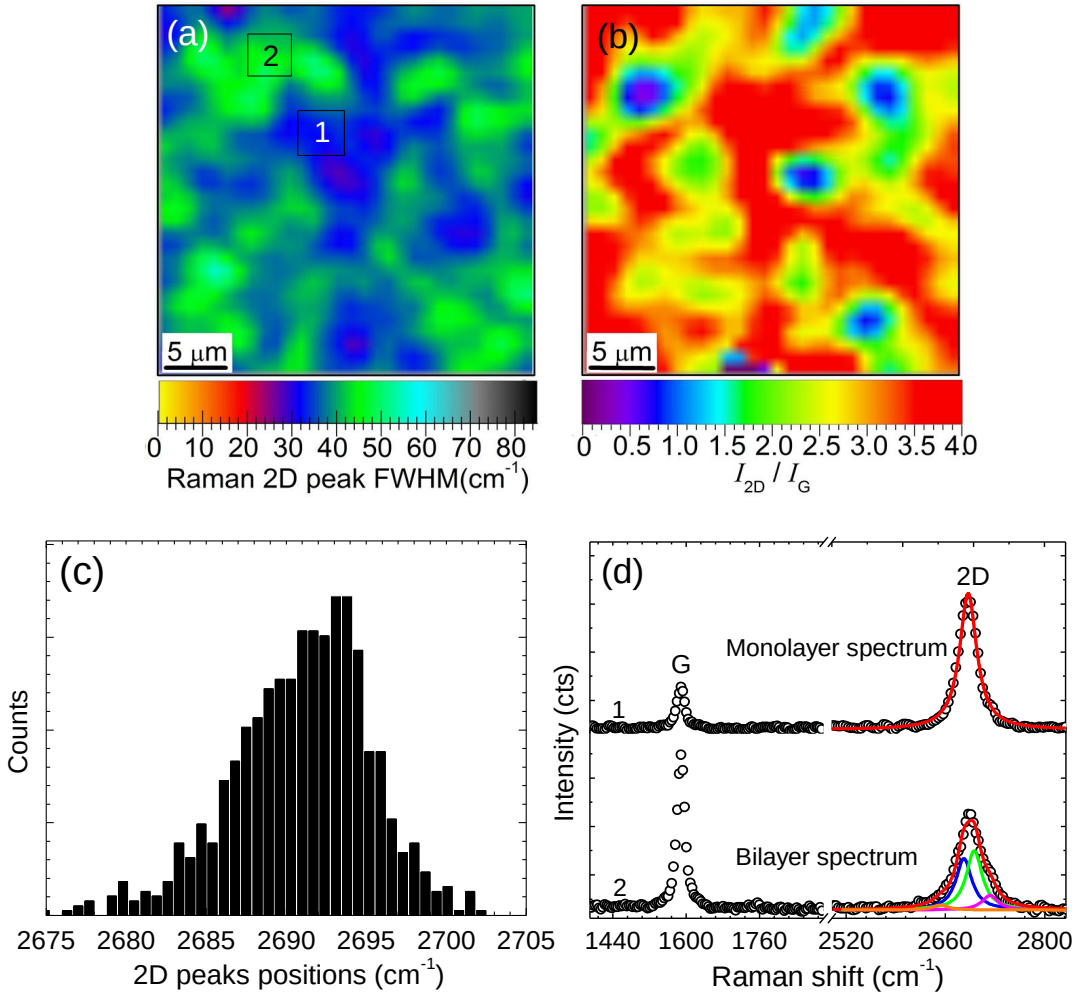

Figure S4. (a) The mapping of 2D peaks FWHMs and of the corresponding (b) 2D to G peaks intensities ratio (I_{2D}/I_G) for bilayer graphene film transferred onto 300 nm SiO_2/Si substrate. (c) The distribution of the 2D peaks positions. (d) Raman spectrum 1 and 2 are from area 1 and 2 in figure S4(a) respectively and the 2D peaks solid-lines are Lorentzians fits.

Table S2. Analysis results of Raman spectra of bilayer graphene film obtained on Cu foil substrate and transferred onto 300 nm SiO_2/Si for characterization.

Graphene	CVD substrate	2D peaks		2D/G peaks
		Position (cm^{-1})	FWHM (cm^{-1})	
Bilayer	Cu	2675−2703	28−53	0.8−4

SEM and Raman data of bilayer graphene obtained on Cu(0.61 at% Ni) foil

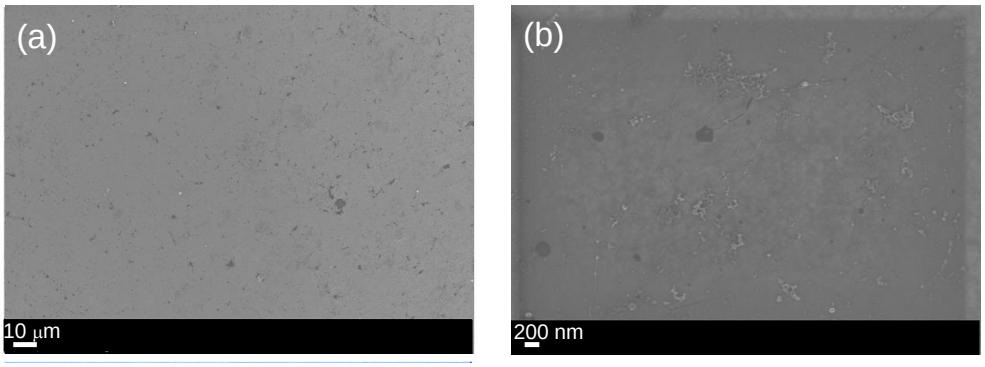

Figure S5. (a-b) SEM micrographs of a bilayer graphene film (at low and high magnifications respectively) transferred onto 300 nm SiO_2/Si substrate.

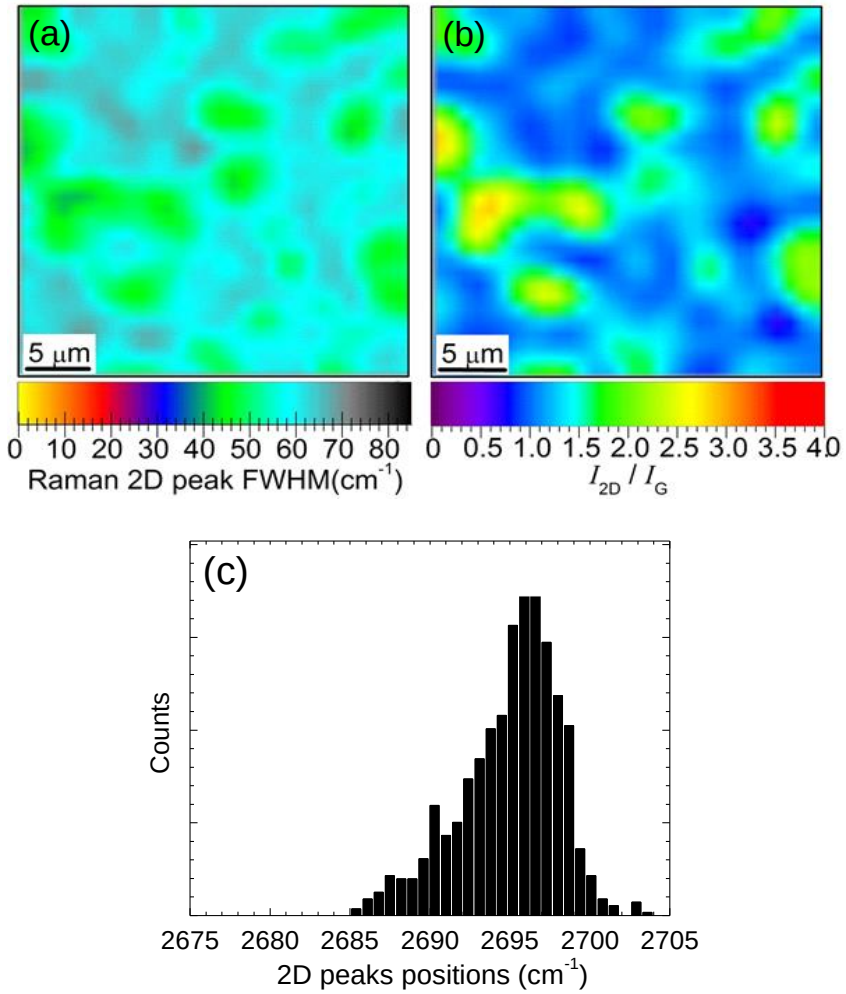

Figure S6. (a) The mapping of 2D peaks FWHMs and of the corresponding (b) 2D to G peaks intensities ratio (I_{2D}/I_G) for bilayer graphene film obtained on Cu(0.61 at% Ni) foil and transferred onto 300 nm SiO_2/Si substrate. (c) The distribution of the 2D peaks positions.

Table S3. Analysis results of Raman spectra of bilayer graphene film obtained on Cu(0.61 at% Ni) foil substrate and transferred onto 300 nm SiO_2/Si for characterization.

Graphene	CVD substrate	2D peaks		2D/G peaks
		Position (cm^{-1})	FWHM (cm^{-1})	
Bilayer	Cu(0.61 at% Ni)	2685−2703	38−70	0.8−2.5

TEM and SAED images of bilayer graphene film obtained on Cu(0.61 at% Ni) foil

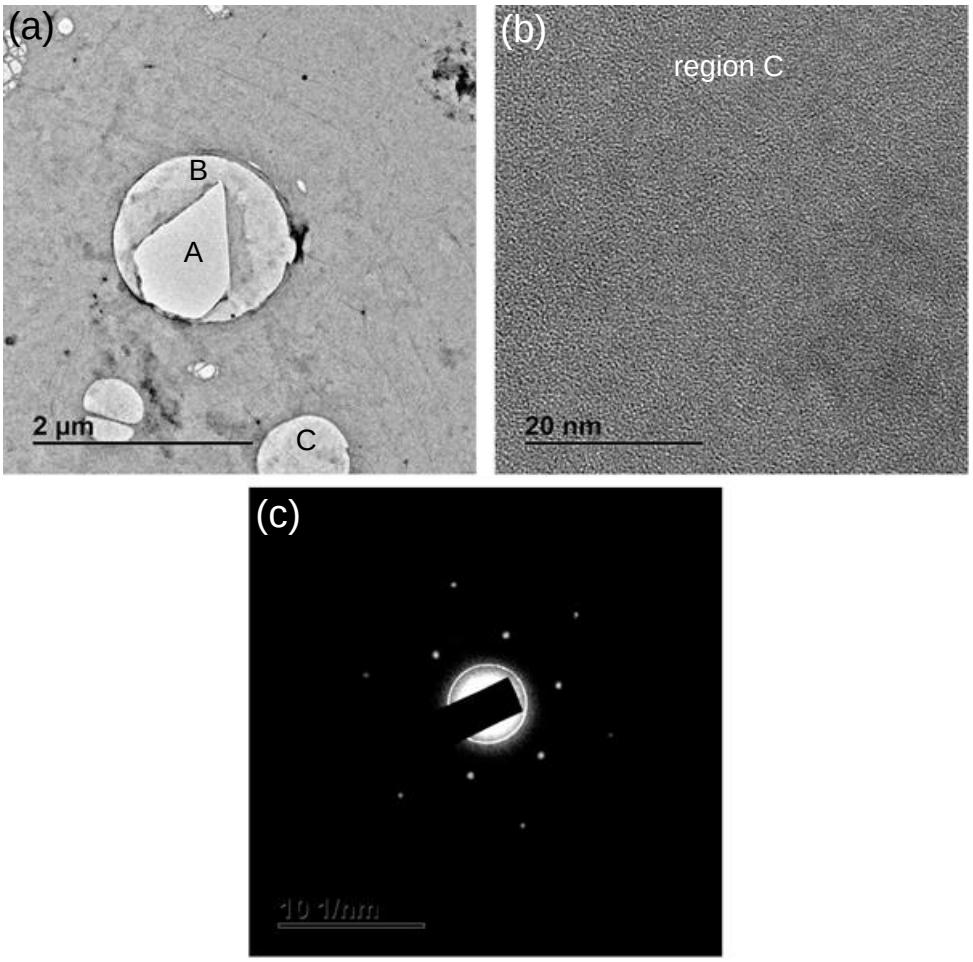

Figure S7. (a) Low magnification TEM image of bilayer graphene film obtained on Cu(0.61 at% Ni) foil and transferred on a lacey carbon TEM grid (region A, B and C shown in holes of a lacey carbon TEM grid show an area without graphene (A) and with graphene (B and C). (b) A high magnification TEM image of graphene in region C of figure (a). (c) A selected area electron diffraction pattern from an area shown in figure (b) and shows two sets of hexagonal diffraction spots.

Sheet resistance of monolayer (1LG) and bilayer (2LG) graphene films obtained on Cu and Cu(0.61 at% Ni) foils

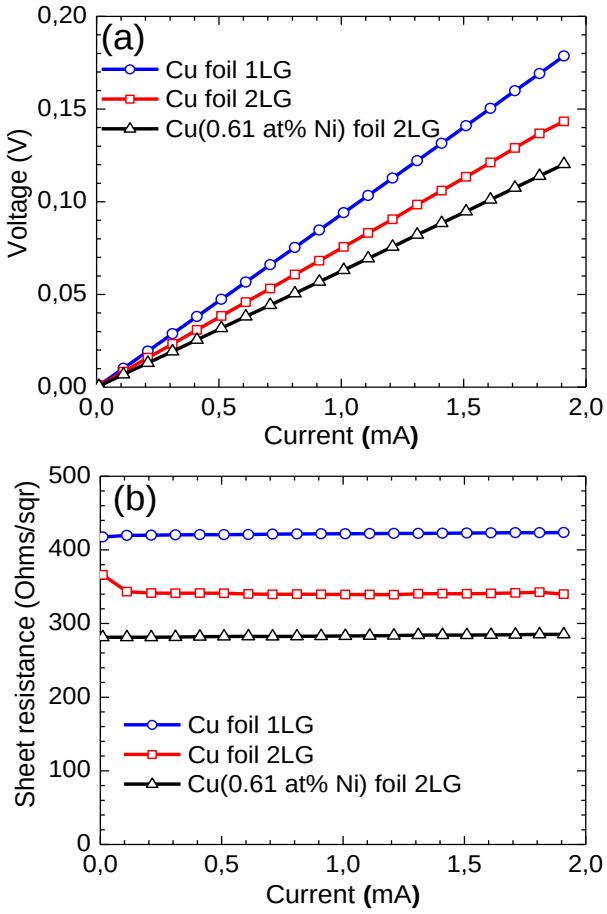

Figure S8. (a) A four-point probe measured voltage drop and (b) the corresponding sheet resistance of monolayer (1LG) and bilayer (2LG) graphene films obtained on Cu and dilute Cu(0.61 at% Ni) foils and transferred onto SiO_2/Si substrates.

Ni surface concentration in Cu(0.61 at% Ni) catalyst during AP-CVD graphene growth

During CVD graphene growth, a catalyst temperature is increased at a constant heating rate from room temperature to the desired growth temperature, and immediately after growth the temperature of the graphene/catalyst is decreased rapidly to room temperature. In a dilute Cu(0.61 at% Ni) catalyst, a temperature increase results in bulk-to-surface diffusion of Ni (due to the dependence on the Arrhenius term) which increases the surface concentration of Ni in the catalyst foil. Such increase in the surface concentration of Ni could be well-described by a semi-infinite solution of Fick's diffusion equation[1]. In the semi-infinite solution of Fick, the surface enrichment factor (β) at temperature, T, is given by

$$\beta(T) = \frac{X^S(T) - X^B}{X^B} \tag{1}$$

where $X^S(T)$ is the surface concentration at temperature, T and X^B is the bulk concentration of the diffusing solute atoms (X^B = 0.61 at% in a dilute Cu(0.61 at% Ni) catalyst).

The temperature dependence of the enrichment factor in the semi-infinite solution of Fick is given by[1]

$$\frac{X^S(T) - X^B}{X^B} = \left\{ \frac{4D_0}{\pi \alpha d^2} \left[\frac{RT^2}{Q} \exp(-Q/RT) \right] \right\}^{\frac{1}{2}} \tag{2}$$

where D_0 is the pre-exponential factor, Q is the activation energy ($D_0 = 7.0 \times 10^{-5}$ m^2/s, Q = 225.0 kJ/mol for Ni diffusion in Cu[2]), α is the constant heating rate, d is interlayer distance (d = 0.181 nm in Cu(001)), R is the gas constant and T is the crystal temperature.

Equation 2 could well describe the temperature dependence of the surface concentration of Ni in dilute Cu(0.61 at% Ni) catalyst, however, cannot describe the temperature dependence of the maximum (or equilibrium) surface concentration of Ni in a catalyst. Nonetheless, the temperature dependence of the maximum surface concentration of Ni in a catalyst could be well-described by the well-known Langmuir– McLean equation[1,3]:

$$\frac{X^\phi(T)}{1 - X^\phi(T)} = \frac{X^B}{1 - X^B} \exp(-\Delta G/RT) \tag{3}$$

where $X^{\phi}(T)$ is the relative surface concentration at temperature, T, $X^{\phi}(T) = \frac{X^{S}(T)}{X^{M}}$, X^{M} is the attainable maximum surface concentration (X^{M} = 25 at% in Cu(001)[4]) of solute atoms in the crystal surface, ΔG is the segregation energy.

Generally, $\Delta G = \Delta H - T\Delta S$, where ΔH is the segregation enthalpy, T is the temperature and ΔS is the segregation entropy. In dilute alloys, ΔS is negligible hence $\Delta G \approx \Delta H$ and the segregation enthalpy can be approximated by[5,6]

$$\Delta H = \left(\frac{\Delta Z}{Z}\right)\left(\Delta H_{B}^{sub} - \Delta H_{A}^{sub}\right) \tag{4}$$

where Z is the bulk coordination number (Z = 12 for Cu crystal), ΔZ is the difference in coordination number between bulk and surface (ΔZ = 4 for Cu(001)), ΔH^{sub} is the heat of sublimation for element A and B ($\Delta H_{\text{Cu}}^{sub} = 339.3$ kJ/mol, $\Delta H_{\text{Ni}}^{sub} = 430.1$ kJ/mol and $\Delta H_{\text{C}}^{sub} = 521.7$ kJ/mol[7]).

Following from equation 4, the segregation energy for Ni in Cu(001) surface is ΔG = 30.3 kJ/mol. Now, using the semi-infinite solution of Fick (equation 2) and the Langmuir– McLean equation (equation 3), a view of the temperature dependence of the Ni surface concentration in a dilute Cu(0.61 at% Ni) catalyst during AP-CVD graphene growth was obtained as shown in figure S9. In figure S9, an increase in catalyst temperature increases the surface concentration of Ni (described by Fick solid-line) until it reaches a maximum (or equilibrium) surface concentration of 8.1 at% (determined by Fick and Langmuir–McLean solid-lines intersection) and a further increase in temperature result in a decrease in surface concentration of Ni due to surface-to-bulk diffusion of Ni or due to the sublimation of Ni, but at these catalyst temperatures (<1000 °C) and higher background pressure (atmospheric pressure) the sublimation of Ni (and Cu) is suppressed. At a CVD growth temperature of 980 °C a surface concentration of Ni is 2.1 at% in Cu(0.61 at% Ni) catalyst.

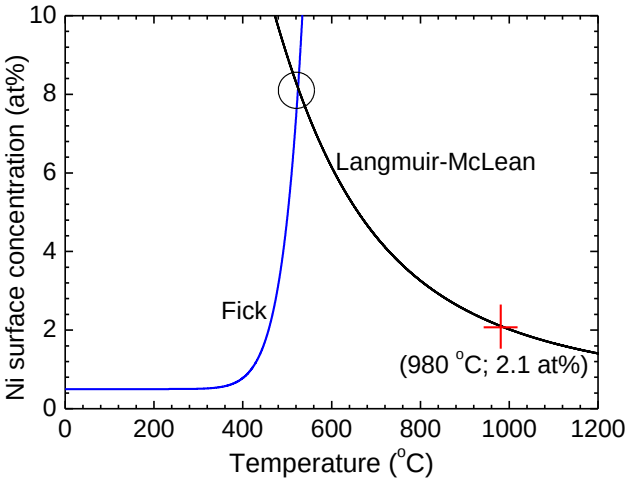

Figure S9. An illustration of the temperature dependence of the Ni surface concentration in a dilute Cu(0.61 at% Ni) catalyst at a constant heating rate of α = 0.5 °C/s.

References

1 E. C. Viljoen and J. du Plessis, *Surface Science*, 1999, **431**, 128–137.

2 W. F. Gale and T. C. Totemeier, Eds., *Smithells Metals Reference Book*, Butterworth-Heinemann, Oxford UK, 8th edn., 2004.

3 D. R. Harries and A. D. Marwick, *Philosophical Transactions of the Royal Society A: Mathematical, Physical and Engineering Sciences*, 1980, **295**, 197–207.

4 E. C. Viljoen and J. du Plessis, *Surface Science*, 2000, **468**, 27–36.

5 K. Wandelt and C. R. Brundle, *Physical Review Letters*, 1981, **46**, 1529–1532.

6 S. Hofmann, R. Frech and W. Germany, *Analytical Chemistry*, 1985, **57**, 716–719.

7 D. R. Lide, *CRC Handbook of Chemistry and Physics*, CRC Press, Inc., 63rd edn., 2005.

7.5 Concluding remarks

This part of the study demonstrated the synthesis of a wafer-scale and high-quality AB-stacked bilayer graphene film on a dilute Cu(0.61 at% Ni) foil using AP-CVD. AFM, SEM, Raman, TEM/SAED and four-point probe/sheet resistance analysis showed that a bilayer graphene film obtained on a dilute Cu(0.61 at% Ni) foil is of high-quality, continuous over entire graphene film and mainly AB stacked. This part of the study clearly showed the capability of a dilute Cu(0.61 at% Ni) foil for growing a wafer-scale bilayer graphene film compared to a pure Cu foil which showed discrete bilayer graphene domains on a monolayer graphene background in AP-CVD. The capability of a dilute Cu(0.61 at% Ni) foil for growing a wafer-scale bilayer graphene film was ascribed to the metal surface catalytic activity of Cu and Ni in a dilute Cu(0.61 at% Ni) foil and the (001) continuous crystallographic surface of a foil. In a dilute Cu(0.61 at% Ni) foil, a high surface concentration of Ni compared to a low bulk concentration of Ni was confirmed with TOF-SIMS and XPS.

CHAPTER 8

General conclusions and future work

8.1 Introduction

In this chapter, the main results reported and discussed in chapter 5, 6 and 7 are summarised below, including a summary of growth substrates and high-quality bilayer graphene coverage obtained on these substrates (using CVD and CH_4 as a carbon source) found in literature and this study. This chapter includes a brief discussion on the possible future work of this study. It is worth mentioning that graphene films prepared in this study were carried out under optimized AP-CVD growth conditions for monolayer and bilayer graphene growth on Cu foils. A detailed study on the optimization of these growth conditions was carried out by M. Fabiane in the PhD thesis [1]. Though, a term wafer usually refers to thin substrates ($\geq$10 cm in diameter) of semiconductor material (e.g silicon) used in electronics industry. In this study, a term wafer-scale was used to refer to the Cu foil substrate size ($\approx$4 cm^2).

8.2 General conclusions

The purpose of this study was to synthesize high-quality large-area or wafer-scale ($\approx 20 \times 20$ mm^2) AB-stacked bilayer graphene films using AP-CVD. The major interest in the AB-stacked bilayer graphene film stems from its unique band structure with a tunable bandgap which determines transport and optical properties; as a result, it offers the possibility for practical applications such as field-effect transistors and light detectors [2-5].

For the synthesis of high-quality large-area or wafer-scale AB-stacked bilayer graphene films using AP-CVD, this study proposed the use of homogeneous dilute Cu(Ni) foil with an average Ni bulk concentration of 0.5 at% and continuous or large-area (001) surface orientation. Firstly, this study focused on growing high-quality large-area AB-stacked bilayer graphene on commercial Cu(0.5 at% Ni) foil (MaTeck) consisting of a diverse crystallographic surface. Secondly, the study focused on the solid state diffusion doping of a 25 μm thick annealed Cu foil for graphene growth (Alfa Aesar) with 0.5 at% Ni. A Ni doping of this particular Cu foil was motivated by its continuous crystallographic surface composed of a single (001) orientation which is known to grow multilayer graphene. Finally, the capability of a Ni-doped Cu foil for growing a wafer-scale AB-stacked bilayer graphene film using AP-CVD was demonstrated.

In chapter 5, this study focused on growing monolayer and bilayer graphene films on commercial dilute Cu(0.5 at% Ni) foils (MaTeck) using AP-CVD and from the Raman optical microscope images of these graphene films, a wafer-scale monolayer and large-area bilayer graphene films were distinguished and confirmed with Raman spectra data. The Raman data suggested a Bernal stacking order in prepared bilayer graphene film. A four-point probe sheet resistance of graphene films confirmed a bilayer graphene film sheet resistance distinguished from that of monolayer graphene. The large-area part of bilayer graphene film obtained was assisted by Ni surface concentration since Ni has higher methane decomposition rate compared to Cu. A relatively higher Ni surface concentration in Cu(0.5 at% Ni) foil was confirmed with TOF-SIMS. The diverse crystallographic surface of a foil (confirmed with EBSD) could be a reason for incomplete wafer-scale bilayer graphene film since Cu(111) surface typically grows monolayer graphene which influences graphene growth of adjacent grains [6-9]. Consequently, this part of the study proposed a homogeneous dilute Cu(0.5 at% Ni) foil consisting of low index Cu(001) or Cu(101) surfaces to achieve a wafer-scale AB-stacked bilayer graphene film in AP-CVD.

Interestingly, a 25 μm thick annealed Cu foil for graphene growth (Alfa Aesar) has a continuous crystallographic surface composed of a single (001) orientation (confirmed with EBSD). Therefore, in chapter 6, this foil was doped with $\approx$0.5 at% Ni for a wafer scale bilayer graphene growth using AP-CVD. In graphene films obtained from the Ni-doped Cu foils, the number of graphene layers contained in films and the AB stacking order of synthesised graphene films were confirmed by Raman and electron diffraction pattern measurements. The Ni-doped Cu foil demonstrated the good capability of growing large-area AB-stacked bilayer graphene by

increasing Ni content in Cu surface layer thus altering a composition of a Cu surface where the decomposition of hydrocarbons occurs.

In chapter 7, this study demonstrated the synthesis of a wafer-scale and high-quality AB-stacked bilayer graphene film on a dilute Cu(0.61 at% Ni) foil (the Ni-doped Cu foil (Alfa Aesar)) using AP-CVD. AFM, SEM, Raman, TEM/SAED and four-point probe/sheet resistance analysis showed that a bilayer graphene film obtained on a dilute Cu(0.61 at% Ni) foil has high-quality and is continuous over entire graphene film (and mainly AB-stacked). A CVD substrate with a surface layer elemental composition of about 97 at% Cu and 3 at% Ni grow bilayer graphene with an AB-stacked yield in the range of 95-100 % which is attributed to the surface catalytic graphene growth mode with a certain methane decomposition rate [10]. In a dilute Cu(0.61 at% Ni) foil, a high surface concentration of Ni compared to a low bulk concentration of Ni was confirmed with TOF-SIMS and XPS.

Generally, a Cu foil (in CVD synthesis of graphene) has a challenge of growing large-area bilayer graphene with uniform thickness (it only grows discrete bilayer graphene domains on monolayer background, (see table 8.1)) and such challenge of Cu is ascribed primarily to the low decomposition rate of hydrocarbon which leads to the insufficient supply of carbon atoms required for large-area bilayer graphene [6,10,19]. A Cu surface engineered with Ni has demonstrated a capability of growing large-area bilayer graphene (see table 8.1). It is worth mentioning that in non-dilute commercial Cu(88.0 wt%)-Ni(9.9 wt%) [20] and Cu(67.8 wt%)-Ni(31.0 wt%) [6] foils and Cu/Ni thin films [10], CVD graphene growth could dominate from carbon segregation process, because of increased solid solubility of carbon in Cu by Ni which leads to variation in the thickness uniformity and reduced yield of AB-stacked bilayer graphene [6,11-13]. However, in dilute Cu(Ni) foils, carbon segregation process would be suppressed due to a much lower solid solubility of carbon in dilute Cu(Ni) foil and as a result, graphene growth will predominantly occur through surface growth mechanism during hydrocarbon exposure.

In summary, this study clearly showed the capability of a dilute Cu(Ni) foil (Alfa Aesar) (the Ni doped Cu foil) for growing a wafer-scale AB-stacked bilayer graphene film (substrate size, $\approx$400 mm^2) compared to a commercial Cu(0.5 at% Ni) foil (MaTeck) which showed large-area bilayer graphene ($\approx$900 μm^2) and a pure Cu foil which showed discrete bilayer graphene domains (lateral size of $\approx$10 μm) on a monolayer graphene background. The capability of a dilute Cu(Ni)

Ref.	Growth substrates	Preferential surface orientation of growth substrates	Largest bilayer domains lateral size	Remarks
[14]	Cu foil enclosure	–	>20 μm (≈70 % foil coverage)	Discrete bilayer graphene domains
[15]	Flat Cu	–	≈10 μm	Discrete multilayer graphene domains
[16]	Cu foil	–	50 μm (67 % foil coverage)	Discrete bilayer graphene domains
[17]	Cu foil	–	20 μm (≈90 % foil coverage)	Discrete graphene domains
[18]	Cu foil	–	–	Discrete bilayer graphene domains
[19]	Cu foil	–	<10 μm	Discrete multilayer graphene domains
[20]	Cu-Ni foil Cu(88.0 wt%) Ni(9.9 wt%) (commercial)	–	>6400 μm^2 (>96 % foil coverage)	Large-area, uniform bilayer graphene
[6]	Cu-Ni foil Cu(67.8 wt%) Ni(31.0 wt%) (commercial)	(111) and (100)	>4900 μm^2	Large-area, uniform bilayer graphene
[10]	Cu/Ni thin films Cu(1200 nm) Ni(400 nm)	–	≈5806 mm^2 (substrate size) (≈98 % foil coverage)	Substrate size, uniform bilayer graphene
This study	Cu foil	Continuous (001) surface	≈10 μm (>90 % foil coverage)	Discrete bilayer graphene domains
This study	Dilute Cu(0.5 at% Ni) foil (MaTeck) (commercial)	Diverse crystallographic surface	≈900 μm^2 (≈80 % foil coverage)	Large-area, uniform bilayer graphene
This study	Dilute Cu(0.5 at% Ni) foil (Alfa Aesar) (Ni doped)	Continuous (001) surface	≈400 mm^2 (substrate size) (≈98 % foil coverage)	Substrate size, uniform bilayer graphene

Table 8.1: Summary of growth substrates and high-quality bilayer graphene (largest domains lateral size and foil coverage) obtained on these substrates using CVD and CH_4 as a carbon source.

foil for growing a wafer-scale AB-stacked bilayer graphene film was ascribed to the metal surface catalytic activity of Cu and Ni and the (001) continuous surface orientation in a dilute Cu(Ni) foil. On a Cu(100) surface, atomic carbon is more stable and the stability is further improved by Ni in Cu-Ni(100) surface [7,21]. Consequently, the surface concentration of carbon on the Cu-Ni(100) surface would be much higher than on pure Cu surface suggesting that the Cu's capability of decomposing the hydrocarbon is mainly enhanced by Ni surface concentration in Cu [7,21].

Both Alfa Aesar and MaTeck dilute Cu(Ni) foils showed the presence of impurities in the foil surface. These impurities have much lower bulk concentrations, in a few ppm and Ni has 5000 ppm (0.5 at%) which act as Ni supplier to reach high Ni surface concentrations in dilute Cu(0.5 at% Ni) foils. As a result, surface Ni in dilute Cu(Ni) foils contributed significantly during CVD graphene growth on dilute Cu(Ni) foils.

8.3 Future work

In this study and other published studies, the capability of Cu-Ni alloy to grow large-area AB-stacked bilayer graphene compared to Cu which is known to grow islands of bilayer graphene with a significant fraction of non-AB stacking is discussed on the basis of hydrocarbon decomposition rate (metal surface catalytic activity). However, a discussion on the driving energy (formation energy) of a favourable growth of AB-stacked bilayer graphene layers on dilute Cu(Ni) substrate compared to Cu is lacking in the literature. In addition, the "surface effect" of the (100), (110) and (111) surface orientations of a dilute Cu(Ni) foil on the AB-stacking of bilayer graphene layers has not received attention.

Possible future work will involve the following: We will investigate the formation energy of a favourable growth of AB-stacked bilayer graphene layers on dilute Cu(Ni) substrate compared to Cu and the influence of the dilute Cu(Ni) surface ("surface effect") on the AB-stacking of bilayer graphene layers both experimentally (using AP-CVD growth) and computationally (using Density Functional Theory). Lastly, we will study the electrochemical performance of the bilayer graphene composites for micro-supercapacitor applications.

Bibliography

1. M. Fabiane, Chemical vapour deposition of graphene: Fundamental aspects of synthesis and characterization, PhD thesis, University of Pretoria, 2014.

2. K. Zou, J. Zhu, Transport in gapped bilayer graphene: The role of potential fluctuations, Physical Review B - Condensed Matter and Materials Physics. 82 (2010) 1-4.

3. T. Taychatanapat, P. Jarillo-Herrero, Electronic transport in dual-gated bilayer graphene at large displacement fields, Physical Review Letters. 105 (2010) 1-4.

4. J. Yan, M.S. Fuhrer, Charge transport in dual gated bilayer graphene with corbino geometry, Nano Letters. 10 (2010) 4521-4525.

5. K.F. Mak, C.H. Lui, J. Shan, T.F. Heinz, Observation of an electric-field-induced band gap in bilayer graphene by infrared spectroscopy, Physical Review Letters. 102 (2009) 100-103.

6. S. Chen, W. Cai, R.D. Piner, J.W. Suk, Y. Wu, Y. Ren, et al., Synthesis and characterization of large-area graphene and graphite films on commercial Cu-Ni alloy foils, Nano Letters. 11 (2011) 3519-3525.

7. W. Zhang, P. Wu, Z. Li, J. Yang, First-principles thermodynamics of graphene growth on Cu surfaces, Journal of Physical Chemistry C. 115 (2011) 17782-17787.

8. L. Hansen, P. Stoltze, K.W. Jacobsen, J.K. Nørskov, Self-diffusion on copper surfaces, Physical Review B. 44 (1991) 6523-6526.

9. J.D. Wood, S.W. Schmucker, A.S. Lyons, E. Pop, J.W. Lyding, Effects of polycrystalline Cu substrate on graphene growth by chemical vapor deposition, Nano Letters. 11 (2011)

4547-4554.

10. W. Liu, S. Kraemer, D. Sarkar, H. Li, P.M. Ajayan, K. Banerjee, Controllable and rapid synthesis of high-quality and large-area bernal stacked bilayer graphene using chemical vapor deposition, Chemistry of Materials. 26 (2014) 907-915.

11. Y. Wu, H. Chou, H. Ji, Q. Wu, S. Chen, W. Jiang, et al., Growth Mechanism and Controlled Synthesis of AB-Stacked Bilayer Graphene on Cu-Ni Alloy Foils, ACS Nano. (2012) 7731-7738.

12. N. Liu, L. Fu, B. Dai, K. Yan, X. Liu, R. Zhao, et al., Universal Segregation Growth Approach to Wafer-Size Graphene from Non-Noble Metals, Nano Letters. 11 (2011) 297-303.

13. A. Reina, X. Jia, J. Ho, D. Nezich, H. Son, V. Bulovic, et al., Large area, few-layer graphene films on arbitrary substrates by chemical vapor deposition, Nano Letters. 9 (2009) 30-35.

14. W. Fang, A.L. Hsu, R. Caudillo, Y. Song, A.G. Birdwell, E. Zakar, et al., Rapid identification of stacking orientation in isotopically labeled chemical-vapor grown bilayer graphene by Raman spectroscopy, Nano Letters. 13 (2013) 1541-1548.

15. X. Li, W. Cai, L. Colombo, R.S. Ruoff, Evolution of Graphene Growth on Ni and Cu by Carbon Isotope Labeling, Nano Letters. 9 (2009) 4268-4272.

16. K. Yan, H. Peng, Y. Zhou, H. Li, Z. Liu, Formation of bilayer bernal graphene: layer-by-layer epitaxy via chemical vapor deposition., Nano Letters. 11 (2011) 1106-10.

17. X. Li, C.W. Magnuson, A. Venugopal, J. An, J.W. Suk, B. Han, et al., Graphene Films with Large Domain Size by a Two-Step Chemical Vapor Deposition Process, Nano Letters. 10 (2010) 4328-4334.

18. S. Nie, W. Wu, S. Xing, Q. Yu, J. Bao, S. Pei, et al., Growth from below: bilayer graphene on copper by chemical vapor deposition, New Journal of Physics. 14 (2012) 093028.

19. S. Bhaviripudi, X. Jia, M.S. Dresselhaus, J. Kong, Role of Kinetic Factors in Chemical Vapor Deposition Synthesis of Uniform Large Area Graphene Using Copper Catalyst, Nano

Letters. 10 (2010) 4128-4133.

20. Y. Wu, H. Chou, H. Ji, Q. Wu, S. Chen, W. Jiang, et al., Growth mechanism and controlled synthesis of AB-stacked bilayer graphene on Cu-Ni alloy foils., ACS Nano. 6 (2012) 7731-8.

21. T. Wu, X. Zhang, Q. Yuan, J. Xue, G. Lu, Z. Liu, et al., Fast growth of inch-sized single-crystalline graphene from a controlled single nucleus on Cu-Ni alloys., Nature Materials. 15 (2015) 43-47.